3D Trajectory Calculation in Crash Testing Using Inertial Sensors

---

A Dissertation

Presented to

the faculty of the School of Engineering and Applied Science

University of Virginia

---

in partial fulfillment
of the requirements for the degree

Doctor of Philosophy

by

Jacek Toczyski

May 2019

APPROVAL SHEET

This Dissertation
is submitted in partial fulfillment of the requirements
for the degree of
Doctor of Philosophy

Author Signature: _Jacek Toczyski_

This Dissertation has been read and approved by the examining committee:

Advisor: Jason R. Kerrigan

Committee Member: Matthew B. Panzer

Committee Member: Shawn Russell

Committee Member: Daniel Quinn

Committee Member: Jason Forman

Committee Member: _____

Accepted for the School of Engineering and Applied Science:

Craig H. Benson, School of Engineering and Applied Science

May 2019

ABSTRACT

Optical motion-tracking systems are an accurate method of capturing motion of a body traveling through a 3-dimensional (3D) space. There are several disadvantages of these systems, including cost, the time consumed in performing the tracking, and especially the requirement of a constant line of sight between the cameras and the tracked object throughout the analyzed event. An alternative to optical based tracking is an approach that utilizes body local acceleration and angular velocity recorded by inertial measurement units (IMUs).

The advancement in the MEMS technology allowed for small, light and inexpensive accelerometers and angular rate sensors to be more accessible. Data from these sensors can be utilized to obtain the position and orientation of the body on which they are attached. Even though sensor-based motion capture offers many benefits, it has been shown to be less accurate than optical motion-tracking due to multiple types of signal and sensor errors and uncertainty associated with the initial orientation of tracked body. In addition, there are multiple numerical formulas (for example the one that is utilized to obtain body's orientation) that can be used as part of the trajectory calculation algorithm but there is no consensus on how these different methods affect the resulting sensor-based position estimation.

Even though sensor-based tracking has its limitations, research has shown that it can be a promising alternative to optical capture systems under certain conditions. Before the IMU-based position estimation can replace more costly and time-consuming optical motion capture, the accuracy of trajectories obtained from processed IMU data needs to be improved and the reasons behind errors in sensor-based predictions better understood, so that the method can be employed in a way to facilitate its success.

This dissertation presents the development of an algorithm that can be used to compute 3D component trajectories of a rigid body – based on locally-mounted inertial sensors – for applications in vehicle crash tests with anthropomorphic test devices. In addition to the algorithm, this dissertation identifies different correction techniques that could be used to minimize the error in the calculated trajectory when sensor readings are affected by measurement inaccuracies. These goals were accomplished through the following tasks. The first task focused on assembling a training set for verification and validation of the proposed algorithm using data from progressively more complex impact scenarios. Next, from different methods identified in the literature, the most accurate technique of updating body orientation based on body's angular rate (Task 2) as well as the most accurate method of obtaining body's local angular acceleration (Task 3) were identified. In Task 4, a comprehensive study investigating the influence of different error types on the IMU-based trajectories was carried out. In the final task, different techniques that could be used to minimize the error in the calculated trajectory were evaluated.

Analysis from Task 2 indicated two algorithms based on the Euler parameters as the most accurate methods of updating body's orientation. In addition, the analysis showed that the accuracy of the method used to update body's orientation depends strongly on the accuracy of the numerical integration scheme utilized in the orientation algorithm. Investigation from Task 3 identified the approach based on differentiation of the local angular velocity as the method that gave the smallest deviation from the reference (from an optical motion capture system) position data. The analysis from Task 4 described the errors in the debias values for linear accelerometers and angular rate sensors, the error in accelerometer sensitivity, as well as the error in initial orientation as error types that can have the most substantial effect on the IMU-based trajectory estimation. The error analysis also showed that by adding two redundant angular rate sensors to a standard "3 ACC + 3 ARS" package, an angular rate sensor with errors in its signal can be identified. Similarly, by adding two redundant linear accelerometers, an accelerometer with a faulty response can be pinpointed. When (in Task 5) either optimization of initial orientation angles in combination with the debias values for linear acceleration data was performed, or known information about 3D position of the tracked body was introduced into the trajectory calculation algorithm, a substantial improvement in the accuracy of the computed position of the tracked body was achieved. Even when only three data points with known position were used throughout the analysis, the position error (when compared to a test without these three points) decreased by more than 93% and the maximum absolute difference for all three trajectory components stayed below 5.5 mm when matched against reference data from the optical system. Finally, in Task 5 two techniques of interpolating an optical data gap were investigated.

This dissertation focused on crash scenarios mainly, but its findings and conclusions can be extrapolated and applied in many other fields, ranging from gait and sport studies, through clinical trials and animal motion analysis, to tracking underwater or underground autonomous vehicles.

<u>DEDICATION</u>

To my parents, my brother, and my one and only Michelle. Without your love and support, this would not have been possible. Thank you so much!

CONTENTS

ACKNOWLEDGMENTS

1. INTRODUCTION

1.1 Motivation

Optical based systems are an accurate method of capturing motion (position and orientation) of a body traveling through a 3-dimensional (3D) space (Lessley et al. 2011, Toczyski et al. 2015). These types of systems are used widely to track human body movement and performance in biomechanics and sport studies, clinical sciences, in the entertainment industry to recreate human-like motion for rendered graphics. 3D tracking is also utilized to analyze animal behavior, drone precision flying, or to assess the repeatability of tasks carried out by industrial robots.

The biggest disadvantage of these systems is the requirement of a constant line of sight between the cameras and the tracked object throughout the analyzed event. In situations where motion of that object is obscured (examples shown in Figure 1), optical motion capture cannot provide accurate information about orientation and position of the tracked body.
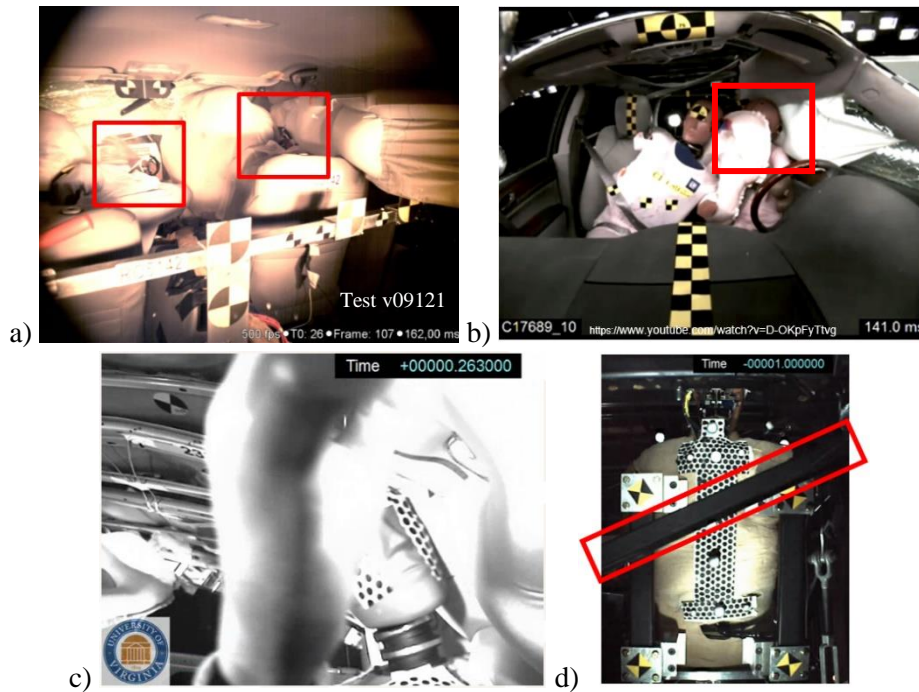
Figure 1. Exemplar obscuration of tracked objects: a) & b) the object (ATD's head) covered by deployed airbags (images from NHTSA 2013 and Laird Wheaton GM 2013, respectively), c) the head obscured by a flailing arm of an ATD (UVA rollover research), d) non-removable object between the cameras and the tracked pattern (Toczyski et al. 2015).

In addition to issues with object occlusion, the post-processing phase for the data obtained from optical systems is often time-consuming and highly user-dependent. The analysis is influenced by a wide range of parameters, including camera type, pixel size, lens and focal length, video resolution, etc. While the systems can be used to capture various ranges of motion, tracked targets requiring additional hardware to be attached to the body are often needed, which may be impractical. Moreover, when the user wants to track motion in a 3D space, tedious calibration is

usually required to define a measurement volume (of a limited size) within which body movement can be recorded.

All of the issues mentioned in the previous paragraph create a challenge in studying body kinematics, especially in a complex environment (e.g. in a car crash). That is why there is a **need** for an **alternative method** of capturing rigid body's motion, a method which will not be affected by whether the tracked object is visible throughout the event or not.

An alternative to optical based tracking is an approach that utilizes the acceleration and angular rate data recorded by inertial measurement units (IMUs), i.e. devices (indirectly) measuring the inertia of a sensing element (e.g. silicon cantilever beam), attached to a body segment. These types of measuring packages are already available, for example, in many different body parts of Anthropomorphic Test Devices (ATDs) used in crash testing, which makes the method convenient to study occupant kinematics inside a vehicle, since no additional sensors or hardware than the ones already installed in an ATD, are required. Moreover, the data from the sensors are ready to use right after the test run is complete, which substantially decreases the time needed for the post-processing analysis when compared to optical motion tracking.

Even though sensor-based motion capture offers many benefits, it has also been known to be less accurate than its optical-based counterpart. Rudd et al. 2006 reported an error up to 59 mm in the trajectory obtained with IMUs with respect to a video analysis of the T1 level for an ATD in a pedestrian-to-vehicle collision. Filippeschi et al. 2017 stated that when an IMU-based prediction of upper limb kinematics was matched against motion measured by the VICON system (Vicon MX, Vicon, Los Angeles, CA, USA), the average position estimation error was approximately 35 mm. In Huculak and Lankarani 2013 the highest difference between the IMU-based and reference (from a video analysis) trajectories (for an ATD head in a sled test) was 43 mm.

On the other hand, though, that maximum difference from Huculak's study was recorded at the end of the analyzed time period, while through most of the test the deviation between both trajectories was less than a few millimeters. Wu et al. 2009 reported the accuracy of their results satisfactory with the relative error at peak of the sensor-based ATD head displacement (again in a sled test) below 5% when compared to the results from a film analysis.

Huculak and Lankarani 2013 and Wu et al. 2009 have shown that body tracking with the use of locally-mounted inertial sensors has a potential and can be a promising alternative to optical capture systems under certain conditions. Before the IMU-based position estimation can replace more costly and time-consuming optical motion capture, the accuracy of trajectories obtained from processed IMU data needs to be improved and the reasons behind errors in sensor-based predictions better understood, so that the method can be employed in a way to facilitate its success.

1.2 Background

1.2.1 Advancement in inertial sensor technology (based on Benser 2015)

Inertial sensor development started over 150 years ago. The first sensor using the inertia of a body – a pendulum utilized to measure Earth's rotation – was demonstrated by Jean Bernard Léon Foucault in 1851. In the early 1900s, large gyroscope-based systems were introduced in ships to reduce their roll motion due to the interaction with waves. In 1914, the first autopilot system for

aircraft was shown during the Airplane Safety Conference in Paris. The system was based on gyroscopes connected with the aircraft's flight controls. Prior to World War II, gyroscope-based systems were integrated with bombs to improve bombing precision.

Strain gauge accelerometers started being used in the mid-1930s in various mechanical applications. Those sensors were big, heavy and expensive, so their application was limited. It changed when piezoelectric accelerometers were introduced. They were developed in the 1940s and 1950s, and offered improved performance at a substantially reduced size and mass.

In the mid-1970s, small Microelectromechanical Systems (MEMS) devices became available. The first MEMS sensors were silicon-based and used to measure fluid flow parameters. MEMS accelerometers were developed in the 1980s to accommodate the automotive industry's need for triggers for the airbag deployment. During the 1990s, MEMS gyroscopes were introduced.

The growing popularity of smartphones and tablets in the 2000s led to an increased number of small inertial measurement units (IMUs) being developed and sold. That drove the price of the sensor packages down substantially, making the inertial sensors more accessible for regular users.

The advancement in the MEMS technology allowed for small but accurate accelerometers and angular rate sensors to be widely used in the automotive safety field. Anthropomorphic Test Devices currently utilized in crash testing are often instrumented with six degree-of-freedom (6DOF) sensor packages, which consist of very light and precise linear accelerometers, angular rate sensors, and angular accelerometers.

1.2.2 Position calculation in real-life scenarios

Inertial sensors have been widely used in navigation systems to provide information about the object's attitude (cf. Savage 1998). Over the years, the research in this field was driven mostly by military applications (aircraft, ballistic missile system, etc.) and it was focused on developing sensors that were more precise (cf. Benser 2015) and methods of updating body position and orientation that were more computationally efficient and sound (Bortz 1971). As time passed, knowledge acquired and developed technologies were adapted to commercial applications (e.g. to track passenger airplanes and ships) and in research related to mobile robots (Barshan et al. 1995, Chen et al. 2012, Qazizada et al. 2016).

Currently, with the growing popularity of wearable devices, smartphones, tablets, etc., more and more tech companies are focusing on using IMUs to monitor human performance and motion: XSens (Xsens Technologies B.V., Enschede, The Netherlands), NANSENSE (NANSENSE Inc., Los Angeles, CA, USA), Shadow (Motion Workshop, Seattle, WA, USA), Invensense (Invensense, San Jose, CA, USA). All of those systems use data from inertial sensors to obtain human body kinematics. The sensors are light and relatively inexpensive which make them more attractive for the researchers investigating human gait (Favre et al. 2009, Mariani et al. 2010, Yang et al. 2012, Rebula et al. 2013, Mannini et al. 2014, Trojaniello et al. 2015, Zhuang et al. 2016). Filippeschi in his 2017 review paper mentioned over 50 studies published within last 10 years in which data from IMUs were utilized to capture upper limb motion.

1.2.3 Principles of 3D trajectory calculation based on sensor data

In a crash-like scenario, to determine the trajectory of a rigid body relative to a fixed reference frame, data from locally mounted accelerometers and angular rate sensors can be used. As outlined in Huculak and Lankarani 2013, and Kerrigan et al. 2013, four steps are required in that process:

- Step 1: Before transforming the acceleration data $a_{sensors}(t)$ from the sensor package to a common body-fixed coordinate system origin, the sensor accelerations need to be corrected for the effect of gravity $g = [0\ 0\ -9.80665]^T$;
- Step 2: Translation of measured (and corrected for gravity) acceleration $a_{sensors,corr}(t)$ from the sensor locations to a common body-fixed coordinate system origin to obtain the time history of the acceleration vector $a_{origin}(t)$ at that point;
- Step 3: Determination of the coordinate transformation $R(t)$ relating, in time, the orientation of the rigid body to the global reference frame;
- Step 4: Transformation of the measured body-fixed accelerations ($a_{origin}(t)$ from Step 2) to the global reference frame (using $R(t)$ from Step 3), introduction of gravity g again, and double integration to determine the time histories of the body position $pos(t)$ (Eq. 1.1):

$$pos(t) = \iint_0^t \left[R(\tau) * a_{origin}(\tau) + g \right] d\tau d\tau \tag{1.1}$$

Step 1: Before transforming the data from locally mounted linear accelerometers to a common local coordinate system, accounting for the influence of gravity on each accelerometer reading is required. The gravity correction is accomplished by initially removing the influence of gravity from the sensor data (Eq. 1.2):

$$a_{sensors,corr}(t) = a_{sensors}(t) - R_{ini}^T g \tag{1.2}$$

where **R$_{ini}$** is initial orientation of the rigid body in the global reference frame.

Step 2: Purely translational accelerations of a body can be determined using the equation for the acceleration of a point p, a_p, on a rigid body (Eq. 1.3):

$$a_p = a_{origin} + \omega \times \omega \times \rho_{op} + \alpha \times \rho_{op} \tag{1.3}$$

where

- a_{origin} is a local coordinate system vector describing the translational acceleration of the body in the body-fixed (local) reference frame,
- a_p is the acceleration (vector) measured at p,
- ρ_{op} is the position vector of point p in the body coordinate system, and
- ω and α are the local coordinate system vectors describing the body's angular velocity and angular acceleration.

Eq. 1.3 shows that accelerations measured by accelerometers at various locations on a rigid body can be used to determine the accelerations of a local coordinate system fixed to that body by translating the sensor measurements to a single point (i.e., tracked point, the origin of the body-fixed system). This is pertinent in the case of any rigid body, since, in general, three directional (component) accelerations are desired to characterize the body's acceleration, and three accelerometers cannot be located in exactly the same location.

If point p is the accelerometer seismic mass, through simple algebraic manipulations on Eq. 1.3, the local accelerations of the origin of the body-fixed frame (i.e., tracked point o) can be found from Eq. 1.4:

$$a_{origin,i}(t) = a_{i-th\ sensor,corr}(t) - \boldsymbol{\omega}(t) \times \boldsymbol{\omega}(t) \times \boldsymbol{\rho}_{i-th\ sensor\ to\ point\ o} - \boldsymbol{\alpha}(t) \times$$
$$\boldsymbol{\rho}_{i-th\ sensor\ to\ point\ o} \tag{1.4}$$

where

- $a_{origin,i}$ is the i-th component of the translational acceleration in the body-fixed (local) reference frame,
- $a_{i\text{-th sensor,corr}}$ is the acceleration measured by an i-th linear accelerometer after gravity correction,
- $\boldsymbol{\rho}_{i\text{-th sensor to point }o}$ is the position vector of the i-th accelerometer in the body coordinate system,
- $\boldsymbol{\omega}$ and $\boldsymbol{\alpha}$ are the local coordinate system vectors describing the body's angular velocity and angular acceleration, and
- $i = $ X, Y, Z.

To determine the three perpendicular component accelerations of a body, in addition to the accelerations measured by three mutually perpendicular accelerometers, the following three pieces of information are needed:

- the vector locations ($\boldsymbol{\rho}$) of each of the three linear accelerometers expressed in the body-fixed coordinate system;
- the local coordinate system angular velocity vector ($\boldsymbol{\omega}$) of the body, and
- the local coordinate system angular acceleration vector ($\boldsymbol{\alpha}$) of the body in cases when the accelerometer sensor block's measurement center (Figure 2) is not coincident with the body-fixed coordinate system origin (i.e. tracked point).
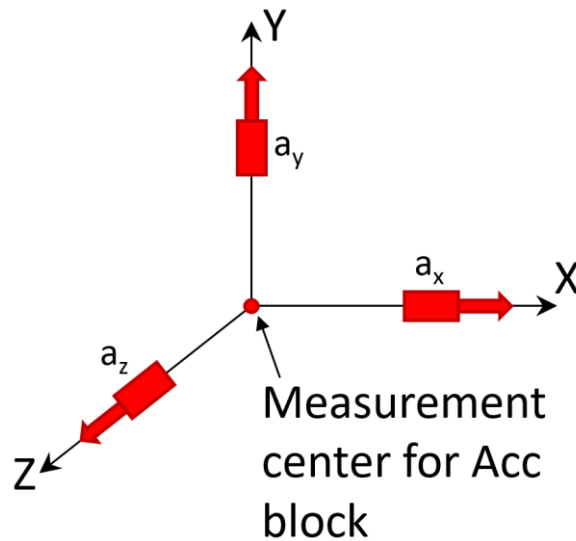
Figure 2. Schematic drawing showing the measurement center for three accelerometers of the same type.

In the case of the head or another ATD body region, item 1 can be determined from the drawings of the dummy showing the locations of the individual accelerometers, or measured with a coordinate measurement machine (CMM). Similarly, for an instrumented crash test vehicle, the locations and orientations of the sensors relative to the desired origin of the body-fixed (vehicle) frame can be found using a CMM.

In most ATDs, the stock sensor block attached to a body part includes a set of angular rate sensors that are oriented to measure the local coordinate system components of the angular velocity. Then, item 2 is captured directly by the installed instrumentation. Similarly, mutually perpendicular angular rate sensors can be used to measure the angular velocity of a crash test vehicle.

If the local body angular acceleration is needed in the calculation process, it can be either measured directly using three mutually perpendicular angular accelerometers or indirectly by post-processing the angular rates or linear acceleration measured by installed IMUs.

Step 3: Initial orientation of a rigid body in the global reference frame, R_{ini}, and the body's angular velocity $\omega(t)$ in the local coordinate system can be measured or determined using current measurement technologies. Using both, $\omega(t)$ and R_{ini} the time-history of the local-to-global rotation matrix $R(t)$, which, in time, relates the orientation of the body's local coordinate system to the global frame, can be obtained.

R is a square matrix composed of an orthogonal set of three unit vectors, each vector describing the orientation of an axis of the local frame in the global coordinate system. R relates any vector's representation in the local coordinates, r_l, to its representation in the global frame, r_g, through Eq. 1.5:

$$r_g = R\, r_l \tag{1.5}$$

By differentiating Eq. 1.5 and then algebraic manipulation, one can show (cf. DiMasi 1995, cf. Hamano 2013) that R is related to the angular velocity skew-symmetric matrix $[\omega \times]$ by Eq. 1.6:

$$[\omega \times] \equiv \begin{bmatrix} 0 & -\omega_z & \omega_y \\ \omega_z & 0 & -\omega_x \\ -\omega_y & \omega_x & 0 \end{bmatrix} = R^{-1}\dot{R} \tag{1.6}$$

$$\text{and thus: } \dot{R} = R[\omega \times] \tag{1.7}$$

where $\dot{R}$ is the rate of change of the matrix R, and ω_x, ω_y, and ω_z are the local coordinate system components of the ω vector.

By solving Eq. 1.7, the time history of the tracked body orientation (local-to-global transformation matrix $R(t)$) can be found.

Step 4: In the final step, the time history of the local body-fixed accelerations ($a_{origin,i}(t)$ from Eq. 1.4) are transformed to the global coordinate system using the time history of the transformation matrix $R(t)$. Next, the gravity is introduced back into calculations. Lastly, the global accelerations are numerically integrated to determine the component velocities, and integrated again to determine the body displacements (trajectory) in the global reference frame.

Once global displacements for each body in question (e.g. ATD and vehicle) are determined, they can be subtracted to determine their relative motion.

1.2.4 No consensus on methods used in sensor-based position and orientation estimation

As it was shown in Section 1.2.3, multiple steps are required to obtain the trajectory of a tracked body from inertial measurements. In some of these steps various methods can be utilized to find the wanted quantity. For example, there are at least five different published methods of determining body's local angular acceleration needed in Eq. 1.4 to transform sensor-based linear acceleration to a common point (Padgaonkar et al. 1975, Kang et al. 2011, Carvalho et al. 2013, Kang et al. 2017). There are at least seven different methods of updating the rotation matrix $\boldsymbol{R}$ based on Eq. 1.7 (Bortz 1971, DiMasi 1995, Beard and Schlick 2003, Rudd et al. 2006, Kang et al. 2011, Kerrigan et al. 2011, Huculak and Lankarani 2013). In addition, researchers have used multiple different filters on the body's local angular rate utilized in both, Eq. 1.4 and Eq. 1.7. All of these leads to multiple ways of performing the same task. Unfortunately, within the research community, there is no consensus on how these different methods affect the resulting sensor-based position estimation and which of these methods and filters should be used when trajectories are computed based on data from IMUs. To the knowledge of the author, no comprehensive study has been performed to address these questions and such a comparison could provide guidance in identifying a particular approach for a particular application.

1.2.5 Errors in sensor-based tracking

3D component trajectories calculated using inertial measurements can be affected by different types of signal errors or uncertainties associated with initial conditions of the tracked body (cf. Schoenebeck et al. 2009, Wu et al. 2009, Sinz et al. 2015).

Schoenebeck et al. 2009, based on his preliminary analysis (not included in the paper), stated that small errors in initial orientation as well as incorrect values for initial velocity can lead to substantial errors in IMU-based trajectories for an ATD head in a frontal crash. Wu et al. 2009 showed that by changing initial orientation of a vehicle in rollover by 5 degrees, the sensor-based trajectory of that car can differ from the reference (i.e. without the "5-degree change") response by approximately 800 mm. Sinz et al. 2015 performed a sensitivity study investigating the effect of errors in initial conditions (orientation and velocity of the tracked body) and debias and scaling errors in the IMU readings on the resulting sensor-based position estimation. Sinz concluded that the position prediction obtained from inertial measurements is highly sensitive to the error in initial angles of the tracked body, the acceleration offsets for all three local body directions, and the scale factors for recorded signals from linear accelerometers and angular rate sensors attached to that body.

The three discussed studies focused on a limited number of error types. In addition, they did not investigate the interactions between these errors. To the author's knowledge, no comprehensive study has been performed to quantify the effect of multiple error types, different from the ones mentioned in the previous paragraph, on the trajectory calculated with the use of IMUs. By performing such an analysis, better understanding of error effects and their interactions would be gained. In the result, such an investigation could guide improvements in the design of new inertial sensors and new measurement devices utilized, for example, to determine initial

conditions of a body one wants to track, and thus, could, in the end, improve the overall accuracy of IMU-based position and orientation estimations.

1.2.6 Summary

- Two main methods of capturing object motion:
  - Through optical systems
  - Through data measured by inertial sensors (IMUs)
- Optical systems deliver high accuracy but suffer from many issues:
  - Expensive (costs related to equipment and software)
  - Data processing time-consuming
  - Requiring constant line of sight between cameras and tracked objects
  - Limited calibrated volume
  - Highly user-dependent
- Rapid advancement in MEMS technology allowed for development of small, light, accurate, and inexpensive sensors
- IMU position and orientation computation based on motion equations of a rigid body
- IMU based tracking presents a promising alternative to optical systems and is widely used by researchers in the fields of mobile robots, wearable devices, human motion and performance (gait analysis)
- No consensus on methods used in sensor-based motion tracking
  - Multiple ways of solving the same task
  - No general agreement on how these different methods affect the resulting sensor-based position estimation and which of these methods should be used when trajectories are computed based on data from IMUs
- 3D component trajectories obtained using IMUs affected by sensor characteristics (e.g. noise level), sensor errors (e.g. error in sensitivity), and test measurement inaccuracies (e.g. error in the measurement of initial orientation)
- Average position error for IMU based estimation of upper limb motion was on the level of 35 mm (Filippeschi et al. 2017). IMU based position error reported in crash testing up to 59 mm (Rudd et al. 2006)
- To obtain accurate IMU based tracking in a crash more research, taking into account propagation of sensor-related errors in time, is required

2. GOAL AND AIMS

The goal of this dissertation is to develop an algorithm that can be used to compute 3D component trajectories of a rigid body – based on locally-mounted inertial sensors – for applications in vehicle crash tests with anthropomorphic test devices (ATD). These inertial sensors are composed of linear accelerometers (ACC), angular rate sensors (ARS), and occasionally angular accelerometers (AAC). In addition to the algorithm, this dissertation identifies different correction techniques that could be used to minimize the error in the calculated trajectory when sensor readings contain an error.

These goals will be accomplished through the following specific aims:

1. To determine the specific methodological steps for computing 3D component trajectories of a rigid body in a crash test with the goal of minimization of the error in the calculated trajectory. This objective consisted of two parts:

    1.1 identification of a robust and efficient method of updating body orientation based on body's angular rate;

    1.2 identification of a sensor package that can be used to predict those trajectories minimizing the error in position and orientation at the same time.

2. To evaluate the effect of sensor characteristics (e.g. noise level), sensor errors (e.g. error in sensitivity), and test measurement inaccuracies (e.g. error in the measurement of initial orientation) on the calculated trajectory to define a set of instructions allowing the user to account for those errors to obtain accurate body kinematics.

3. To identify a method of obtaining body's angular acceleration that minimizes the error in the calculated trajectory, and to evaluate the effect of filtering of the input data (used in obtaining AAC) in the non-ideal case, i.e. when the local angular acceleration of a rigid body needs to be included in the trajectory calculation.

3. RESEARCH PLAN

The research plan was divided into five tasks (Figure 3). The first task, spanning Chapter 4 to Chapter 7, was focused on assembling the training set for verification and validation of the proposed algorithm using data from progressively more complex impact scenarios. The set was then used to investigate:

- different methods identified in the literature to determine which is the most accurate technique of updating the body orientation based on the body's angular rate (Task 2; Chapter 8);
- different methods to determine which is the most accurate approach of obtaining local angular acceleration often needed in the trajectory calculation process (Task 3; Chapter 9);
- which sensor and measurement errors have the greatest effects on the trajectory calculation (Task 4; Chapter 10), what are the interactions between those errors (also Chapter 10), and if it is possible to reduce the error in the calculated trajectory by adding redundant sensors to the stock sensor package (Chapter 11).

In the fifth task (spanning from Chapter 12 to Chapter 15), the knowledge gained from Task 2 to Task 4 was used to identify the specific methodological steps for computing 3D component trajectories in vehicle crash tests, steps that minimize the error in the calculated trajectory. As part of Task 5, the Kalman filter technique (Kalman 1960; Chapter 12), optimization of initial body conditions to increase the accuracy of trajectory calculations (Chapter 13), the introduction of known data points from an optical system as an error correction (Chapter 14), and different methods of providing kinematics data over a missing part of optical data (Chapter 15) were investigated.
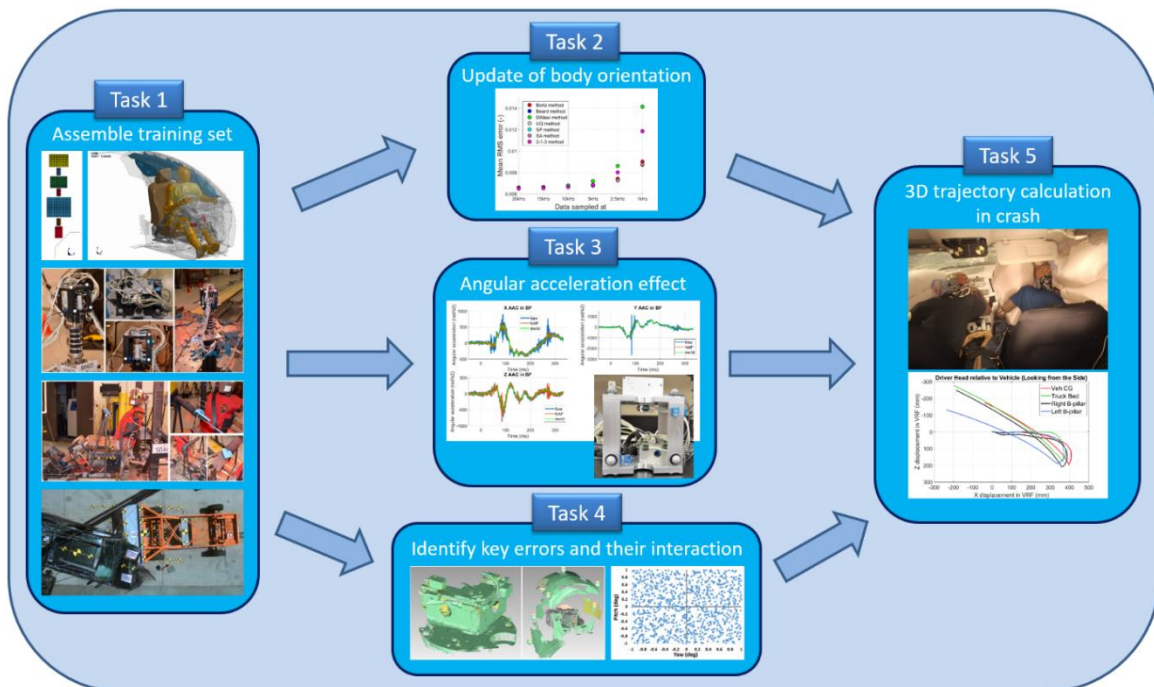
Figure 3. Flow chart for the research effort.

It is worth reminding the reader, that IMU tracking can be utilized to obtain the relative motion between two analyzed bodies (for example, the ATD's head and the vehicle). If, during the impact, the vehicle structure deforms at the sensor mounting location, though, this local deformation will affect the calculated orientation and position of the car, and, subsequently, the occupant's relative trajectory. To address that issue, in Chapter 16, a brief discussion about the effect of vehicle deformations at sensor mounting locations on the calculated position of the ATD's head in reference to the vehicle local coordinate system was presented.

Concluding remarks summarizing the research effort performed in this dissertation were provided in Chapter 17.

4. ASSEMBLE TRAINING SET

4.1 Training set description

A comprehensive training set of progressively more complex impact conditions was used throughout the dissertation research. The proposed set included complete 6 degree-of-freedom (DOF) kinematic time histories for different rigid bodies (with the focus on the head), which were obtained from computer models (to verify the proposed algorithm of trajectory calculation) as well as from sled and crash testing (to assess the algorithm accuracy in real case scenarios). Impacts were chosen from loading conditions that result in the load magnitude and duration seen in real crashes.

Over the course of this dissertation 50 tests were performed. This set consists of impact kinematics taken from:

- computer models of rigid bodies connected with kinematic joints,
- a box-like structure (called Simplified Head) connected with the neck of the THOR Anthropomorphic Test Device (THOR ATD; NHTSA 2018) and mounted on a sled system,
- the THOR ATD utilized in various test conditions.

To investigate: a) how the calculated trajectory varies in relation to the location of the sensor package mounted on the vehicle, and b) the effect of different types of errors on the predicted ATD motion, occupant and vehicle data from two frontal oblique offset tests (Test v10119 and Test v10133, NHTSA 2017a & NHTSA 2017b, respectively) were collected. The two tests are briefly described in *Section 4.2 NHTSA crash tests – brief overview*.

A detailed list of the test conditions used in this dissertation is provided below in Table 1.

Table 1. Summary of tests that have been performed for this dissertation.

Test category (sample size)	Test condition (sample size)	Test details
Computer simulation (2)	Multi-body simulation (2)	4 rigid bodies connected with kinematic joints and simulated in LS-Dyna software (2) * Trajectory from the simulation available for comparison * Two different sampling rates investigated
Sled tests (48)	Simplified Head (40)	Simplified Head positioned at 0 degree relative to sled travel direction (10) Simplified Head positioned at 45 degree relative to sled travel direction (30) * Multiple sensor types utilized in all tests * VICON trajectory data available for comparison
	THOR Mod-kit (8)	All tests run with UVa Gold Standard 3 (GS3) buck;

		Without head impact (5)
		With head impact (3)
		* Multiple sensor types utilized in all but one tests
		* VICON trajectory data available for comparison
Crash tests (2)	NHTSA Oblique RMDB with THOR ATD (near side; n = 2)	90 km/h barrier into stationary vehicle at 15 degree oblique offset with 35% overlap; Test v10119: pickup truck (1) Test v10133: small sedan (1)
		* No reference trajectory data available for comparison

4.2 NHTSA crash tests – brief overview

The sensor data from two frontal oblique offset tests performed for the National Highway Safety Administration were collected and used in this dissertation. In both tests, a moving barrier was driven into the front-left side of the vehicle at approx. 90 km/h. In Tests v10119 (NHTSA 2017a) a pickup truck was utilized. In Test v10133 (NHTSA 2017b) a small sedan was used. In both vehicles, the THOR ATD was positioned in the driver's seat. The impact with the barrier caused ATD-to-vehicle relative motion.

The THOR ATD's head was instrumented with three linear accelerometers (Endevco 7264C, Meggitt Sensing Systems, CA, USA) and three angular rate sensors (DTS ARS Pro, Diversified Technical Systems, Seal Beach, CA, USA). In addition, in Test v10119, four identical 6 degree-of-freedom sensor packages (DTS 6DX Pro, Diversified Technical Systems, Seal Beach, CA, USA) were mounted inside the car to obtain the head motion relative to each of the four vehicle reference points. Prior to testing, the initial orientation of the THOR's head (both tests) and the mounting plates for the vehicle sensor cubes (only Test v10119) – in the global frame – were determined with a Coordinate Measuring Machine (CMM).

The sensor data were recorded at the sampling rate of 10 kHz (Test v10119) or 20 kHz (Test v10133). The local coordinate systems of the head and of the vehicle were defined as outlined in the SAE J211 document (SAE 1995).

5. ALGORITHM VERIFICATION THROUGH COMPUTER SIMULATIONS

5.1 Introduction

The goal of Chapter 5 was to verify if the algorithm described in Section 1.2.3, i.e. the algorithm used throughout this dissertation, was coded correctly. The verification was performed using kinematics data obtained from a simple computer model. It was assumed that those kinematics data utilized as the input to the algorithm were ideal and did not contain any errors.

The chapter is organized as follows. Section 5.2 focuses on the methods used in the algorithm verification analysis. The results of the study for two different data sampling frequencies are presented in Section 5.3. Concluding remarks are provided in Section 5.4.

5.2 Methods

5.2.1 Model description

A multi-body model (Figure 4) was simulated in a commercial Finite Element (FE) package (LS-Dyna 8.1.0, LSTC, Livermore, CA). The model contained four "main" bodies (termed "Body1 – Head", "Body2 – Torso", "Body3 – Abdomen", and "Body4 – Pelvis") and three additional bodies ("Body5", "Body6" and "Body7") in-between the "main" bodies. The parts were modeled with 5 mm thick shell elements and were assumed rigid.
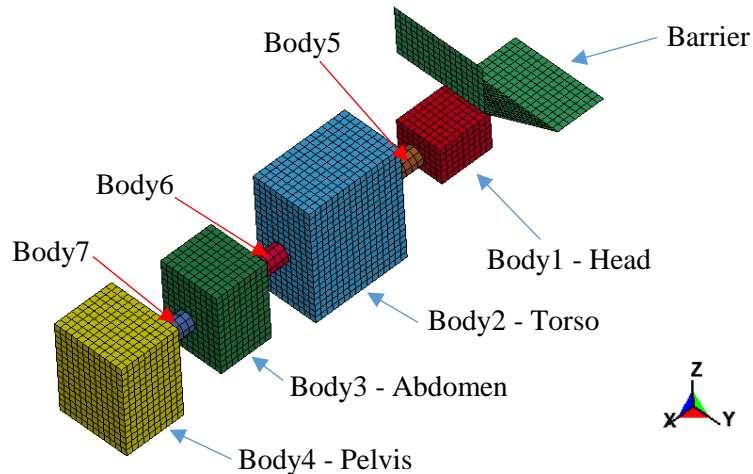
Figure 4. Model overview.

The model was given initial velocity of 10 m/sec in both, global y- and global z-direction. The scenario was designed in a way that at some point during the simulation the "Head" interacted with an undeformable and rigidly fixed barrier (Figure 4). That contact disturbed the initial orientation of all connected bodies, causing relative translations and rotations of the parts.

For each of the "main" bodies a local coordinate system was defined according to the sign convention specified in the SAE J211 document (Society of Automotive Engineers (SAE) J211,

24

1995; Figure 5). The origin of the local coordinate frame was coincident with the body center of gravity (CG).
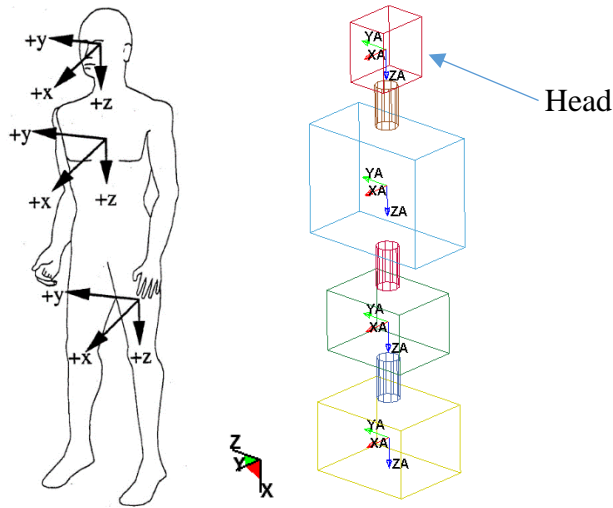
Figure 5. SAE J211 sign convention (left), local coordinate systems defined for the simple model (right).

5.2.2 Inertial properties

Inertial properties were assigned to each body accordingly. The masses and the inertia tensor components used are presented below in Table 2.

Table 2. Inertial properties of the model parts.

Part name	Mass [kg]	Inertia [kg·m2]					
		Ixx	Ixy	Ixz	Iyy	Iyz	Izz
Body1/"Head"	5.0	0.0435	0.05	0.0579	0	0	0
Body2/"Torso"	15.0	0.582	0.748	0.47	0	0	0
Body3/"Abdomen"	8.0	0.182	0.169	0.129	0	0	0
Body4/"Pelvis"	20.0	0.0621	0.0558	0.0441	0	0	0
Body5	1.0	0.00144	0.00345	0.00345	0	0	0
Body6	1.0	0.00144	0.00345	0.00345	0	0	0
Body7	1.0	0.00144	0.00345	0.00345	0	0	0

5.2.3 Kinematic joint characteristics

All model parts were connected by spherical joints with defined rotational stiffness (Figure 6). The initial orientation of all of the joint local coordinate systems was the same as the initial orientation of the head coordinate system (Figure 5).

25
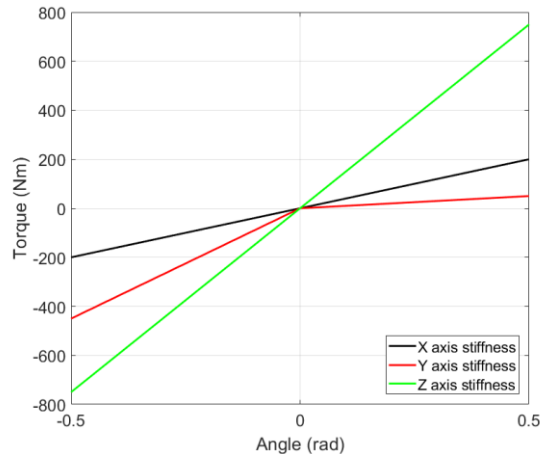
Figure 6. Rotational stiffness characteristics for local X, Y, Z axes.

5.2.4 Contact definition

In the simulation contact between "Head" and "Barrier" was defined. The two material properties needed for the FE software to calculate contact stiffness – and provided in the material card for the "Head" part – were as follows: Young's modulus: 2 GPa, Poisson's ratio: 0.29.

No other interactions between parts than the one between "Head" and "Barrier" were modeled. In all of the simulations carried out friction was added to the contact definition with the static coefficient of friction set to 0.8.

5.2.5 Outputs

In the simulations, linear accelerations and angular velocities were measured in the local body-fixed coordinate frames on two articulated masses ("Torso" and "Pelvis") and used later as an input to compute 3D component trajectories of those parts (in the global frame and relative to each other).

For both tracked bodies, for validation purposes, the following outputs were also defined:

- Position and orientation of each body in the global coordinate frame,
- Relative position of the "Pelvis" body relative to the "Torso" body.

In addition, nine different locations for numerical accelerometers were selected to be able to use the Nine Accelerometer Package (NAP) approach (Padgaonkar et al. 1975) to calculate local angular accelerations. These numerical accelerometers were rigidly attached to the corresponding parts in a way that the point for which the 3D trajectory was later calculated, was coincident with the CG of that part (package for "Torso" shown in Figure 7).

26
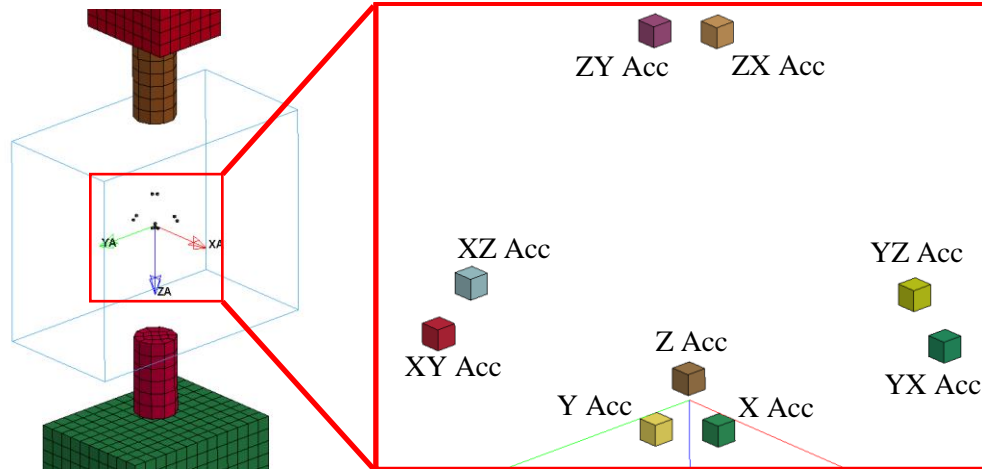
Figure 7. NAP configuration.

The coordinates of all of the NAP accelerometers, in the body-fixed local coordinate frame, same for both tracked parts, were gathered in Table 3.

Table 3. Coordinates of NAP accelerometers in local body frame.

Accelerometer	X (m)	Y (m)	Z (m)
X Acc	0.007	0	0
Y Acc	0	0.007	0
Z Acc	0	0	-0.0066
XY Acc	-0.0508	0.007	0
XZ Acc	-0.0508	0	-0.0066
YX Acc	0.007	-0.0482	0
YZ Acc	0	-0.0482	-0.0066
ZX Acc	0.007	0	-0.0685
ZY Acc	0	0.007	-0.0685

5.2.6 Simulation setup – brief overview

Two computer simulations were run up to 300 msec. The difference between the simulations was the sampling rate of the results: 10 kHz (Simulation 1) and 100 kHz (Simulation 2). Local linear accelerations and angular rates of two bodies ("Torso" and "Pelvis" in Figure 4) outputted

from the FE software were used as an input to the 3D trajectory calculation algorithm. Next, computed global positions (measured at the body's CG), "Pelvis" relative position to "Torso", as well as body local angular accelerations (obtained using the NAP approach; Padgaonkar et al. 1975) were compared with the equivalent outputs from FE. In addition, for all three discussed quantities, the time histories of the absolute difference (error) between values calculated and as recorded by the FE software were determined and presented.

In both following sections, for "Pelvis" and "Torso", the method described in Rudd et al. 2006 was utilized to update the body's rotation matrix **R**.

5.3 Results

In this subsection, the results from the algorithm verification analysis are presented: first, based on Simulation 1 (sampling rate of 10 kHz; Section 5.3.1), and next, based on Simulation 2 (sampling rate of 100 kHz; Section 5.3.2). In Section 5.3.3, a brief discussion explaining the differences in position calculation accuracy between both performed computer simulations is provided.

5.3.1 Simulation 1 (results sampled at 10 kHz)

5.3.1.1 Angular Acceleration (in body's local coordinate system)

In general, the calculated local angular acceleration (AAC), for "Torso" (Figure 8) as well as for "Pelvis" (Figure 9), was in a good agreement with AAC outputted from the FE software. The maximum absolute difference for both tracked bodies and for the three AAC components stayed below 0.1 rad/sec^2 throughout the whole event. That shows that the NAP method, which was implemented as a subroutine in the 3D trajectory calculation algorithm, was coded correctly.
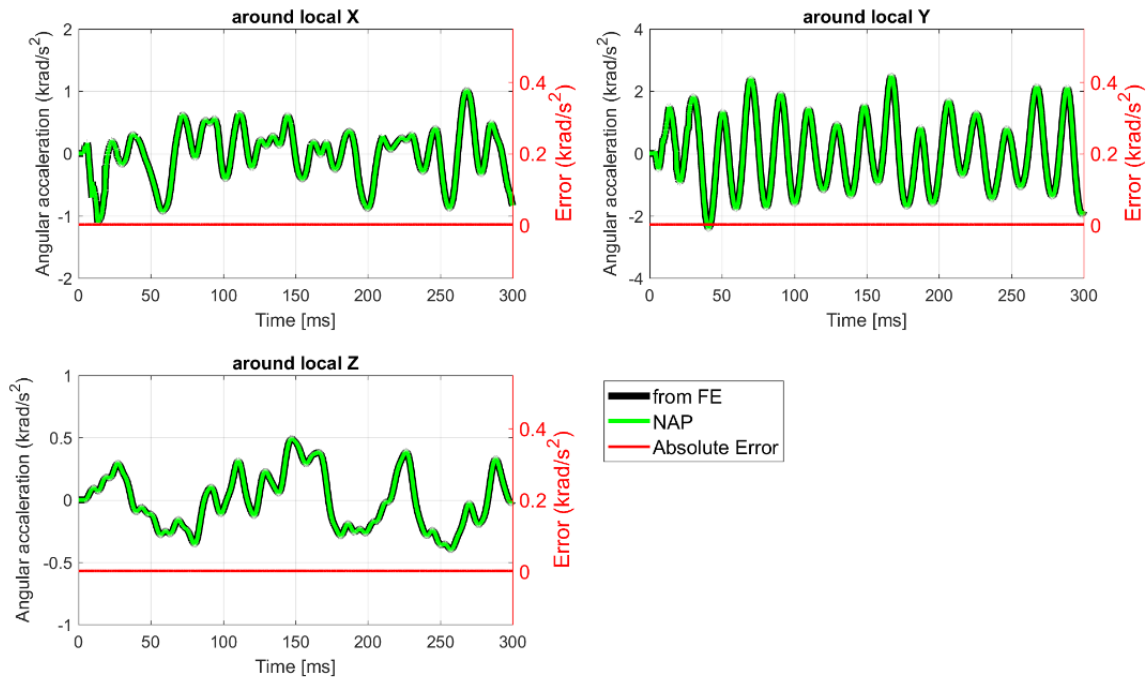
Figure 8. Angular acceleration components for the "Torso" body calculated from NAP.
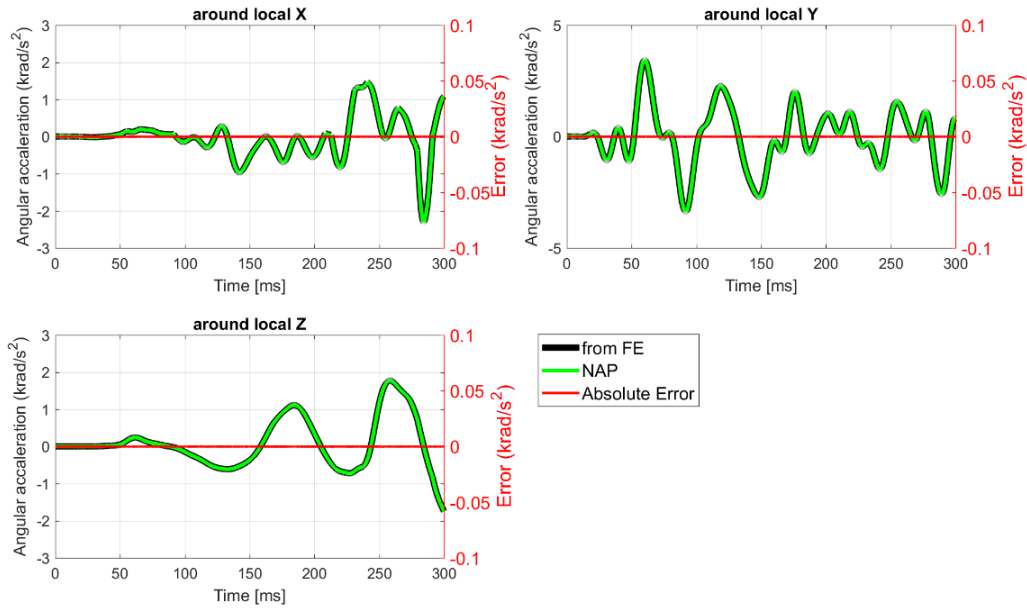
Figure 9. Angular acceleration components for the "Pelvis" body calculated from NAP.

5.3.1.2 Global position

For both tracked masses, the maximum absolute error seen for the Y and Z position components was substantially smaller than the maximum error found for the X-axis position (Figure 10 and Figure 11). For the two bodies, the maximum absolute difference between the LS-Dyna results and the calculated Y and Z positions was less than 1.5 mm. The maximum trajectory error in the X direction reached over 22 millimeters for "Torso" (Figure 10) and approx. 25 mm for "Pelvis" (Figure 11).
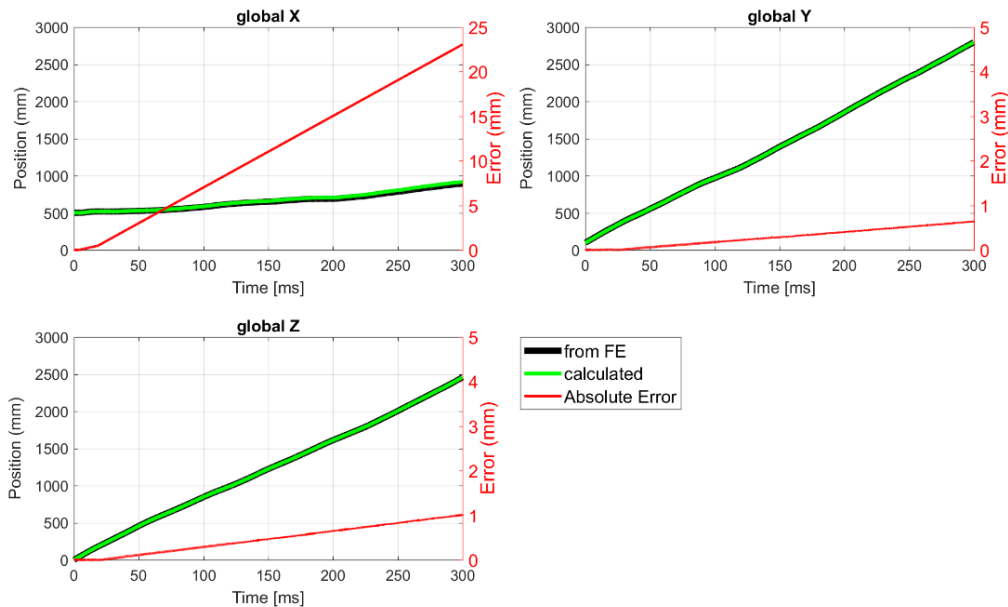
Figure 10. 3D global trajectory for the "Torso" body.
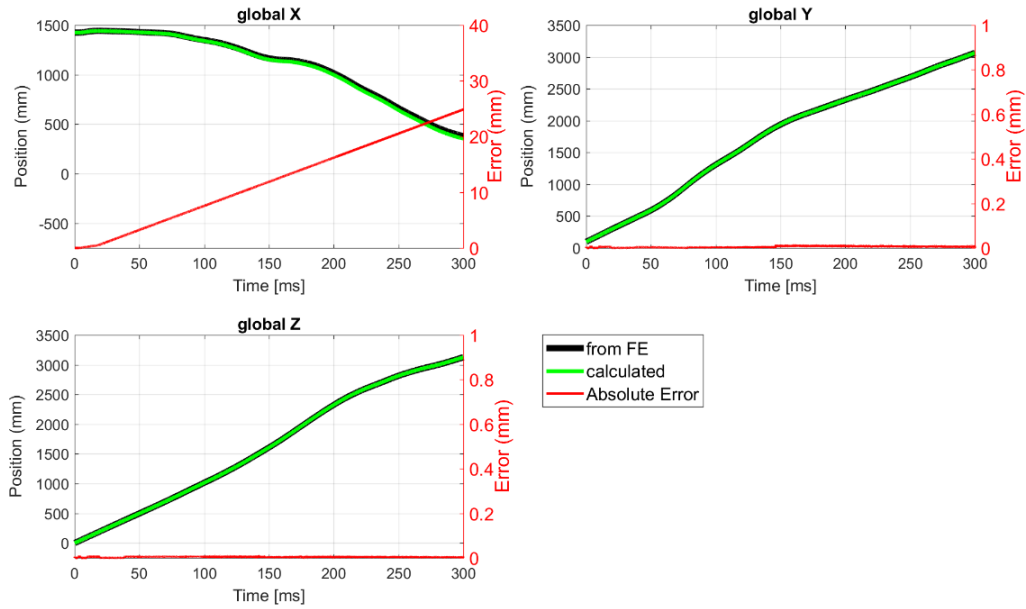
Figure 11. 3D global trajectory for the "Pelvis" body.

5.3.1.3 Relative position

As a result of the errors in the calculated global trajectories, the relative position between "Pelvis" and "Torso", computed with the algorithm, did not match well the relative position obtained from the FE software (Figure 12). In the X (local) direction the maximum absolute error (deviation from the FE results) was approx. 35 mm, in the Y direction, approx. 31 mm, and in Z, approx. 17 mm.
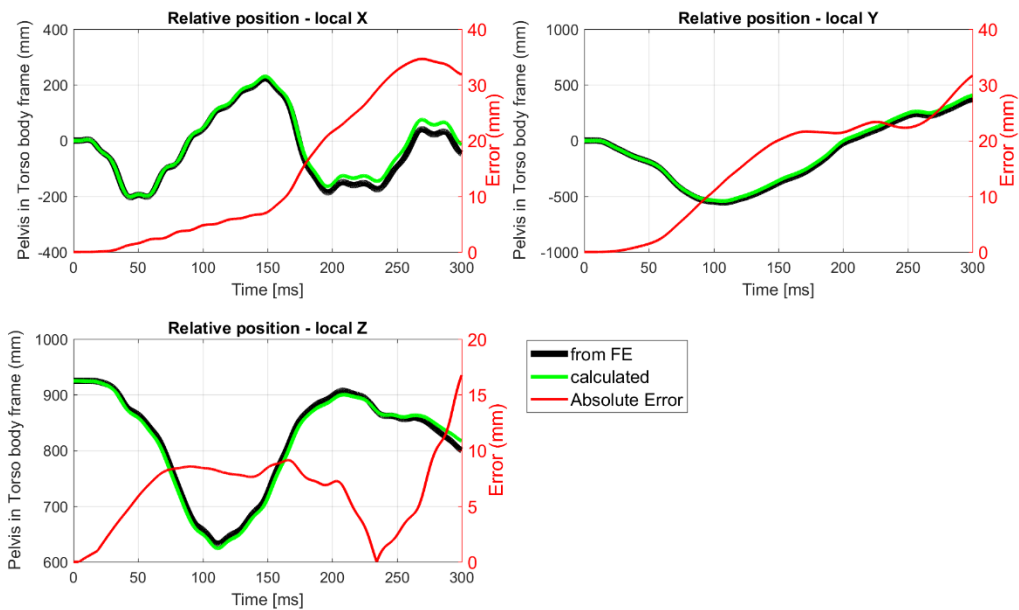
Figure 12. 3D trajectory of "Pelvis" in the local coordinate frame of "Torso".

30

5.3.2 Simulation 2 (results sampled at 100 kHz)

5.3.2.1 Angular Acceleration (in body's local coordinate system)

As it was done for the "10 kHz" case also this time for both tracked bodies angular accelerations in the body-fixed coordinate frame were calculated and then compared to the results obtained from the FE software. Again, the computed AAC components were in a good agreement with the angular acceleration recorded by the FE package (Figure 13 and Figure 14). It is worth mentioning here that the increase in the sampling rate did not influence the accuracy of the NAP calculations. The maximum absolute error seen across the three AAC components for both tracked masses stayed at the level of 0.1 rad/s² (the same as in the "10 kHz" case).
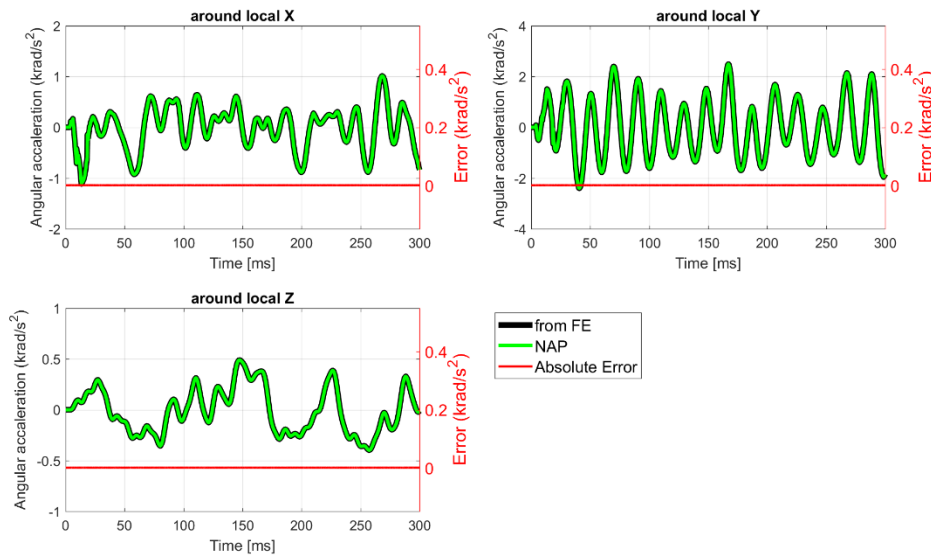
Figure 13. Angular acceleration components for the "Torso" body calculated from NAP.
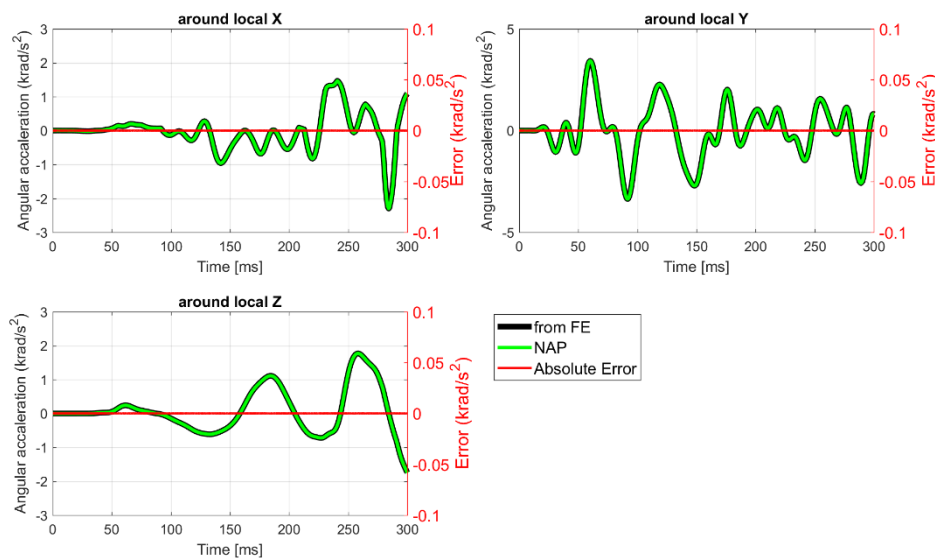
Figure 14. Angular acceleration components for the "Pelvis" body calculated from NAP.

31

5.3.2.2 Global position

Changing the sampling rate from "10 kHz" to "100 kHz" decreased the error in the calculated global trajectories substantially, especially in the X direction. For "Torso" the maximum absolute error in X decreased by 99%, from approx. 22 mm to 0.2 mm (Figure 15), and for "Pelvis" by 99.6%, from approx. 25 mm to less than 0.1 mm (Figure 16). For both bodies, the error in the Y and Z trajectory components stayed below 0.1 mm throughout the entire simulation.
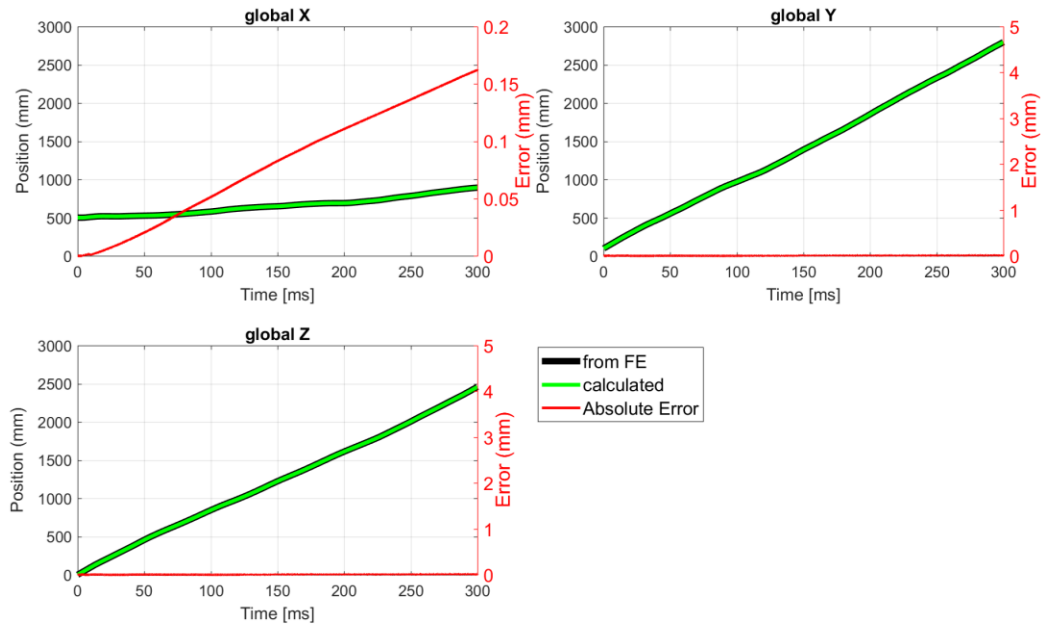
Figure 15. 3D global trajectory for the "Torso" body.
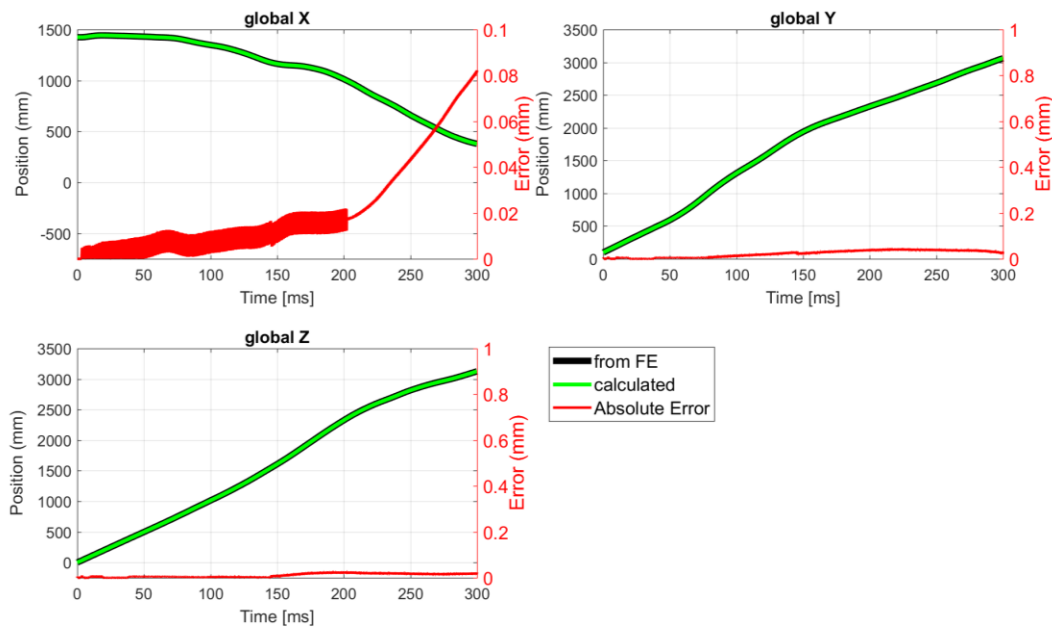
Figure 16. 3D global trajectory for the "Pelvis" body.

5.3.2.3 Relative position

Due to the decrease in the global trajectory error seen for both tracked bodies, the accuracy of the relative motion prediction between "Pelvis" and "Torso" (as obtained from the 3D trajectory calculation algorithm) improved substantially. The maximum absolute error between the computed and the "from FE" responses was at the level of 0.1 mm for all three trajectory components (Figure 17). That showed that the discussed algorithm of obtaining body's motion was able to calculate the global and relative positions of two articulated masses accurately when given ideal sensor data as an input.
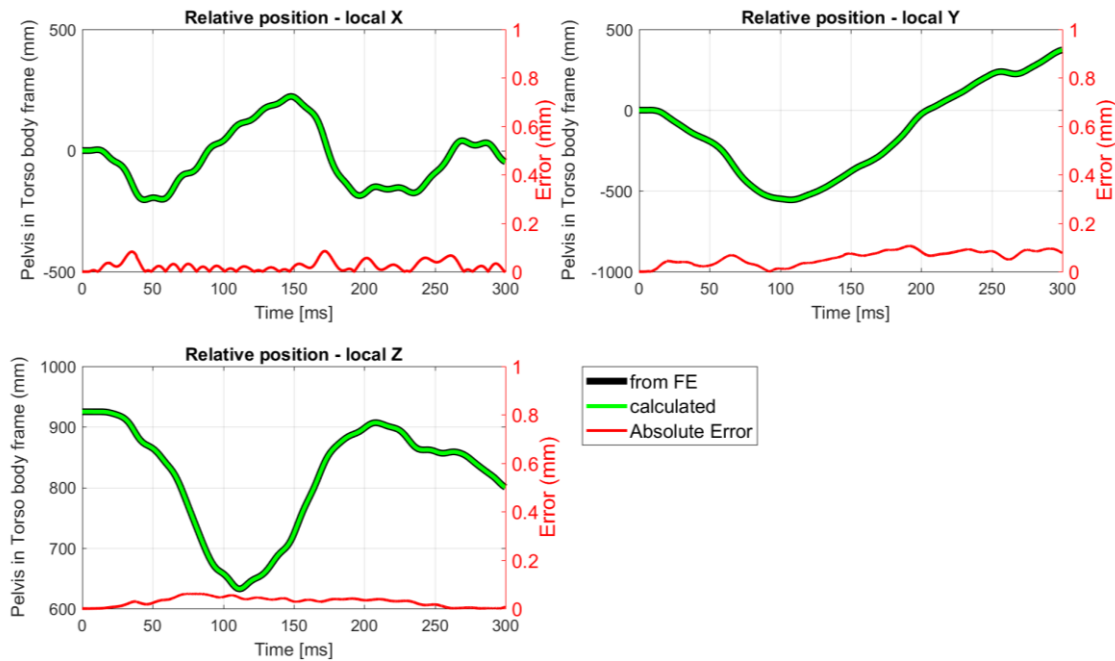
Figure 17. 3D trajectory of "Pelvis" in the local coordinate frame of "Torso".

5.3.3 Global position – discussion

To obtain 3D component trajectories of a rigid body in the global coordinate frame the global acceleration of that body needs to be integrated twice in time. The accuracy of the numerical integration is related to the time step used in the integration procedure. The smaller the time step, the better the accuracy. With the time step being too large numerical errors can accumulate, grow as time increases, and cause a difference between the expected and calculated values. This error can be amplified if the numerical integration is carried out more than once.

When the "10 kHz" sampling rate was used, a substantial error was introduced into the trajectory calculations for both tracked bodies, especially in the global X direction (Figure 10 and Figure 11). During the integration of the global X acceleration a constant error of approx. 0.08 m/s for "Torso" (Figure 18a), and of approx. 0.087 m/s for "Pelvis" (Figure 18b) was introduced in the body global X velocity. This error was carried through the second integration and caused the global X position to be substantially different from the expected (LS-Dyna) value. The error in the global

X-velocity was approx. 100 times smaller when the results sampled at 100 kHz were used as an input to the trajectory calculation algorithm (Figure 19).
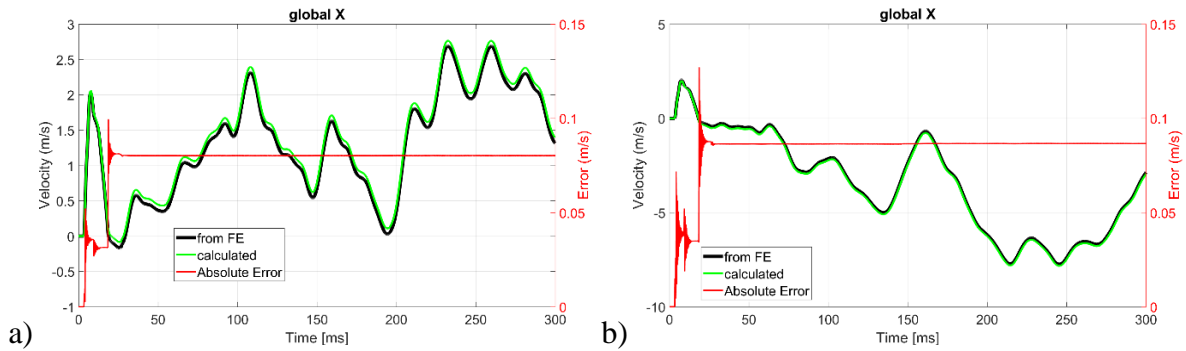
Figure 18. Global X-velocity sampled at 10 kHz: a) "Torso", b) "Pelvis".
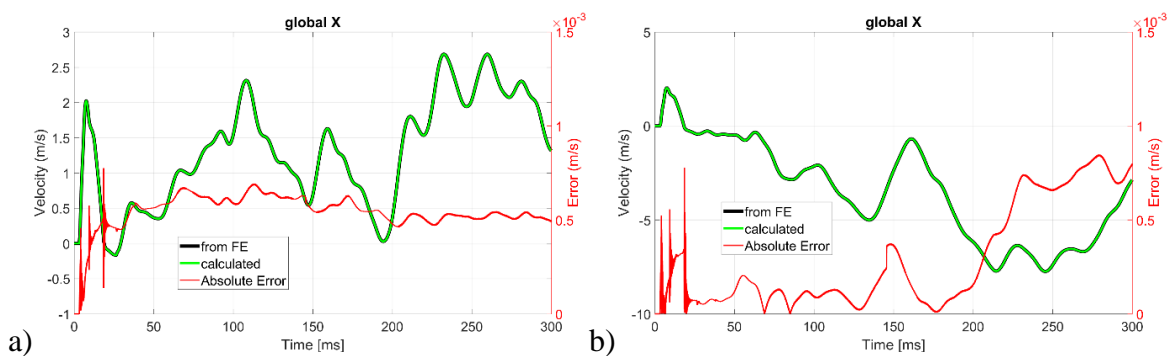
Figure 19. Global X-velocity sampled at 100 kHz: a) "Torso", b) "Pelvis".

5.4 Conclusions

The aim of the current study was to evaluate the ability of the algorithm described in Section 1.2.3 to calculate accurate trajectories based on 6DOF kinematics data obtained from computer models (to verify the proposed algorithm of trajectory calculation). The following can be concluded from the results of the study:

- In general, there are numerical artifacts that are present in local kinematics data calculated using LS-Dyna that affect the magnitude of predicted kinematics calculation errors. The artifacts result from numerical effects of integration time steps and other non-physical properties of the models, including the relative stiffness of adjacent structures in the model and the defined contacts. These artifacts, and their effects, will not be present in test data captured by sensors, and, as a result, the error magnitudes calculated in the "Computer simulations" study are not indicative of the error magnitudes that are expected when similar analyses are performed with experimental test data.

- There was a substantial difference in error calculations between kinematics data captured at 10 kHz (Simulation 1) vs. data captured at 100 kHz (Simulation 2). In fact, by increasing the sampling rate by a factor of 10, a 10 fold reduction in error was realized. This is because much of the error was related to an integration error, which could have a real effect on actual sensor data.

- Since there is a tradeoff between magnitude of acceleration and jerk and the sampling rate, it was not clear that 10 kHz or 100 kHz sampling used in the simulations was a real representation of what the algorithms would produce when applied to experimental data from sled testing.

- Despite the numerical issues, overall, it can be concluded that all parts of the algorithm used to calculate 3D component trajectories based on data from locally-mounted inertial sensors were coded correctly.

6. SIMPLIFIED HEAD TESTING

6.1 Introduction

After the algorithm verification analysis was completed (Chapter 5), to assess the algorithm accuracy in real case scenarios (using inertial data from real sensors), forty sled tests were performed with the Simplified Head assembly (Figure 20). Upon preparation of the head for testing, the structure was attached to a sled base (Seattle Safety, Auburn, WA), and then a test was performed. After testing, damages to the Simplified Head were assessed and the test data were processed and analyzed. If any damage or failure to the head or instrumentation was found, it was fixed first and then the next sled test was performed. This procedure was repeated until the test series was completed.
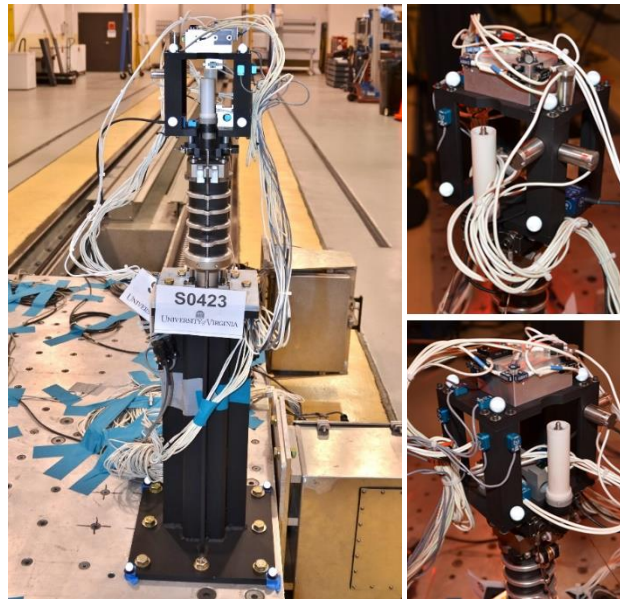
Figure 20. Simplified Head assembly used during testing.

The chapter is organized as follows. Section 6.2 focuses on the methods used during testing and later in the position calculation analysis. The results of the study (calculated orientation and position) are presented in Section 6.3. Concluding remarks summarizing the effort are provided in Section 6.4.

6.2 Methods

6.2.1 Test matrix

APPENDIX A shows the complete matrix of all forty Simplified Head tests carried out within the dissertation. The details about the items listed in APPENDIX A Table A1 and about testing in general are described in the following sections.

6.2.2 Sled input

The acceleration time history used for the sled system as the input was determined based on a frontal oblique offset test of a minivan (Test v09127, NHTSA 2013). In the test, a moving barrier

was driven into the vehicle at 90.1 km/h. The THOR ATD was positioned inside the car, in the driver's seat. The dummy was instrumented with an accelerometer package on the T1 level. T1 local X acceleration recorded during that test was filtered with the use of the Channel Frequency Class (CFC) 60 filter, scaled down (due to safety concerns) and used as the input for the sled at the University of Virginia Center for Applied Biomechanics.

Six time-histories with the same shape but different magnitude were utilized (Figure 21). Five of them (with peaks ranging from 4.9g to 29.3g) were used only once, in five consecutive tests. The time history with its peak at 27g was used for all of the remaining tests.
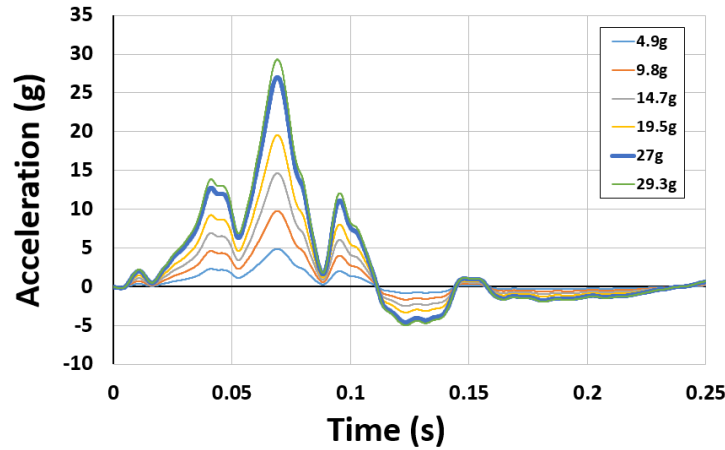
Figure 21. Acceleration time histories used during Simplified Head testing.

6.2.3 Coordinate Systems

Two coordinate systems were used to process and present the data from the tests. The local coordinate system for the Simplified Head, which remained fixed to the assembly during testing, was defined using standardized conventions (SAE J211, 1995; Figure 22). The positive X axis pointed from the rear to the front of the head. The positive Y axis pointed from the head left hand side to the head right hand side. The positive Z axis pointed from the top to the bottom of the assembly.
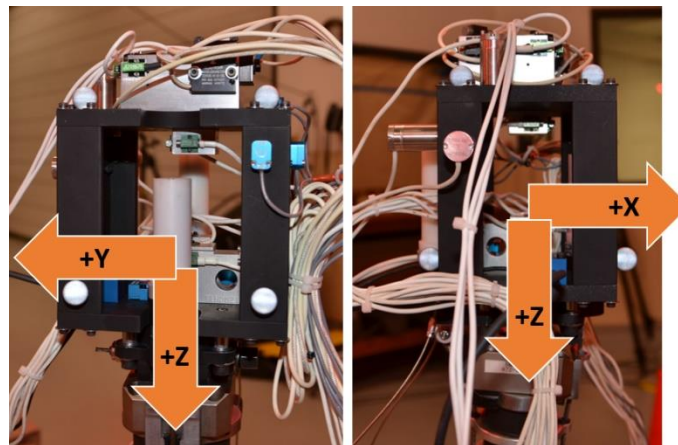
Figure 22. Simplified Head (local) coordinate system was chosen to match the SAE standard (J211) coordinate system for the head.

The global or inertial reference frame (IRF) was defined using the initial orientation of the VICON markers attached to the base of the stand the head-neck assembly was mounted on (Figure 23). The Y axis was aligned with the direction of the sled travel. The sled traveled in the positive Y direction. The Z axis was oriented normal to the sled base top surface, with positive pointing upward. The positive X-axis was mutually perpendicular to the Y and Z axes, with positive direction shown in Figure 23. The origin of the IRF was coincident with the center of the "2S" marker in its initial – before the start of a test – position.
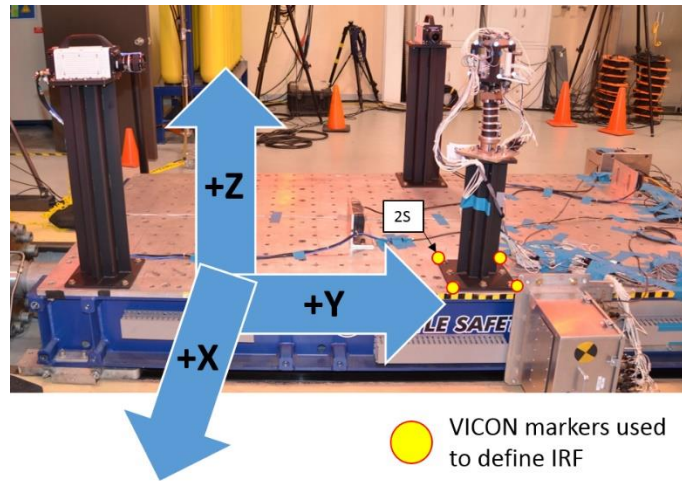
Figure 23. Inertial (global) coordinate frame defined with the use of VICON markers.

6.2.4 Test conditions – head orientation

In all performed tests, the head was facing opposite to the sled travel direction. Several different orientations of the head-neck assembly, with regard to the sled base, were investigated to cover broader response space. In thirty tests the Simplified Head was positioned at 45° with reference to the sled travel direction (IRF Y-axis; long axis of the sled base; Figure 24a). In seven of those tests a 20° wedge between the stand and the neck mounting plate was utilized (Figure 24b) to evaluate if more complex initial orientation of the structure would affect the accuracy of calculated trajectories.
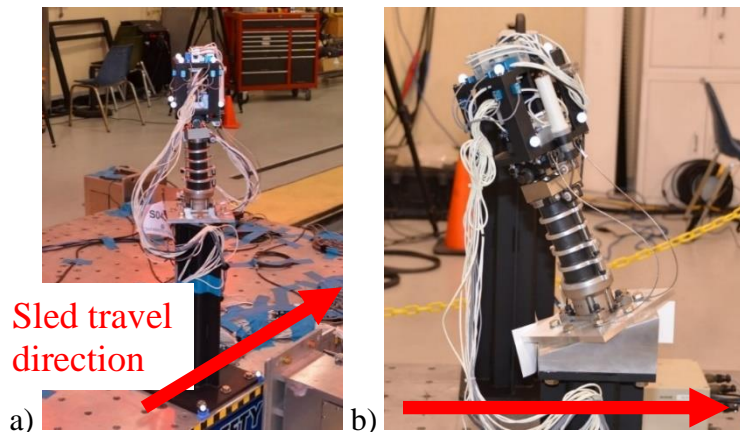
Figure 24. Simplified Head orientation at 45°: a) flat, without the 20° wedge; b) with the 20° wedge.

In ten tests the Simplified Head was positioned at 0° with reference to the sled travel direction (Figure 25a). In four of those tests a 20° wedge between the stand and the neck mounting plate was used (Figure 25b).
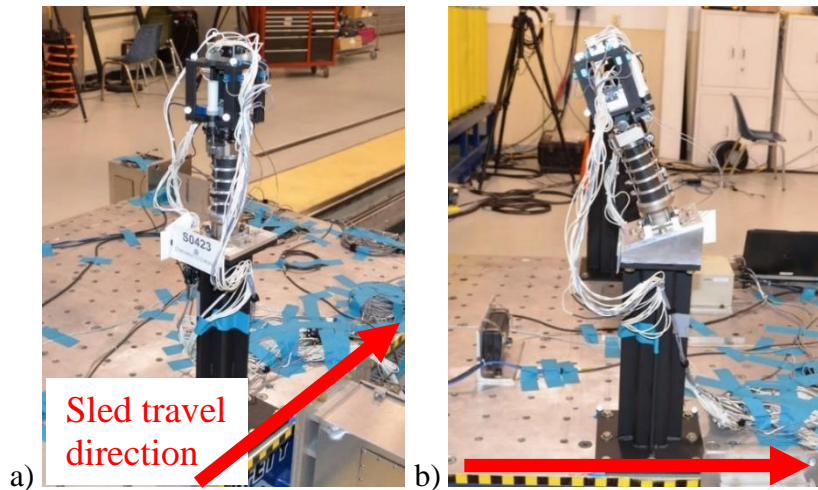
Figure 25. Simplified Head orientation at 0°: a) flat, without the 20° wedge; b) with the 20° wedge.

6.2.5 Test conditions – investigated parameters

Other than the head orientation several different parameters, that potentially could influence the calculated trajectory accuracy, were investigated.

For the use of this study, three different accelerometer blocks were utilized: a standard block being used currently in the THOR ATD head (Figure 26a), and two blocks fabricated at the University of Virginia (UVa) Center for Applied Biomechanics (Figure 26b & c).
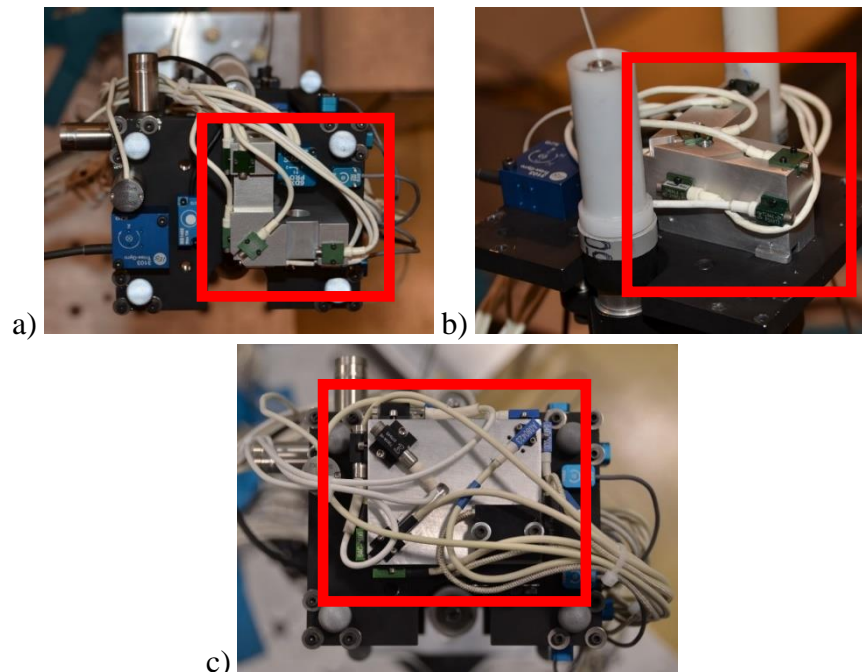
Figure 26. Accelerometer blocks used during testing: a) THOR's NAP block; b) UVa NAP block; c) UVa 4Acc block.

The Simplified Head structure allowed to mount accelerometer blocks on two different levels: bottom (Figure 27a) and top (Figure 27b). Changing the level changed the magnitude of linear acceleration recorded by the sensors.
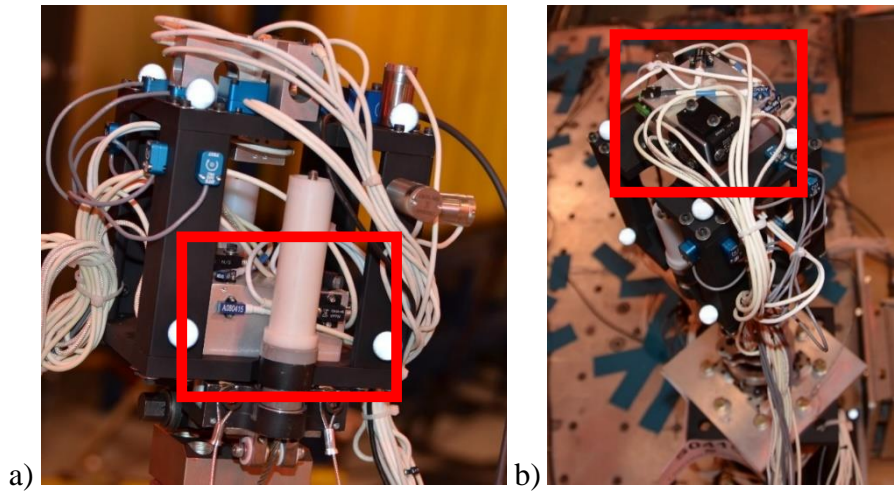
Figure 27. The same accelerometer block mounted on: a) bottom plate; b) top plate.

In addition, both of the UVa blocks allowed for mounting linear accelerometers in a way that the distance between the center of gravity (CG) of the sensor seismic mass and the measurement center (Figure 2) was either minimal (Figure 28a, dictated by the sensor geometry, varying from 6.35mm to 12.7mm) or the same (12.7mm; Figure 28b) for all used linear accelerometers. Moreover, the UVa NAP block accounted for an off-axis position of the 7264C accelerometer seismic mass (for more information see APPENDIX B).
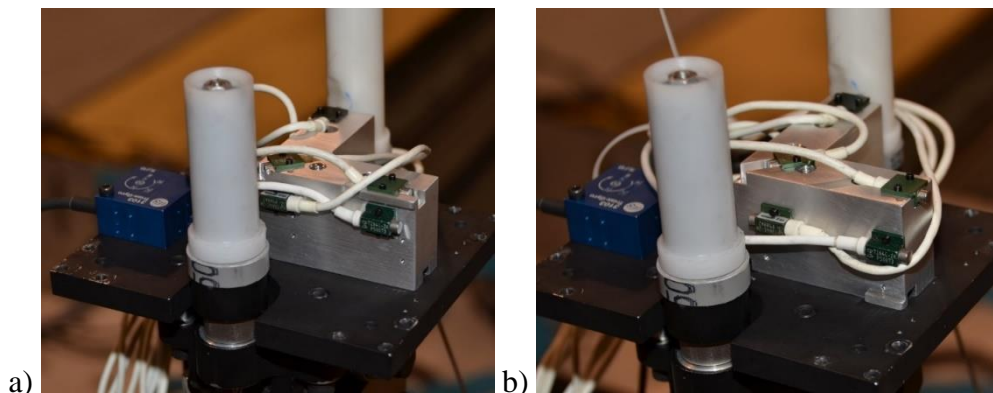
Figure 28. UVa NAP block with: a) minimum distance between sensor seismic mass CG and measurement center; b) 12.7mm distance between sensor seismic mass CG and measurement center.

6.2.6 Optoelectronic stereophotogrammetric system

Simplified Head kinematics were captured at 500 Hz with a 16 camera optoelectronic stereophotogrammetric system (OSS) (VICON MX, VICON, Los Angeles, CA). The motion capture system tracked the trajectories of spherical retroreflective markers through a calibrated 3D space (dimensions: 6m x 6m x 2m) within the cameras' collective field of view.

Four markers were attached to the base of the stand the head-neck assembly was mounted on (Figure 23) and eight markers were secured to the Simplified Head structure. Labeling convention for the VICON markers attached to the head is shown in Figure 29. Red bold labels represent the markers in the tests where the assembly was positioned at 45° with reference to the sled travel direction. Black labels represent the tests where the head was at 0° with reference to the sled travel direction.

Naming convention for the stand base markers was kept unchanged between the tests and it followed the naming convention from the "0°" angle tests, with "S" (sled) used instead of "B" (bottom) or "T" (top).
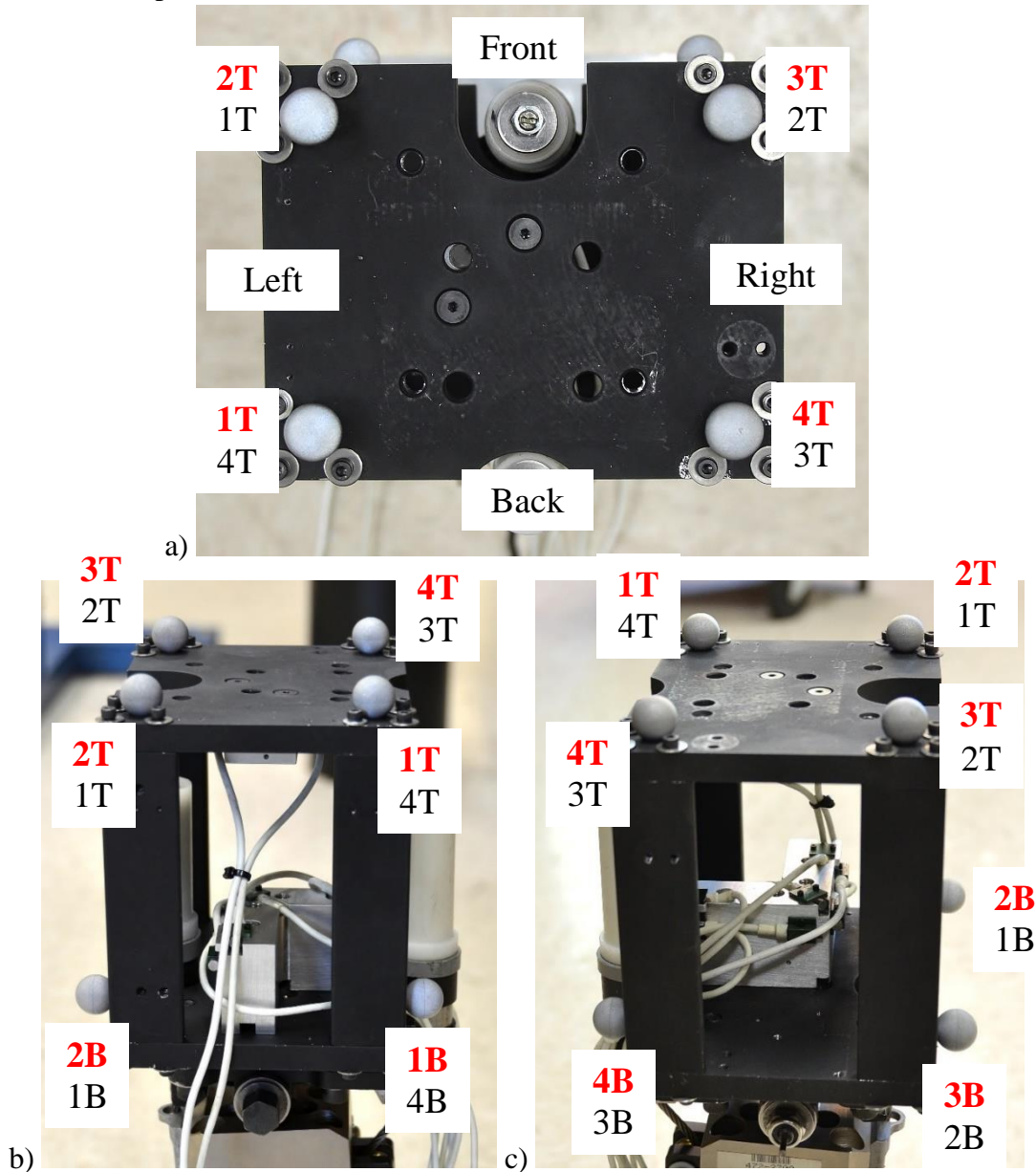
Figure 29. Naming convention for the VICON markers attached to the head. Labels in red correspond to the tests where the assembly was positioned at 45° with reference to the sled travel direction. Black labels represent the tests where the head was at 0° with reference to the sled travel direction: a) top view; b) left view; c) right view.

Based on the four top ("T") and four bottom ("B") markers two temporary coordinate systems were created (Figure 30) and then averaged together to establish the coordinate system describing the head assembly orientation in the IRF. The data from the start of the test was assumed to be the initial orientation of the head (in IRF) used later in the 3D trajectory calculation process.
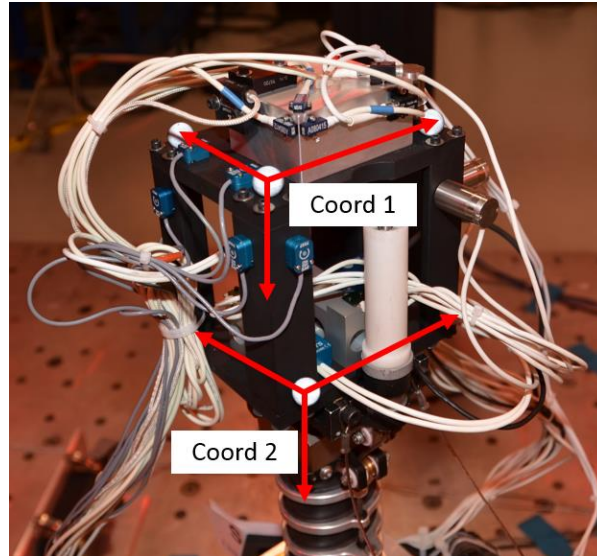
Figure 30. Two temporary coordinate systems used to establish the head orientation.

Head sensor/accelerometer block configuration was changed several times during testing. After each change, the assembly was 3D scanned to record the location and the orientation of the sensors relative to the head and the eight VICON markers secured to it (Figure 31).
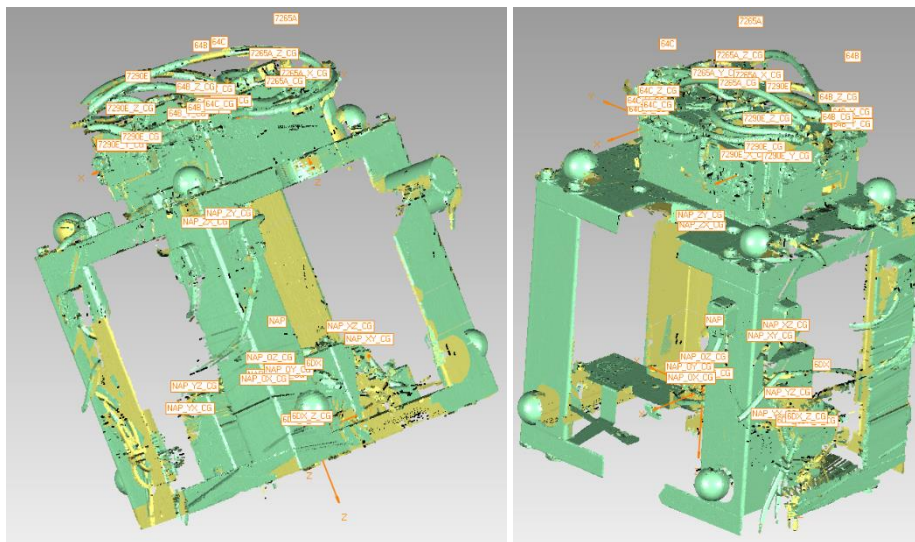
Figure 31. 3D scan of the head structure.

Using the data from the stereophotogrammetric system, the 3D scans of the sensor blocks, and the Least-Squares Pose Estimator approach (Cappozzo et al. 1997) the measurement center trajectories were determined, in the inertia coordinate frame, for all sensor packages utilized during

42

testing. Additionally, in the post-processing phase, a 3-point moving average was applied to the head optical data to eliminate isolated spikes.

6.2.7 Instrumentation

On the tests, head's accelerations were recorded by six different types of linear accelerometers (APPENDIX B). The head's local angular rate was measured by four types of angular rate sensors. Twenty four sets of 6DOF kinematics data were created and then utilized to compute 3D component trajectories for six measurement centers (one per each accelerometer type) as described in Section 1.2.3. Linear acceleration filtered with CFC 1000 and local angular rate filtered to CFC 60 were used in the process.

To update the orientation of the head (its rotation matrix $\boldsymbol{R}$), the body's local angular velocity and the method described by Rudd et al. 2006 were utilized.

6.2.8 Error metrics used in 3D trajectory calculations

In all tests and for all sensors (their different combinations), the following metric was used to evaluate the accuracy of the head's computed trajectory:

$$Res_{err} = \sqrt{\frac{\sum_{i=1}^{N}\left[\left(x_{OSS,i}-x_{calc,i}\right)^2+\left(y_{OSS,i}-y_{calc,i}\right)^2+\left(z_{OSS,i}-z_{calc,i}\right)^2\right]}{N}} \tag{6.1}$$

where N – number of data (time) points, $x_{OSS,i}$, $y_{OSS,i}$, $z_{OSS,i}$ – X, Y, Z components of the reference trajectory (from VICON OSS) at the data point i, $x_{calc,i}$, $y_{calc,i}$, $z_{calc,i}$ – X, Y, Z components of the calculated trajectory (based on sensor data) at the data point i.

For several different sensor packages used during testing, the peak value, the mean value, and the standard deviation for Res_{err} were reported. In addition to Res_{err}, the time history of the absolute difference (error) between the calculated and reference (from the VICON system) trajectories was determined and presented.

6.3 Results

In this subsection, the tracked body's orientation (Section 6.3.1) calculated using angular velocity recorded by different types of angular rate sensors and the calculated (based on inertial measurements) global trajectories for the Simplified Head (Section 6.3.2) are shown and described for exemplar tests. In addition, in Section 6.3.3, sensor packages that produced the smallest deviation between the computed and the reference trajectories are identified. Finally, in Section 6.3.4, peak, mean, and standard deviation values for Res_{err} (Eq. 6.1) are discussed for the sensor combinations from Section 6.3.3.

6.3.1 Orientation based on data from different angular rate sensors

For two tests: S0426 (test fixture positioned at 0° with reference to the sled travel direction) and S0442 (test fixture at 45°) the time history of the rotation matrix $\boldsymbol{R}$, computed using four different types of angular rate sensors, was compared to the orientation time-history obtained from the VICON system (Figure 32 to Figure 37).

In both tests, the angular velocity recorded around either one or two head local axes exceeded 1000 deg/sec. The IES sensor full scale range was 600 deg/sec. The data above that value, treated

as invalid for IES, substantially influenced the calculated orientation as obtained using the IES ARS (green line in "R21" in Figure 32, "R22" in Figure 36, or "R33" in Figure 37).

In general, though, the orientation computed with the data from different ARS (except when the local angular rate excided the full scale range of a sensor) matched VICON closely, with DTS ARS PRO (the model with the bandwidth up to 300Hz) diverging from the reference data slightly more than the other sensors in cases where there was no substantial change in the value of a component of the rotation matrix R (e.g. "R11" in Figure 32 or "R22" and "R32" in Figure 33).
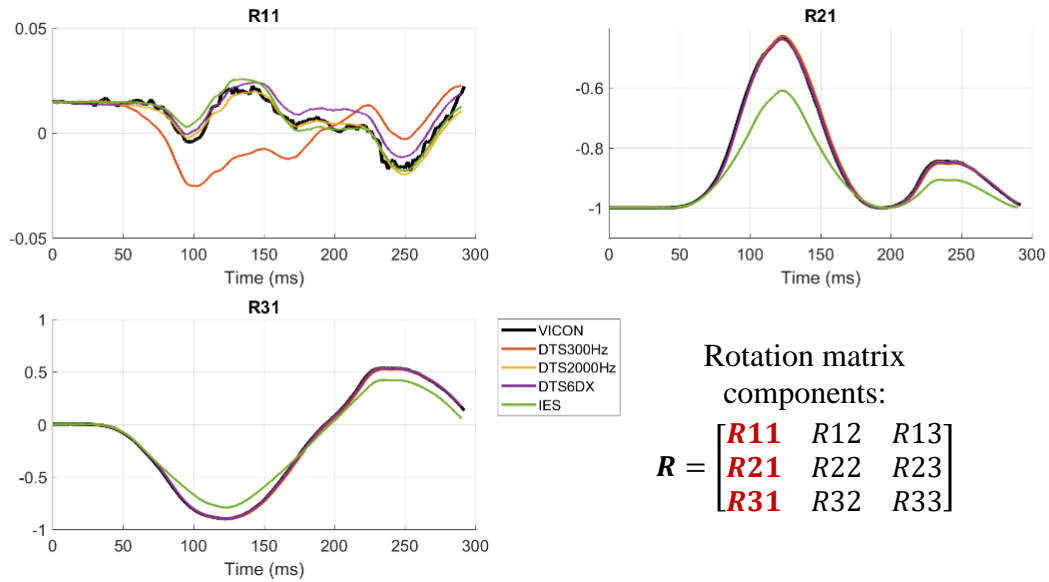
Figure 32. Test S0426 – Head's 1st unit vector components (1st column of the R matrix) obtained with four angular rate sensors compared to the VICON data.
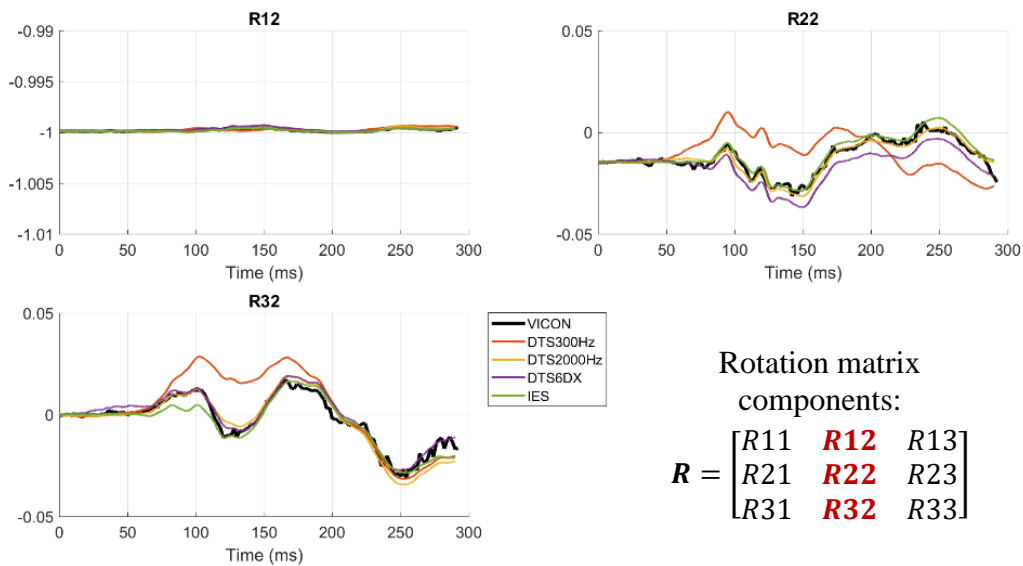
Figure 33. Test S0426 – Head's 2nd unit vector components (2nd column of the R matrix) obtained with four angular rate sensors compared to the VICON data.

44
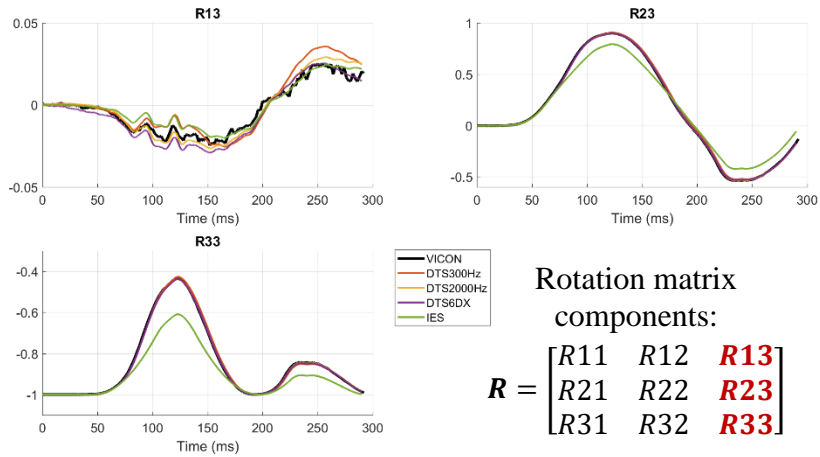
Figure 34. Test S0426 – Head's 3rd unit vector components (3rd column of the R matrix) obtained with four angular rate sensors compared to the VICON data.
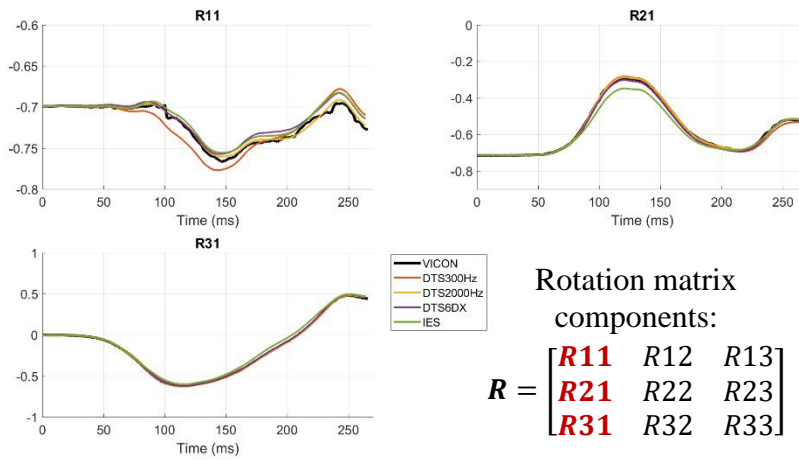
Figure 35. Test S0442 – Head's 1st unit vector components (1st column of the R matrix) obtained with four angular rate sensors compared to the VICON data.
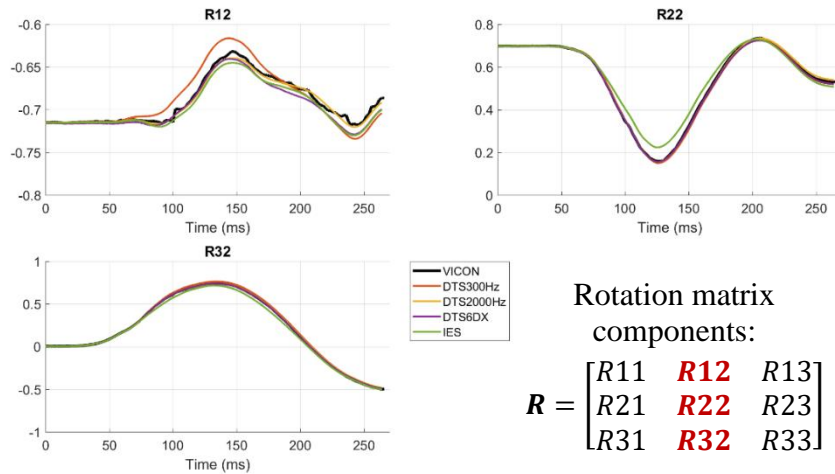
Figure 36. Test S0442 – Head's 2nd unit vector components (2nd column of the R matrix) obtained with four angular rate sensors compared to the VICON data.
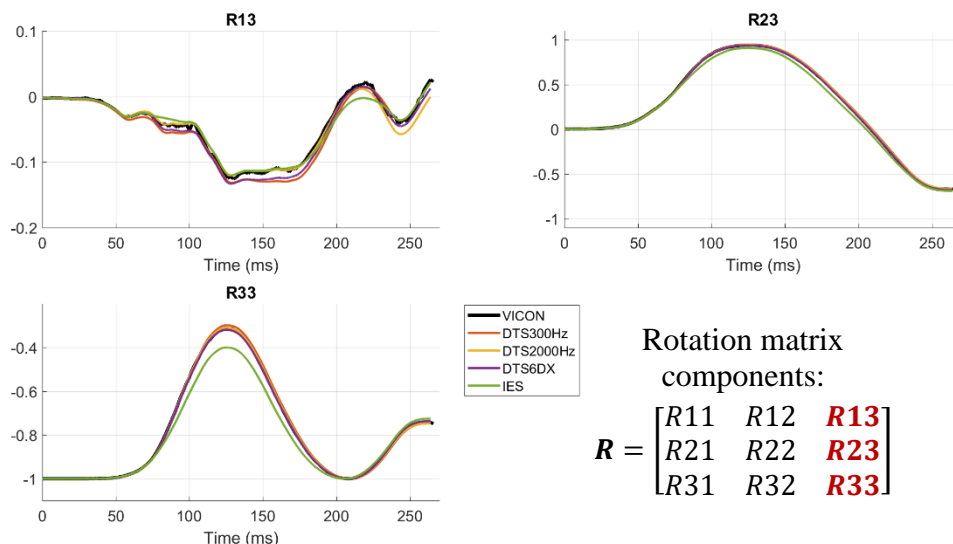
Figure 37. Test S0442 – Head's 3rd unit vector components (3rd column of the R matrix) obtained with four angular rate sensors compared to the VICON data.

6.3.2 Calculated global position

In this section the time histories of the global position of the measurement center (MC) for one of the sensor packages was compared to the reference (VICON) data for that MC in four exemplar tests: S0426 (test fixture at 0° relative to the sled travel direction, no wedge between the fixture and the stand), S0431 (at 45°, with the wedge), S0433 (at 0°, without the wedge), and S0442 (at 45°, without the wedge) (Figure 38 to Figure 41). In those four tests, the results for the sensor package that gave the smallest Res_{err} (Eq. 6.1) were presented. In the figures, the absolute error between the measured and calculated trajectories was indicated with a red line.

In all four tests, the calculated global trajectories (green lines) followed the general trend of the VICON curves (black). In some of the graphs, e.g., X and Z positon components in Test S0426 (Figure 38), a non-zero error (less than a millimeter) in the trajectories before time $t_0=0$ (before the sled started moving) was observed. That non-zero error was a result of the accelerometer data drift related to debiasing of the accelerometer readings just prior to the t_0 (trigger) time.

The absolute error values recorded in the exemplar tests varied between 4 mm (Z component in Test S0433; Figure 40) to approx. 35 mm (X component in Test S0433; Figure 40). It was expected that the absolute difference between the calculated and reference trajectories would grow in time due to the accumulation of errors coming from the integration process of global ACC. In some cases, the error steadily increased during the test and was highest at the end of the considered time period (e.g. in Test S0442; Figure 41). In other tests, though, the error first increased and then started decreasing (e.g., Y and Z components in Test S0433; Figure 40), which suggests that the error in the computed response was influenced by multiple factors, not only the accuracy of the integration process.

46
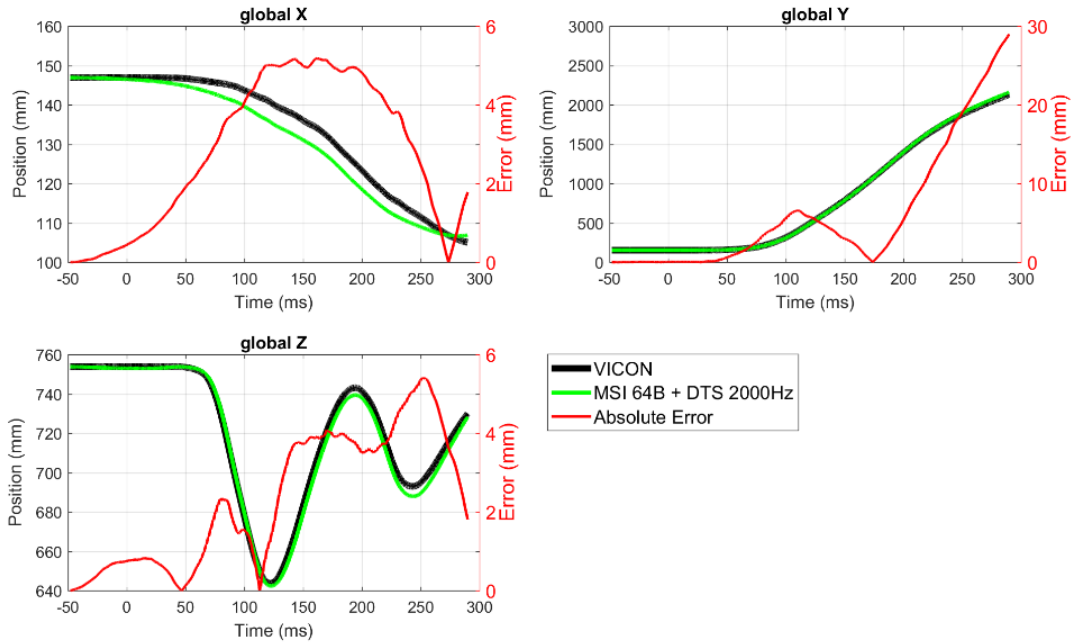
Figure 38. Test S0426 – Head global trajectories comparison: VICON (black) and calculated (green).
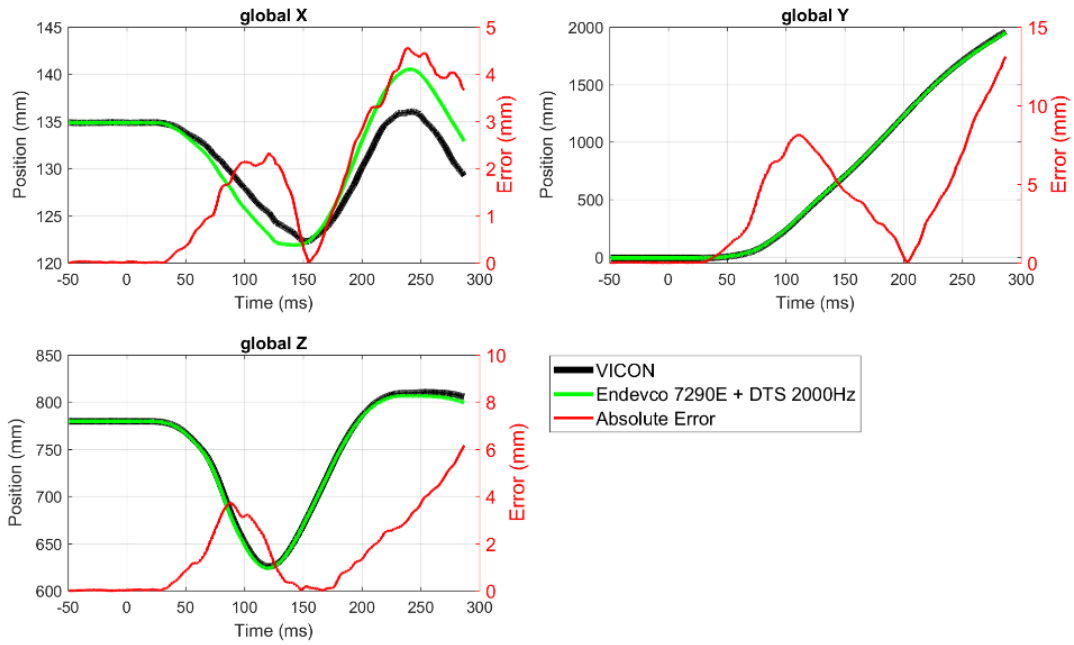
Figure 39. Test S0431 – Head global trajectories comparison: VICON (black) and calculated (green).
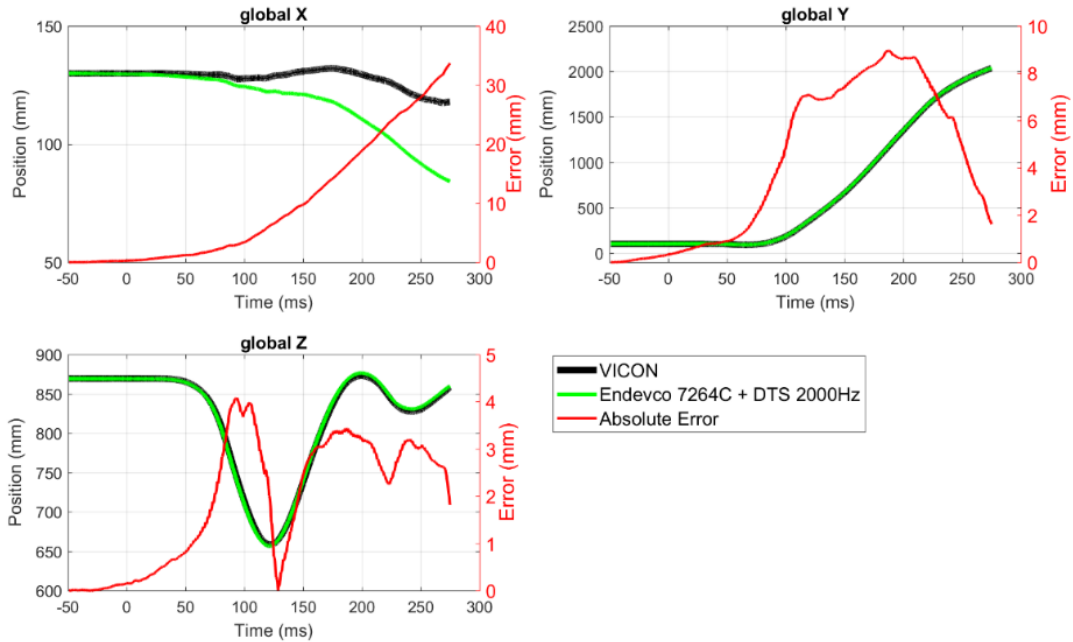
Figure 40. Test S0433 – Head global trajectories comparison: VICON (black) and calculated (green).
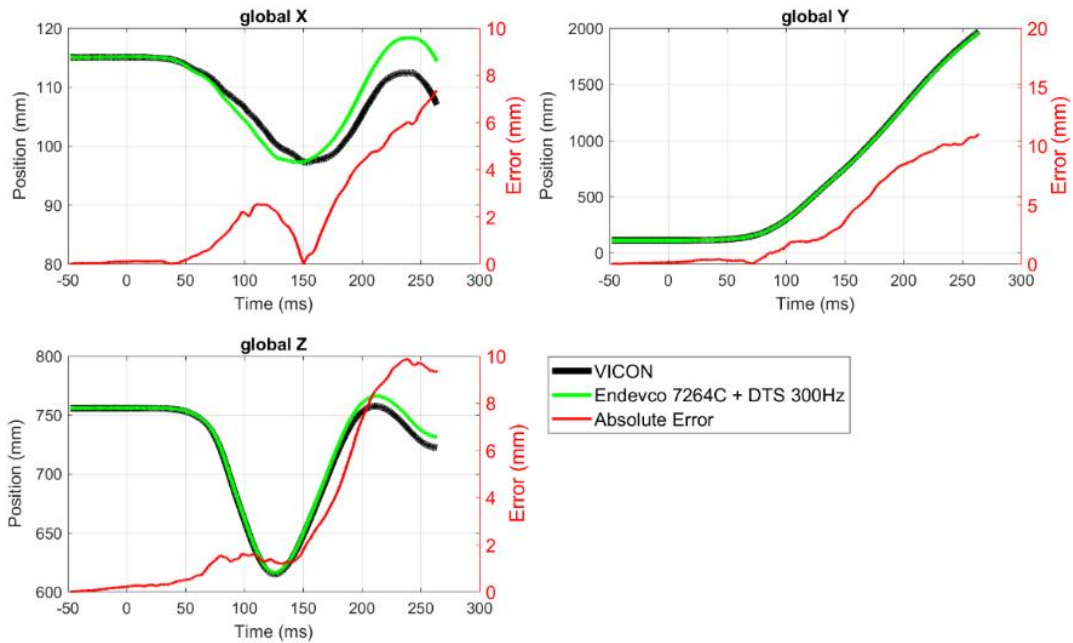
Figure 41. Test S0442 – Head global trajectories comparison: VICON (black) and calculated (green).

6.3.3 Sensor package with the smallest error

To remind the reader, the Simplified Head kinematics were captured with six types of linear accelerometers and four types of angular rate sensors which gave twenty four "ACC + ARS" data sets that were then used to compute 3D component trajectories of the analyzed structure.

The *Res_{err}* metric (Eq. 6.1) identified Endevco 7264C accelerometers combined either with DTS ARS PRO 300Hz or DTS ARS PRO 2000Hz as the package that produced the smallest

48

deviation between the computed and the reference trajectories in eighteen out of the forty Simplified Head tests (Table 4). MSI 64B-DTS 2000Hz and Endevco 7290E-DTS ARS PRO 2000Hz each gave the smallest Res_{err} in five tests. The other six sensor combinations mentioned in Table 4 were most accurate in the remaining twelve tests.

Table 4. # of times when the sensor combination produced the smallest Res_{err} acoss all used sensor packages.

#	Sensor combination (ACC – ARS)	# of times with the smallest Res_{err} (out of 40 tests)
1	END 7264C – DTS ARS PRO 300Hz	9
2	END 7264C – DTS ARS PRO 2000Hz	9
3	MSI 64B – DTS ARS PRO 2000Hz	5
4	END 7290E – DTS ARS PRO 2000Hz	5
5	END 7264C – IES	3
6	END 7264C – DTS 6DX PRO	3
7	END 7290E – IES	2
8	END 7290E – DTS 6DX PRO	2
9	MSI 64C – IES	1
10	MSI 64C – DTS ARS PRO 300Hz	1

Remark: Res_{err} for all tests and across all sensor combinations can be found in APPENDIX C.

6.3.4 Sensor combinations – summary

After taking into account only the "27g" pulse tests (Test S0420 to Test S0454; see APPENDIX A), for the two Endevco 7264C combinations as well as for the MSI 64B-DTS ARS PRO 2000Hz package, the peak value, the mean value, and the standard deviation (SD) of Res_{err} were calculated:

- Endevco 7264C – DTS ARS PRO 300Hz:
    - peak: 48.7 mm
    - mean: 16.7 mm
    - SD: 9.5 mm
- Endevco 7264C – DTS ARS PRO 2000Hz:
    - peak: 45 mm
    - mean: 15 mm
    - SD: 8.14 mm
- MSI 64B – DTS ARS PRO 2000Hz:
    - peak: 38.4 mm
    - mean: 22.4 mm
    - SD: 7 mm

For Endevco 7290E with DTS ARS PRO 2000Hz, the peak value, the mean value, and the standard deviation for Res_{err} were calculated using the results from Tests S0425-S0454 (see APPENDIX A – *additional remarks* for details about exclusion of Tests S0420-S0424):

- Endevco 7290E - DTS ARS PRO 2000Hz:
    - peak: 20.7 mm
    - mean: 12.5 mm
    - SD: 3.6 mm

In addition, for the four discussed sensor packages a scatter plot of Res_{err} was created to show how well the three combinations, other than the one with the smallest Res_{err} recorded on the test, predicted the 3D trajectory of the Simplified Head (Figure 42).
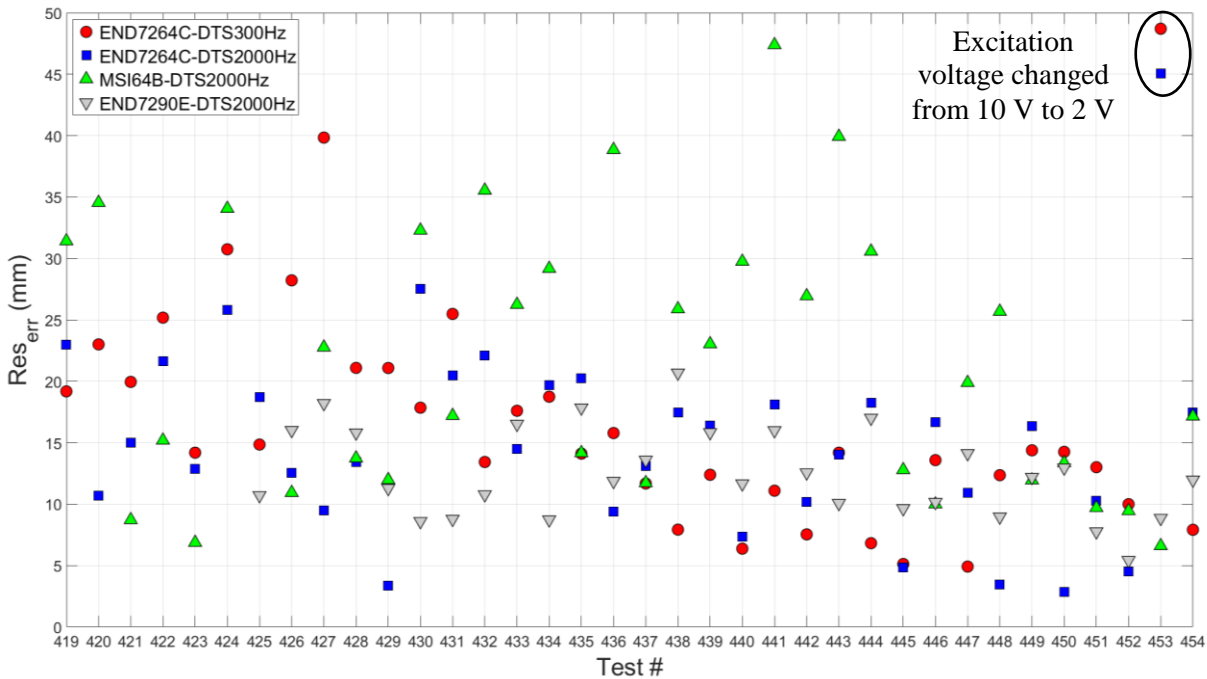
Figure 42. Res_{err} for the four discussed sensor packages.

The sensor package with the highest mean value of Res_{err} (22.4 mm), across the four discussed sensor combinations, was MSI 64B – DTS ARS PRO 2000Hz. Endevco 7264C – DTS ARS PRO 300Hz had the greatest variability (highest SD of 9.5 mm) with six tests in which Res_{err} excided 25 mm (Figure 42; red dots). In Test S0453, though, the excitation voltage was modified from 10 V to 2 V and that change is believed to be responsible for the increased difference between VICON and the calculated 3D results for both, Endevco 7264C – DTS ARS PRO 300Hz and Endevco 7264C – DTS ARS PRO 2000Hz. The most consistent Res_{err} (across the analyzed tests), with the smallest mean value (12.5 mm) and smallest SD (3.6 mm), was found for Endevco 7290E with DTS ARS PRO 2000Hz (Figure 42; grey triangles). In terms of the results variability, Endevco 7264C – DTS ARS PRO 2000Hz and MSI 64B – DTS ARS PRO 2000Hz were in-between Endevco 7264C – DTS ARS PRO 300Hz and Endevco 7290E with DTS ARS PRO 2000Hz, with SD of 8.14 mm and 7 mm, respectively.

6.4 Conclusions

The aim of the current study was to evaluate the ability of the algorithm described in Section 1.2.3 to calculate accurate trajectories in sled testing where a simplified structure representing an ATD's head-to-neck assembly was utilized. The following can be concluded from the results of the study:

- In general, the orientation computed with the data from different types of angular rate sensors matched the reference response (from the VICON system) closely, except for the

situation when the local angular rate excided the full scale range of the sensor used (IES sensor, e.g., "R21" component in Figure 32).

- The absolute error values recorded in the four exemplar tests varied between 4 mm (Z component in Test S0433; Figure 40) to approx. 35 mm (X component in Test S0433; Figure 40).

- After excluding the IES sensor from the analysis, the highest Res_{err} recorded across the "27 g" pulse tests and all possible sensor combinations was 123.2 mm (DTS6DX PRO ACC-DTS ARS PRO 300Hz; Test S0426). The smallest Res_{err} of approx. 2.9 mm was identified for Endevco 7264C – DTS ARS PRO 2000Hz in Test S0450.

- The Res_{err} metric identified Endevco 7264C accelerometers combined either with DTS ARS PRO 300Hz or DTS ARS PRO 2000Hz as the package that produced the smallest deviation between the computed and the reference trajectories in eighteen out of the forty Simplified Head tests, which constituted for 45% of all performed test (Table 4).

- In Test S0453, the excitation voltage for the Endevco 7264C accelerometers was modified from 10 V to 2 V and that change is believed to be responsible for the substantial increase in the trajectory error seen for both, the Endevco 7264C – DTS ARS PRO 300Hz and the Endevco 7264C – DTS ARS PRO 2000Hz sensor packages.

7. THOR MOD-KIT TESTING

7.1 Introduction

To assess the proposed algorithm accuracy in a more complex and challenging scenario than the one described in Chapter 6 (where only a head-to-neck assembly was utilized), eight sled tests were performed with the THOR Mod-kit ATD (S/N: T0015), with either the THOR stock head or the Simplified Head (Figure 43 top right and left, respectively). The ATD arms were removed to reduce the chance of motion tracking camera occlusions. THOR was seated in the Gold Standard (GS) buck positioned at 30 deg relative to the sled travel direction (Figure 43 bottom). After testing, damages to the structure were assessed and the test data were processed and analyzed. Any damage or failure to the dummy or instrumentation was rectified before the next sled test was performed. This procedure was repeated until the test series was completed.
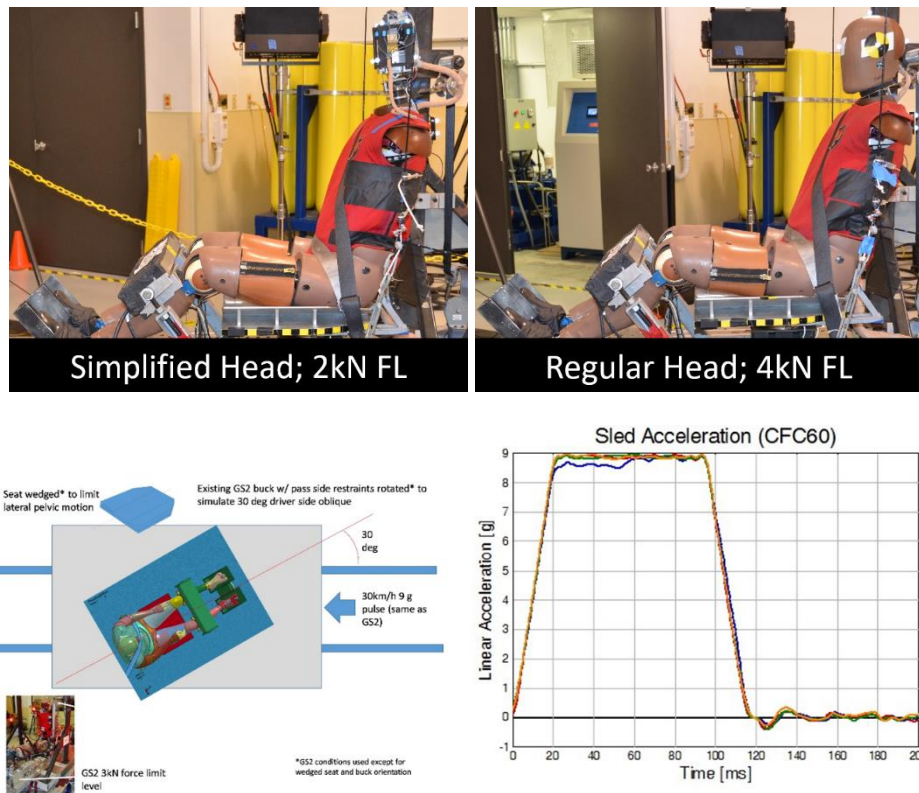
Figure 43. THOR dummy, two sample tests: with Simplified Head (top left) and with stock ATD head (top right). Gold Standard 3 configuration shown in bottom. A shoulder belt with two levels of force-limiting (FL; cf. Shaw et al. 2014) was used for upper body restraint.

The chapter is organized as follows. Section 7.2 focuses on the methods used during testing and later in the position calculation analysis. The results of the study (calculated orientation and position) are presented in Section 7.3. Concluding remarks summarizing the research effort presented here are provided in Section 7.4.

7.2 Methods

7.2.1 Test matrix

The complete matrix of all eight THOR sled tests carried out within the dissertation is presented in APPENDIX D. The following sections describe the testing procedure.

7.2.2 Sled input

The acceleration time history utilized for the sled system as the input was a 9g trapezoidal pulse (Figure 44) used previously for Gold Standard tests (Montesinos-Acosta et al. 2016).
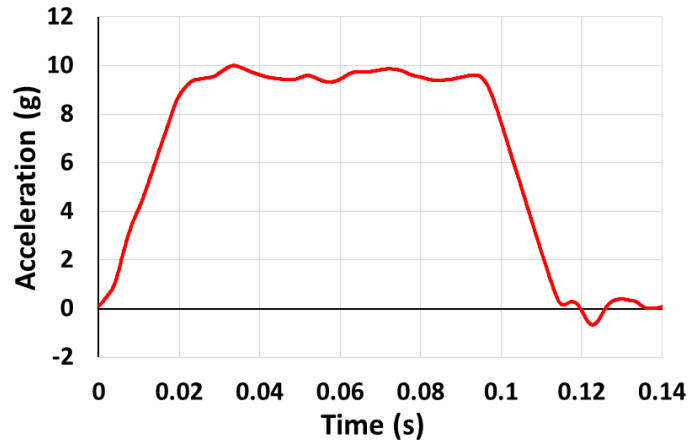
Figure 44. Acceleration time histories used during testing.

7.2.3 Coordinate systems

7.2.3.1 Test S0455

Two coordinate systems were used to process and present the data from the test. The Simplified Head local coordinate system, which remained fixed to the head assembly during the test, was defined using standardized conventions (SAE J211, 1995; Figure 45). The positive X axis pointed from the rear to the front of the head. The positive Y axis pointed from the head left hand side to the head right hand side. The positive Z axis pointed from the top to the bottom of the assembly.
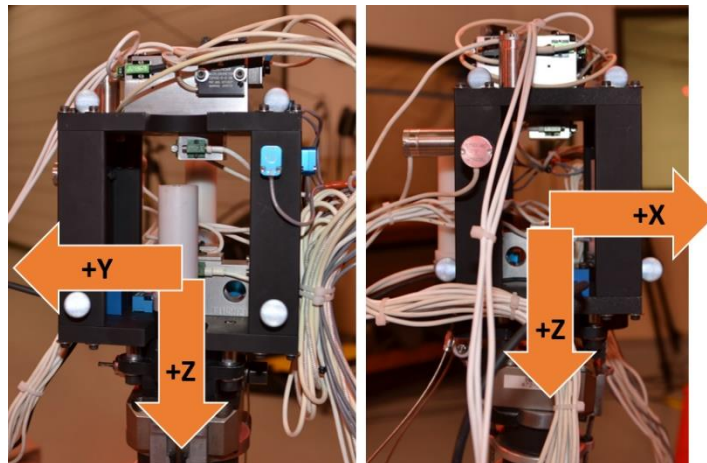
Figure 45. Simplified Head (local) coordinate system was chosen to match the SAE standard (J211) coordinate system for the head.

The global or inertial reference frame (IRF) was defined in the following way: the Y axis was aligned with the direction of the sled travel. The sled traveled in the positive Y direction. The Z axis was oriented normal to the sled base top surface, with positive pointing upward. The positive X-axis was mutually perpendicular to the Y and Z axes, with positive direction shown in Figure 46.
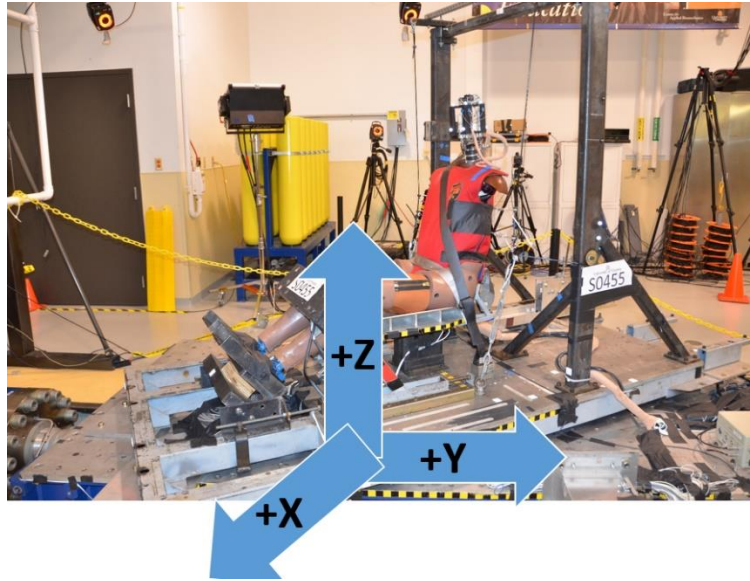
Figure 46. Inertial (global) coordinate frame definition.

7.2.3.2 Tests S0456 – S0462

Two coordinate systems were used to process and present the data from the tests. The THOR head coordinate system, which remained fixed to the body during testing, was defined using standardized conventions (SAE J211, 1995; Figure 47). The positive X axis pointed from the rear to the front of the head. The positive Y axis pointed from the head left hand side to the head right hand side. The positive Z axis pointed from the top to the bottom of the head.
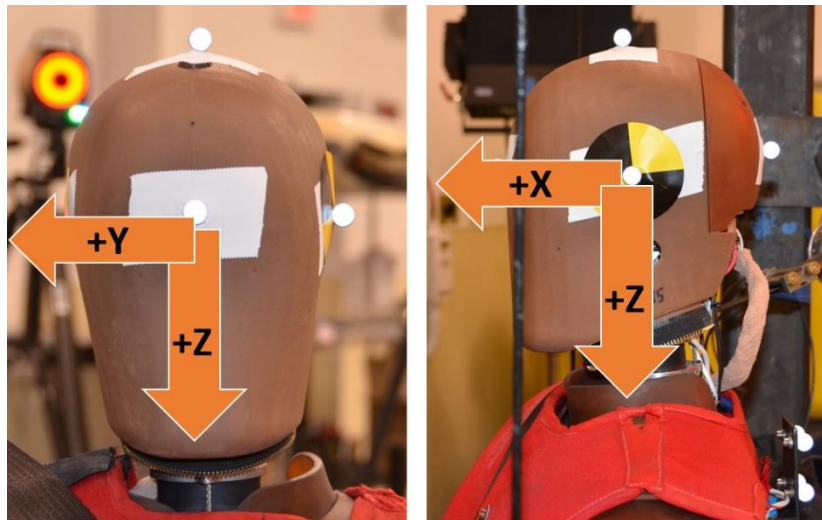
Figure 47. Head (local) coordinate system was chosen to match the SAE standard (J211) coordinate system for the head.

The global or inertial reference frame (IRF) was defined in the following way: the Y axis was aligned with the direction of the sled travel. The sled traveled in the positive Y direction. The Z axis was oriented normal to the sled base top surface, with positive pointing upward. The positive X-axis was mutually perpendicular to the Y and Z axes, with positive direction shown in Figure 48.
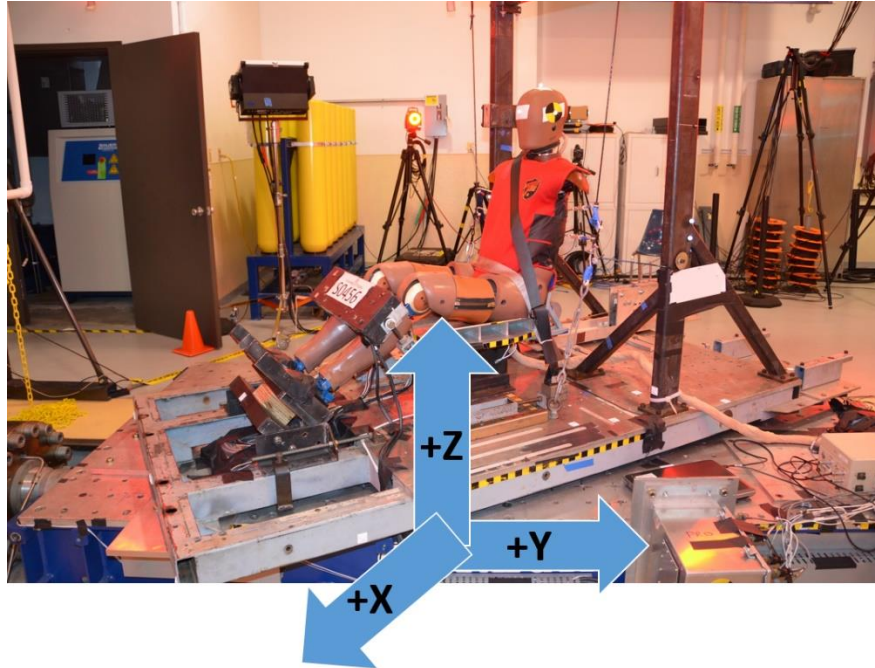
Figure 48. Inertial (global) coordinate frame definition.

7.2.4 Head type

In the first test of the series (S0455) the Simplified Head (Figure 49 left) was used to gather data for a larger number of sensors. In the seven remaining tests, the regular THOR ATD head was utilized (Figure 49 right).
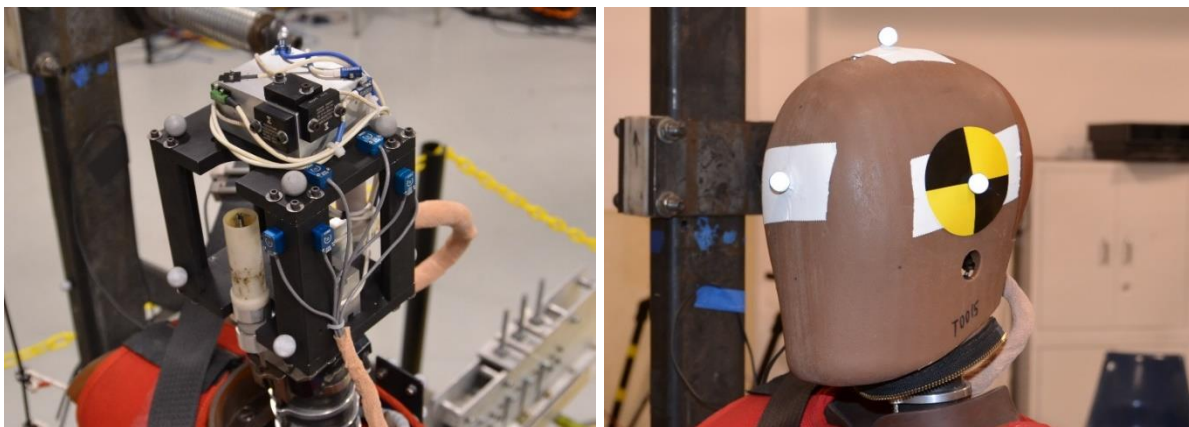
Figure 49. Different head types used during testing: Simplified Head (left) and THOR Stock Head (right).

7.2.5 Head tether

In two out of the eight tests (S0458 and S0459) a head tether was used to force the head to rotate about its local Z axis, in the negative direction (toward the left shoulder). In Test S0458 a

one-layer short piece of the 2"-wide Gaffer's tape® was utilized (Figure 50 left). In Test S0459 a four-layer long piece (Figure 50 right) was used to give the head more slack before causing the head rotation. In both cases, the tape was attached to the dummy chin and, next, to the steel frame of the Gold Standard buck (Figure 50 right).

Figure 50. Head tether: Test S0458 (left), Test S0459 (right).

7.2.6 Simulated impact

Three sled tests (see Table) involved THOR ATD head impact to assess the influence of impact kinematics on the calculated 3D trajectories. The impact was produced by mounting a foam-padded steel bar in the path of the moving head (Figure 51).
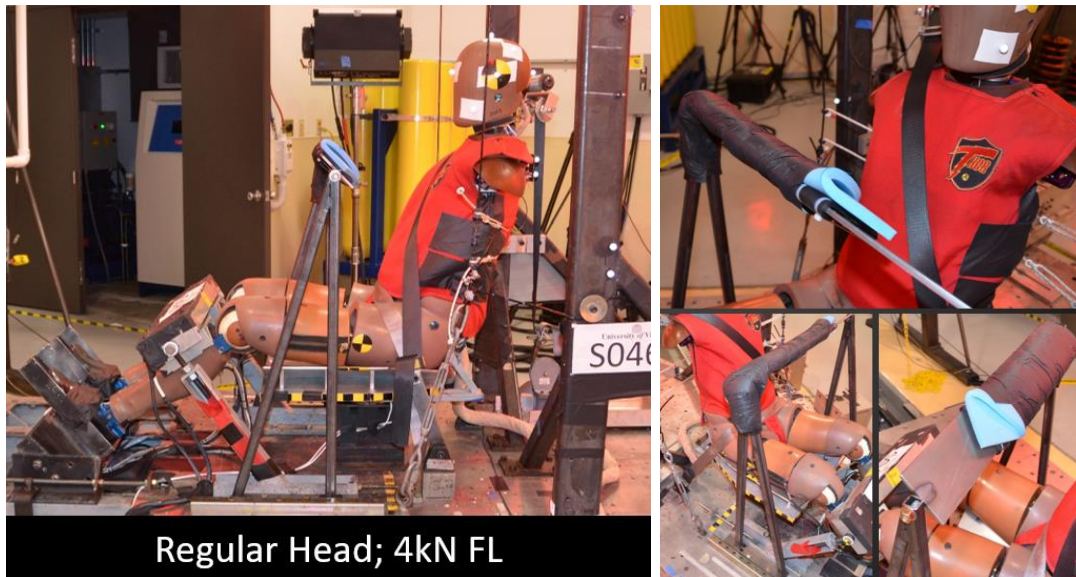
Figure 51. Steel structure to simulate head impact.

7.2.7 Optoelectronic stereophotogrammetric system

The head kinematics data were captured at 1000 Hz with a 16 camera optoelectronic stereophotogrammetric system (OSS) (VICON MX, VICON, Los Angeles, CA). The motion capture system tracked the trajectories of spherical retroreflective markers through a calibrated 3D space within the cameras' collective field of view.

7.2.7.1 Test S0455

In Test S0455 eight markers were secured to the Simplified Head structure. Labeling convention for the VICON markers attached to the head is shown in Figure 52.
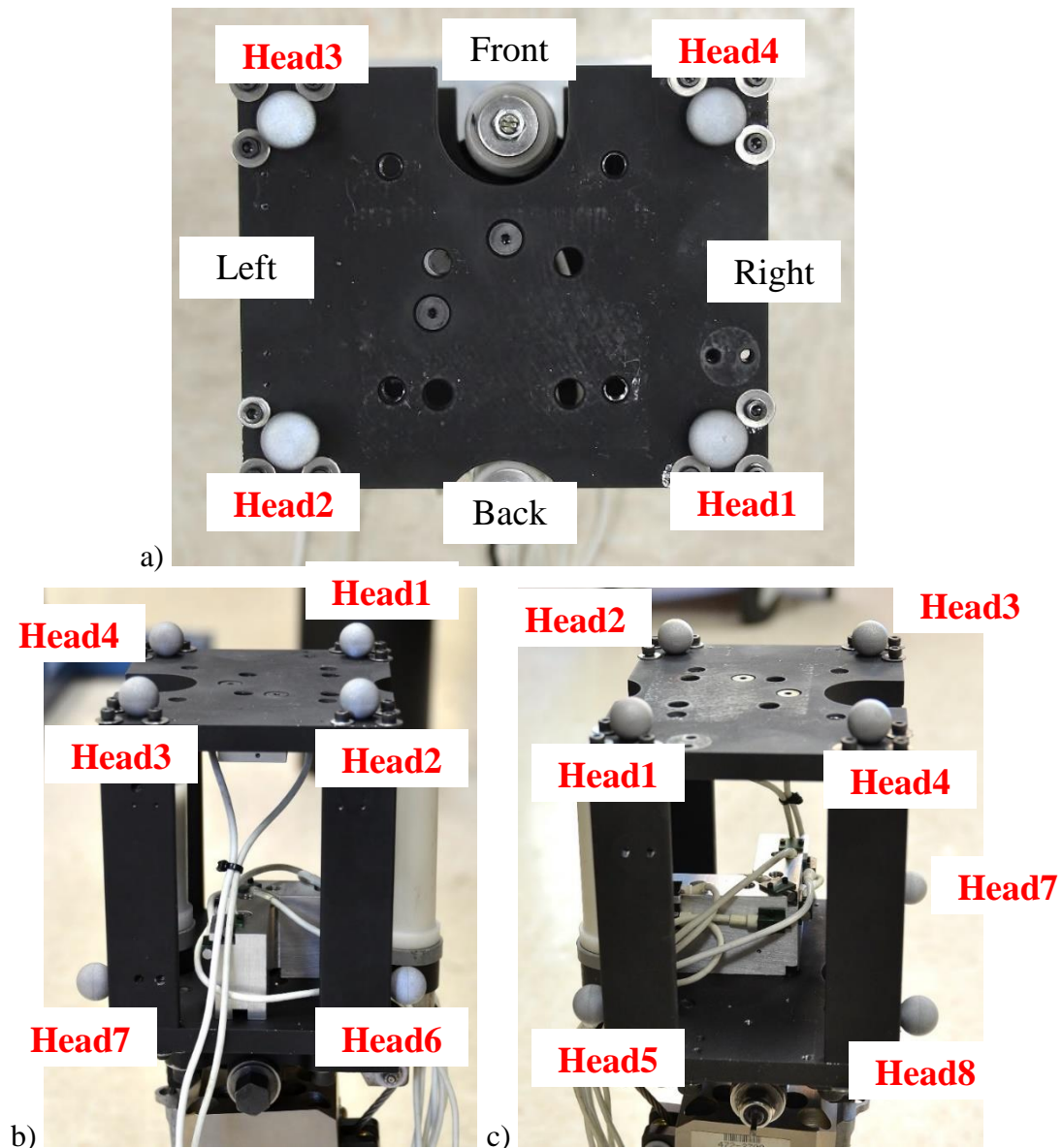
Figure 52. Naming convention for the VICON markers attached to the simplified head: a) top view; b) left view; c) right view.

7.2.7.2 Tests S0456-S0459

In Tests S0456-S0459 five markers were secured to the THOR head. Labeling convention for the VICON markers attached to the head is shown in Figure 53.
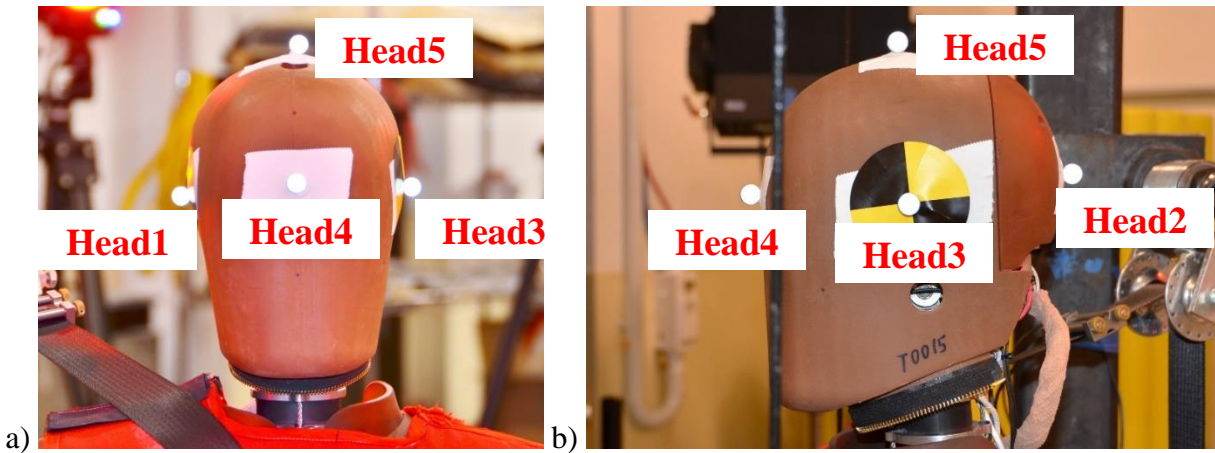
Figure 53. Naming convention for the VICON markers attached to the head: a) front view; b) left view.

7.2.7.3 Tests S0460-S0462

In Tests S0460-S0462 eight markers were secured to the THOR head. Labeling convention for the VICON markers attached to the head is shown in Figure 54.
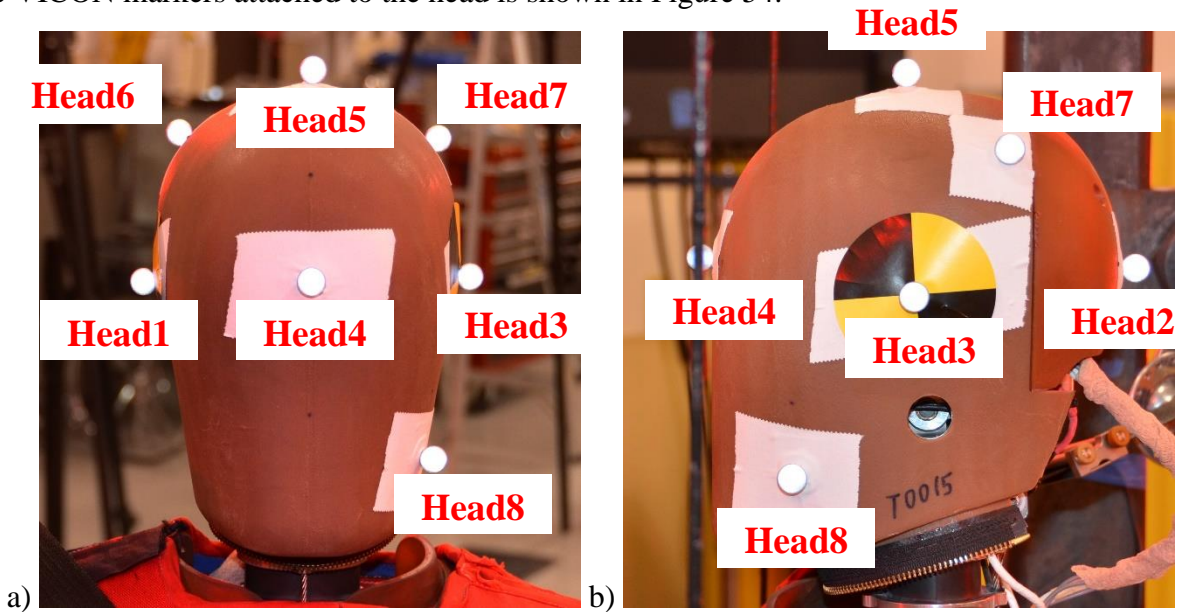
Figure 54. Naming convention for the VICON markers attached to the head: a) front view; b) left view.

7.2.8 3D scans of the head

Head sensor/accelerometer block configuration was changed several times during testing. After each change the sensor configuration was 3D scanned to record the location and the orientation of the sensors relative to the head and the VICON markers secured to it (Figure 55).
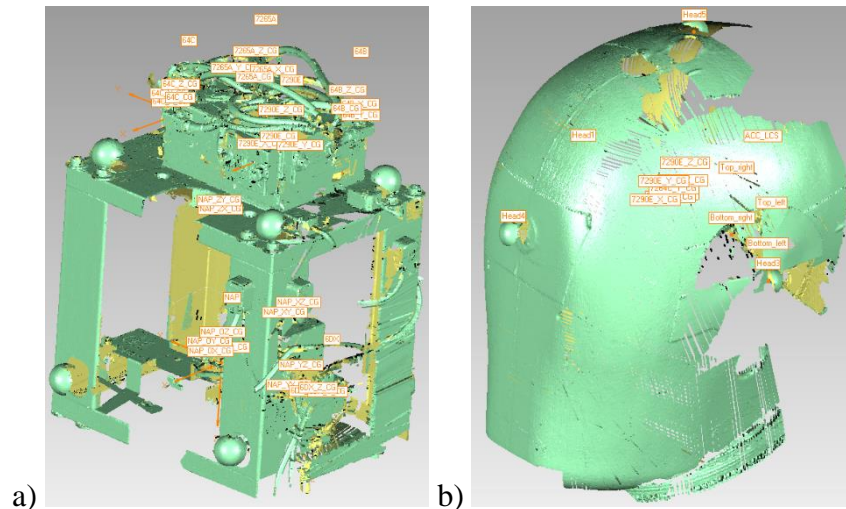
Figure 55. 3D scan of: a) Simplified Head, b) THOR head.

Using the data from the stereophotogrammetric system, the 3D scans of the sensor blocks, and the Least-Squares Pose Estimator approach (Cappozzo et al. 1997) the measurement center trajectories were determined, in the inertia coordinate frame, for all linear accelerometer packages utilized during testing. Additionally, in the post-processing phase, a 3-point moving average was applied to the head VICON data to eliminate isolated spikes.

7.2.9 Instrumentation

On the tests, head's 6DOF kinematics were captured with linear accelerometers (ACC) and angular rate sensors (ARS) attached the analyzed body (see APPENDIX E). In the first test of the series (Test S0455), five different types of linear accelerometers and two types of angular rate sensors were used. In the last test (Test S0462), only one type of ACC and one type of ARS were utilized. In the remaining six tests, head's kinematics data were measured by two different types of ACC and two types of ARS. Recorded data were then utilized to compute 3D component trajectories of the head as described in Section 1.2.3. Linear acceleration filtered with CFC 1000 and local angular rate filtered to CFC 60 were used in the process.

7.2.10 Head orientation update

To update the orientation of the tracked body (its rotation matrix R), the head's local angular velocity and the method described by Rudd et al. 2006 were used. Initial orientation of the head – in the global frame – was determined with a Coordinate Measuring Machine (CMM) in conjunction with the data from the VICON system (at the start of the test), 3D scans of the sensor blocks mounted inside the ATD's skull, and the Least-Squares Pose Estimator approach (Cappozzo et al. 1997).

7.2.11 Error metrics used in 3D trajectory calculations

In all eight tests, the following metric was utilized to evaluate the accuracy of the head's computed trajectory:

$$Res_{err} = \sqrt{\frac{\sum_{i=1}^{N}\left[(x_{OSS,i}-x_{calc,i})^2+(y_{OSS,i}-y_{calc,i})^2+(z_{OSS,i}-z_{calc,i})^2\right]}{N}} \qquad (7.1)$$

where N – number of data (time) points, $x_{OSS,i}$, $y_{OSS,i}$, $z_{OSS,i}$ – X, Y, Z components of the reference trajectory (from VICON OSS) at the data point i, $x_{calc,i}$, $y_{calc,i}$, $z_{calc,i}$ – X, Y, Z components of the calculated trajectory (based on sensor data) at the data point i.

In addition to Res_{err}, the time history of the absolute difference (error) between the calculated and VICON trajectories was determined and presented.

7.3 Results

In this subsection, the tracked body's orientation (Section 7.3.1) calculated using angular velocity recorded by different types of angular rate sensors and the calculated (based on inertial measurements) global trajectories for the THOR Head (Section 7.3.2) are shown and described for exemplar tests.

7.3.1 Orientation based on data from different angular rate sensors

For three tests: S0455 (Simplified Head; 2kN FL; without impact), S0457 (Regular Head; 4kN FL; without impact), and S0461 (Regular Head; 4kN FL; simulated impact) the time history of the head rotation matrix **R**, obtained using two types of angular rate sensors, was compared to the corresponding VICON data.

In the presented cases both, DTS ARS PRO 300Hz and DTS ARS PRO 2000Hz, were able to predict the general shape and the magnitude of the head's rotation. In Test S0455 (Simplified Head), DTS ARS PRO 300Hz appeared to diverge more from the VICON results than DTS ARS PRO 2000Hz ("R11" component in Figure 56 or "R32" component in Figure 57). In Test S0457, where the regular THOR head was used, DTS ARS PRO 300Hz followed VICON more closely than DTS ARS PRO 2000Hz ("R11" in Figure 59 or "R32" in Figure 60). In some of the tests both angular rate sensors were either underestimating ("R12" and "R22" in Figure 60) or over-predicting ("R21" in Figure 59) the rotation of the head. In Test S0461, in which a head-to-structure impact was simulated, DTS ARS PRO 300Hz as well as DTS ARS PRO 2000Hz were able to capture the abrupt change in the head's rotational movement (at approx. t = 116ms, when the head hit the barrier) with both ARS either overshooting or underestimating the VICON value slightly (e.g. "R21" component in Figure 62, "R12" in Figure 63, and "R33" in Figure 64).
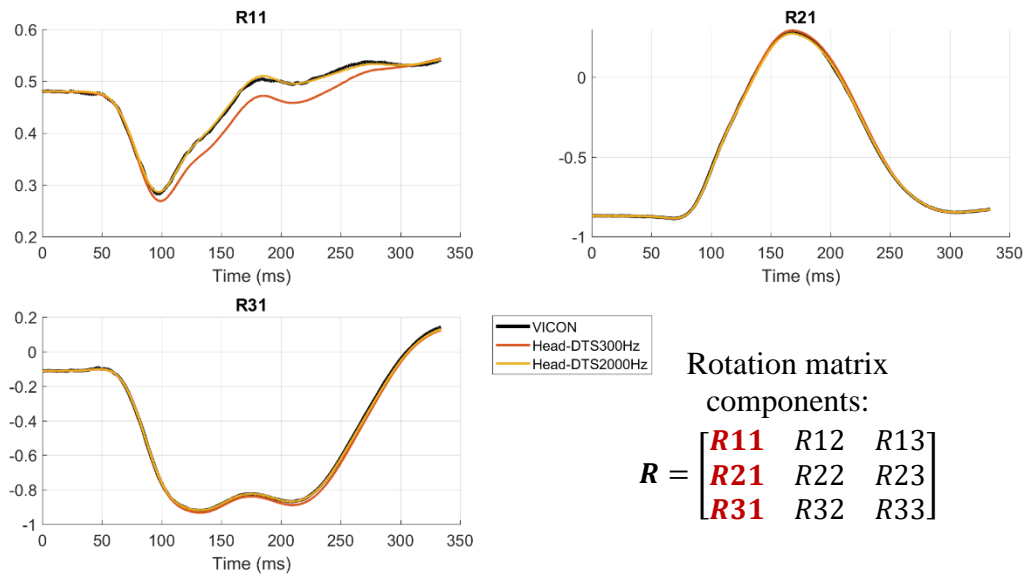
Figure 56. Test S0455 – Head's 1st unit vector components (1st column of the R matrix) obtained with four angular rate sensors compared to the VICON data.
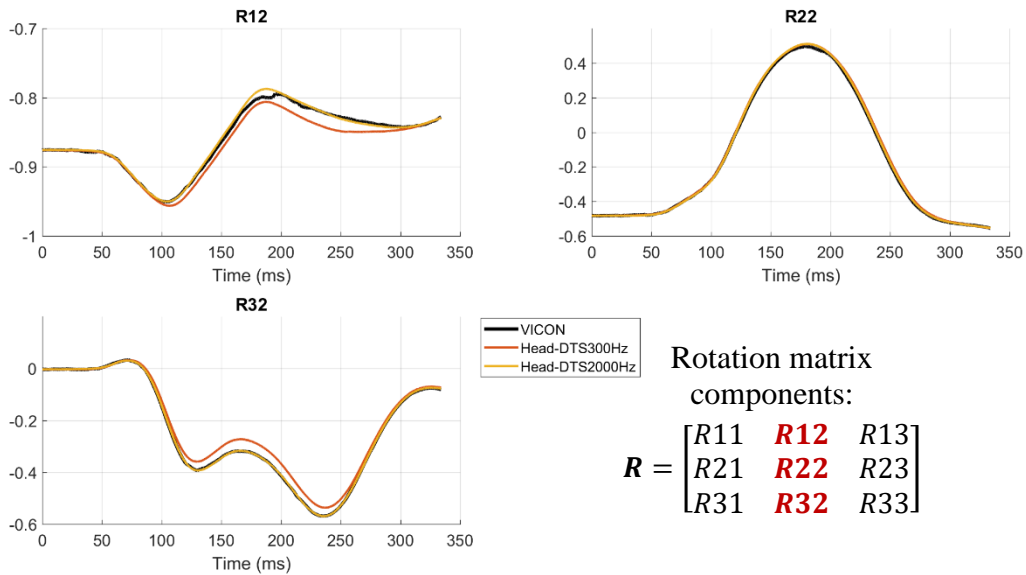
Figure 57. Test S0455 – Head's 2nd unit vector components (2nd column of the R matrix) obtained with four angular rate sensors compared to the VICON data.

61
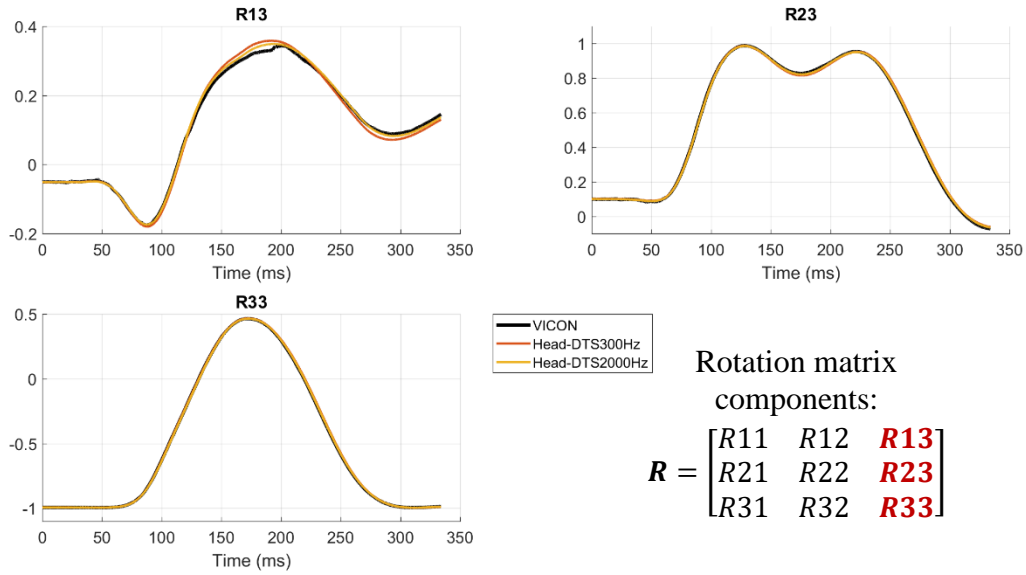
Figure 58. Test S0455 – Head's 3rd unit vector components (3rd column of the R matrix) obtained with four angular rate sensors compared to the VICON data.
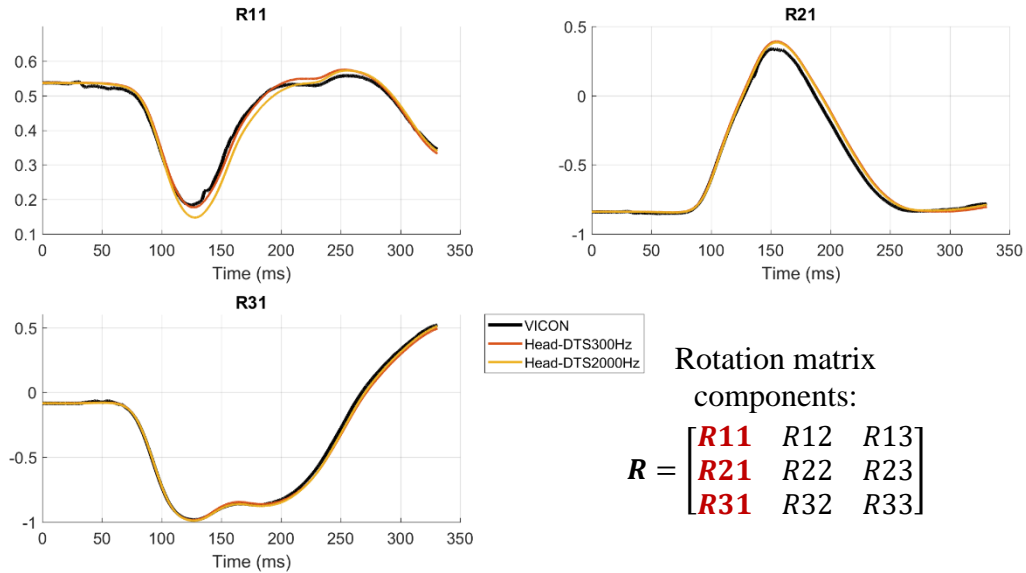
Figure 59. Test S0457 – Head's 1st unit vector components (1st column of the R matrix) obtained with four angular rate sensors compared to the VICON data.
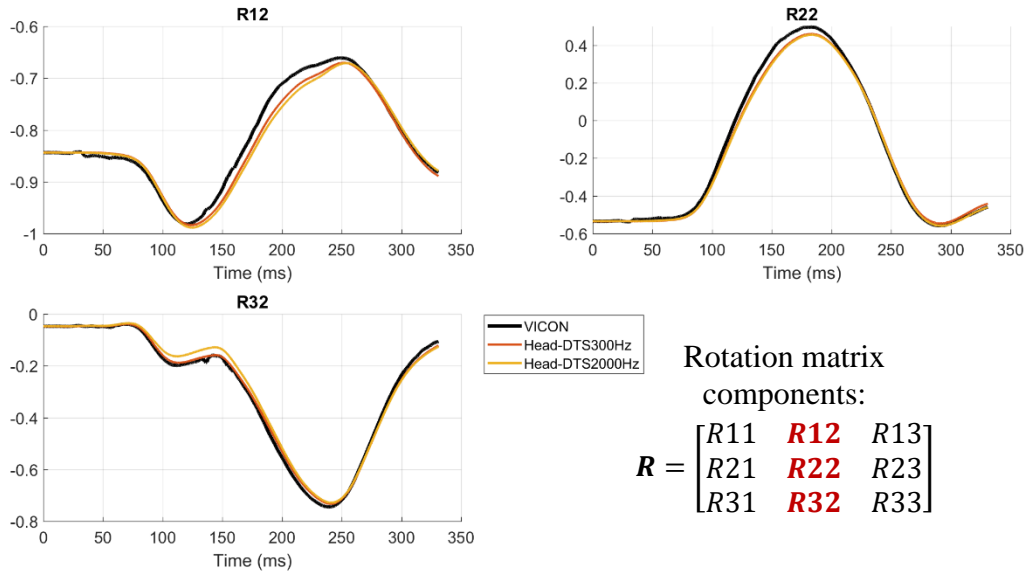
Figure 60. Test S0457 – Head's 2nd unit vector components (2nd column of the R matrix) obtained with four angular rate sensors compared to the VICON data.
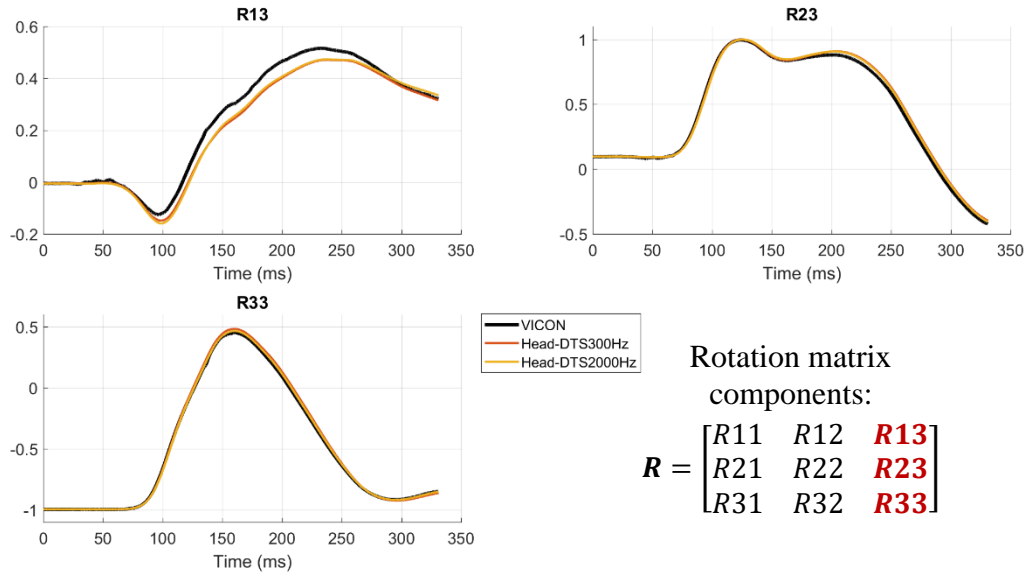
Figure 61. Test S0457 – Head's 3rd unit vector components (3rd column of the R matrix) obtained with four angular rate sensors compared to the VICON data.
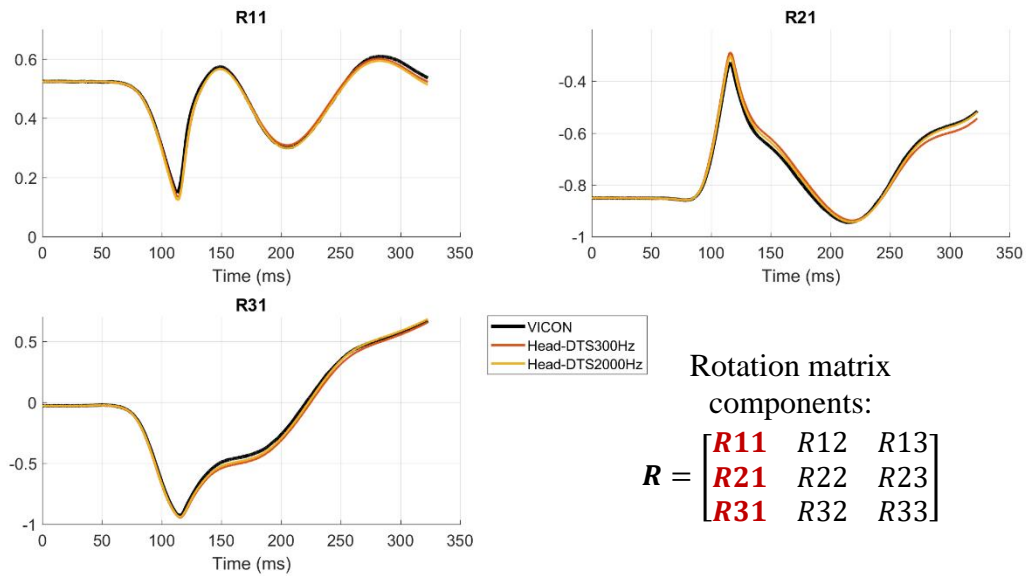
Figure 62. Test S0461 – Head's 1st unit vector components (1st column of the R matrix) obtained with four angular rate sensors compared to the VICON data.
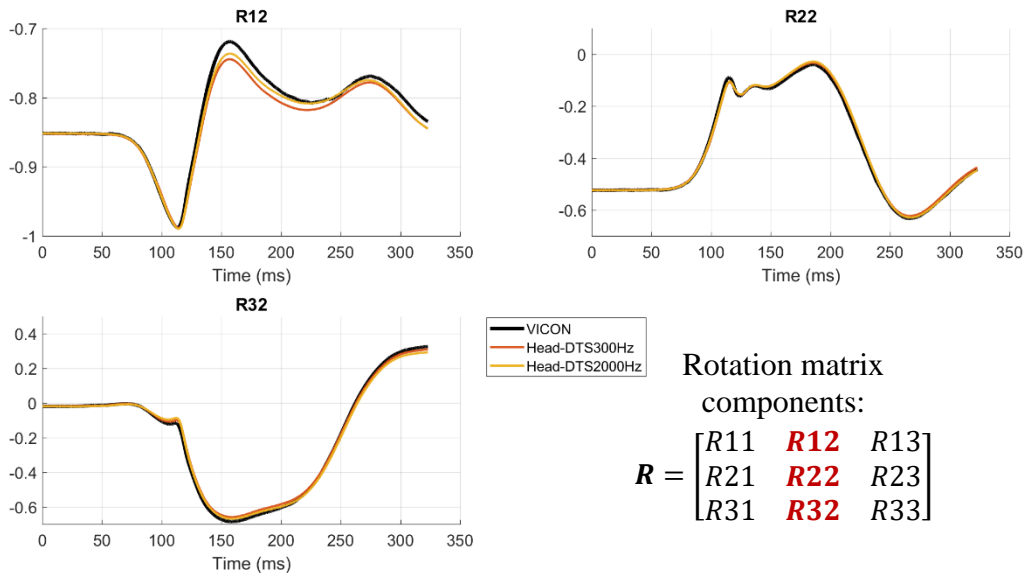
Figure 63. Test S0461 – Head's 2nd unit vector components (2nd column of the R matrix) obtained with four angular rate sensors compared to the VICON data.

64
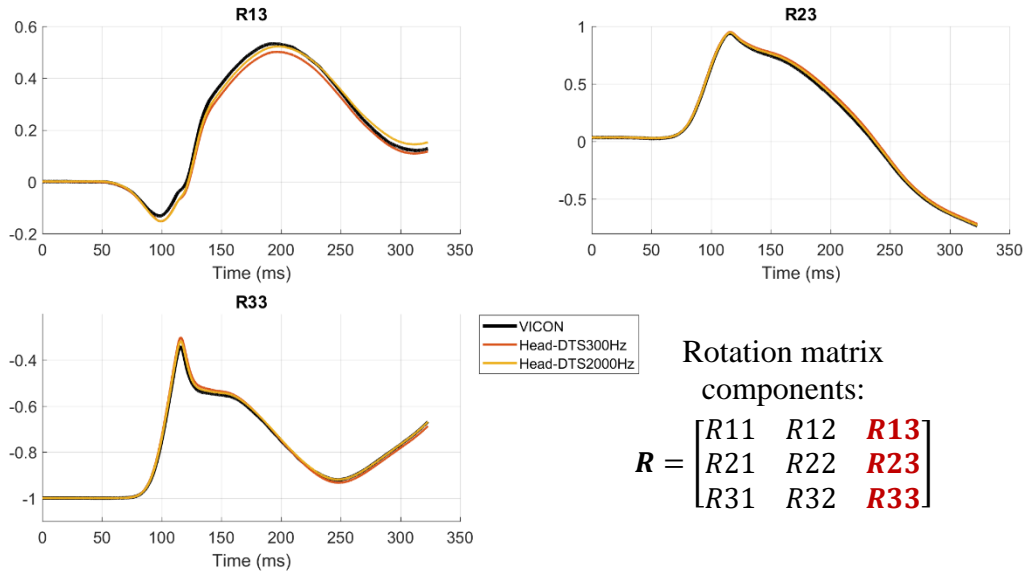
Figure 64. Test S0461 – Head's 3rd unit vector components (3rd column of the R matrix) obtained with four angular rate sensors compared to the VICON data.

7.3.2 Calculated global position

In this section, the time histories of the global position of the measurement center (MC; Figure 2) for one of the sensor packages were compared to the VICON data for that MC. For clarity only three tests were presented here: Test S0455 (Simplified Head; 2kN FL; without impact), Test S0457 (Regular Head; 4kN FL; without impact), and Test S0461 (Regular Head; 4kN FL; simulated impact). In these three tests, the results for the sensor package that gave the smallest Res_{err} were presented. In the figures, the absolute error between the measured and calculated trajectories was indicated with a red line.

The absolute error values recorded in the exemplar tests varied between 9 mm (Y component in Test S0461; Figure 67) to approx. 90 mm (X component in Test S0457; Figure 66). In all three tests (with the exception of the Y component in Test S0457 and Test S0461), the error increased in time and was the highest at the end of the considered time period. The error in the Y component in Test S0457 (Figure 66) and Test S0461 (Figure 67) first increased, then decreased, increased again, and reached its maximum at the end of the test.

In Test 461 (Figure 67), in which a head-to-structure impact was simulated, the sensor package used (ENDEVCO 7264C-DTS ARS PRO 2000Hz) was able to capture the abrupt change in the body trajectory (at approx. t = 116ms), just after the head hit the barrier.

65
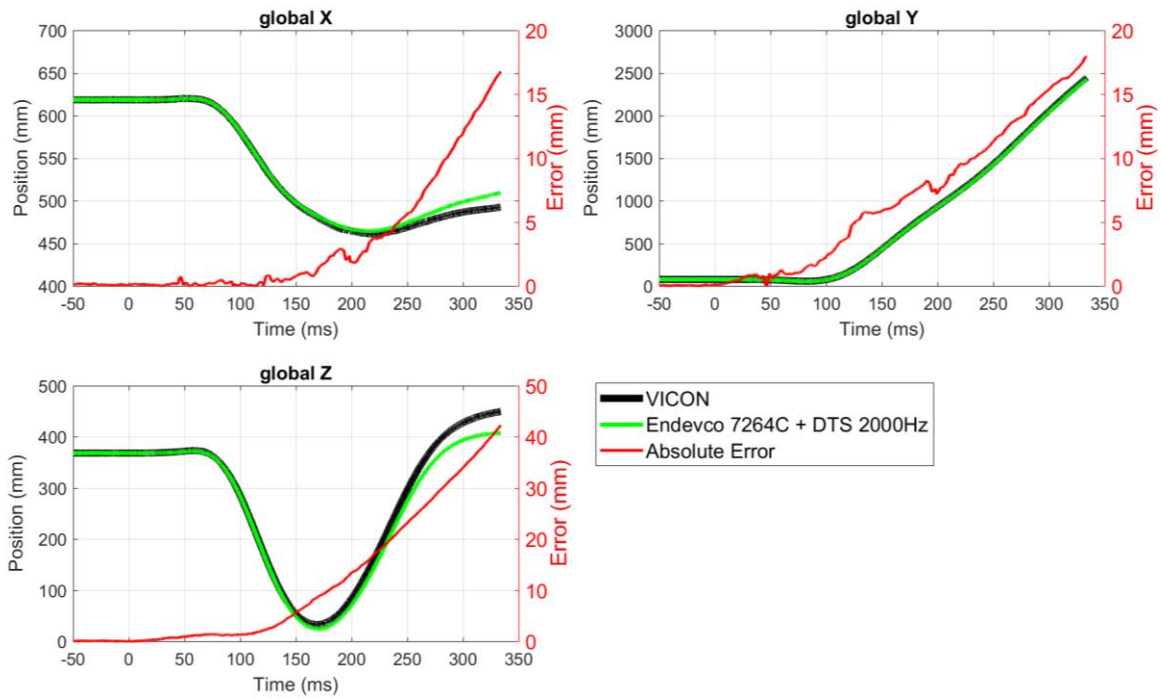
Figure 65. Test S0455 – Head global trajectories comparison: VICON (black) and calculated (green).
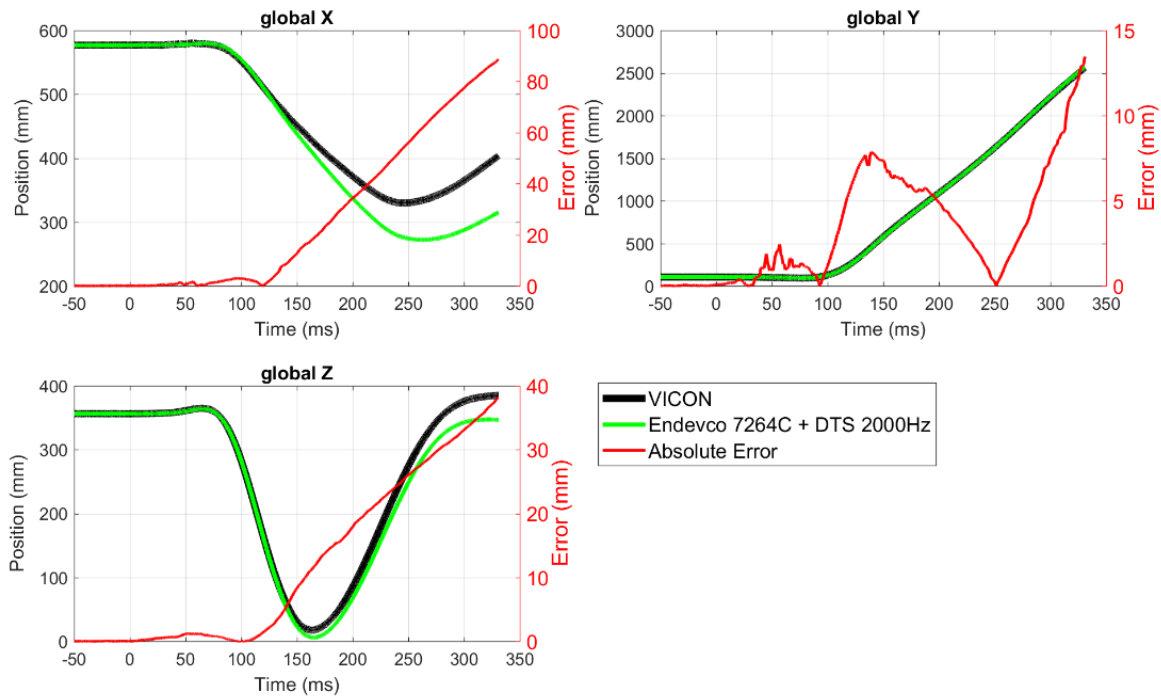
Figure 66. Test S0457 – Head global trajectories comparison: VICON (black) and calculated (green).
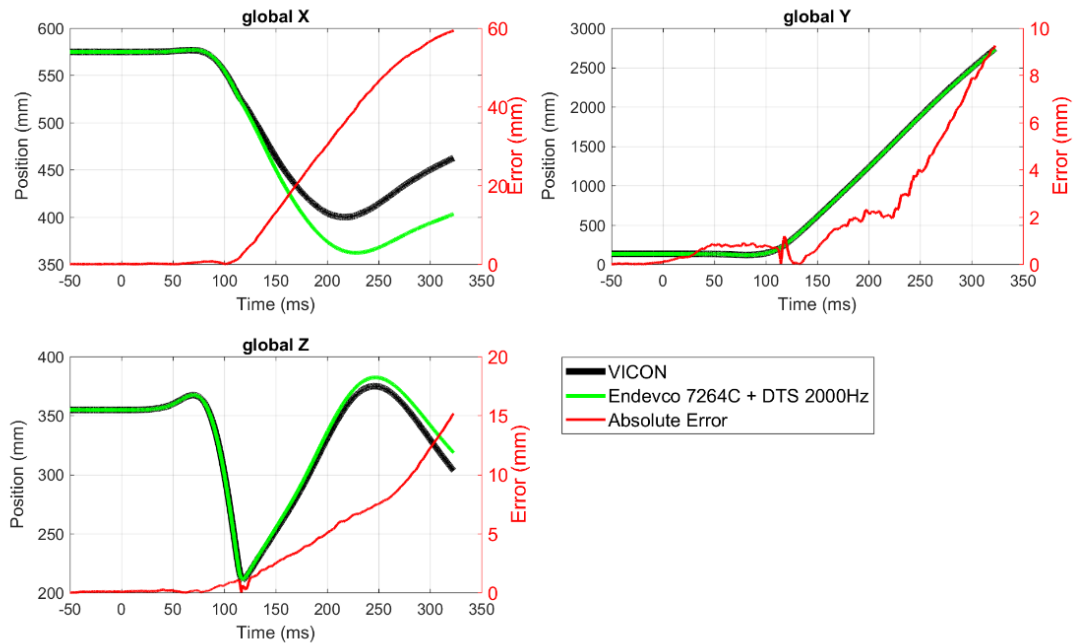
Figure 67. Test S0461 – Head global trajectories comparison: VICON (black) and calculated (green).

It is worth mentioning here that in all presented cases, as well as throughout the whole test series, the deviation between the head's calculated and reference trajectories (as indicated by Res_{err}; see APPENDIX G) was noticeably higher than for the tracked body in the Simplified Head test series.

7.4 Conclusions

The aim of the current study was to evaluate the ability of the algorithm described in Section 1.2.3 to calculate accurate trajectories in a complex scenario (sled test) where a crash test dummy was utilized. The following can be concluded from the results of the study:

- Similarly to the study with the Simplified Head, the angular rate sensors used on the ATD's head were able to predict the general shape and the magnitude of the head's rotation.
- In tests, in which the head-to-structure impact was simulated, the proposed algorithm of updating the head's orientation (based on the data from the angular rate sensors used on the tests), was able to capture the abrupt change in the head's rotational movement caused by the impact (e.g. Figure 62, Figure 63, and Figure 64).
- The absolute error values (between the computed and reference trajectories) recorded in the three exemplar tests varied between 9 mm (Y component in Test S0461; Figure 67) to approx. 90 mm (X component in Test S0457; Figure 66).
- In Test S0456, the Head X accelerometer (Endevco 7264C) recorded only noise due to a broken connector. In Test S0460 and Test S0461, the Head X and Z accelerometers (both, Endevco 7290E) exceeded their maximum full-scale range of 30g. After excluding these three cases from the analysis, the highest Res_{err} of 86.57 mm was recorded in Test S0458 for the Endevco 7290E – DTS ARS Pro 300Hz sensor package. The lowest Res_{err} (of

67

approx. 29.5 mm) was identified for Endevco 7264C – DTS ARS PRO 2000Hz in Test S0459.

- Across the THOR ATD tests, on average the deviation between the head's calculated and reference trajectories was noticeably higher than for the tracked body in the Simplified Head test series (APPENDIX G and APPENDIX C, respectively).

8. UPDATE OF BODY ORIENTATION

8.1 Introduction

Knowing body orientation in a three dimensional (3D) space is crucial in many engineering applications, varying from human body motion analysis (Kitagawa and Ogihara 2016) and vehicle crash testing (Wu et al. 2009) to strapdown inertial navigation systems in airplanes (Demoz 2004, Ma et al. 2012), underwater vehicles (Miller et al. 2010) and mobile robots (Cho et al. 2011).

Over the years, various analytical methods were developed to calculate the orientation of a body from the body's measured angular rate (Jordan 1969, Bortz 1971, DiMasi 1995, Beard and Schlick 2003, Litmanovich et al. 2000, Rudd et al. 2006, Khoder et al. 2008, Kang et al. 2011, Kerrigan et al. 2011, Vepa and Zhahir 2011, Wang et al. 2011, Huculak and Lankarani 2013, Zhenhuan et al. 2013). Much of the previous research in the study of orientation (or attitude) algorithms comes from the field of navigation (cf. Savage 1998). Some related work has been done to study Brownian dynamics with focus on the motion of molecular systems (Beard and Schlick 2003). At the same time, in the field of crash testing the attitude algorithms have been used extensively, too, e.g., to obtain kinematics of pedestrian's limbs during an impact (Rudd et al. 2006), of a car in rollover (Wu et al. 2009, Kerrigan et al. 2011), in head angular acceleration calculations (Kang et al. 2011), to process crash test dummy's head data (DiMasi 1995), or to predict the head trajectory in aircraft seat certification testing (Huculak and Lankarani 2013).

There seems to be a number of various approaches that have been used within the field of crash testing (short events with rapid changes in the body's angular velocity) and navigation (much longer tasks, in which the body's angular rate does not shift in time as abruptly) to determine body orientation. All of the orientation-calculation algorithms, though, are based on the same underlying physics, which suggests that their approaches should be at least similar. Yet, a cursory review suggests there are differences in these algorithms, either analytically in the calculation of the rotation matrix, or numerically in time integration. To date, there have been no studies providing a comprehensive comparison of the various methods of obtaining the body orientation from the body's local angular rate using data from experiments that included separate and highly accurate reference data (e.g. from video tracking or a motion capture system). Such a comparison could provide guidance in identifying a particular approach for a particular application. Thus, the goal of this study was to assess the accuracy of the various algorithms by comparing their predictions to reference kinematics data. For this study, the reference data comes from computer simulations as well as from dynamic crash-like experiments that incorporated 3D optical motion capture. Specifically, this study examines these algorithms to determine if they are actually different, which method produces results that are most similar to the reference data, and whether or not there are advantages or disadvantages to using one or the other for applications in crash testing analysis.

8.2 Methods

To achieve the goal of this study, first, the *Orientation time-history* section describes the theoretical background of obtaining the body orientation from the body's local angular rate. Then, the *Seven Algorithms* sections present the list of identified attitude-calculation algorithms with

differences and similarities, both analytically and numerically, between them. Following, the methods to generate data from four test cases (one computational and three experimental) are described and error metrics used to evaluate selected orientation algorithms are defined. Next, because it was hypothesized that the error in the calculated orientation would be a function of the sampling time step, as well as the magnitude and frequency content of the angular velocity signal, a simplified two-dimensional (2D) analytical analysis was performed to investigate those sensitivities.

8.2.1 Orientation time-history

Initial orientation of a rigid body in the global reference frame, R_{ini}, and the body's angular velocity $\omega(t)$ in the local coordinate system can be measured or determined using current measurement technologies. Using both, $\omega(t)$ and R_{ini} the time-history of the local-to-global rotation matrix R, which, in time, relates the orientation of the body's local coordinate system to the global frame, can be obtained.

R is a square matrix composed of an orthogonal set of three unit vectors, each vector describing the orientation of an axis of the local frame in the global coordinate system. R relates any vector's representation in the local coordinates, r_l, to its representation in the global frame, r_g, through Eq. 8.1:

$$r_g = R \, r_l \tag{8.1}$$

By differentiating Eq. 8.1 and then algebraic manipulation, one can show (cf. DiMasi 1995, cf. Hamano 2013) that R is related to the angular velocity skew-symmetric matrix $[\omega \times]$ by Eq. 8.2:

$$[\omega \times] \equiv \begin{bmatrix} 0 & -\omega_z & \omega_y \\ \omega_z & 0 & -\omega_x \\ -\omega_y & \omega_x & 0 \end{bmatrix} = R^{-1}\dot{R} \tag{8.2}$$

$$\text{and thus: } \dot{R} = R[\omega \times] \tag{8.3}$$

where $\dot{R}$ is the rate of change of the matrix R, and ω_x, ω_y, and ω_z are the local coordinate system components of the ω vector.

8.2.2 Seven algorithms – list

In an effort to determine the time-history of the matrix R seven different methods were identified in the literature:

1. *Bortz method*: based on the Rodrigues' rotation formula (cf. Shabana 2010) and integration of: a) the local angular velocity vector $\omega(t)$, and b) inertially non-measurable non-commutativity rate vector $\dot{\sigma}(t)$ (Bortz 1971);

2. *Beard method*: based on integration of the time derivatives of the local coordinate system unit vectors (Beard and Schlick 2003);

3. *DiMasi method*: based on a simple numerical integration of Eq. 8.3 assuming small incremental (finite) angular rotations between each time step (Beard and Schlick 2003);

4. *Rate of Euler Parameters (ER) method*: based on relating local angular velocities *ω(t)* to the rate of change of the Euler parameters *e*; numerical integration of that rate of change to obtain *e*; and defining the rotation matrix *R* in terms of *e* (Huculak 2011, Vepa and Zhahir 2011, Huculak and Lankarani 2013);

5. *2-1-3 method*: based on the 2-1-3 Euler angles utilized to build *R* and numerical integration of the rate of change of the Euler angles (Kang et al. 2011, Kitagawa and Ogihara 2016);

6. *Unit Quaternion (UQ) method*: based on the use of the instantaneous axis of rotation and the rotation angle, both derived from the angular velocity vector *ω(t)*, to obtain the Euler parameters *e* and, next, utilizing *e* to define the rotation matrix *R* (Rudd et al. 2006);

7. *SP method*: based on the Euler exponential solution of Eq. 8.3 and an integration factor (Kerrigan et al. 2011).

8.2.3 Seven algorithms – differences and similarities

8.2.3.1 Rotation matrix

To construct the matrix *R*, the *Bortz method* uses the Rodrigues' rotation formula (Eq. 8.4) combined with the rotation angle θ obtained by solving Eq. 8.5.

$$\boldsymbol{R} = \boldsymbol{I} + sin\theta[\boldsymbol{\omega} \times] + (1 - cos\theta)[\boldsymbol{\omega} \times] \tag{8.4}$$

$$\dot{\boldsymbol{\theta}}(\boldsymbol{t}) = \boldsymbol{\omega}(\boldsymbol{t}) + \dot{\boldsymbol{\sigma}}(\boldsymbol{t}) \tag{8.5}$$

where *I* is the identity matrix, $[\boldsymbol{\omega} \times]$ is the angular velocity skew-symmetric matrix from Eq. 8.2, $\dot{\theta}$ is the rate of change of the rotation angle θ, *ω(t)* is the body local angular velocity vector, and $\dot{\boldsymbol{\sigma}}(\mathbf{t})$ is the non-commutativity rate vector.

Eq. 8.5 states that to determine the angle of rotation θ the inertially measurable angular motion *ω(t)* needs to be integrated along with the inertially non-measurable non-commutativity rate vector $\dot{\boldsymbol{\sigma}}(\boldsymbol{t})$ (cf. Bortz 1971). That non-commutativity rate vector accounts for the non-communitive nature of rotations.

Three discussed methods (*Beard*, *ER*, *UQ*) utilize the Euler parameters (either in their contracted or expanded form) to build *R*. The only difference between those three methods is the way how the Euler parameters are determined from the measured local angular velocity *ω(t)*. Two of the methods (*Beard* and *UQ*) integrate *ω(t)* directly and the obtained finite rotations are utilized to calculate the Euler parameters *e*. The *ER method* solves ordinary differential equations (ODE) to find *e*.

The *2-1-3 method* builds the matrix *R* based on three consecutive rotations defined by the Euler angles in the following order: pitch, roll, and yaw.

The *DiMasi method* updates *R* by finding a numerical solution to ODE described with Eq. 8.3, assuming sufficiently small incremental angular rotations between each time step.

The *SP method* assumes that Eq. 8.3 can be rewritten as Eq. 8.6:

$$\dot{\boldsymbol{x}} - \boldsymbol{P}\boldsymbol{x} = \boldsymbol{0} \tag{8.6}$$

Then, the discretized Euler exponential solution of Eq. 8.6 is Eq. 8.7:

$$\boldsymbol{x} = e^{\Delta t \boldsymbol{P}}\boldsymbol{x_0} \tag{8.7}$$

where Δt is the input data time step, x corresponds to R at time t, x_0 corresponds to R at time $t - \Delta t$, and P, as defined by Eq. 8.8, is the function of <u>global</u> angular velocity $\omega_G = [\omega_{x,G}, \omega_{y,G}, \omega_{z,G}]$:

$$P = \begin{bmatrix} 0I & -\omega_{z,G}I & \omega_{y,G}I \\ \omega_{z,G}I & 0I & -\omega_{x,G}I \\ -\omega_{y,G}I & \omega_{x,G}I & 0I \end{bmatrix} \qquad (8.8)$$

Before utilizing body's local angular velocity to build the matrix P, the *SP method* requires to transform ω from step $t - \Delta t$ to the global coordinate frame using $R_{t-\Delta t}$.

8.2.3.2 Numerical integration

In the seven methods, two types of numerical integration are used. One calculates the value of a definite integral (e.g. a finite rotation from measured angular velocity). The other finds a numerical solution of ODE.

In two methods (*Beard* and *SP*) the rectangular (also called mid-point) integration scheme, the most basic numerical scheme for integration, is used to obtain finite rotations from $\omega(t)$. To accomplish the same task, the *UQ method* uses the trapezoidal rule. The trapezoidal rule is also used in the *2-1-3 method* – to integrate the rate of change of the Euler angles to obtain pitch, roll, and yaw.

The *Bortz method*, the *DiMasi method*, and the *ER method* at some step in the algorithm require solving ODE to either find the rotation angle (*Bortz*), the Euler parameters (*ER*), or to update the matrix R directly (*DiMasi*). DiMasi 1995 based the integration on the forward Euler method, while Huculak 2011 applied the fourth-order Runge-Kutta (RK4) numerical approach in the *ER algorithm*. For the purpose of this paper, RK4 was utilized in the *ER algorithm*, and the forward Euler method was used to integrate ODE in the *Bortz method*.

8.2.4 Test cases

All seven methods were compared to each other using the same input data: time-history of the vector $\omega(t)$ and the initial orientation of the body, R_{ini}. Four different data sets ("cases") were sourced for these comparisons.

Case 1: A multi-body model (Figure 68) was simulated in a commercial Finite Element (FE) package (LS-Dyna 8.1.0, LSTC, Livermore, CA).
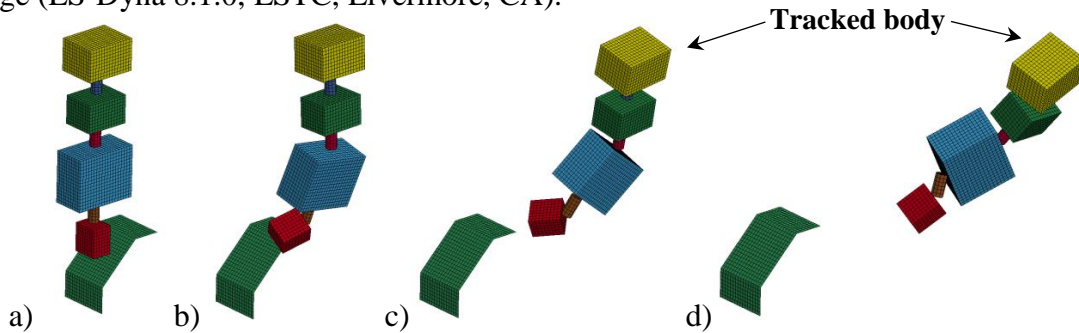
Figure 68. Multi-body model used in the analysis: a) starting position (t = 0), b) model at t = 40 msec, c) model at t = 80 msec, d) model at t = 120 msec.

The model consisted of rigid bodies connected with kinematic joints. It was given an initial velocity. The scenario was designed in a way that at some point during the simulation one of the bodies collided with an undeformable barrier (rigidly fixed at 45° w.r.t. the model travel direction). That contact disturbed the initial orientation of all connected bodies, causing relative translations and rotations of the parts (Figure 68). For one of the bodies ("yellow" in Figure 68), its initial orientation and the time-history of the local angular velocity data were recorded.

Case 2: A box-like structure (called for simplicity "Simplified Head"; SH; Figure 103) was connected with the neck of the Test device for Human Occupant Restraint (THOR) Anthropomorphic Test Device (ATD) (NHTSA 2018) and then attached to a sled system (Seattle Safety, Auburn, WA). In the sled test, the assembly was positioned at 45° relative to the sled travel direction. The acceleration pulse used as the sled input was a scaled down and filtered T1 local X-acceleration of the driver ATD recorded during one of the frontal oblique offset crash tests performed for the National Highway Traffic Safety Administration (NHTSA 2013).
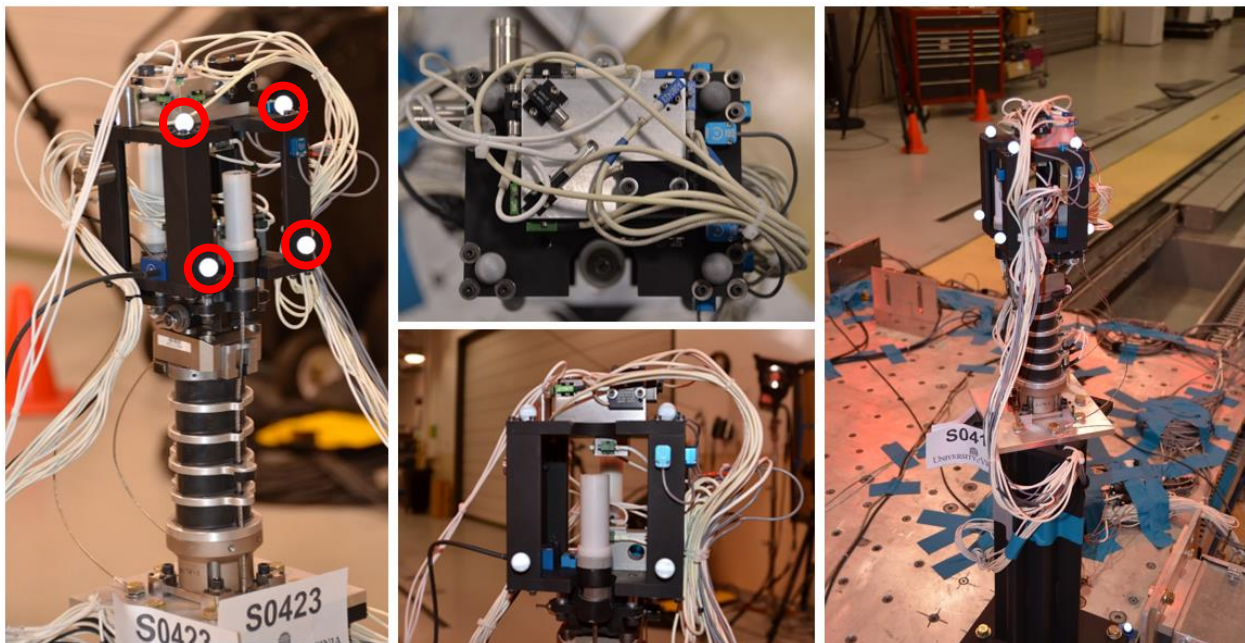
Figure 69. Simplified Head structure (left figure: retroreflective markers marked in red).

On the test, three angular rate sensors (ARS) (DTS ARS Pro, Diversified Technical Systems, Seal Beach, CA, USA) were attached to SH and the angular velocity around the three local axes of the body was recorded. The local coordinate system of the head was defined as outlined in the SAE J211 document (Society of Automotive Engineers (SAE) 1995). Prior to testing the initial orientation of the assembly – in the global frame – was determined with the use of a Coordinate Measuring Machine (CMM) (Hexagon Manufacturing Intelligence, North Kingstown, RI). Recorded angular velocity data were filtered with a 4-order Butterworth low pass Channel Frequency Class (CFC) 180 filter.

In the following test series, two sled tests were performed with the THOR Mod-kit ATD: without (**Case 3**) and including head impact (**Case 4**). THOR was seated in the Gold Standard (GS)

buck positioned at 30° relative to the sled travel direction (cf. Montesinos-Acosta et al. 2016). The acceleration time history utilized for the sled system was the 9g trapezoidal pulse used previously in Montesinos-Acosta et al. 2016.

Case 4 involved a head impact to assess the influence of impact kinematics on the calculated 3D orientation time-history. The impact was produced by mounting a foam-padded steel bar in the path of the head travel (Figure 104).
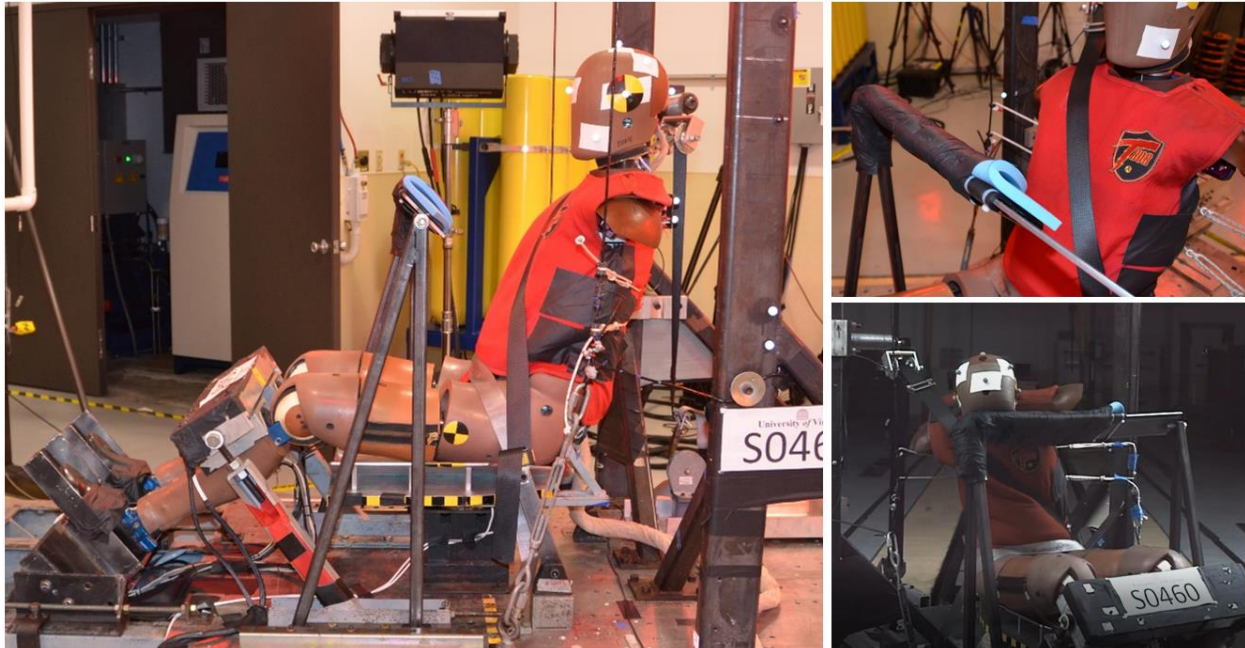
Figure 70. Seated THOR ATD (left) and the foam-padded steel structure (top right) to simulate head impact (bottom right).

In the ATD tests, the dummy head was instrumented with three angular rate sensors (DTS ARS Pro, Diversified Technical Systems, Seal Beach, CA, USA) and the angular velocity around the three axes of the head local coordinate system (defined according to SAE J211, SAE 1995) was recorded. Prior to testing the initial orientation of the ATD head – in the global frame – was determined with a CMM. Upon the test completion, recorded angular velocity data were filtered with CFC 180 filter.

8.2.5 Reference orientation data

In Case 1, for four points on the tracked body ("yellow" body in Figure 68) global displacements were obtained and utilized to determine the time-history of the local-to-global rotation matrix R as calculated by the FE software.

In the three sled tests the head kinematics were captured with an optoelectronic stereophotogrammetric system (OSS) (Vicon MX, Los Angeles, CA) at 500 Hz (Case 2) or at 1 kHz (Case 3 and 4). The motion capture system tracked the trajectories of spherical retroreflective markers (exemplar markers marked in Figure 103 left) through a calibrated 3D space within the cameras' collective field of view. Using the data from OSS and the Least-Squares Pose Estimator approach (Cappozzo et al. 1997) the time-history of the head orientation (head's

local-to-global rotation matrix R), in the global coordinate frame, was determined. The data from OSS were treated as the ground truth due to the established high measurement accuracy of the system (Lessley et al. 2011).

8.2.6 Input data to the algorithms

All seven methods were compared to each other using the same input: the recorded time-history of the vector $\omega(t)$ and the initial orientation of the body, R_{ini}. In all four cases, $\omega(t)$ and R_{ini} were used as the input to the seven methods. The obtained orientation time history was then compared to the R calculated based on the reference (computer simulation or from OSS) data.

8.2.7 Sampling frequency

To better understand how the input data sampling rate influences the accuracy of the calculation of the rotation matrix R, the angular velocity vector, obtained through the computer simulation (Case 1) or recorded during testing (Cases 2-4), was utilized in its original "20 kHz" form (time step Δt = 5e-5 s) and then down-sampled to: 10 kHz (Δt = 1e-4 s), 5 kHz (Δt = 2e-4 s), 2.5 kHz (Δt = 4e-4 s), 1.428 kHz (Δt = 7e-4 s) and 1 kHz (Δt = 0.001 s), respectively. In Cases 1-4, where needed, the reference orientation data available were resampled for direct comparison.

8.2.8 Test data – error metrics

To evaluate the seven methods used to update R two error metrics ($RMS_{avg,R}$ and RMS for θ_{INS}) were utilized. To determine those metrics, the following analysis was performed:

1. the Root Mean Square Error (RMS_i) was calculated separately for each of the components of the matrix R, utilizing the reference time-history of R (obtained from the simulation or from OSS);

2. the average value $RMS_{avg,R}$ was found based on RMS_i calculated for all nine components of R (Eq. 8.9):

$$RMS_{avg,R} = \frac{\sum_{i=1}^{9} RMS_i}{9} \qquad (8.9)$$

3. based on the rotation matrix R and the mathematical definition of the quaternion $q = q_r + q_i \mathbf{i} + q_j \mathbf{j} + q_k \mathbf{k}$ (where $\mathbf{i}$, $\mathbf{j}$, $\mathbf{k}$ are unit vectors representing the three Cartesian axes), the time history of $\theta_{INS}(t)$, the angle of rotation around the instantaneous axis of rotation, was determined (Eq. 8.10):

$$\theta_{INS}(t) = 2\left[atan2\left(\sqrt{q_i^2 + q_j^2 + q_k^2}, q_r\right)\right] \qquad (8.10)$$

4. as the last step, the Root Mean Square Error (RMS for θ_{INS}) between $\theta_{INS}(t)$ calculated from the reference R and R obtained with the seven methods was calculated.

Those two error metrics were then used to compare the accuracy of the discussed seven methods of updating R. The analysis was performed for the four test cases and all sampling steps Δt described in the *8.2.7 Sampling frequency* section. After the metrics were calculated, the following error distributions were plotted: $RMS_{avg,R}$ vs. Δt and RMS for θ_{INS} vs. Δt. Next, a simple linear regression model was fitted to each of them and the coefficient of determination, R^2, was

computed. R^2 was then utilized to evaluate if the plotted distributions exhibited a linear or non-linear behavior.

8.2.9 Error analysis – analytical approach

To test our hypothesis and evaluate the sensitivity of the computed orientation to the time step Δt, the magnitude of the measured angular velocity $\boldsymbol{\omega(t)}$, and the frequency content of the data, an analytical approach that investigated errors in a simplified 2D case was performed.

Body rotation around an axis in a 2D space can be described with a 2-by-2 rotation matrix $\boldsymbol{R_{2D}}$ (Eq. 8.11):

$$R_{2D} = \begin{bmatrix} R_{2D,11} & R_{2D,12} \\ R_{2D,21} & R_{2D,22} \end{bmatrix} = \begin{bmatrix} cos\theta & -sin\theta \\ sin\theta & cos\theta \end{bmatrix} \tag{8.11}$$

where θ is the angle of rotation.

For the purpose of this analysis, the following was assumed as body's angular velocity $\omega_{an}(t)$ (Eq. 8.12):

$$\omega_{an}(t) = A\big(sin(2\pi ft) + cos(2\pi ft)\big) \tag{8.12[1]}$$

where t – time (s); f – frequency (Hz), A – constant.

If the body rotates only around one axis, the time history of the angle of rotation $\theta_{an}(t)$ can be found by integrating the body's angular velocity (Eq. 8.13):

$$\theta_{an}(t) = \int_0^t \omega_{an}(\tau)d\tau \tag{8.13}$$

By substituting Eq. 8.12 into Eq. 8.13, the analytical form of the angle of rotation (for the assumed form of the angular velocity) can be found from Eq. 8.14:

$$\int_0^t \omega_{an}(\tau)d\tau = \int_0^t \big(A\big(sin(2\pi f\tau) + cos(2\pi f\tau)\big)\big)d\tau = \frac{A}{2\pi f}\big(1 - cos(2\pi ft) +$$

$$sin(2\pi ft)\big) \tag{8.14}$$

The angle of rotation can also be found by numerical integration of Eq. 8.12. Assuming a constant integration interval – time step Δt – and using the trapezoidal integration rule the angle of rotation θ_{NUM} at discrete time $t = \tau$ can be obtained from Eq. 8.15:

$$\theta_{NUM,\tau} = \theta_{\tau-1} + \frac{\omega_{\tau-1}+\omega_\tau}{2} * \Delta t \tag{8.15}$$

where the subscript $\tau - 1$ indicates the previous step and the subscript τ indicates the current integration step.

---

[1] For simplicity of the derivation, the assumed <u>analytical</u> form of the angular velocity $\omega_{an}(t)$ was modeled as the sum of two periodic functions. Eq. 8.12 can be then treated as a special case of the Fourier series. It is hypothesized that through this relatively simple 2D example, general trends caused by changes in the time step, the magnitude of the angular rate, and the frequency content of the data, can be identified and investigated. It is assumed that those identified trends hold true also for a more complex 3D motion.

Having both, the angle of rotation obtained analytically (θ_{an}) and numerically (θ_{NUM}) the absolute error $E[R]$ in the rotation matrix (evaluated at the same discrete points as used for integration of Eq. 8.12) can be determined based on Eq. 8.16:

$$E[R_{2D}] = \begin{bmatrix} |cos(\theta_{an,\tau}) - cos(\theta_{NUM,\tau})| & |sin(\theta_{NUM,\tau}) - sin(\theta_{an,\tau})| \\ |sin(\theta_{an,\tau}) - sin(\theta_{NUM,\tau})| & |cos(\theta_{an,\tau}) - cos(\theta_{NUM,\tau})| \end{bmatrix} \tag{8.16}$$

It is worth pointing out here that since the absolute values are considered in Eq. 8.16, $E[R_{2D,12}] = E[R_{2D,21}]$.

The absolute error in the rotation matrix components, at discrete data points, is Eq. 8.17:

$$E[R_{2D,11}] = E[R_{2D,22}] = |cos(\theta_{an,\tau}) - cos(\theta_{NUM,\tau})| = \left|cos\left(\frac{A}{2\pi f}(1 - cos(2\pi f\tau) + \right.\right.$$

$$\left.\left. sin(2\pi f\tau))\right) - cos\left(\theta_{\tau-1} + \frac{\omega_{\tau-1} + \omega_\tau}{2} * \Delta t\right)\right| \tag{8.17a}$$

$$E[R_{2D,12}] = E[R_{2D,21}] = |sin(\theta_{NUM,\tau}) - sin(\theta_{an,\tau})| = \left|sin\left(\theta_{\tau-1} + \frac{\omega_{\tau-1} + \omega_\tau}{2} * \Delta t\right) - \right.$$

$$\left. sin\left(\frac{A}{2\pi f}(1 - cos(2\pi f\tau) + sin(2\pi f\tau))\right)\right| \tag{8.17b}$$

Using Eq. 8.17 a sensitivity study was performed varying:
- the time step Δt,
- the parameter A, which affected the magnitude of the angular velocity, and
- the frequency f of the angular velocity from Eq. 8.12.

For the analysis, it was assumed that the whole event lasted 0.25 s. The parameters were modified one at a time. The time step Δt varied from 5e-5 s to 0.002 s, the parameter A from 1 to 30 (where 30 represented the level of maximum angular velocity seen in Cases 2-4), and the frequency f from 10 Hz to 500 Hz (frequencies seen in the angular velocity signals from Cases 2-4).

To quantify the effect of the three variables on the calculated orientation, the procedure detailed in Step 1 and Step 2 in the *8.2.8 Test data – error metrics* section was carried out.

In the results section for the analytical analysis, the error in the rotation matrix R was presented in the function of parameter A, time step Δt, frequency f, normalized frequency $\Delta t * f$, and lastly, in the function of adjusted normalized frequency $x * \Delta t * f$, with x described by:

$$x = 1.028 * \left(\frac{f}{f_{ref}}\right)^{-0.43} \tag{8.18}$$

where f_{ref} is a frequency for which the error in R is known and used as a reference to compare to.
Remark: The methodology of finding Eq. 8.18 was described more in detail in APPENDIX I.

8.3 Results

8.3.1 Test cases

$RMS_{avg,R}$ (Figure 71) and RMS for θ_{INS} (Figure 72) indicated the *UQ* and *ER algorithms* as the most accurate (from the seven considered in the paper) in all four test cases. In addition, the two

algorithms gave almost identical results at each of the data sampling frequencies for both error metrics used. According to $RMS_{avg,R}$ (Figure 71) the method that was the least accurate was either the *2-1-3 method* (in Case 2 and Case 3 across all considered time steps and in Case 4 for Δt = 5e-5 s, Δt = 1e-4 s, and Δt = 2e-4 s), or the *DiMasi method* (in Case 1 for all considered Δt and in Case 4 for Δt equal or higher than 4e-4 s). According to *RMS for θ_{INS}* (Figure 72) the least accurate method of updating **R**, across all considered Δt, was also either the *2-1-3* method (Case 2, 3 and 4) or the *DiMasi* algorithm (Case 1). When the time step Δt of the ARS data (used as the input) increased, the difference between the calculated and reference rotation matrix grew as well according to $RMS_{avg,R}$ (Figure 71) for five out of the seven tested algorithms (*Bortz*, *Beard*, *DiMasi*, *SP*, and *2-1-3*). Similarly, the error in the angle of rotation θ_{INS} increased with higher values of Δt for the same five methods (Figure 72). The *ER* and *UQ algorithms* appeared to be noticeably less susceptible to the increase in Δt.
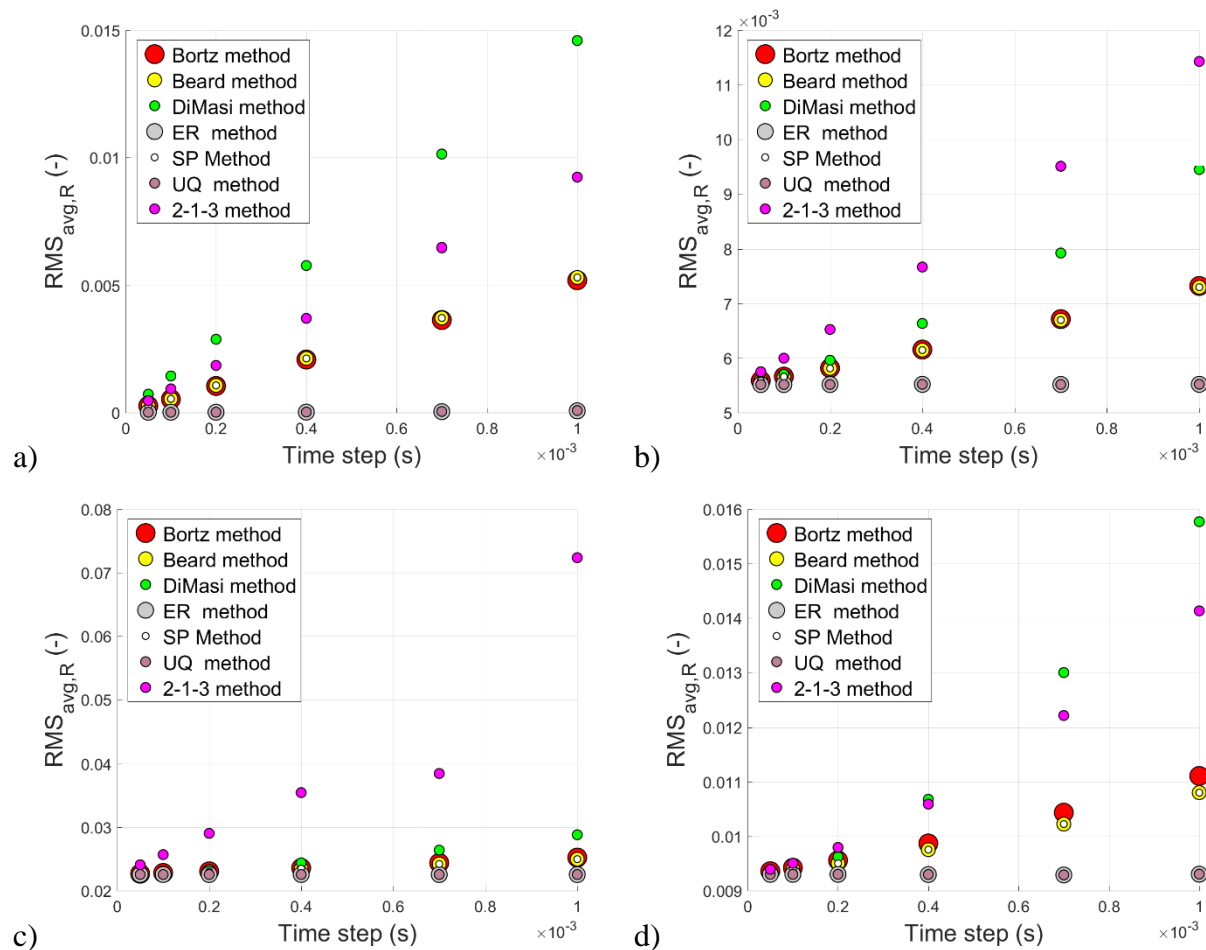
Figure 71. $RMS_{avg,R}$ error vs. the ARS data time step Δt for the seven investigated methods of updating the rotation matrix R: a) FE model (Case 1), b) Simplified Head test (Case 2), c) THOR ATD sled test (Case 3), d) THOR ATD sled test with head impact (Case 4).
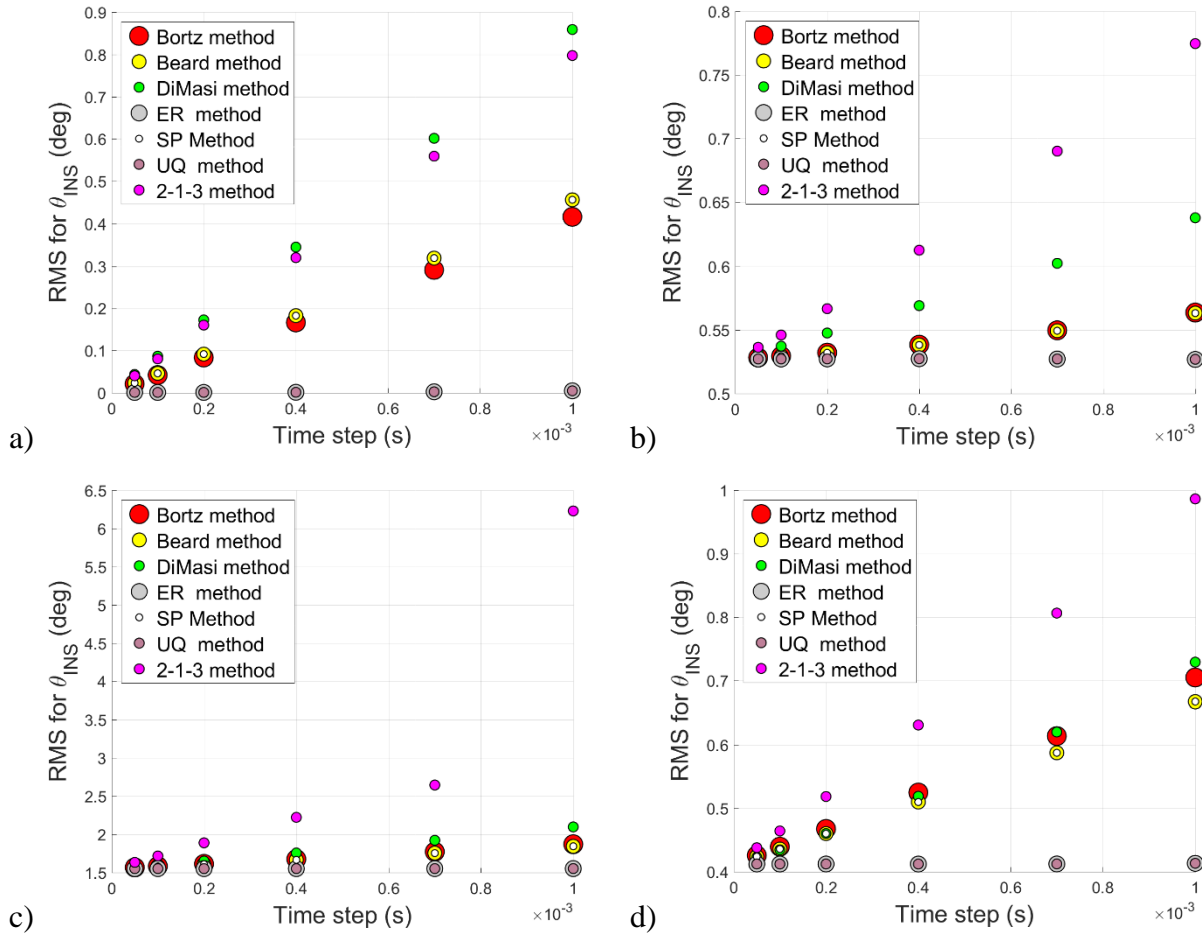
Figure 72. RMS error for $\theta_{INS}(t)$ vs. the ARS data time step Δt for the seven investigated methods of updating the rotation matrix R: a) FE model (Case 1), b) Simplified Head test (Case 2), c) THOR ATD sled test (Case 3), d) THOR ATD sled test with head impact (Case 4).

As expected, for Δt = 5e-5 s the discrepancy between the reference and the calculated rotation matrix was the smallest and for Δt = 0.001 s the highest across all considered values of Δt for all seven methods of updating **R**.

When a simple linear regression model was fitted to the error distributions from Figure 71 and Figure 72, the calculated coefficient of determination, R^2, indicated that the two error metrics (Eq. 8.9 and Eq. 8.10) increased (in the function of Δt) almost linearly with respect to the size of Δt for four methods of updating **R** (*Bortz*, *Beard*, *DiMasi*, *SP*) (Table 5 and Table 6). For the *2-1-3 method* the error character exhibited linear behavior in Case 1, Case 2, and Case 4 (R^2 of approx. 0.99 for $RMS_{avg,R}$ and RMS for θ_{INS}) with R^2 deviating noticeably from 1 (when 1 means linear) in Case 3 (R^2 of approx. 0.86 for $RMS_{avg,R}$ and of approx. 0.79 for RMS for θ_{INS}). In the *UQ* and *ER algorithms* the coefficient of determination varied from 0.96 (Case 3 for *ER*) to 0.007 (Case 4 for *UQ*) according to $RMS_{avg,R}$ and from 0.89 (Case 1 for both, *UQ* and *ER*) to 0.15 (Case 3 for *ER*) according to *RMS for θ_{INS}*. That indicated non-linear behavior of both error metrics in the two discussed methods of computing **R**.

Table 5. Coefficient of determination for RMS$_{avg,R}$.

	Bortz	**Beard**	**DiMasi**	**ER**	**SP**	**UQ**	**2-1-3**
Case 1	1	1	1	0.906	1	0.913	1
Case 2	0.998	0.998	0.989	0.606	0.998	0.773	0.999
Case 3	0.999	0.999	0.989	0.96	0.999	0.639	0.857
Case 4	0.992	0.990	0.973	0.033	0.990	0.007	0.985

Table 6. Coefficient of determination for RMS for θ_{INS}.

	Bortz	**Beard**	**DiMasi**	**ER**	**SP**	**UQ**	**2-1-3**
Case 1	1	1	1	0.893	1	0.894	1
Case 2	0.991	0.991	0.999	0.499	0.991	0.376	0.997
Case 3	0.999	0.999	0.999	0.153	0.999	0.817	0.792
Case 4	0.999	0.999	0.997	0.644	0.999	0.665	0.999

8.3.2 Error analysis – analytical approach

When the time step Δt increased, the difference between the rotation matrices obtained analytically and numerically increased in a non-linear manner (Figure 73 and Figure 74). The non-linear relationships was observed regardless of the value of f (Figure 73a and Figure 74a) or the parameter A (Figure 73b and Figure 74b) used. It is in contrary to most of the test case results, where the character of that change was either linear or close to linear (Table 5).

a)   b)
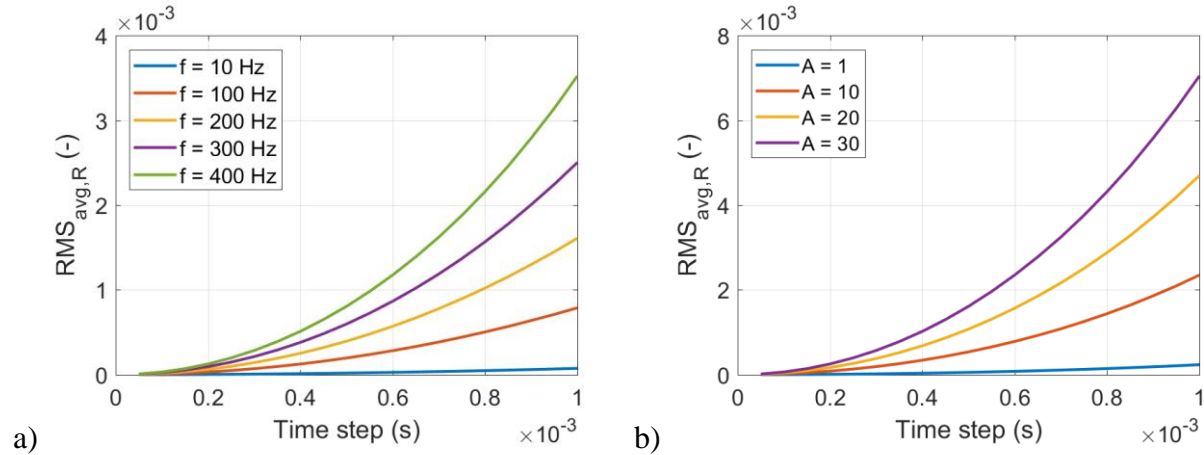
Figure 73. RMS$_{avg,R}$ error vs. time step Δt up to 0.001 s for variations in: frequency f (with constant A = 15), b) parameter A (with constant f = 400 Hz).

Due to the time step Δt being equal to the period of the investigated function, the error in the computed rotation matrix grew substantially for $\Delta t = 0.002$ s and the input angular velocity with $f = 500$ Hz (period: $1/f = 0.002$ s) (Figure 74). Part of the information contained in the input signal was lost as the effect of the integration error, what then resulted in a steep increase in the $RMS_{avg,R}$ metric.

a)

b)
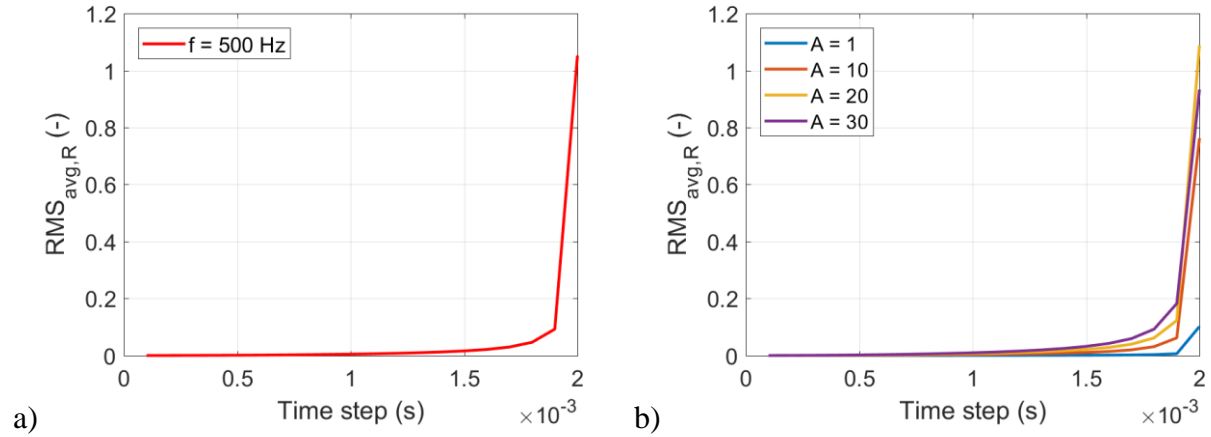
Figure 74. RMS$_{avg,R}$ error vs. time step Δt up to 0.002 s for variations in: frequency f (with constant A = 15), b) parameter A (with constant f = 500 Hz).

From the results of the analytical analysis it can also be seen that for the same time step Δt, the error in the numerically obtained rotation matrix grew with the increase in the frequency f (Figure 75a) or the magnitude (parameter A; Figure 75b) of the input angular velocity. In the range of Δt up to 0.001 s the error change maintained linear character in all presented cases. It can be shown, though, that the character of the error distributions becomes non-linear when the value of Δt approaches the period of the integrated function $\omega_{an}(t)$.

a)

b)
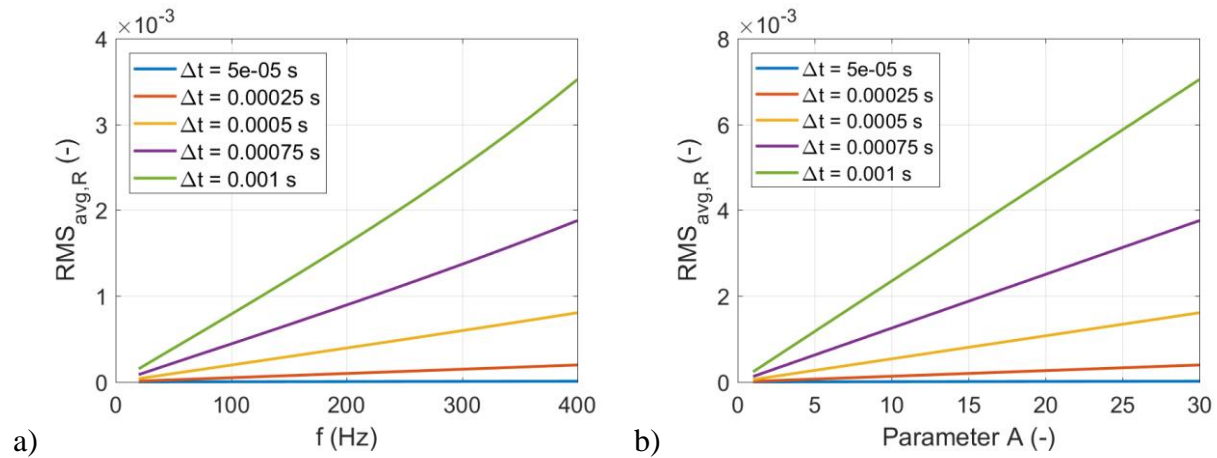
Figure 75. RMS$_{avg,R}$ error vs.: a) frequency f (with A = 15 and varied Δt), b) parameter A (related to magnitude of the assumed form of the angular velocity; with f = 400 Hz and varied Δt).

Similarly to the error in the function of the sampling step Δt (Figure 73a) or in the function of the frequency f (Figure 75a), with the increase in the normalized frequency ($\Delta t * f$), the error in the rotation matrix $\boldsymbol{R}$ grew (Figure 76a). The character of that error increase was non-linear in its nature for all four investigated frequencies f.

a) b)
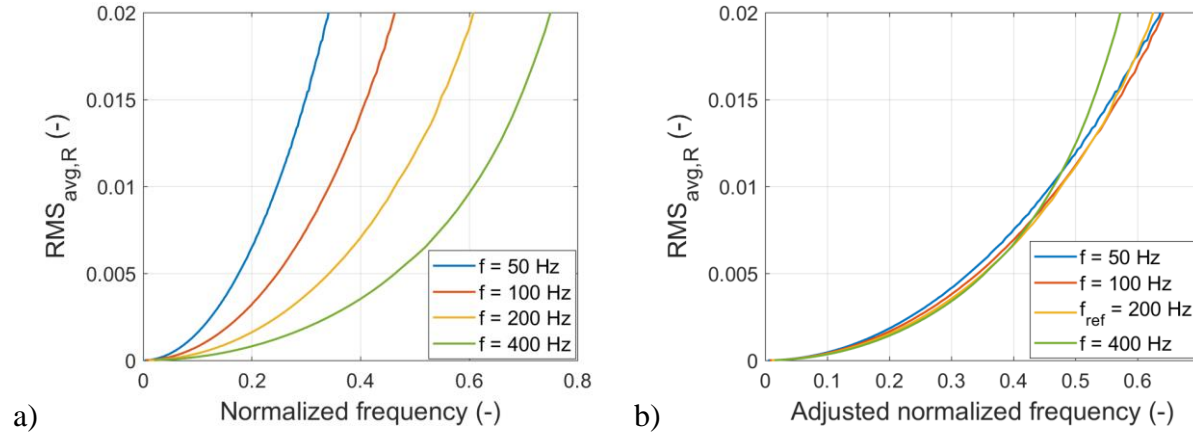
*Figure 76. RMS$_{avg,R}$ error (with A = 15) vs.: a) normalized frequency (Δt * f),*
*b) adjusted normalized frequency (x * Δt * f, where x is described by Eq. 8.18).*

After using Eq. 8.18 with f_{ref} of 200 Hz (treated here as an example), the "50 Hz", "100 Hz", and "400 Hz" curves matched the reference "200 Hz" response closely, with the exception of the "400 Hz" curve above the adjusted normalized frequency of approx. 0.45 (Figure 76b). Beyond the adjusted normalized frequency of 0.45, the time step Δt in the "400 Hz" case started approaching the value of the investigated function's period. As it was shown in Figure 74, the closer the sampling step is to the period of the analyzed function, the increase in the error in **R** more rapid and non-linear.

Remark: It needs to be pointed out here that the range of the adjusted normalized frequency from Figure 76b would have been different if a different value of f_{ref} had been used in the normalization procedure.

8.4 Discussion

Bortz 1971 showed that, as a general case, integration of the angular velocity vector **ω(t)** does not result in angular displacement. To account for the non-commutative nature of finite rotations a correction step in an attitude algorithm is necessary (Savage 1998, cf. Savage 2010). That correction is commonly called *coning correction* and it describes the coning motion of a body, an effect caused by two or more orthogonal rotations.

In five out of the seven discussed methods of updating the local-to-global rotation matrix **R**, integration of **ω(t)** is performed. In four of those methods (*Beard*, *DiMasi*, *SP*, and *UQ*), the integration process does not include the *coning correction*. The fifth method, and the only one explicitly accounting for the coning motion, is the *Bortz method*. To construct the rotation matrix the *ER method* numerically integrates the rate of change of the Euler parameters and the *2-1-3 method* integrates the rates of the Euler angles.

Even though the coning effect was not accounted for in most of the methods discussed in the paper, the *Beard*, *SP*, *ER*, and *UQ algorithms* gave an error that was either comparable or smaller than that calculated for the *Bortz method*. This is because the integration interval was sufficiently

82

small, which rendered the error coming from the coning motion negligible in the four presented test cases.

The *Beard method* utilizes a rectangular integration scheme to obtain finite rotations from the local angular velocity vector $\boldsymbol{\omega(t)}$, whereas the *UQ method* uses trapezoidal integration to accomplish the same task. The integration rule used is the only difference between the two algorithms, which provided for an ideal situation to evaluate the effect of the integration rule on method accuracy. In all four test cases, the *UQ method* gave more accurate results than the *Beard method*, while, at the same time, error in the *UQ method* was remarkably less susceptible to the increase in Δt (Figure 71 and Figure 72). The accuracy of the method used to update $\boldsymbol{R}$ will then depend strongly on the accuracy of the numerical integration scheme utilized to obtain the finite rotations from $\boldsymbol{\omega(t)}$. In methods that require solving ODE, the accuracy of the numerical approach utilized to find the solution for an ordinary differential equation, will drive the attitude algorithm results.

It was shown in *Error analysis – analytical approach* that when the time step Δt increased, the difference between the rotation matrices obtained analytically and numerically increased as well (Figure 73 and Figure 75). The observed change was non-linear in its nature which was in contrary to the test case results for five methods of obtaining the matrix $\boldsymbol{R}$ (*Bortz*, *Beard*, *DiMasi*, *SP*, and *2-1-3*). The character of the discussed change was either linear or close to linear for those five methods (with the exception of the *2-1-3 method* in Case 3; Table 5). Four methods out of the five (*Bortz*, *Beard*, *DiMasi*, and *SP*) used the first order integration schemes at some step in the algorithm. In the analytical analysis presented in the paper, the second order (trapezoidal) integration rule was utilized. When that rule was changed to rectangular (first order) and the analytical analysis was carried out once more for the same time step range as in the test cases (Δt from 5e-5 s to 0.001 s), the error increase due to the change in Δt became linear or close to linear (Figure 77). This further reinforces the statement that the error in computed orientation is driven mostly by the accuracy of the numerical integration used in the method of obtaining the rotation matrix $\boldsymbol{R}$.

a) b)
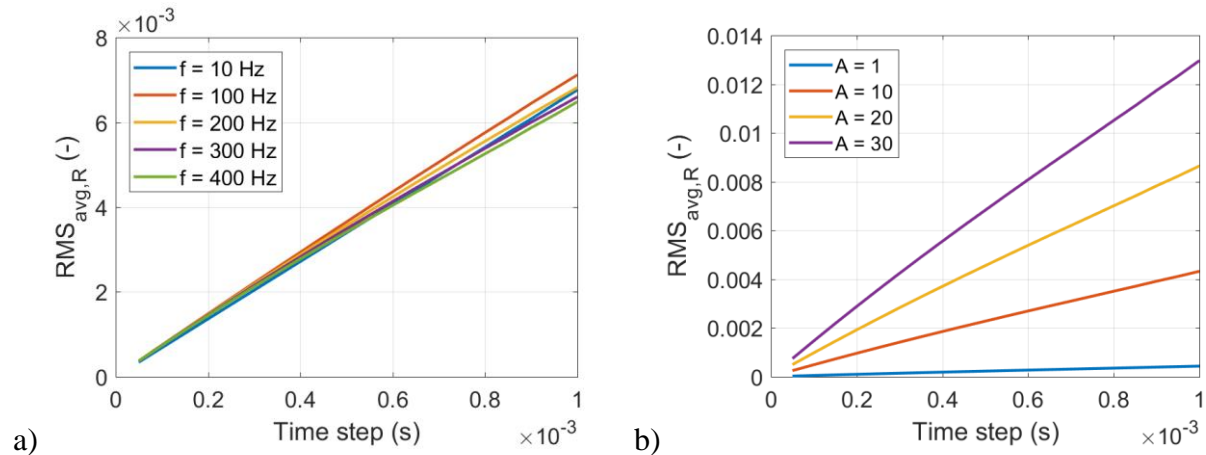
Figure 77. RMS_{avg,R} error vs. time step Δt up to 0.001 s for variations in: frequency f (with constant A = 15), b) parameter A (with constant f = 400 Hz).

When used to transform vectors (e.g. acceleration or position), an orthonormal matrix preserves vector lengths and the angles between them. The *DiMasi method* is the only method out of the discussed seven algorithms in which the updated matrix R does not remain orthonormal throughout the analysis, i.e. $RR^T \neq I$, where I is the identity matrix. An additional orthogonality correction step would be required to improve the method's accuracy, but this was not investigated here.

The *Beard*, *Bortz*, and *UQ algorithms* are subject to a divide-by-zero error in the case that the angular velocity were to be zero across multiple time steps. While this will most likely not present a problem with real data, this does cause issues with the data from computer simulations where angular velocity can remain equal to zero if it is part of the input.

It is worth mentioning here that there is a typographical error in the *R(2,2)* term presented in Beard and Schlick 2003. In *R(2,2)*, the term Ω_a^2 (squared finite rotation around axis *a*) appears twice when it should only be mentioned once. The second appearance should be Ω_b^2 instead.

The method of formulating the matrix R using Eq. 8.11 is equivalent to the *2-1-3* method (Kang et al. 2011) when a rigid body rotation (around more than one axis) is described by successive multiplications of the matrix from Eq. 8.11 expanded into three dimensions. Beard and Schlick 2003 showed that the order of matrix multiplications introduces a bias into the coordinate rotation. Another disadvantage of using the Euler angles is that they are prone to gimbal lock and, thus, they may not give a unique solution.

Similar error analysis as the one described in the *8.2.9 Error analysis – analytical approach* section can be performed for the *Unit Quaternion (UQ) method* (Rudd et al. 2006), where instead of the direct use of the angle of rotation to build R, the Euler parameters would be utilized to formulate the rotation matrix. Assuming the same analytical form of the angular velocity as presented in Eq. 8.12, rotation only around one axis, and the trapezoidal integration scheme (Eq. 8.15), the method described by Eq. 8.11 to Eq. 8.17 and the *UQ method* would be then analytically equivalent and thus only the former was discussed in the *8.2.9 Error analysis – analytical approach* part.

The analytical error analysis presented in the paper could be also performed for a body that rotates around more than one axis. Even though that analysis (which would be more mathematically complex) was not performed here, it is believed that the general trends seen in the "one-axis rotation" case (Figure 73 and Figure 75) would still hold true for the "2+ orthogonal rotations" case.

When the computational cost is considered, the *Beard method* seemed to be the most time-efficient and the *SP method* the least. The computation time was measured while the algorithms were run with MATLAB 2017a (MathWorks, Natick, MA, USA) on a desktop computer with the Intel i7 Dual Core unit processing the local angular rate vector with 15960 data points per each component. The computation time ranged from approx. 1.9 seconds (*SP method*) to 0.06 s (*Beard method*). The other five methods required less than half of a second to accomplish the same task. Those values may differ when a different code than MATLAB (software optimized for matrix manipulations) is used.

The results of this study showed that the error in the method used to obtain the rotation matrix R, depends not only on the time step Δt but also on the characteristics of the angular velocity signal (its magnitude and the frequency content). It is possible that for the same value of the time step Δt, the error in R would be smaller the smaller the magnitude or frequency of the input ARS data. That indicates that when choosing data sampling rate, one needs to take into account the type of the event being investigated. When the time step Δt is larger than the period of an integrated function, substantial part of the information contained in the input signal, will be lost. On the other hand, high sampling frequency appropriate for a crash test (short event with rapid changes in the angular velocity) might not be necessary, e.g., for a gait analysis (much longer event with smaller magnitude of $\omega(t)$ than seen in crash).

In the *8.3.2 Error analysis – analytical approach* section it was shown that for a simple 2D model there is a normalizing factor that can be used to match error curves for different frequencies of the analyzed angular velocity if f_{ref} is given. That normalizing factor can be utilized to extrapolate the results of the error analysis from a 2D event, in which the input data frequency f_1 and the sampling step Δt_1 are known, to a new 2D event (for example, with a larger time scale) in which the frequency of the angular velocity f_2 is also known. Assuming the same magnitude of the angular rate (as defined by the parameter A used in the analysis) between the two events, the sampling step Δt_2 that would yield a comparable magnitude of the $RMS_{avg,R}$ metric between the investigated scenarios can be estimated from Eq. 8.19:

$$1.028 * \left(\frac{f_1}{f_{ref}}\right)^{-0.43} * \Delta t_1 * f_1 = 1.028 * \left(\frac{f_2}{f_{ref}}\right)^{-0.43} * \Delta t_2 * f_2 \Rightarrow \Delta t_2 = \left(\frac{f_1}{f_2}\right)^{0.57} * \Delta t_1 \quad (8.19)$$

It needs to be pointed out here, though, that both, Eq. 8.18 and Eq. 8.19 were derived using the assumptions described in Section 8.2.9. Further research effort is required to identify similar mathematical connections for more complex 3D scenarios or a 2D scenario in which different magnitudes of the angular velocity are considered.

To summarize, the focus of this study was put on crash testing. Nevertheless, the results from the chapter can be extrapolated to other applications. When the relationships for different parameters describing the ARS signal are similar between investigated scenarios, the same attitude algorithm used in those cases should yield similar error results regardless of the difference in the time scale or angular rate magnitude/frequency.

8.5 Conclusions

The paper investigated the use of seven previously published algorithms of updating the local-to-global rotation matrix R in crash-like scenarios to identify which one of those methods was most applicable for test conditions like these. Additionally, an analytical analysis focusing on the effect of the data sampling step Δt and the characteristics of the measured angular velocity signal (its magnitude and frequency) was performed.

The main conclusions of this study are as follows:

- For the four test cases presented in the paper the most accurate methods of updating the rotation matrix R were the *UQ method* (Rudd et al. 2006) and the *ER method* (Huculak and

Lankarani 2013) – algorithms based on the Euler parameters derived from the angular velocity vector $\boldsymbol{\omega(t)}$. In addition, both methods appeared to be noticeably less susceptible (than the other discussed algorithms) to changes in error resulting from the increase in the sampling step $\varDelta t$.

- The accuracy of the method used to update $\boldsymbol{R}$ depends strongly on the accuracy of the numerical integration scheme utilized to obtain finite rotations from $\boldsymbol{\omega(t)}$ or on the accuracy of the numerical method used to solve ordinary differential equations, if that step is required in the algorithm.
- Characteristics of the angular velocity signal (its magnitude, period, etc.) affect the magnitude of the error in the calculated rotation matrix $\boldsymbol{R}$. It was shown that for the same value of the time step $\varDelta t$, the error in $\boldsymbol{R}$ is greater for greater magnitude or higher frequency of the input ARS data (Figure 75).
- In both, the analytical error analysis and when experimental data were used, the increase in the time step $\varDelta t$ of the ARS data (used as the input), caused, as expected, an increase in the difference between the calculated and reference rotation matrix (Figure 71). Similarly, the error in the angle of rotation θ_{INS} increased with higher values of $\varDelta t$ (Figure 72).

9. ANGULAR ACCELERATION ANALYSIS

When a sensor package is at a distance from the tracked point in all three dimensions, the time-history of the position of that point can be found with the use of rigid body motion equations and body's local angular acceleration (see Eq. 1.4). The goal of Chapter 9 was to investigate how different methods of obtaining angular acceleration (AAC) affect the process of 3D trajectory calculation. Five different and previously published techniques were analyzed. In addition, the sensitivity of calculated trajectories to the change in the filter class used on the AAC input data was evaluated.

The chapter is organized as follows. Section 9.1 a) introduces the reader to different techniques of obtaining local angular acceleration of a rigid body, b) describes the advantages and disadvantages of these techniques, c) discusses how these techniques have been used in crash-related research, d) shows what type of filters have been utilized previously in the process of finding AAC, e) shows two variations of one of the discussed methods of obtaining AAC, and f) briefly presents an alternative method of computing trajectory of a point which is at a distance from the sensor package used in the position calculation. Section 9.2 focuses on the methods used in this AAC analysis. The results of the study are presented in Section 9.3. Section 9.4 provides a general discussion about AAC filtering and about the accuracy of different AAC methods used in trajectory calculation process. Concluding remarks are provided in Section 9.5.

9.1 Calculation of angular acceleration

When an accelerometer block is designed in a way that its measurement center (Figure 2) is coincident with the tracked point, i.e. when only one component of the accelerometer seismic mass position vector ρ, the one aligned with the sensor sensing axis, is non-zero, the angular acceleration (AAC) is not needed in the process of calculating 3D trajectory of that point. When ρ has two or three non-zero components, the angular acceleration needs to be accounted for. That correction needs to be performed, e.g., when a 6 degree-of-freedom sensor cube is attached to the side of a rigid body but the researcher wants to obtain acceleration (and then position) at the body's CG, or when sensor fabrication tolerances and mounting inaccuracies are taken into consideration.

AAC measurement techniques are usually divided into two categories:
- indirect measurements:
  - where either angular position or angular velocity is differentiated to obtain AAC. A commonly used method that is based on differentiation of the body's angular rate is often called *3aω* (cf. Kang et al. 2011),
  - angular acceleration is determined using data from nine linear accelerometers (*Nine Accelerometer Package* (NAP) method; Padgaonkar et al. 1975) ,
  - angular acceleration is determined using linear accelerations in conjunction with body's local angular rates (*6aω* method; Martin et al. 1998, Kang et al. 2011, Kang et al. 2017);
- direct measurements by angular accelerometers (Amarasinghe et al. 2005, Wolfaardt et al. 2008, Li et al. 2013, Carvalho et al. 2013, Zhao et al. 2015, Nusbaum et al. 2018).

9.1.1 Advantages and disadvantages of different methods of obtaining AAC

NAP is based on analytical equations and it requires data from nine linear accelerometers to compute AAC but also one integration to obtain angular velocity (if needed). The *6aω* approach, similarly to NAP, uses analytical equations to determine the angular acceleration components from six linear accelerometers and three angular rate sensors. The advantage of this method over NAP is that the angular velocity is measured directly.

It has been shown that NAP is numerically stable (cf. Liu 1976) but the channel count and the space required to accommodate nine sensors can limit its usage. In addition, because of a large number of linear accelerometers utilized, the method is more prone to errors resulting from sensor misalignment, debias, noise, etc. (Voo et al. 2003, cf. Bussone et al. 2010). It is hypothesized that similar issues can affect the *6aω* scheme.

In the *3aω* method, angular acceleration is computed by numerical differentiation of the angular velocity vector $\omega(t)$. Obtained acceleration, though, depends strongly on the characteristics of the noise in the differentiated signal and/or on a filter class used on the input angular rate data (cf. Bussone et al. 2010). This puts the method at a disadvantage to NAP and *6aω*, two approaches that are based on algebraic manipulations rather than on a numerical differentiation.

AAC can be also measured directly by angular accelerometers. There is a number of angular accelerometers available on the market (e.g., 7302BM5 angular accelerometers manufactured by Endevco Meggit Sensing Systems) but they have not been used widely in crash or impact testing and therefore there are no recommendations on how to post-process the data from those sensors when needed in 3D trajectory calculation (e.g., what type of filters should be used, etc.).

9.1.2 AAC measurement in impact and crash testing

Over the years, the NAP configuration (Figure 78) has been commonly used in impact and crash testing (Viano et al. 1986, DiMasi 1995, Hardy et al. 2001, Voo et al. 2003, Yoganandan et al. 2006, Kang et al. 2015, Sanchez 2017) and by many the method is treated as the gold standard in obtaining AAC (Martin et al. 1998, Bussone et al. 2010, Kang et al. 2011, Kang et al. 2017, Nevins et al. 2018).
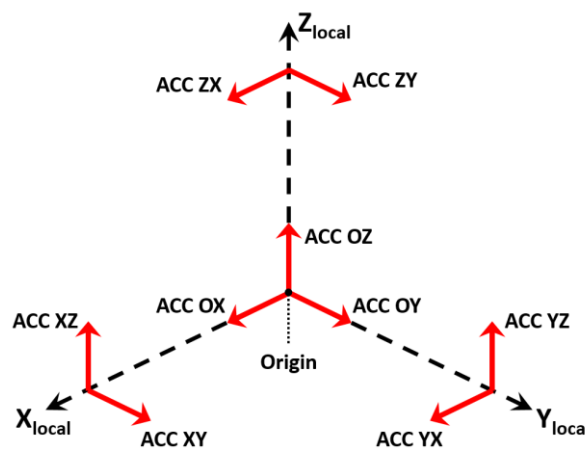
Figure 78. NAP configuration.

Kang et al. 2011 and Kang et al. 2017 used *3aω*, *6aω* and NAP to obtain 6DOF kinematics of the head in an array of tests in which the head-neck assembly of the HIII 50 ATD was impacted by a pneumatic ram at various rates and in various directions. Bussone et al. 2010 compared NAP and *3aω* in multiple short- and long-duration events. Gabler et al. 2016 used differentiated angular velocity to assess existing metrics for predicting strain-based brain response. Rudd et al. 2006 utilized the *3aω* scheme to obtain kinematics of pedestrian's limbs during an impact. Huculak and Lankarani 2013 applied the method to compute the head trajectory in aircraft seat certification testing, and Wu et al. 2009 and Kerrigan et al. 2011 used the *3aω* configuration to describe motion of a vehicle in rollover.

While Kang's and Bussone's research focused mainly on the comparison between different methods of computing AAC (with NAP being treated as the gold standard), Rudd, Huculak, Wu, and Kerrigan used AAC obtained with the *3aω* method to calculate the trajectory of a body in a 3D space. In addition, Wu et al. 2009 and Huculak and Lankarani 2013 assessed the accuracy of their position predictions using reference data from video tracking. Wu et al. 2009 showed a good agreement between the computed and the reference trajectories, while the position error in Huculak and Lankarani 2013 varied between 1 mm to 43 mm.

Even though *3aω*, *6aω* and NAP were compared between each other using sensor data recorded on the same test, none of the research effort mentioned above, utilized the three methods to compute 3D trajectories of a body loaded in the same environment and in the same way. To the author's knowledge there is no publically available comprehensive investigation on if (and how much) the selection of the AAC obtaining method would affect that calculation process. Because of lack of that type of a study there is no current standard stating which of the discussed algorithms should be utilized, when needed in trajectory calculation for a body in a crash.

9.1.3 Filtering of impact data used in obtaining AAC

The SAE J211 document (SAE 1995) recommends the Channel Frequency Class (CFC) 1000 filter (1,650 Hz cut-off frequency) to be utilized on the head accelerations (both, linear and angular) when the ATD's head impact data are processed. The same document suggests the CFC 180 (300 Hz cut-off) filter for vehicle structural accelerations when they are integrated for velocity or displacement, and CFC 60 (100 Hz cut-off) when the acceleration is used in vehicle comparisons. SAE J211, though, does not specify what filter class should be utilized when the angular velocity of a body is analyzed.

Majority of biomechanical researchers follows SAE J211's recommendations. The CFC 1000 filter was used in multiple studies, e.g. on the input linear acceleration to *6aω* (Kang et al. 2011, Kang et al. 2015) or NAP (Voo et al. 2003, Yoganandan et al. 2006, Bussone et al. 2010, Kang et al. 2011, Kang et al. 2015). In contrary, Hardy et al. 2001 utilized CFC 180 on the head's local acceleration (used – among others – for the NAP calculations) to eliminate the resonance of the head and the NAP fixture itself. Martin et al. 1998 first filtered the HIII ATD head's acceleration with CFC 1000 and then, to reduce the noise in AAC obtained from NAP and *6aω*, with a 4-pole Butterworth filter with a 600 Hz cut-off frequency.

While there is a general consensus about filter class utilized on linear accelerations, researchers have used multiple different filters on the head or vehicle angular rate. Kang et al. 2011 utilized CFC 1000 on angular rate used in the *6aω* method and CFC 180 (high severity impacts) or CFC 60 (low severity impacts) for the *3aω* scheme. Kang et al. 2017 used the same CFC 1000 filter on the head angular rate for *6aω* but CFC 600 (1,000 Hz cut-off) for *3aω*. Gabler et al. 2016 utilized CFC 60 for the head ARS in strain-based metrics (some of which required AAC as an input) to assess the brain response. Martin et al. 1998 used CFC 180 for the local angular velocity in head impacts. Kerrigan et al. 2013 utilized vehicle angular velocity filtered to CFC 180 to obtain the vehicle's 3D kinematics but for calculating the local angular accelerations he filtered the vehicle's ARS data with a low-pass filter with a 25 Hz cut-off. Lastly, Bussone et al. 2010 proposed a filtering cut-off frequency based on a residual analysis performed on the ARS channels used to obtain AAC (for more details about the residual analysis see Winter 2004). The results from Bussone's study suggested a cut-off of 150 Hz in a non-impact event stating at the same time that "(…) an *a priori* selection of cutoffs is difficult" and "In the absence of a compelling pre-selected cutoff, the recommended solution is a per-channel analysis (…)."

In summary, the selection of a proper filter for angular rate or linear acceleration data is not a trivial task. The cut-off frequency used will be test and application specific. When the obtained results (e.g. AAC computed through differentiation of ARS data in the *3aω* method) depend strongly on the characteristics of the noise in the measured signal, selection of an appropriate filtering technique is of great importance.

9.1.4 Two variations of the 6aω configuration

The *6aω* method does not constrain the researcher to only one geometric configuration of the sensors used within the scheme. The flexibility in choosing the location of six linear accelerometers led to different designs of the *6aω* sensor package seen in the literature. Two of the designs, coplanar *c6aω* configuration (Figure 79a) and three-arm *t6aω* (Figure 79b) were evaluated in impact testing and compared with NAP and *3aω* (Kang et al. 2011, Kang et al. 2017). Because of that it was decided that both would be also investigated in this dissertation.
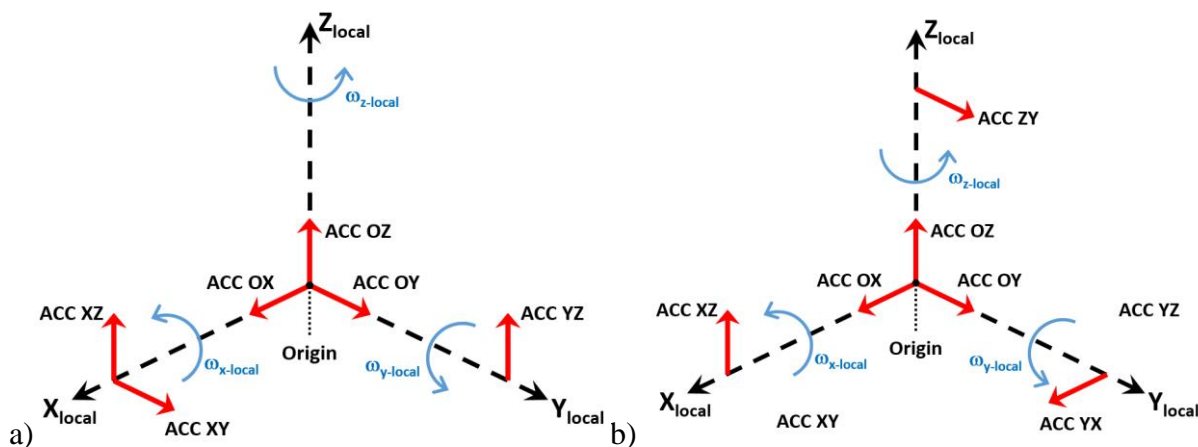
Figure 79. Two variations of the sensor package used in the 6aω method: a) coplanar 6aω configuration (c6aω), b) three-arm 6aω configuration (t6aω).

9.1.5 Methods of computing trajectories for a point positioned away from the sensor block

When a sensor package is at a distance from the tracked point o in all three dimensions, the time-history of the global position of that point can be obtained using body's local acceleration transformed to point o (with the use of AAC) double integrated in time (as shown in Section 1.2.3). The position can be also found using an alternative approach that minimizes (or completely ignores) the effect of the body's local angular acceleration. This alternative method requires the following information:

- known vector $\boldsymbol{\rho_{o\text{-}to\text{-}MC}}$ (in the body's local coordinate frame) between point o and the measurement center (MC; Figure 2) for the sensor block,
- the position time history of MC, $\boldsymbol{r_{MC}(t)}$, computed as described in Section 1.2.3, but assuming that all sensors were perfectly aligned with the axes of the body's local coordinate system, i.e. no AAC was needed in the process of trajectory calculation,
- the time history of the local-to-global rotation matrix $\boldsymbol{R(t)}$ for the tracked rigid body.

If those three pieces of information are known, 3D component trajectories of point o can be computed based on Eq. 9.1:

$$\boldsymbol{r_o(t) = r_{MC}(t) + R(t) * \rho_{o-to-MC}} \tag{9.1}$$

where t – time, $\boldsymbol{r_o}$ – global position vector of point o, $\boldsymbol{r_{MC}}$ – global position vector of the measurement center for the sensor block attached to the tracked body, $\boldsymbol{R}$ – local to global rotation matrix for the tracked body, $\boldsymbol{\rho_{o\text{-}to\text{-}MC}}$ – local position vector of point o relative to the measurement center MC.

Because the focus of this study was put on the effect of local angular acceleration on the calculated trajectory of a tracked point, only the method that amplifies that effect, i.e. the method that utilizes the body's local acceleration transformed to the tracked point and then double integrated in time, was analyzed here. The method described by Eq. 9.1 and its accuracy in predicting 3D component trajectories were not investigated in the dissertation.

9.1.6 Summary

There are currently no recommendations on which of the methods of obtaining body's local angular acceleration should be utilized, if needed for 3D trajectory calculation. That is why the goal of this study was to evaluate motion predictive capabilities of all five methods mentioned in this chapter (and listed again below) for the head in a crash-like scenario:

- Nine Accelerometer Package approach (NAP; Padgaonkar et al. 1975),
- *c6aω* (Kang et al. 2017),
- *t6aω* (Kang et al. 2011),
- *3aω* (cf. Rudd et al. 2006),
- Angular acceleration recorded by angular accelerometers (sensors used during Simplified Head testing: Meggitt Endevco 7302BM5).

Additionally, different Channel Frequency Class filters were used on the input data to the five algorithms to assess the sensitivity of the calculated trajectory to the change in the filter cut-off frequency.

9.2 Methods

In this subsection, the methods used in the angular acceleration analysis are described. The methods are organized as follows. First, five test configurations utilized in the study are presented. Next, sensors and filters used are discussed. Then, tracked points and their coordinates relative to the sensor block utilized in the calculation process are given. Following, error metrics used throughout the analysis are discussed. A consistency check for the sensors employed in the NAP method is presented next. In the last part of the methods, the process of minimization of errors in the initial orientation of the tracked body is discussed.

9.2.1 Test configurations

Four Simplified Head tests and one THOR Mod-kit test were selected for the analysis:

- Test S0425 (test fixture positioned at 45° with reference to the sled travel direction; no wedge),
- Test S0433 (test fixture positioned at 0° with reference to the sled travel direction; no wedge),
- Test S0436 (test fixture positioned at 45° with reference to the sled travel direction; with the wedge),
- Test S0442 (test fixture positioned at 45° with reference to the sled travel direction; no wedge),
- Test S0461 (THOR Mod-kit; head impact included).
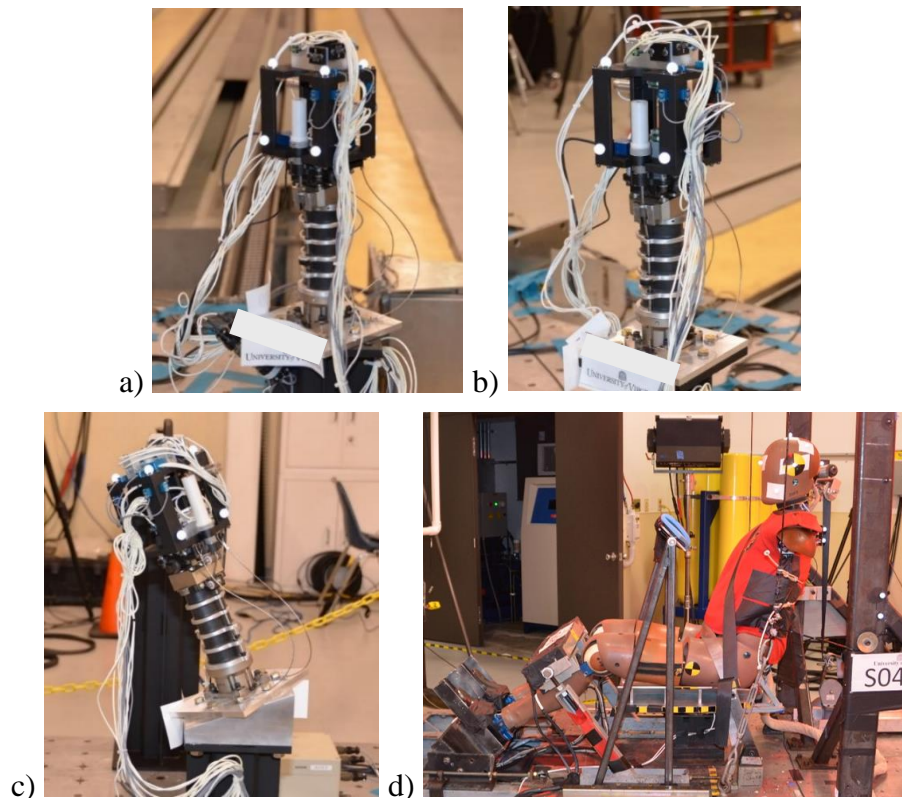
Figure 80. Exemplar test configurations: a) Test S0425, b) Test S0433, c) Test S0436, d) Test S0461.

The Simplified Head setup allowed for comparison between all five discussed methods of obtaining AAC. In Test S0461, due to the used sensor configuration only *3aω* was utilized in the process of 3D trajectory calculation.

9.2.2 Sensors used

Data from two types of angular rate sensors were used in the study:
- DTS ARS Pro 8k deg/s with bandwidth up to 2000Hz (Simplified Head tests),
- DTS ARS Pro 18k deg/s with bandwidth up to 2000Hz (THOR ATD test).

Nine Endevco 7264C accelerometers (three at the origin of the sensor local coordinate system and three sets of two accelerometers at three different locations away from the origin; Figure 78) were used to obtain local linear accelerations of the Simplified Head. In test S0461, three Endevco 7264C accelerometers (all at the head CG) were utilized.

On all of the Simplified Head tests, AAC was also measured directly by Endevco 7302BM5 sensors attached to the structure.

9.2.3 Filters used

To investigate the influence of filtering on the obtained position of a tracked body, different Channel Frequency Class (CFC) filters were used on the input data (either acceleration or angular rate).

In the trajectory algorithm, body's local linear acceleration, directly from the sensors, can be used twice:
- In calculations needed to obtain angular acceleration (NAP and the *6aω* methods);
- In the process of transforming measured acceleration from the sensor locations to the tracked point (Eq. 1.4).

The angular rate measured by ARS can be used trice:
- In calculations needed to obtain angular acceleration (*6aω* and *3aω* methods);
- To update the local-to-global transformation matrix $\boldsymbol{R}$;
- To transform linear accelerations measured by the linear accelerometers to the tracked point (Eq. 1.4).

Before translating linear accelerations to the tracked point, the accelerometer data were <u>always</u> filtered with CFC 1000. On the linear acceleration used in the NAP and both *6aω* methods the following filters were utilized: CFC 60, CFC 180, CFC 600, and CFC 1000. Additionally, as a reference, raw (not filtered) ACC data were used in the trajectory calculation process.

On the ARS data in both *6aω* methods and in the *3aω* scheme the following filters were utilized: CFC 60, CFC 180, CFC 600, and CFC 1000. Additionally, raw ARS data were exercised in the calculations. Only angular rate filtered to CFC 180 was used to transform linear acceleration to the tracked point (as described by Eq. 1.4) and in the algorithm described by Rudd et al. 2006, utilized to update the transformation matrix $\boldsymbol{R}$.

On the data from the angular accelerometers the following filters were used: CFC 60, CFC 180, CFC 600, and CFC 1000. Additionally, as a reference, raw AAC data were utilized.

9.2.4 Location of accelerometers in body's local frame

To investigate the influence of angular acceleration on the calculated trajectory, the sensor data recorded on the tests were used to track two of the VICON markers attached to the Simplified Head (Figure 81a and b) and one VICON marker attached to the THOR ATD's head (Figure 81c).
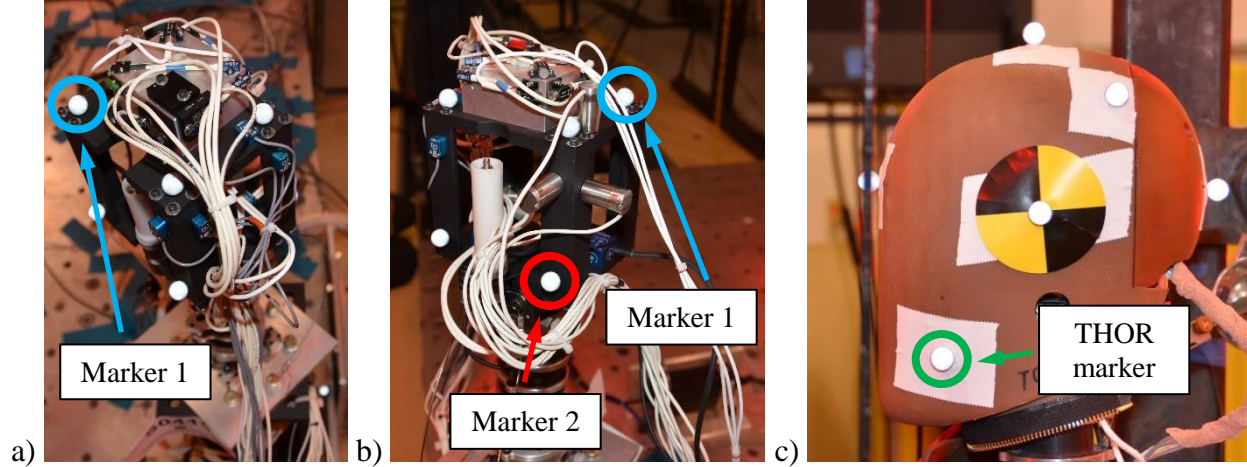
Figure 81. Placement of tracked markers: a) Simplified Head (top-front view), b) Simplified Head (back view), c) THOR head (side view). For the location of the sensor block used, see the test matrices for both test series.

The locations of the linear accelerometer seismic mass CGs relative to the marker positions for the Simplified Head tests and for the THOR test were gathered in APPENDIX J.

9.2.5 Error metrics

Throughout the analysis the following metric was used to evaluate the accuracy of the head's calculated trajectory:

$$Res_{err} = \sqrt{\frac{\sum_{i=1}^{N}\left[\left(x_{OSS,i}-x_{calc,i}\right)^2+\left(y_{OSS,i}-y_{calc,i}\right)^2+\left(z_{OSS,i}-z_{calc,i}\right)^2\right]}{N}} \tag{9.2}$$

where N – number of data (time) points, $x_{OSS,i}$, $y_{OSS,i}$, $z_{OSS,i}$ – X, Y, Z components of the reference trajectory (from VICON OSS) at the data point i, $x_{calc,i}$, $y_{calc,i}$, $z_{calc,i}$ – X, Y, Z components of the calculated trajectory (based on sensor data).

For all five test cases, within the same method of obtaining AAC but across different filters, Res_{err}'s minimum value, mean value, standard deviation (SD), and the coefficient of variation (CV) were found. In the initial orientation optimization investigation (see APPENDIX K), the maximum absolute difference *diff_max* between the calculated and reference trajectories was computed and reported for the three trajectory components. Additionally, in the Results section for the Simplified Head and the THOR ATD tests, the time history of the absolute difference (error) between the computed and VICON trajectories was determined and presented.

9.2.6 NAP consistency check

In the Simplified Head tests, the NAP sensor package was attached to the analyzed structure. Takhounts et al. 2009 showed that by using rigid body constraints a closed-form solution for each arm sensor measurement, in terms of the eight other sensor readings and arm lengths, can be

obtained. That method, called also NAP consistency check, was utilized in this dissertation on the linear acceleration data set recorded on the four Simplified Head sled tests. All used accelerometer readings were identified as consistent, i.e. none of the accelerometer measurements needed to be replaced by the NAP consistency check prediction.

9.2.7 Initial orientation optimization

As it will be shown in *Chapter 10: Error Effect Analysis* and *Chapter 13: 3D Trajectory Calculation in THOR Tests Utilizing the Knowledge Gained from Error Effects Analysis*, the error in the initial orientation (R_{ini}) of a tracked body can substantially affect the calculated trajectory. To minimize that effect, **an optimization of the initial Euler angles** for both, the Simplified Head and the THOR ATD's head (in the five tests discussed in Section 9.2) **was performed <u>before</u> the AAC analysis was carried out**. The methods and the results from the optimization analysis can be found in APPENDIX K.

9.3 Results

In this subsection, the results from the AAC analysis are presented: first, for the tests with the Simplified Head, and next, for the THOR test.

9.3.1 Simplified Head tests

9.3.1.1 Angular accelerometer data compared to the other four methods of obtaining AAC

Different methods of obtaining body local AAC require different input. NAP uses only linear acceleration (ACC), *3aω* is based solely on angular rate (ARS), while the angular accelerometers measure AAC directly. When all of that data (ACC, ARS, and AAC) from two exemplar tests (Test S0436 and Test S0442) were filtered to the same software filter (CFC 60) and AAC from the five methods was compared, the shapes and magnitudes of the angular acceleration time-histories matched well (Figure 82 and Figure 83), i.e. by removing the noise related to the resonance frequency, the AAC traces from the Endevco sensors were comparable with those from the NAP, both *6aω* methods, and the *3aω* configuration. (<u>Remark</u>: For more details about the frequency content of the signal recorded by the AAC sensors, see APPENDIX H).
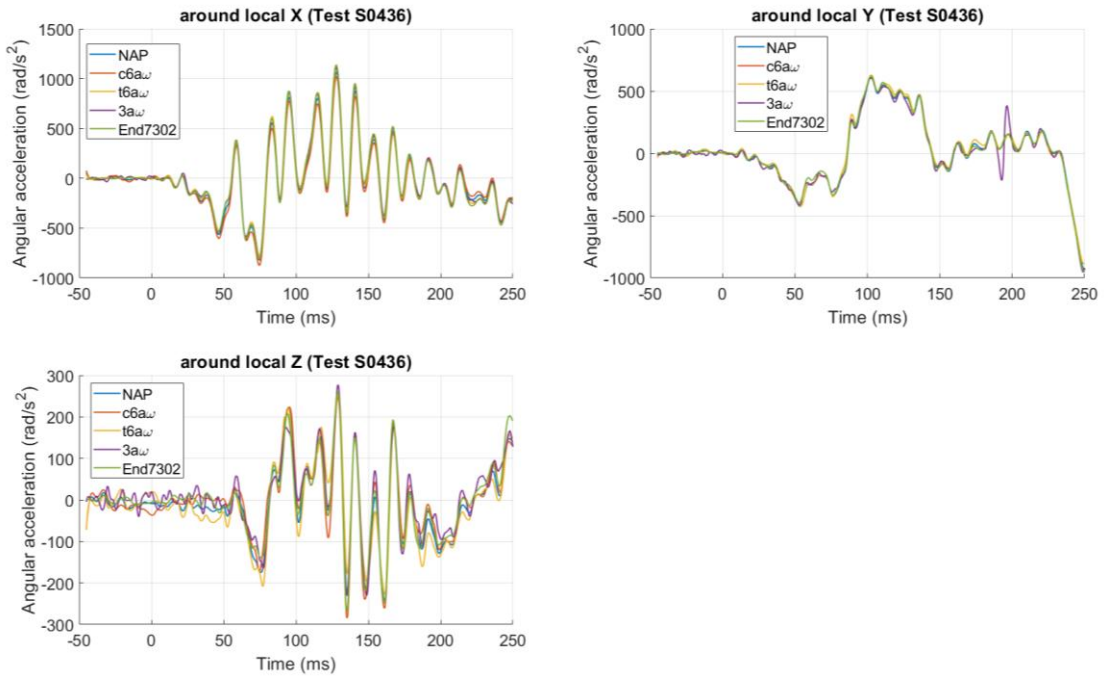
Figure 82. Test S0436: Angular acceleration data from the five discussed methods of obtaining AAC. Input linear acceleration data, angular velocity and the angular acceleration from the Endevco sensors filtered with CFC 60.
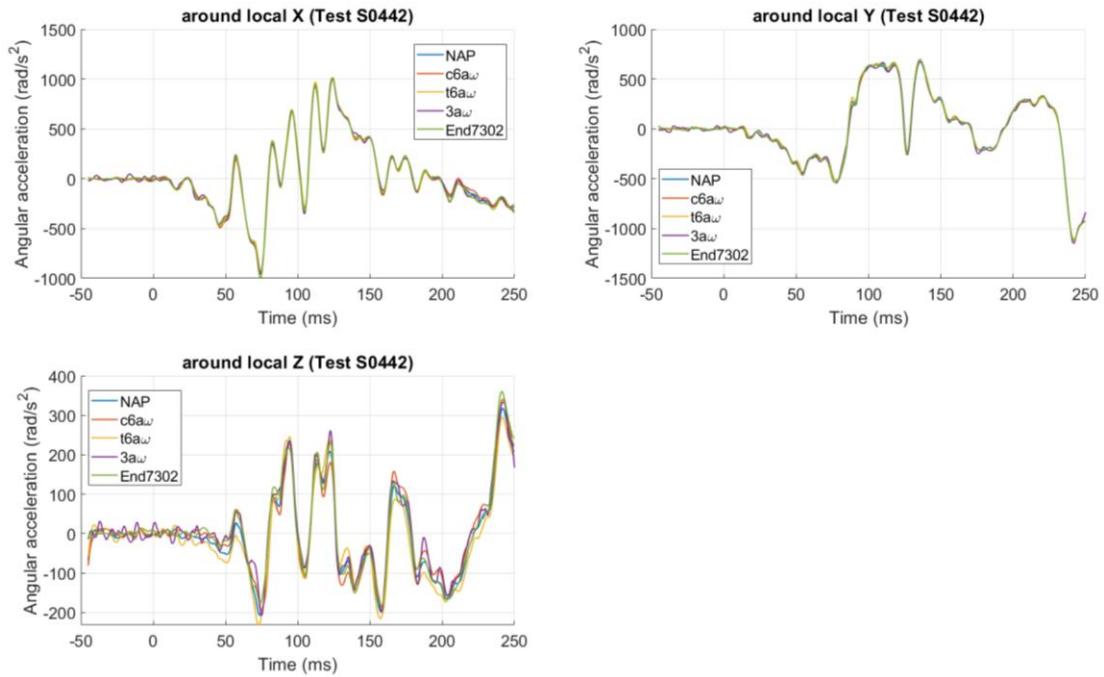
Figure 83. Test S0442: Angular acceleration data from the five discussed methods of obtaining AAC. Input linear acceleration data, angular velocity and the angular acceleration from the Endevco sensors filtered with CFC 60.

9.3.1.2 Summary based on Res_{err}

In all four analyzed Simplified Head tests and for both tracked markers, the smallest value of Res_{err} was found when the $3a\omega$ method was utilized to compute body's local angular acceleration (Table 7 and Table 8). For that method of obtaining AAC, the filter class that gave the smallest Res_{err} for Marker 1 was CFC 60 in Test S0425 and CFC 180 in the remaining three tests (Table 7). In case of Marker 2, in all four tests, angular rate data filtered to CFC 60 gave 3D trajectory with the smallest error (Table 8).

The second best results, for both markers and across the analyzed test cases, were obtained with the use of the angular accelerometers. For those sensors, though, there was no consistency in a filter class that gave the smallest Res_{err}. The filters varied from CFC 60 (both markers in Test S0436, and Marker 1 in Test S0442), through CFC 180 (Marker 1 in Test S0425 and Marker 2 in Test S0433), to CFC 600 (Marker 1 in Test S0433). For Marker 2, in Test S0425 and Test S0442, the trajectory computed with the raw unfiltered data was the one deviating the least from VICON.

NAP, $c6a\omega$, and the $t6a\omega$ methods generated a noticeably high deviation of the calculated trajectory from the reference VICON data. For Marker 1, Res_{err} varied from 11.78 mm for NAP in Test S0425 to 74.07 mm for $c6a\omega$ in Test S0436, while for Marker 2 Res_{err} varied from 12.21 mm in Test S0442 to 89.47 mm in Test S0433, both obtained when the $c6a\omega$ method was utilized. Similarly to the Endevco sensors, in case of NAP, $c6a\omega$, and $t6a\omega$ there was no consistency in filter class that minimized Res_{err}.

The highest value of Res_{err} recorded for each of the test cases, was computed when AAC was excluded from the trajectory calculation (last column in Table 7 and Table 8).

Remark: Plots of angular acceleration calculated with the five methods, in the four Simplified Head tests, for both tracked markers, for the filter combination that minimized Res_{err}, can be found in APPENDIX L. Values of Res_{err} for all used filter combinations in the four analyzed Simplified Head tests can be found in APPENDIX M.

Table 7. Minimum Res$_{err}$ for Marker 1 for the five methods of obtaining angular acceleration and when AAC was not included in the trajectory calculation process.

Test #	NAP		$c6a\omega$		$t6a\omega$		$3a\omega$		Endevco 7302BM5		No AAC included
	Res_{err} (mm)	Filter used	Res_{err} (mm)	Filter used (ARS/ACC)	Res_{err} (mm)	Filter used (ARS/ACC)	Res_{err} (mm)	Filter used	Res_{err} (mm)	Filter used	Res_{err} (mm)
S0425	11.78	CFC60	17.51	Raw/CFC60	16.34	CFC60/Raw	4.19	CFC60	4.39	CFC180	45.2
S0433	28.12	CFC60	39.41	CFC60 /CFC60	27.97	CFC60 /CF60	2.73	CFC180	10.32	CFC600	63.3
S0436	41.49	CFC60	74.07	CFC60 /CFC60	17.32	CFC60 /CFC60	5.94	CFC180	16.98	CFC60	128.77
S0442	15.97	Raw	18.94	CFC60/Raw	19.26	CFC60/Raw	3.42	CFC180	5.16	CFC60	190.64

Table 8. Minimum Res_err for Marker 2 for the five methods of obtaining angular acceleration and when AAC was not included in the trajectory calculation process.

Test #	NAP		c6aω		t6aω		3aω		Endevco 7302BM5		No AAC included
	Res_{err} (mm)	Filter used	Res_{err} (mm)	Filter used (ARS/ACC)	Res_{err} (mm)	Filter used (ARS/ACC)	Res_{err} (mm)	Filter used	Res_{err} (mm)	Filter used	Res_{err} (mm)
S0425	21.42	CFC60	17.98	CFC600 /CFC180	36.66	CFC60/Raw	**3.19**	CFC60	7.81	Raw	275.12
S0433	71.1	CFC600	89.47	CFC1000 /CFC1000	59.72	CFC60 /CF60	**2.6**	CFC60	15.61	CFC180	255.45
S0436	23.3	Raw	27.79	Raw/Raw	22.8	CFC60 /CFC1000	**5.41**	CFC60	10.8	CFC60	112.75
S0442	16.97	Raw	12.21	CFC60 /CFC1000	23.66	CFC60/Raw	**3.12**	CFC60	4.38	Raw	162.19

For the two tracked markers, for NAP, both *6aω* methods, and the angular accelerometers, the standard deviation of Res_{err} seen across different filters used in the four analyzed tests was less than 0.5 mm (Table 9 Table 10). The standard deviation for the *3aω* configuration, for Marker 1 varied between 0.07 mm (Test S0433) to 2.28 mm (Test S0442; Table 9), and for Marker 2, between 0.4 mm (Test S0436) to 1.17 mm (Test S0425; Table 10).

The coefficient of variation CV was the highest also when AAC was computed with *3aω*. It varied between 2.51% (Marker 1 in Test S0433) to 41.48% (Marker 1 in Test S0442; Table 9). For the other four methods of obtaining AAC, CV was noticeably lower and it was between 0.04% (Marker 1, NAP, Test S0433) to 2.43% (Marker 1, *t6aω*, Test S0425; Table 9).

Table 9. Marker 1: Mean value, standard deviation (SD), and coefficient of variation (CV) for Res_err across all used filters.

Test #	NAP			c6aω			t6aω			3aω			Endevco 7302BM5		
	Mean (mm)	STD (mm)	CV (%)	Mean (mm)	STD (mm)	CV (%)	Mean (mm)	STD (mm)	CV (%)	Mean (mm)	STD (mm)	CV (%)	Mean (mm)	STD (mm)	CV (%)
S0425	11.83	0.03	0.24	17.62	0.06	0.35	16.63	0.4	2.43	5.05	0.61	12.04	4.4	0.01	0.22
S0433	28.14	0.01	0.04	39.44	0.02	0.04	28.4	0.24	0.84	2.84	0.07	2.51	10.34	0.02	0.24
S0436	41.74	0.15	0.36	74.95	0.47	0.63	17.47	0.08	0.46	6.37	0.47	7.34	17.02	0.02	0.12
S0442	16.09	0.2	1.25	19.04	0.14	0.74	19.38	0.13	0.69	5.5	2.28	41.48	5.19	0.02	0.45

Table 10. Marker 2: Mean value, standard deviation (SD), and coefficient of variation (CV) for Res_err across all used filters.

Test #	NAP			c6aω			t6aω			3aω			Endevco 7302BM5		
	Mean (mm)	STD (mm)	CV (%)	Mean (mm)	STD (mm)	CV (%)	Mean (mm)	STD (mm)	CV (%)	Mean (mm)	STD (mm)	CV (%)	Mean (mm)	STD (mm)	CV (%)
S0425	21.83	0.25	1.14	18.02	0.03	0.15	36.85	0.18	0.5	4.48	1.17	26.02	7.84	0.05	0.62
S0433	71.14	0.04	0.06	89.58	0.13	0.15	60.42	0.39	0.64	3.44	0.71	20.58	15.63	0.02	0.14
S0436	23.4	0.16	0.69	27.84	0.05	0.19	23.01	0.33	1.44	5.96	0.4	6.66	10.87	0.04	0.39
S0442	17.12	0.25	1.43	12.4	0.28	2.29	23.78	0.16	0.67	3.95	1.14	28.9	4.44	0.1	2.14

Relatively small values of SD seen across the five methods of obtaining local angular acceleration (Table 9 and Table 10) suggest that the computed trajectories (within the same method of determining AAC) were not highly sensitive to the change in filtering of the method's input (either acceleration or angular velocity). To second that, for four out of the five methods, the relative variability due to the filter selection was low (up to 2.43%). The only method with a high relative variability (up to approx. 40%) was the *3aω* method.

9.3.1.3 Global position

The global trajectories of the two tracked markers, calculated with the five different methods of obtaining AAC, followed the general shape of the XYZ position components measured by the VICON system (Figure 84 to Figure 91).

In the four Simplified Head tests, the trajectories computed with the use of the *3aω* scheme matched the reference position time-histories the best, with the other four methods deviating from the reference mocap data more noticeably. When local angular acceleration was not included in the calculation, the error in the predicted response grew noticeably. That can be seen, e.g., in all three trajectory components of Marker 2 in Test S0425 (Figure 85), or in Marker 1's Y and Z components in Test S0436 (Figure 88).
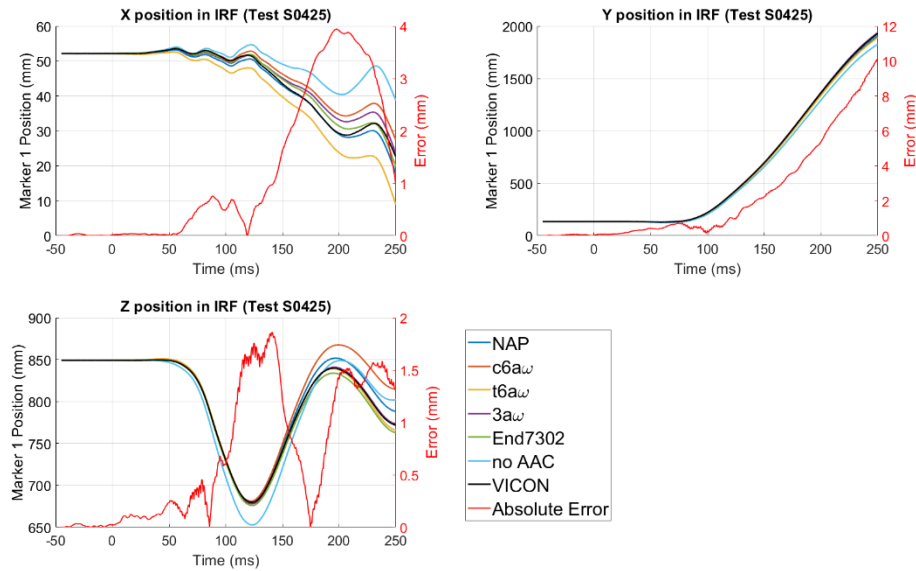
Figure 84. Test S0425 – Comparison between mocap and calculated trajectories for Marker 1, for five methods of obtaining AAC, for the CFC filter(s) that minimized Res_{err}. Absolute error between the reference trajectory and the trajectory computed with the use of the 3aω method (best prediction; Table 7) is plotted in red.
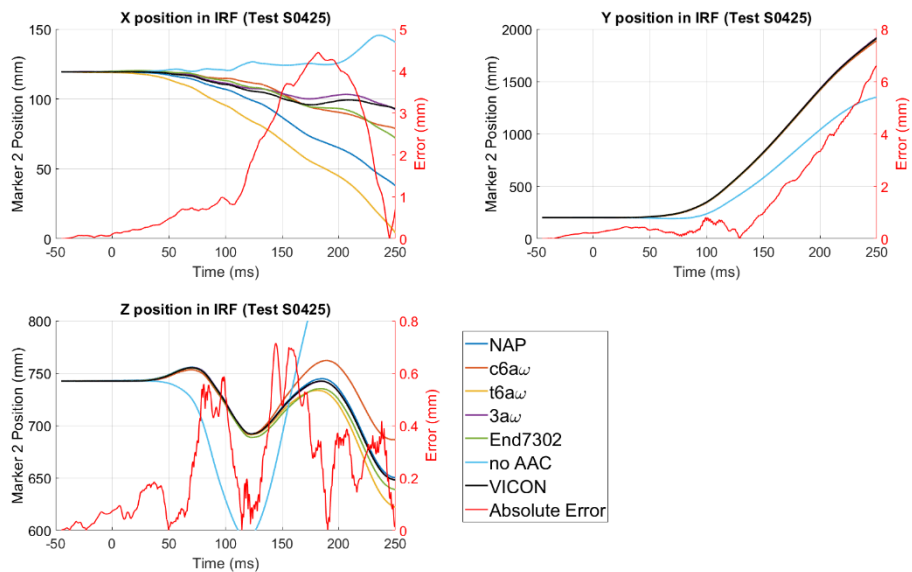
Figure 85. Test S0425 – Comparison between mocap and calculated trajectories for Marker 2, for five methods of obtaining AAC, for the CFC filter(s) that minimized Res_{err}. Absolute error between the reference trajectory and the trajectory computed with the use of the 3aω method (best prediction; Table 8) is plotted in red.
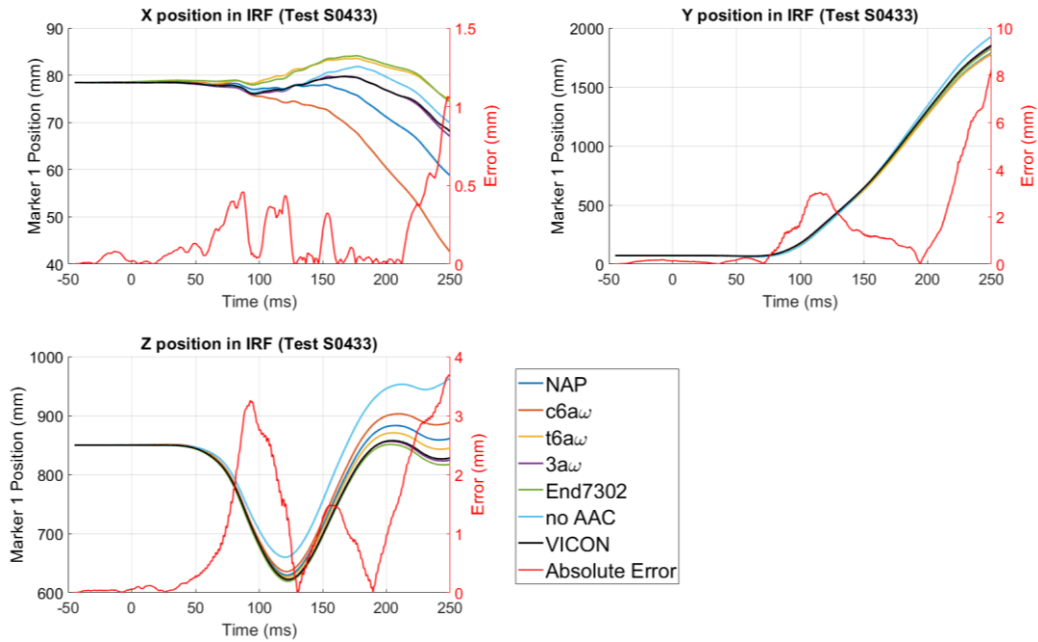
Figure 86. Test S0433 – Comparison between mocap and calculated trajectories for Marker 1, for five methods of obtaining AAC, for the CFC filter(s) that minimized Res_{err}. Absolute error between the reference trajectory and the trajectory computed with the use of the 3aω method (best prediction; Table 7) is plotted in red.
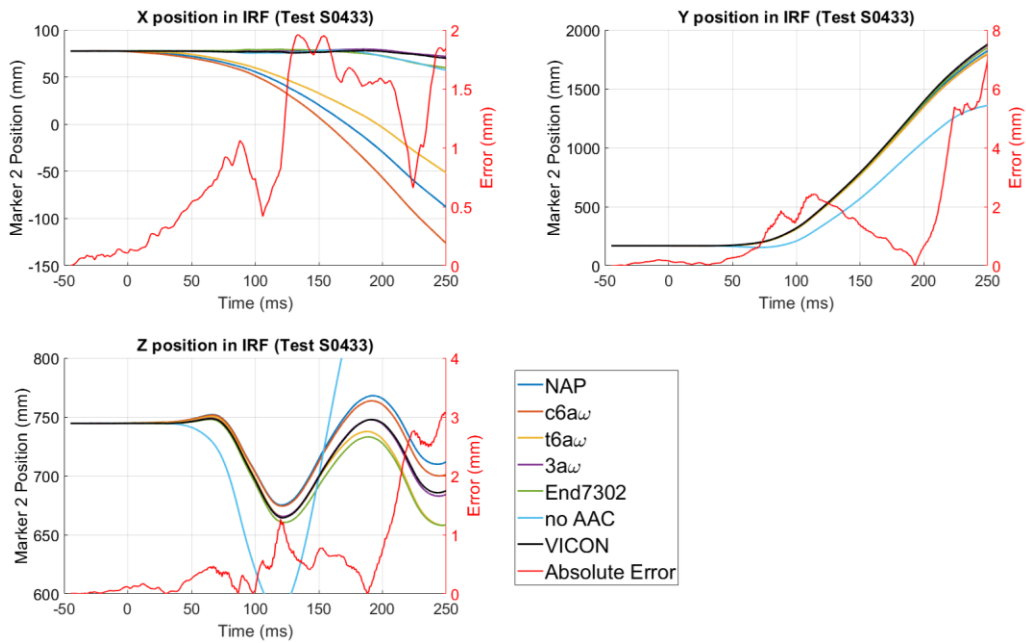
Figure 87. Test S0433 – Comparison between mocap and calculated trajectories for Marker 2, for five methods of obtaining AAC, for the CFC filter(s) that minimized Res_{err}. Absolute error between the reference trajectory and the trajectory computed with the use of the 3aω method (best prediction; Table 8) is plotted in red.
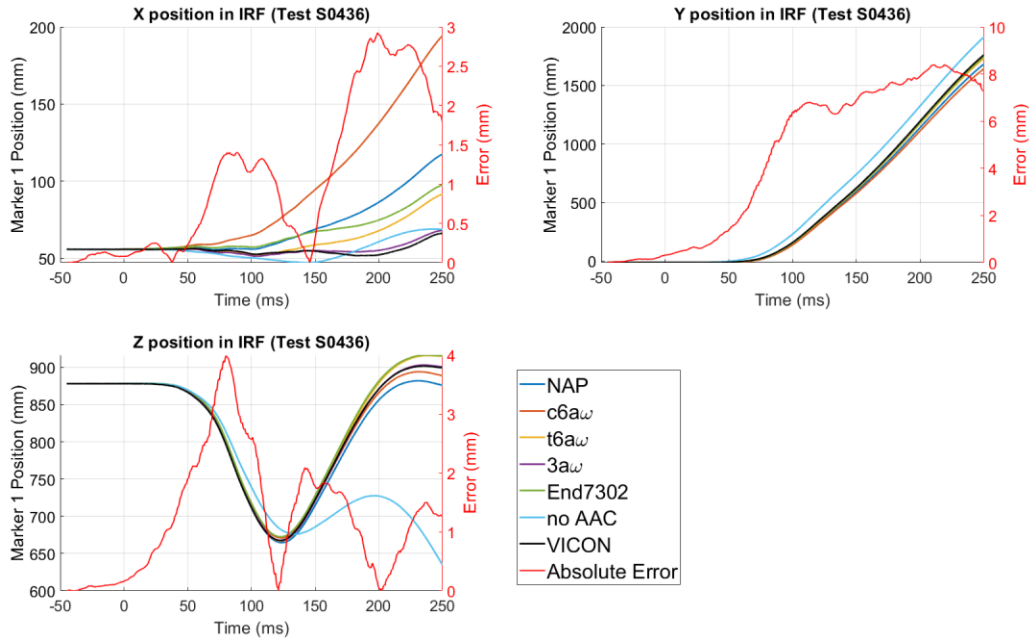
Figure 88. Test S0436 – Comparison between mocap and calculated trajectories for Marker 1, for five methods of obtaining AAC, for the CFC filter(s) that minimized Res_{err}. Absolute error between the reference trajectory and the trajectory computed with the use of the 3aω method (best prediction; Table 7) marked in red.
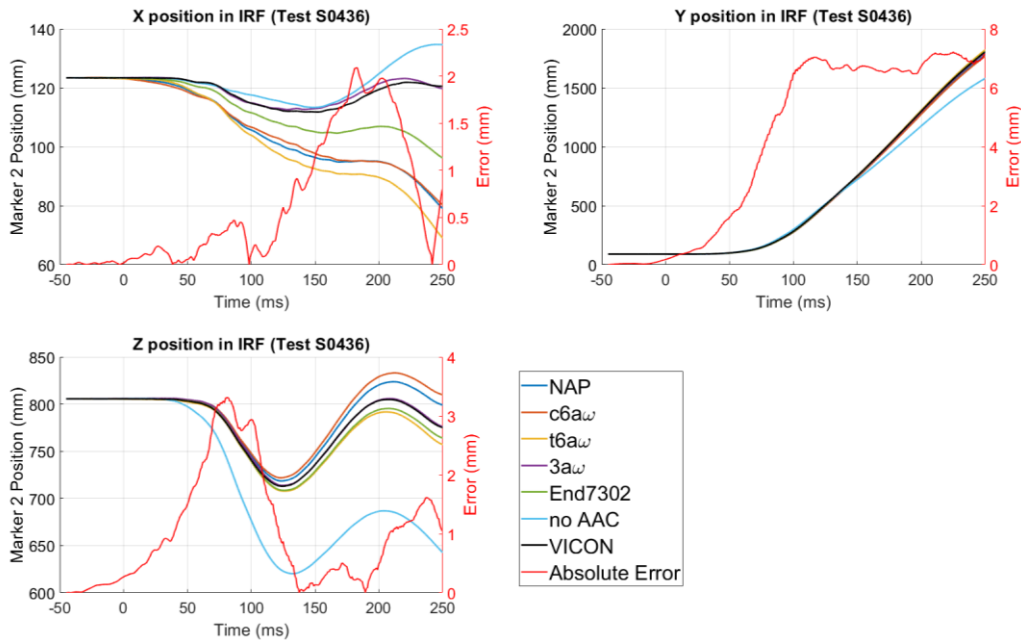
Figure 89. Test S0436 – Comparison between mocap and calculated trajectories for Marker 2, for five methods of obtaining AAC, for the CFC filter(s) that minimized Res_{err}. Absolute error between the reference trajectory and the trajectory computed with the use of the 3aω method (best prediction; Table 8) marked in red.
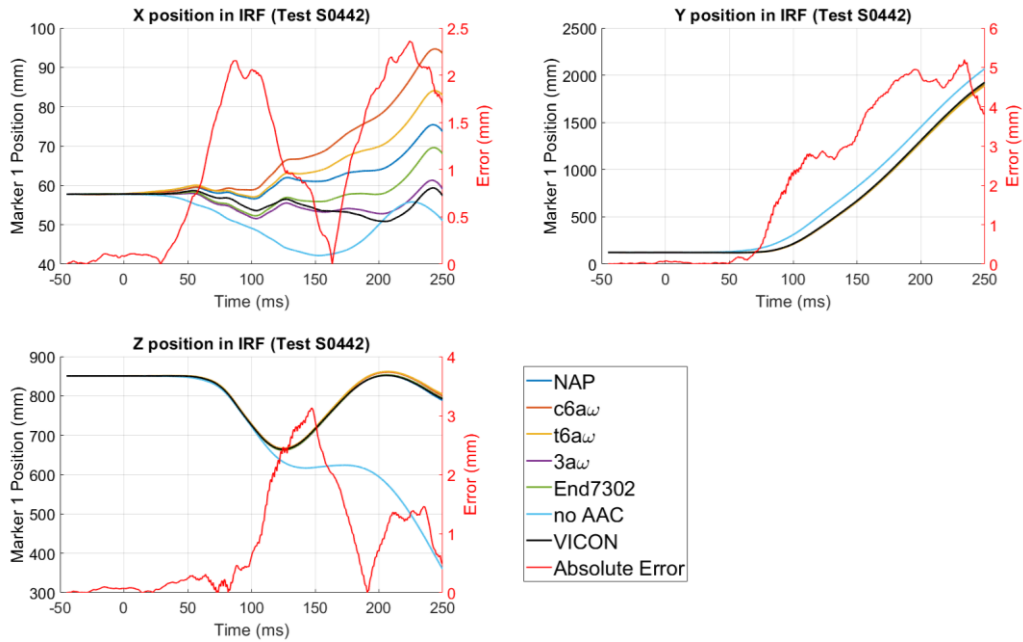
Figure 90. Test S0442 – Comparison between mocap and calculated trajectories for Marker 1, for five methods of obtaining AAC, for the CFC filter(s) that minimized Res_{err}. Absolute error between the reference trajectory and the trajectory computed with the use of the 3aω method (best prediction; Table 7) marked in red.
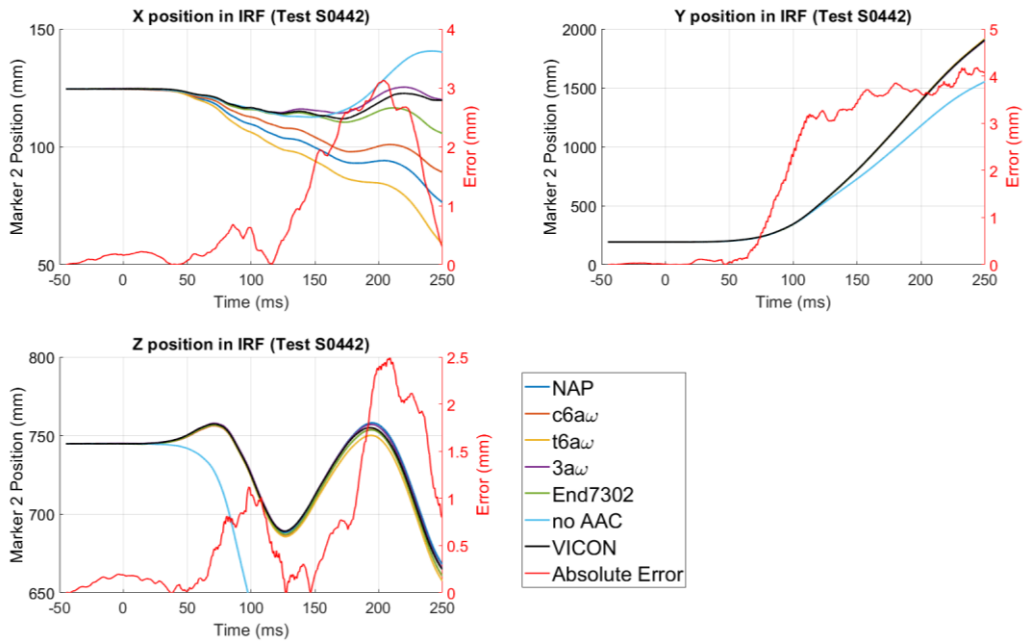
Figure 91. Test S0442 – Comparison between mocap and calculated trajectories for Marker 2, for five methods of obtaining AAC, for the CFC filter(s) that minimized Res_{err}. Absolute error between the reference trajectory and the trajectory computed with the use of the 3aω method (best prediction; Table 8) marked in red.

The trajectories computed with the *3aω* configuration not only matched the reference response well in shape, but also in magnitude (Table 11). The highest *diff_{max}* of 10.11 mm (less than half of an inch) was computed for Marker 1's Y trajectory in Test S0425. The smallest *diff_{max}* of 0.67 mm was recorded for Marker 1's X in Test S0433. *diff_{max}* for Marker 2 varied between 0.71 mm (Z component in Test S0425) to 7.22 mm (Y, Test S0436).

On average, the Y component had the highest deviation from the reference data among the three trajectory components. X and Z had comparable errors.

Table 11. diff_{max} for both tracked markers for the CFC filter that minimized Res_{err} in the trajectory computed with the 3aω method.

Test #	Marker 1 – $diff_{max}$ (mm)			Marker 2 – $diff_{max}$ (mm)		
	X	Y	Z	X	Y	Z
S0425	3.25	10.11	1.86	3.82	6.59	0.71
S0433	0.67	8.28	3.54	1.96	6.79	2.19
S0436	2.31	8.28	3.33	2.09	7.22	3.31
S0442	2.28	5.2	2.73	1.91	3.03	2.49

9.3.2 THOR ATD test

In the THOR sled test, the smallest value of Res_{err} was found when the CFC 60 filter was applied to the angular rate data used in the *3aω* method (Table 12). It is worth mentioning, though, that there is no substantial difference between Res_{err} calculated for the other three CFC filters along with the raw unfiltered data. The mean value for Res_{err} was 4.46 mm (comparing to the minimum of 4.19 mm from Table 12) with the standard deviation and the coefficient of variation equal to 0.29 mm and 6.5%, respectively. When the angular acceleration was not included in the trajectory calculation process, the error in the calculated trajectory grew substantially (up to approx. 340 mm).

Table 12. Res_{err} for the THOR marker for different CFC filters used. Minimum value of the Res_{err} metric indicated in green.

CFC filter	$Res_{err}(mm)$
CFC 60	4.19
CFC 180	4.21
CFC 600	4.72
CFC 1000	4.82
Raw	4.36
No AAC included	339.33

For the four used CFC filters along with the raw unfiltered data, the calculated trajectory matched closely the reference (from VICON) time-history for all three trajectory components (Figure 92). When the THOR marker was tracked utilizing AAC obtained from the angular rate filtered to CFC 60 (best prediction according to Res_{err}; Table 12), the maximum deviation (absolute error) from the mocap data was less than 5 mm in X, less than 6 mm for Y, and less than 4 mm for Z (Figure 92). When the local angular acceleration was not included in the trajectory

calculation process, the computed response (light blue curve in Figure 92) deviated noticeably from the reference.
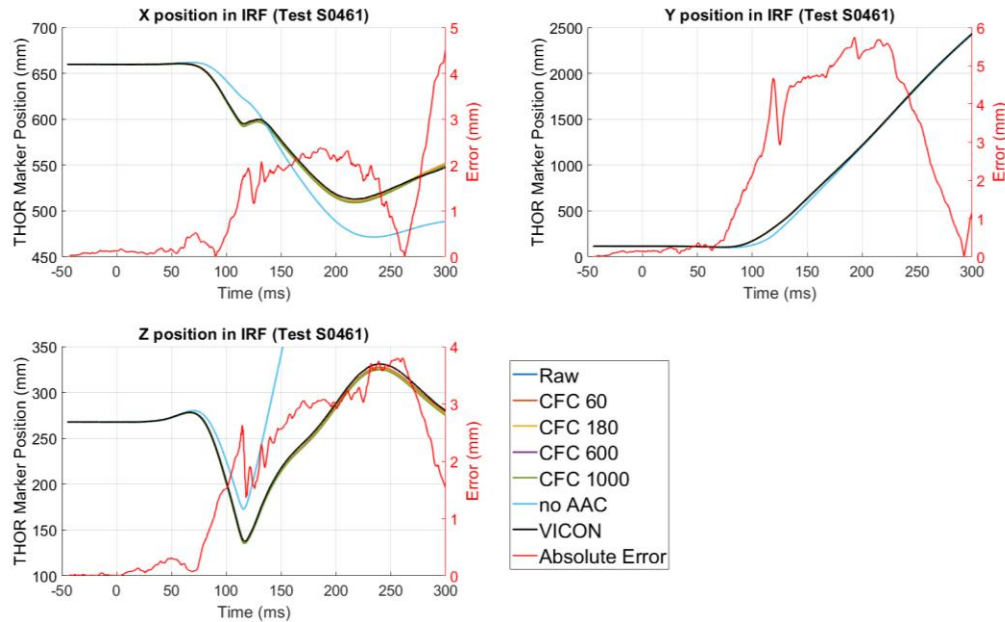
Figure 92. Test S0461 – Comparison between mocap and calculated trajectories for the THOR marker. In the legend: CFC filter used on the head local ARS data which was then utilized to obtain AAC and the absolute error between the reference trajectory and the trajectory calculated using ARS filtered at CFC 60.

Remark: Plots of angular acceleration calculated for ARS data filtered to CFC 60 can be found in APPENDIX L.

9.4 Discussion

Every sensor has an uncertainty associated with its reading. The reading can be affected, for example, by the error in sensitivity, by sensor misalignment due to fabrication and mounting tolerances, by the debias error, etc. (Sinz et al. 2015). While in *3aω* one needs to control for errors related only to three sensors, in NAP and both *6aω* methods the uncertainty in nine sensors (and their measured positions) needs to be taken into account. It is believed that that combined uncertainty might have been responsible for the lower performance of NAP, *c6aω* and *t6aω* in computing 3D trajectories when compared to the AAC methods that require smaller number of sensors.

The effect of optimization of the body's initial orientation on the five methods of obtaining AAC was not the main focus of this study and, thus, it was not quantified here. It is hypothesized, though, that due to the optimization process performed prior to the AAC analysis, the errors that could potentially affect the direct measurement of body angular velocity were mostly accounted for. It is assumed that without that step, the 3D trajectories computed – with the use of the *3aω* method – in the Simplified Head and the THOR ATD tests would be affected by measurement errors more substantially and would not match the reference response that well.

The filter class applied to the data utilized to obtain body's local angular acceleration, within the same AAC method did not affect the calculated trajectory in a meaningful way. The filter selection might have a much greater effect, though, when the magnitude of AAC is the main focus of the analysis. Through filtering that magnitude can be affected (cf. Kang et al. 2015) and, in result, influence, for example, a metric that is based on the maximum value of AAC (e.g. *UBrIC* proposed by Gabler et al. 2018).

Based on the performed analysis, to compute accurate trajectories with the use of *3aω*, the CFC 60 or CFC 180 filter should be utilized for the head's angular rate measured during a crash. However, a blank selection of those filters is not appropriate, as the frequency content of the measured signal is case specific and, thus, in many situations CFC 60 or CFC 180 might pass an inappropriate amount of noise or remove important information from the analyzed data.

9.5 Conclusions

The chapter investigated the use of different methods of obtaining angular acceleration utilized in the process of 3D trajectory calculation. Five different techniques were analyzed. In addition, the sensitivity of the calculated trajectory to the change in the filter class used on the AAC input data (either acceleration or angular rate) was evaluated.

The main conclusions of this study are as follows:

- In the four Simplified Head tests, after optimization of the initial orientation of a tracked body, the smallest deviation from the reference data was observed in cases where the *3aω* method was utilized to compute body's local angular acceleration (Table 7 and Table 8).

- The trajectories computed with the *3aω* configuration matched the mocap reference data well in shape and in magnitude in all five considered test cases. The highest absolute difference between the reference and calculated trajectories (across the five tests) was 10.11 mm (less than half of an inch; Table 11 and Figure 92).

- Relatively small values of standard deviation seen across the five methods of obtaining local angular acceleration (Table 9 and Table 10) suggest that, in the analyzed test configurations, the computed trajectories (within the same method of determining AAC) were not highly sensitive to the change in filtering of the AAC method input.

- While the *3aω* method generated trajectories most closely matching the reference data, those trajectories were also characterized with the highest relative variability (coefficient of variation up to approx. 40%) among the five methods of obtaining AAC.

- The variation in the calculated trajectory was higher due to the choice in the method used to obtain AAC than due to the filter class used on the input data to that method.

10. ERROR EFFECTS ANALYSIS

The aim of Chapter 10 was to evaluate the effect of sensor characteristics (e.g. noise level), sensor errors (e.g. error in sensitivity), test measurement inaccuracies (e.g. error in the measurement of initial orientation), and error interactions on trajectories computed with the use of data from IMUs. First, different error types and bounds for these errors were identified (Section 10.1). Next, a simplified analytical analysis was performed to better understand the propagation of the errors in time (Section 10.2). In Section 10.3, guided by the analytical investigation, numerical analyses were carried out a) to quantify the effect of individual errors on the IMU-based trajectory estimation, and b) to identify main interaction between these errors. In Section 10.4, an analytical relationship that allows for identification of a faulty sensor, based on addition of one or two redundant sensors, was presented.

10.1: Identification of common error types and their bounds

10.1.1 Error types and bounds

3D component trajectories calculated using inertial measurements can be affected by multiple types of signal errors or uncertainties associated with test procedure measurements. Those errors are usually classified into the following four categories: misalignment and mislocation, miscalibration, noise, and debias (also known as zero-bias) error (cf. Bussone et al. 2010, cf. Sinz et al. 2015).

For the purpose of this dissertation, seven error types were investigated (Table 13). In addition, eleven upper and lower, physically possible, resulting from a regular equipment use in a lab environment, error-bounding values were identified. The methods of determining the error boundaries are described in the following parts of Section 10.1.

Table 13. Error bounds for sensor error and test measurement inaccuracies used in the error effects analysis.

#	Error type	Sensor type	Component	Bounds
1	**Accelerometer seismic mass CG position (in body local coordinate frame)**	Accelerometer	X Y Z	**± 1 mm**
2	**Head initial orientation (in inertia reference frame)**	Not applicable	Yaw Pitch Roll	**± 1 deg**
3	**Head CG initial position (in inertia reference frame)**	Not applicable	X Y Z	**± 2.5 mm**

4	**Sensitivity error**	Accelerometer	X	
			Y	**± 4%**
			Z	
		Angular Rate Sensor	X	
			Y	**± 1%**
			Z	
5	**Debias error**	Accelerometer	X	
			Y	**± 2g**
			Z	
		Angular Rate Sensor	X	
			Y	**± 50 deg/sec**
			Z	
6	**Noise Level (SF)**	Accelerometer	X	
			Y	**0 - 2**
			Z	
		Angular Rate Sensor	X	
			Y	**0 - 50**
			Z	
7	**Sensor angle misalignment**	Accelerometer	X	
			Y	**0 – 3 deg**
			Z	
		Angular Rate Sensor	X	
			Y	**0 – 1 deg**
			Z	

10.1.2 Accelerometer seismic mass CG position in body local coordinate frame (BF)

The sensor block used during sled testing with the Simplified Head (SH) structure was 3D scanned multiple times to record the location and the orientation of the linear accelerometers relative to the head structure. Between the scans, different accelerometers were taken off and then attached back to the sensor block to introduce position variability due to sensor fabrication and mounting tolerances.

In the ideal situation the center of gravity (CG) of an accelerometer seismic mass would be at an offset from the origin of the local coordinate system associated with the sensor block only in the direction in which the accelerometer measures the acceleration (see Chapter 9 for more detailed description). As mentioned before, it is rarely a case due to fabrication and mounting tolerances. Additionally, the measured sensor position can contain an error resulting from the accuracy of the position measurement itself.

During SH testing the maximum offset in the direction other than along the accelerometer sensing (main) axis was found to be 0.51 mm. That value was then rounded up to 1 mm and used as the seismic mass CG position error upper bound for further analysis. The error lower bound was set to -1 mm. The same error bounds were utilized for all three coordinates of the three accelerometers ($\boldsymbol{\rho}$ from Eq. 1.4) used in this study.

10.1.3 Initial orientation in inertial reference frame (IRF)

To establish the bounds for the error in the head initial orientation in the inertial reference frame (IRF), the local coordinate frame of the THOR ATD head was determined in two different ways:

- "from CAD", where three reference landmarks on the dummy head were digitized and used along with the THOR ATD CAD model (NHTSA 2016);
- "from CMM", where the initial orientation was determined based only on points digitized on three orthogonal surfaces of the head sensor block.

The "from CMM" points were taken at the same time as the three reference head landmarks ("from CAD" points) for direct comparison between the two methods.

In the "from CAD" approach, first, the Left CG, Right CG, and Nasion (NS) points (Figure 93) were digitized in the global coordinate frame. Based on the Left and Right CG landmarks the head CG was found as the midpoint between the two points. Next, a temporary vector $Y_{local,temp}$ was established between the head CG and the Right CG (Figure 93).
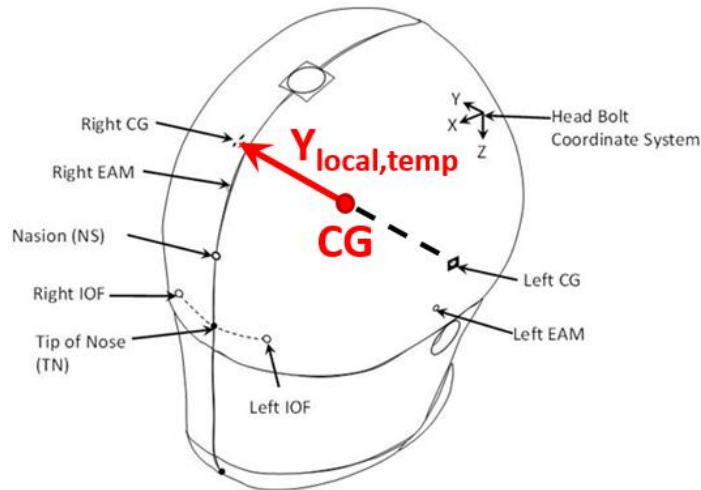
Figure 93. THOR Head reference landmarks with head CG and temporary Y axis marked in red. Baseline figure taken from NHTSA 2015a.

It was assumed that both, the NS and head CG points, were on the midsagittal plane of the head. From the CAD model of the assembly the angle between the horizontal line (projection of the top surface of the head sensor block to the midsagittal plane) and the vector connecting the head CG to the NS point was determined (Figure 94). That vector was then rotated down by 7.6762 deg to establish the X_{local} axis (Figure 95a). Next, Z_{local} axis was found as the cross product of X_{local} and $Y_{local,temp}$ vectors. To correct for orthogonality, Y_{local} was re-calculated as the cross product of the Z_{local} and X_{local} axes. As the final step, all three vectors were normalized by their length to obtain three unit vectors defining the initial local-to-global rotation matrix, i.e. the head initial orientation in the global coordinate frame (Table 14).
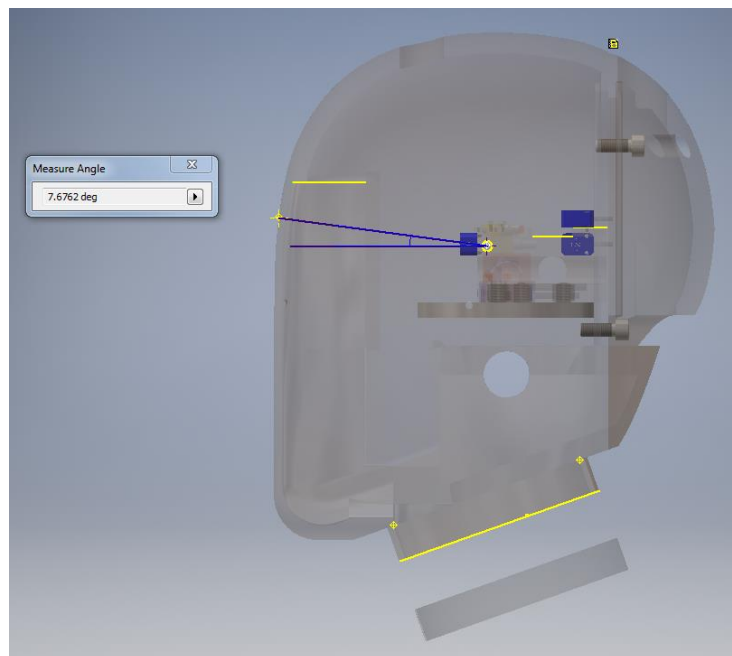
Figure 94. THOR Head CAD model (NHTSA 2016).

109

The local axes of the head were consistent with the SAE J211 standard (SAE 1995) with X_{local} pointing from the back to the front, Y_{local} from the left hand side to the right hand side of the head, and Z_{local} from top to bottom (Figure 95b).
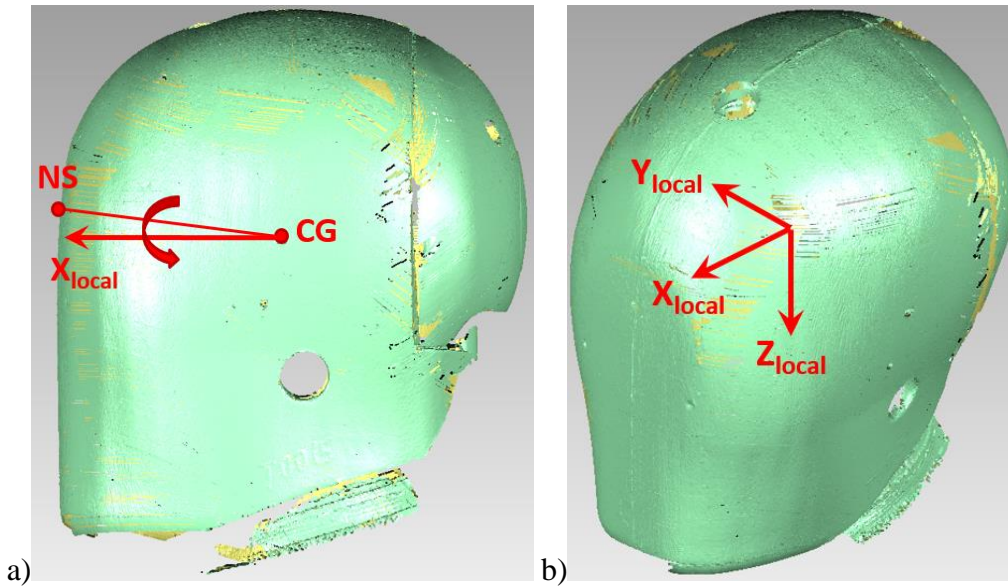
Figure 95. THOR Head: a) X_{local} axis definition; b) local coordinate system definition.

In the "from CMM" approach, points were digitized on three orthogonal flat surfaces of the head sensor block (Figure 96).
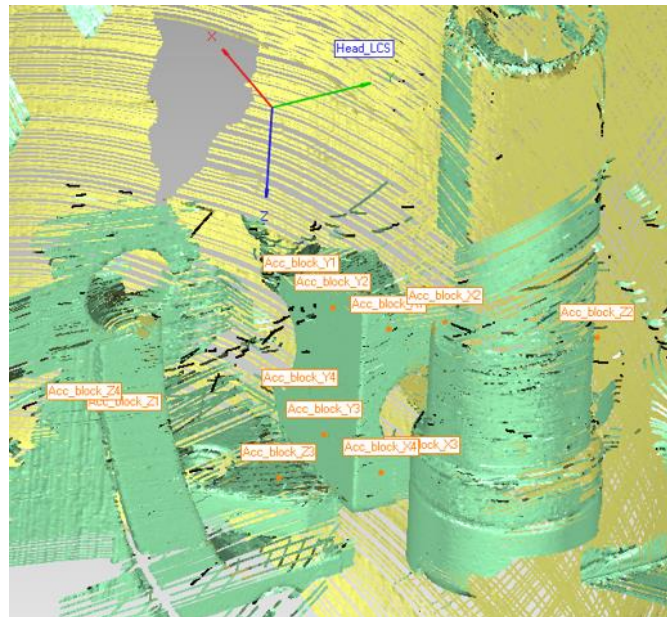
Figure 96. Points digitized on three surfaces of the head sensor block.

Four points for each plane (12 points in total) were selected. The four points were used to define two vectors. Assuming that those two vectors were in the same plane, they were utilized to calculate the plane normal. Next, the normal vector was divided by its length to find a unit vector aligned with one of the head local frame axes. This procedure was performed for all three

orthogonal surfaces of the sensor block, accounting for vector mutual orthogonality. As the final step, the three unit vectors were combined together to construct the initial local-to-global rotation matrix defining the head initial orientation in the global coordinate frame (Table 14).

Based on the two initial rotation matrices ("from CAD" and "from CMM"), two sets of the head initial Euler angles were calculated (Table 14 bottom).

Table 14. Initial local-to-global rotation matrices (top) and Euler angles (bottom) found in two different ways.

from CAD			from CMM		
X_{local}	Y_{local}	Z_{local}	X_{local}	Y_{local}	Z_{local}
0.982878	0.141385	-0.11815	0.984416	0.138711	-0.10809
-0.12711	0.984516	0.120714	-0.12691	0.985869	0.109345
0.133391	-0.10363	0.985631	0.121733	-0.09392	0.988109
Yaw (deg)	Pitch (deg)	Roll (deg)	Yaw (deg)	Pitch (deg)	Roll (deg)
8.19	6.79	6.98	8.02	6.21	6.31

Next, the absolute difference between the two sets was found (Table 15). The highest difference of 0.67 degree was observed for the Roll angle. That value was then rounded up to 1 degree and used as the initial orientation error upper bound for further analysis. The error lower bound was set to -1 degree. The same error bounds were utilized for all three Euler angles.

Table 15. Absolute difference between the Euler angles found using the "from CAD" and "from CMM" approaches.

Absolute difference		
Yaw (deg)	Pitch (deg)	Roll (deg)
0.17	0.58	**0.67**

10.1.4 Head CG initial position in inertia reference frame (IRF)

Left CG and Right CG points (Figure 97) were digitized in the inertial reference frame (IRF). Based on those two landmarks the head CG was found as the midpoint between the two points.
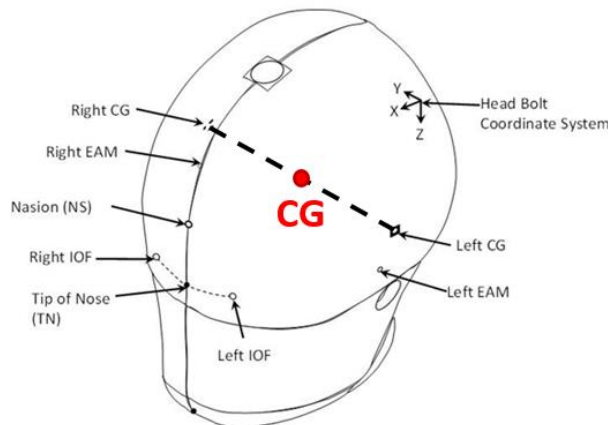
Figure 97. Head CG found using THOR Head landmarks. Baseline figure taken from NHTSA 2015a.

Next, a 3D scan of the stock THOR head sensor block (Figure 98a) was aligned with the head 3D scan (Figure 98b) using the same geometric features available in both scans. The head scan contained information about the THOR head landmarks from Figure 97 utilized in the process of finding the head CG.

a)   b)
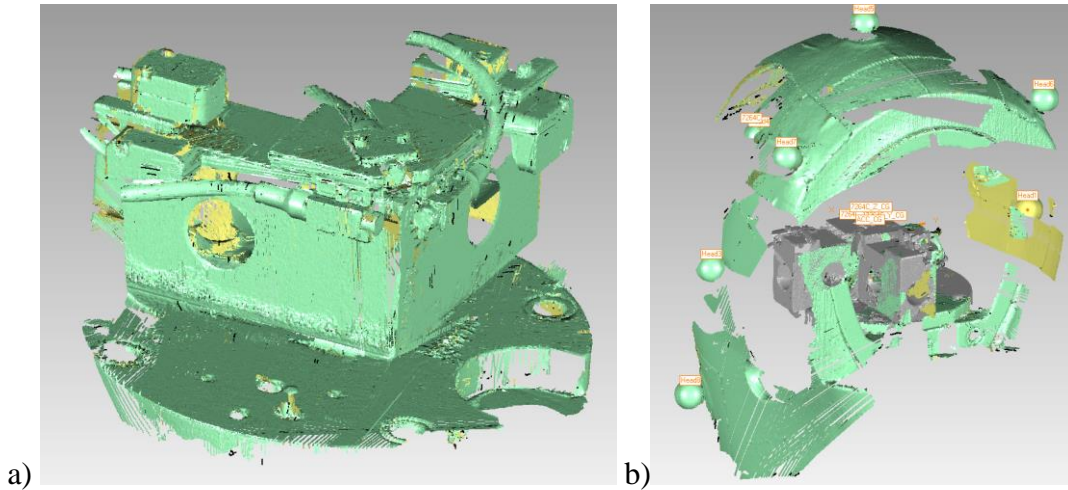
Figure 98. 3D scans of: a) THOR head stock sensor block; b) THOR Head (green) and THOR sensor block (grey) aligned together.

In the 3D scan of the sensor block the measurement center (MC) for the three accelerometers was identified (Figure 99).
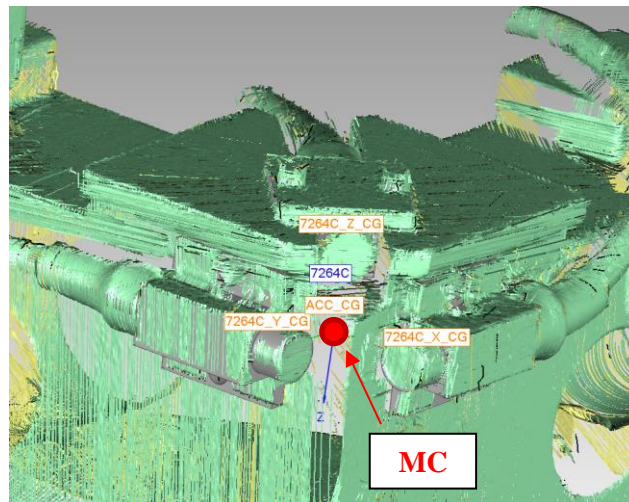
Figure 99. Measurement center for the three accelerometers (marked in red).

In the ideal case, the measurement center MC would be coincident with the head CG. To verify that the two points were at the same location the distance between both, MC and the CG landmarks (which were put in the same 3D scan) was measured and recorded (Table 16).

Table 16. Absolute difference between the head CG and the accelerometer measurement center.

Head CG (from CMM) vs ACC MC (from 3D scans)	
Component (SAE J211)	**Difference (mm)**
X	2.2
Y	0.7
Z	0.6
Resultant	**2.35**

The resultant difference between the head CG and the accelerometer MC was found to be 2.35mm. That value was then rounded up to 2.5mm and used as the head CG initial error upper bound for further analysis. The error lower bound was set to -2.5mm. The same error bounds were utilized for all three head coordinates.

10.1.5 Sensitivity error

Sensitivity data from calibration sheets available at the University of Virginia Center for Applied Biomechanics for different types of accelerometers and angular rate sensors were gathered and analyzed. Calibration sheets for multiple sensor models were used. The data were taken into account only if a sensor was calibrated more than once. Next, the percentage difference in sensitivity (*%diff*) was found based on Eq. 10.1:

$$\%diff = \frac{|first_{calib} - last_{calib}|}{first_{calib}} * 100\% \tag{10.1}$$

where *$first_{calib}$* – sensitivity as received from manufacturer when sensor sold as new, *$last_{calib}$* – sensitivity from the most recent calibration sheet.

The maximum *%diff* identified for different sensor types were as follows:

Accelerometers:

- Endevco Meggitt Sensing Systems 7264B-500g: 1.05%
- Endevco Meggitt Sensing Systems 7264C-2000g: 0.47%
- Endevco Meggitt Sensing Systems 7290E-30g: 0.25%
- Measurement Specialties (MSI) 64B-2000g: 0.81%
- Diversified Technical Systems (DTS) 6DX PRO-2000g: 3.9%

Angular Rate Sensors:

- DTS ARS PRO / DTS 6DX PRO: 0.24% / 0.27%
- IES 3103-600 3-Axis Gyro Sensor: 0.77%

The maximum *%diff* found within the same sensor type (either accelerometer or angular rate sensor) was rounded up to the closest integer number and that value was then used as the sensitivity error bound in the error effects analysis. The error upper bound for the accelerometer was determined to be 4%, for the angular rate sensor: 1%. The error lower bound was -4% and -1%, respectively.

10.1.6 Debias error

Based on the pre-trigger data from different sensors used on the Simplified Head tests (example shown in Figure 100), for all three axes, the <u>maximum absolute</u> noise level was identified: one for an accelerometer (1.75g) and one for an angular rate sensor (49 deg/s). Those two values were then rounded up to 2g and 50 deg/s, respectively, and used as the error upper bounds. The error lower bounds were set to -2g (ACC) and -50 deg/s (ARS).

It is worth mentioning here that "one-point" debiasing is rarely a case and in terms of the magnitude of an introduced error, it should be treated as the worst-case scenario.
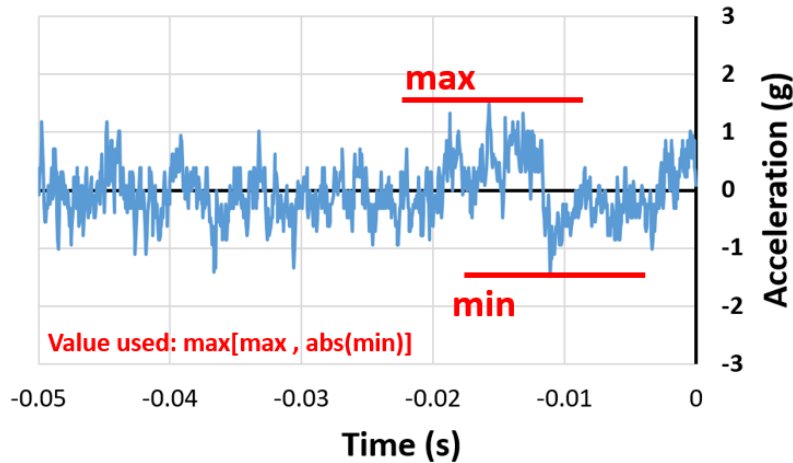
Figure 100. Pre-trigger data used to determine debias error bounds.

10.1.7 Noise level

For the analysis of the noise level effect, as the first step, the pre-trigger data for accelerometers and angular rate sensors used on the Simplified Head tests were normalized individually by their maximum absolute value (see Figure 100 for details). Next, the pre-trigger data were multiplied by a scaling factor (SF) and then copied multiple times along the noiseless sensor response as described in Section 10.3.3.

The lower bound for SF was assumed to be zero (no noise). The upper bound for the debias error (see Section 10.1.6) was utilized as the upper value for SF: 2 for the accelerometers, and 50 for the angular rate sensors.

10.1.8 Sensor angle misalignment

Due to fabrication imperfections external surfaces of a sensor might not stay orthogonal to each other. When a sensor with skewed surfaces is mounted on a body, the sensor sensing axis might unknowingly be pointing away from the axis along (around) which the measurement should be taken (Figure 101). More importantly, because of the mounting angle misalignment the measured signal would be of a smaller magnitude than the signal obtained with a sensor mounted correctly.

θ - misalignment angle
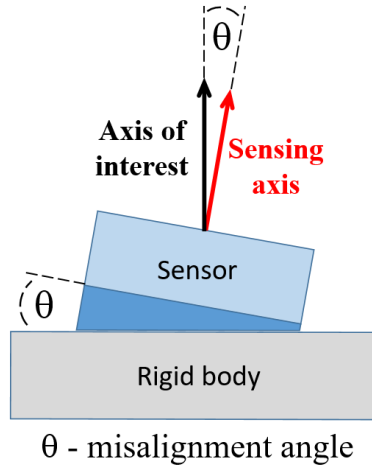
Figure 101. Sensor with skewed surfaces mounted on a body (dimensions not in scale).

To identify error bounds of angle misalignment for linear accelerometers (ACC) and angular rate sensors (ARS) used in this dissertation, dimensions (height, width, and length) for seven different sensors employed during Simplified Head or THOR testing, and their corresponding fabrication tolerances (as given by the manufacturers), were utilized (Table 17).

Table 17. Sensors and their fabrication tolerances.

Sensor	Fabrication tolerance (mm)	Height (mm)	Width (mm)	Length (mm)
Endevco Meggitt Sensing Systems 7264B (ACC)	±0.254	4.70	10.16	12.19
Endevco Meggitt Sensing Systems 7264C (ACC)	±0.254	5.13	10.16	10.16
Endevco Meggitt Sensing Systems 7265A (ACC)	±0.254	7.75	16.00	11.94
Endevco Meggitt Sensing Systems 7290E (ACC)	±0.508	3.18	21.59	25.40
Diversified Technical Systems (DTS) 6DX-PRO (ACC + ARS)	±0.0508	14.48	19.05	19.05
DTS ARS Pro (ARS)	±0.0508	7.62	10.16	14.61
Measurement Specialties (MSI) 64B (ACC)	±0.0762	4.70	10.16	12.19

In Figure 102 two examples were shown of how inaccuracies in fabrication could potentially affect the sensor surface orthogonality. Both examples assumed the worst-case scenario ("+ fabrication tolerance" on one side/end of the sensor and "- fabrication tolerance" on the other side) for one of the dimensions.
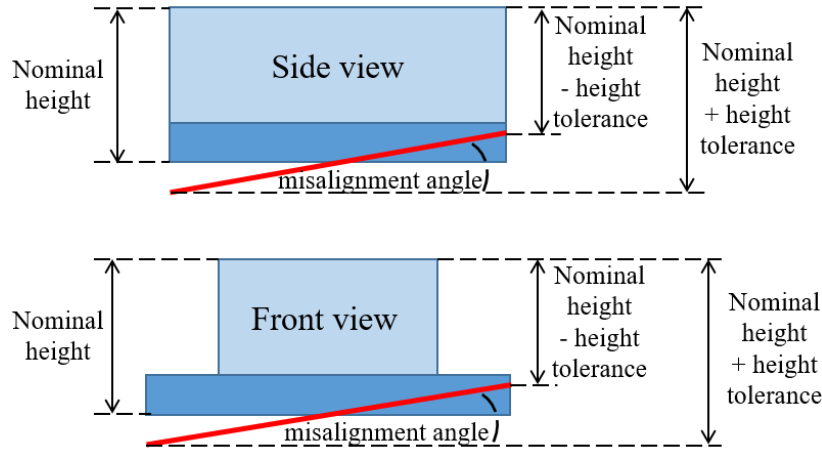
Figure 102. Example of a skewed surface of a sensor (marked in red) due to fabrication inaccuracies for the sensor height (dimensions not in scale).

Assuming that the height, width, and length of the same sensor were affected by fabrication inaccuracies, through a geometric analysis utilizing the maximum values of the dimension tolerances, it was determined that the largest possible misalignment angle for an accelerometer would be 2.94 deg, and for an angular rate sensor: 0.58 deg. Those two values were rounded up to 3 deg and 1 deg, respectively, and used as the sensor misalignment error upper bounds for further analysis. The lower bounds were set to 0 (i.e. zero deviation from the sensor nominal dimensions and sensor mounted perfectly).

10.2: Investigation of the effect of sensor and measurement errors based on analytical equations describing motion of a rigid body

The goal of this subsection was to perform an analytical analysis that would focus on understanding how different error types in sensor readings propagate through the calculation process of body's global position. Due to the non-linear nature of the rotation matrix R in a case (called from here on "general case") when the tracked body translates and rotates at the same time, solving Eq. 1.1 (double integration of global acceleration of the tracked body) is non-trivial, and thus, the effect of sensor-related errors on the resulting orientation and position cannot be easily predicted analytically. Since the goal of this task was to assess these effects through an analytical investigation, a three-step analysis was performed, varying the mathematical complexity of the equation used to describe the global linear acceleration of the analyzed body.

The subsection is organized as follows. Section 10.2.1 describes the expansion of Eq. 1.4 (local linear acceleration of a rigid body based on sensor data) from the matrix into the component form. Section 10.2.2 introduces a model of a sensor output with two error terms (one scaling and one additive) added. Section 10.2.3 presents the steps that were performed to define erroneous kinematics data used in the analytical investigation performed in this study. Section 10.2.4 defines equations of different mathematical complexity ("test cases") for the global acceleration of the tracked body. In Section 10.2.4, three test cases are discussed: a) a simplified case where linear acceleration, as defined by the component form from Section 10.2.1, is equivalent to body's global acceleration, b) a case where local acceleration vector is multiplied by a constant rotation matrix

116

of the tracked body, c) the general case. In Section 10.2.5, the analytical analysis for the simplified case and the case with the constant rotation matrix is presented. In Section 10.2.6, the general case is discussed. Concluding remarks are provided in Section 10.2.7.

10.2.1 Component form of rigid body acceleration equation

Eq. 10.2 describes the expansion of Eq. 1.4 (linear acceleration of the origin of a rigid body based on kinematics data recorded at point p belonging to that body) from the matrix to the component form:

$$a_{ox} = a_{px} - \omega_y(\rho_y\omega_x - \rho_x\omega_y) - \omega_z(\rho_z\omega_x - \rho_x\omega_z) - \rho_z\alpha_y + \rho_y\alpha_z = a_{px} + \rho_x\omega_y^2 + \rho_x\omega_z^2 - \rho_y\omega_x\omega_y - \rho_z\omega_x\omega_z - \rho_z\alpha_y + \rho_y\alpha_z \qquad (10.2a)$$

$$a_{oy} = a_{py} + \omega_x(\rho_y\omega_x - \rho_x\omega_y) - \omega_z(\rho_z\omega_y - \rho_y\omega_z) + \rho_z\alpha_x - \rho_x\alpha_z = a_{py} + \rho_y\omega_x^2 + \rho_y\omega_z^2 - \rho_x\omega_x\omega_y - \rho_z\omega_y\omega_z + \rho_z\alpha_x - \rho_x\alpha_z \qquad (10.2b)$$

$$a_{oz} = a_{pz} + \omega_x(\rho_z\omega_x - \rho_x\omega_z) + \omega_y(\rho_z\omega_y - \rho_y\omega_z) - \rho_y\alpha_x + \rho_x\alpha_y = a_{pz} + \rho_z\omega_x^2 + \rho_z\omega_y^2 - \rho_x\omega_x\omega_z - \rho_y\omega_y\omega_z - \rho_y\alpha_x + \rho_x\alpha_y \qquad (10.2c)$$

where a_{oi} – linear acceleration components at the origin of the body local coordinate frame, a_{pi} – linear acceleration components at point p, ρ_i – components of the position vector of point p in the body local frame, ω_i and α_i – local coordinate system components describing the body's local angular velocity and local angular acceleration, i = X, Y, Z.

10.2.2 Model of a sensor with measurement errors included

As it was already mentioned in Section 10.1, accelerometer (both, linear and angular) as well as angular rate sensor readings can be affected by different types of errors (Table 13). Guided by previous research (cf. Savage 2002), those errors were separated into two groups:

- errors that scale the sensor reading (e.g. error in sensor sensitivity). These errors will be represented in this dissertation as a scaling factor **b**,
- errors that add an offset to the reading (e.g. error in the senor debias value). These errors will be represented in this study as an additive term **c**.

Using **b** and **c**, the senor output, affected by the measurement errors, was modeled as Eq. 10.3:

$$sensor_{output}(t) = b * sensor_{reading}(t) + c \qquad (10.3)$$

For the purpose of this analysis, it was assumed that both, **b** and **c** were constant in time.

10.2.3 Description of the analytical data set

To analyze the effect of different error types on the calculated trajectory analytically, Eq. 10.3 was used to define time histories for kinematics measurements obtained from three linear accelerometers and three angular rate sensors attached to the tracked body. To each of the six sensors, a set composed of a scaling factor **b** and an additive term **c** was assigned. To distinguish between sensor types and sensor axes, the error terms for the accelerometers had a subscript acc_i (where i = X, Y, Z). For the angular rate sensors the subscript was ars_i (where i = X, Y, Z). Next, the kinematics measurements (with the error terms included) were substituted into Eq. 10.2. That equation was then transformed to the global reference frame (using the rotation matrix **R**; see

Chapter 8) to obtain the body's global acceleration and then double integrated in time to compute 3D component trajectories of the tracked body.

10.2.4 Analytical analysis – methods

To better understand how the error terms propagate through time integration, first, Eq. 10.2 (with the erroneous sensor outputs introduced) was double integrated in time in a simplified scenario where body's local acceleration was assumed to be equivalent to body's global acceleration and body's local angular velocity was allowed to vary in time. In the following analysis, a more complex case was considered. Eq. 10.2 was multiplied by a constant rotation matrix $\boldsymbol{R}$ and then double integrated. In addition, in this case, local angular velocity was time dependent. After the two analyses were completed, the implications of the rotation matrix $\boldsymbol{R}$ varying in time were discussed more in detail.

10.2.5 Error propagation – results

Simplified case: In this section, it was assumed that the local acceleration of the tracked body was equivalent to body's global acceleration. In that situation, the transformation of Eq. 10.2 to the global frame was not required and the double integration (in time) of Eq. 10.2 (with the error terms included; see APPENDIX N) directly produced the components of the global position of the tracked body (Eq. 10.4):

$$
\begin{aligned}
pos_{ox}(t) = &\ \boldsymbol{b_{acc\_x}} A_{px}(t) + \boldsymbol{c_{acc\_x}} \frac{t^2}{2} \\
&+ \rho_x \left(\boldsymbol{b_{ars\_y}^2} W_{y^2}(t) + \boldsymbol{b_{ars\_z}^2} W_{z^2}(t) + 2\left(\boldsymbol{b_{ars\_y}} \boldsymbol{c_{ars\_y}} W_y(t) + \boldsymbol{b_{ars\_z}} \boldsymbol{c_{ars\_z}} W_z(t) \right) \right. \\
&\left. + \left(\boldsymbol{c_{ars\_y}^2} + \boldsymbol{c_{arc\_z}^2} \right) \frac{t^2}{2} \right) \\
&- \rho_y \left(\boldsymbol{b_{ars\_x}} \boldsymbol{b_{ars\_y}} W_{xy}(t) + \boldsymbol{b_{ars\_x}} \boldsymbol{c_{ars\_y}} W_x(t) + \boldsymbol{b_{ars\_y}} \boldsymbol{c_{ars\_x}} W_y(t) - \boldsymbol{b_{aac\_z}} \Phi_z(t) \right. \quad (10.4a) \\
&\left. + \left(\boldsymbol{c_{ars\_x}} \boldsymbol{c_{ars\_y}} - \boldsymbol{c_{aac\_z}} \right) \frac{t^2}{2} \right) \\
&- \rho_z \left(\boldsymbol{b_{ars\_x}} \boldsymbol{b_{ars\_z}} W_{xz}(t) + \boldsymbol{b_{ars\_x}} \boldsymbol{c_{ars\_z}} W_x(t) + \boldsymbol{b_{ars\_z}} \boldsymbol{c_{ars\_x}} W_z(t) + \boldsymbol{b_{aac\_y}} \Phi_y(t) \right. \\
&\left. + \left(\boldsymbol{c_{ars\_x}} \boldsymbol{c_{ars\_z}} + \boldsymbol{c_{aac\_y}} \right) \frac{t^2}{2} \right)
\end{aligned}
$$

$$
\begin{aligned}
pos_{oy}(t) = &\ \boldsymbol{b_{acc\_y}} A_{py}(t) + \boldsymbol{c_{acc\_y}} \frac{t^2}{2} \\
&- \rho_x \left(\boldsymbol{b_{ars\_x}} \boldsymbol{b_{ars\_y}} W_{xy}(t) + \boldsymbol{b_{ars\_x}} \boldsymbol{c_{ars\_y}} W_x(t) + \boldsymbol{b_{ars\_y}} \boldsymbol{c_{ars\_x}} W_y(t) + \boldsymbol{b_{aac\_z}} \Phi_z(t) \right. \\
&\left. + \left(\boldsymbol{c_{ars\_x}} \boldsymbol{c_{ars\_y}} + \boldsymbol{c_{aac\_z}} \right) \frac{t^2}{2} \right) \\
&+ \rho_y \left(\boldsymbol{b_{ars\_x}^2} W_{x^2}(t) + \boldsymbol{b_{ars\_z}^2} W_{z^2}(t) + 2\left(\boldsymbol{b_{ars\_x}} \boldsymbol{c_{ars\_x}} W_x(t) + \boldsymbol{b_{ars\_z}} \boldsymbol{c_{ars\_z}} W_z(t) \right) \right. \quad (10.4b) \\
&\left. + \left(\boldsymbol{c_{ars\_x}^2} + \boldsymbol{c_{arc\_z}^2} \right) \frac{t^2}{2} \right) \\
&- \rho_z \left(\boldsymbol{b_{ars\_y}} \boldsymbol{b_{ars\_z}} W_{yz}(t) + \boldsymbol{b_{ars\_y}} \boldsymbol{c_{ars\_z}} W_y(t) + \boldsymbol{b_{ars\_z}} \boldsymbol{c_{ars\_y}} W_z(t) - \boldsymbol{b_{aac\_x}} \Phi_x(t) \right. \\
&\left. + \left(\boldsymbol{c_{ars\_y}} \boldsymbol{c_{ars\_z}} - \boldsymbol{c_{aac\_x}} \right) \frac{t^2}{2} \right)
\end{aligned}
$$

$$pos_{oz}(t) = \boldsymbol{b_{acc\_z}}A_{pz}(t) + \boldsymbol{c_{acc\_z}}\frac{t^2}{2}$$

$$- \rho_x \left(\boldsymbol{b_{ars\_x}b_{ars\_z}}W_{xz}(t) + \boldsymbol{b_{ars\_x}c_{ars\_z}}W_x(t) + \boldsymbol{b_{ars\_z}c_{ars\_x}}W_z(t) - \boldsymbol{b_{aac\_y}}\Phi_y(t) \right.$$

$$\left. + \left(\boldsymbol{c_{ars\_x}c_{ars\_z}} - \boldsymbol{c_{aac\_y}} \right)\frac{t^2}{2} \right)$$

$$- \rho_y \left(\boldsymbol{b_{ars\_y}b_{ars\_z}}W_{yz}(t) + \boldsymbol{b_{ars\_y}c_{ars\_z}}W_y(t) + \boldsymbol{b_{ars\_z}c_{ars\_y}}W_z(t) + \boldsymbol{b_{aac\_x}}\Phi_x(t) \right. \quad (10.4c)$$

$$\left. + \left(\boldsymbol{c_{ars\_y}c_{ars\_z}} + \boldsymbol{c_{aac\_x}} \right)\frac{t^2}{2} \right)$$

$$+ \rho_z \left(\boldsymbol{b^2_{ars\_x}}W_{x^2}(t) + \boldsymbol{b^2_{ars\_y}}W_{y^2}(t) + 2\left(\boldsymbol{b_{ars\_x}c_{ars\_x}}W_x(t) + \boldsymbol{b_{ars\_y}c_{ars\_y}}W_y(t) \right) \right.$$

$$\left. + \left(\boldsymbol{c^2_{ars\_x}} + \boldsymbol{c^2_{arc\_y}} \right)\frac{t^2}{2} \right)$$

where t – time, b_{rrr_u} – scaling term, c_{rrr_u} – additive term, subscript rrr – sensor type (linear accelerometer ACC or angular rate sensor ARS), subscript u – body local axis along which the error was introduced (u = X, Y, Z), $A_{pi}(t)$ – linear acceleration of point p measured in the i direction and then double integrated, $W_i(t)$ – body local angular velocity around the i axis after double integration, $W_{ij}(t)$ – double integrated product of multiplication of local angular velocity around the i axis and local angular velocity around the j axis, $\Phi_i(t)$ – local angular acceleration around the i axis after double integration, i, j = X, Y, Z.

Constant rotation matrix: When body local acceleration (Eq. 10.2) is multiplied by a constant rotation matrix $\boldsymbol{R}$, the global acceleration of the tracked body is:

$$a_{global\_x}(t) = R11 * a_{ox}(t) + R12 * a_{oy}(t) + R13 * a_{oz}(t) \quad (10.5a)$$
$$a_{global\_y}(t) = R21 * a_{ox}(t) + R22 * a_{oy}(t) + R23 * a_{oz}(t) \quad (10.5b)$$
$$a_{global\_z}(t) = R31 * a_{ox}(t) + R32 * a_{oy}(t) + R33 * a_{oz}(t) \quad (10.5c)$$

where t – time, a_{global_i} – global components of body's linear acceleration, a_{oi} – linear acceleration components at the origin of the body local coordinate frame, i = X, Y, Z, $\boldsymbol{R} = \begin{bmatrix} R11 & R12 & R13 \\ R21 & R22 & R23 \\ R31 & R32 & R33 \end{bmatrix}$.

The results of double integration of Eq. 10.5, with the error terms from Eq. 10.3 introduced, are then:

$$pos_{global\_x}(t) = R11 * pos_{ox}(t) + R12 * pos_{oy}(t) + R13 * pos_{oz}(t) \quad (10.6a)$$
$$pos_{global\_y}(t) = R21 * pos_{ox}(t) + R22 * pos_{oy}(t) + R23 * pos_{oz}(t) \quad (10.6b)$$
$$pos_{global\_z}(t) = R31 * pos_{ox}(t) + R32 * pos_{oy}(t) + R33 * pos_{oz}(t) \quad (10.6c)$$

where t – time, pos_{global_i} – global components of body's position vector, pos_{oi} – position components of the origin of the tracked body from Eq. 10.4, i = X, Y, Z.

10.2.6 Error propagation – general case (translation and rotation at the same time)

When a tracked body rotates while traveling through a 3D space the body's rotation matrix $\boldsymbol{R}$ does not stay constant in time throughout the event. As it was shown in Chapter 8, the components of $\boldsymbol{R}$ are defined with the use of either Euler parameters $\boldsymbol{e}$ or Euler angles α-β-γ. Both, $\boldsymbol{e}$ and the angles α-β-γ are functions of body's local angular velocity vector $\boldsymbol{\omega(t)}$, which is, frequently,

nonlinear in the time domain. Nonlinearity in $\omega(t)$ increases complexity in the mathematical description of e or α-β-γ utilized to define $\mathbf{R}$. By taking that nonlinear nature of the rotation matrix into consideration, global linear acceleration of the tracked body is:

$$a_{global\_x}(t) = f_{11}(\omega(t)) * a_{ox}(t) + f_{12}(\omega(t)) * a_{oy}(t) + f_{13}(\omega(t)) * a_{oz}(t) \qquad (10.7\text{a})$$

$$a_{global\_y}(t) = f_{21}(\omega(t)) * a_{ox}(t) + f_{22}(\omega(t)) * a_{oy}(t) + f_{23}(\omega(t)) * a_{oz}(t) \qquad (10.7\text{b})$$

$$a_{globalz\_}(t) = f_{31}(\omega(t)) * a_{ox}(t) + f_{32}(\omega(t)) * a_{oy}(t) + f_{33}(\omega(t)) * a_{oz}(t) \qquad (10.7\text{c})$$

where t – time, a_{global_i} – global components of body's linear acceleration, a_{oi} – linear acceleration components at the origin of the body local coordinate frame, $i = $ X, Y, Z, $\mathbf{R}\left(\mathbf{f}(\omega(t))\right) = \begin{bmatrix} f_{11}(\omega(t)) & f_{12}(\omega(t)) & f_{13}(\omega(t)) \\ f_{21}(\omega(t)) & f_{22}(\omega(t)) & f_{23}(\omega(t)) \\ f_{31}(\omega(t)) & f_{32}(\omega(t)) & f_{33}(\omega(t)) \end{bmatrix}$, $\mathbf{f}(\omega(t))$ – functions of the local angular velocity vector $\omega(t)$.

To obtain the global position of a body that translates and rotates at the same time, Eq. 10.7 needs to be double integrated in time. Due to the nonlinear form of $\mathbf{R}$, that integration is non-trivial. When sensor-related errors are present in the measured angular rate $\omega(t)$ or the linear acceleration vector $\mathbf{a_o}(t)$, the effect of these errors on the resulting orientation and position is then convoluted and cannot be easily predicted analytically. That is why, to investigate the effect of sensor errors and test inaccuracies on the calculated global position of a body that rotates while traveling through a 3D space, numerical investigations are often performed (Wu et al. 2009, Sinz et al. 2015).

10.2.7 Conclusions

The aim of this section was to analytically evaluate the effect of data signal errors on the calculated 3D component trajectories of a rigid body in a case where the effect of the rotation matrix on the transition between the local and global coordinate frames was either excluded from the analysis (simplified case) or constant in time.

The following can be concluded from the results of the study:

10.2.7.1 Error propagation – simplified case

- When the additive term c (debias error) was introduced into the reading of one of the linear accelerometers, that error affected only one of the global position components of the tracked body (the one along the same direction as the acceleration with the error).
- When only the debias error (additive term c) in one of the angular rate sensors was introduced into the analysis, it affected all three of the calculated position components.
- When two ARS debias errors were included into the angular velocity signals, in one of the global position components the term $\left(c_{ars\_x}^2 + c_{arc\_z}^2\right)\frac{t^2}{2}$ (where t – time) was introduced.
- When only the debias error in one of the angular acceleration components was introduced, it affected two position components along the two axes orthogonal to the axis around which the angular acceleration with the error was defined.

- The error in the ACC sensitivity (scaling term b_{acc}) affected one position component, in the same direction as the measured acceleration with the error.

10.2.7.2 Error propagation – constant rotation matrix

- When the additive term c (debias) was introduced into the reading of one of the linear accelerometers, that error affected all three calculated global position components.
- All three position components were affected also when the debias error was introduced in one of the angular rate sensors or in one of the angular accelerometers.

10.2.7.3 Error propagation – simplified case and the case with constant rotation matrix; general comments

- The resulting error in position due to the debias error in a linear acceleration component grows in time as described by the term $c_{acc} \frac{t^2}{2}$.
- The resulting error in position due to the debias error in an angular velocity component grows in time as described by the term $c_{ars}^2 \frac{t^2}{2}$.
- When two ARS debias errors were introduced into the data, part of their effect was multiplicative, i.e., when, e.g., c_{ars_x} and c_{ars_z} were non-zero, the error term $c_{ars\_x} c_{ars\_z} \frac{t^2}{2}$ appeared in at least two of the calculated position components.
- The error in one ARS sensitivity affected all three position components.
- When two ARS sensitivity errors were introduced into the analysis, part of their effect was also multiplicative, i.e., when, e.g., b_{ars_x} and b_{ars_z} were different than 1, some of the terms in the global position components were scaled by the product of $b_{ars\_x} b_{ars\_z}$.
- When an ARS sensitivity error and an ARS debias error were introduced into the analysis together, part of their effect was multiplicative as well, i.e., when, e.g., c_{ars_x} was non-zero and b_{ars_z} was different than 1, some of the terms in the three global position components were scaled by the product of $b_{ars\_z} c_{ars\_x}$.

10.2.7.4 Error propagation – general case (translation and rotation at the same time)

- Due to the nonlinear nature of R, the double integration of the body's global acceleration (determined from the multiplication of R and the body's local acceleration vector a) is non-trivial or impossible to accomplish analytically.
- The effect of sensor-related errors (that are present in the measured angular rate $\omega(t)$) on the calculated global position of the tracked body is convoluted.

10.3: Error effects – uni- and multivariable analysis

This subsection had two aims:

a) to evaluate the effect of data signal errors (e.g. noise level) or test procedure inaccuracies (e.g. discrepancy between measured and true initial orientation of a body) on 3D component trajectories calculated for an ATD head. It was accomplished through a numerical (univariable)

investigation in which only one error at a time (from Table 13) was introduced into the position calculation algorithm;

b) to identify main interactions between the investigated error types, based on a multivariable analysis in which all errors from Table 13 were introduced into trajectory calculation at the same time.

The section is organized as follows. Section 10.3.1 presents a brief overview of five test cases used in this study. Section 10.3.2 describes instrumentation mounted on the ATD head, the body that was tracked in the five test cases. Section 10.3.3 shows the steps that were performed to obtain baseline responses (i.e., reference trajectories) for the ATD head. Section 10.3.4 summarizes the error types used in both numerical investigations. Section 10.3.5 discusses the error metrics employed through the analysis. Details about the methods for the *Univariable* and *Multivariable* analyses are described in Section 10.3.6 and Section 10.3.7, respectively. The results from both investigations are presented in Section 10.3.8. Concluding remarks are provided in Section 10.3.9.

10.3.1 Test cases – description

To analyze the effect of different error types on the calculated 3D trajectory in a scenario where the tracked body changes its orientation in time, and to identify the main interactions between these errors, sensor data from five data sets ("cases") were sourced.

Case 1 & 2 (two tests from Chapter 6): A box-like structure ("Simplified Head"; SH; Figure 103) was connected with the neck of the Test device for Human Occupant Restraint (THOR) Anthropomorphic Test Device (ATD; NHTSA 2018) and then attached to a sled system (Seattle Safety, Auburn, WA). The SH assembly was positioned at 0° (**Case 1**; Test S0433) or 45° (**Case 2**; Test S0442) relative to the sled travel direction.
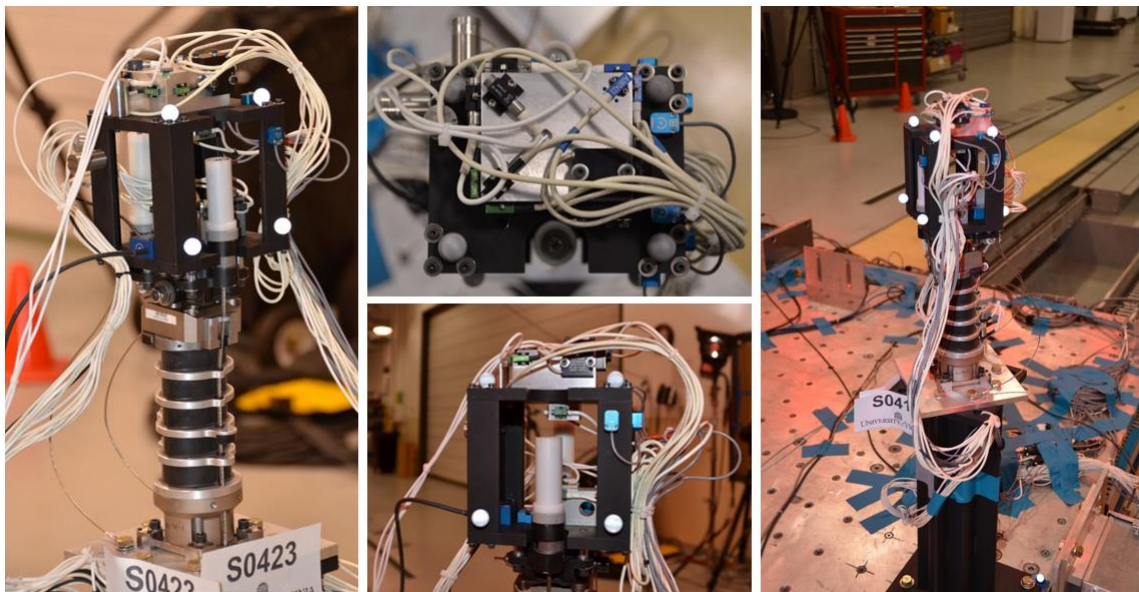
Figure 103. Simplified Head structure.

Case 3 & 4 (two tests from Chapter 7): Two sled tests were performed with the THOR Mod-kit ATD: without (**Case 3**; Test S0457) and including head impact (**Case 4**; Test S0461). THOR

was seated in the Gold Standard (GS) buck positioned at 30° relative to the sled travel direction (cf. Montesinos-Acosta et al. 2016). **Case 4** involved a head impact to assess the influence of impact kinematics on the calculated 3D position time-history.
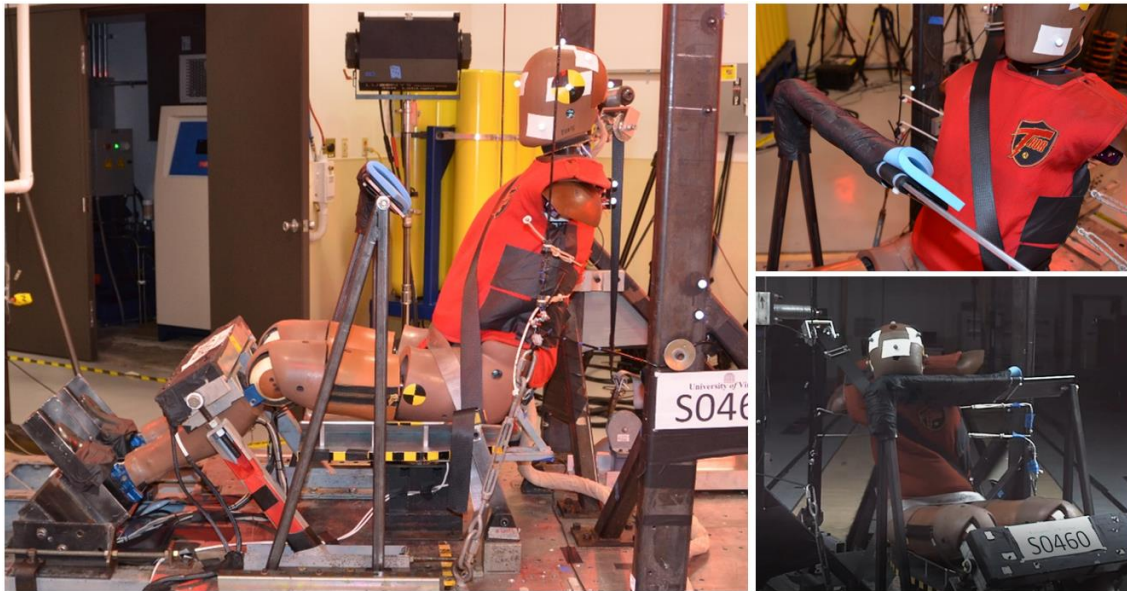
Figure 104. Seated THOR ATD (left) and the foam-padded steel structure (top right) to simulate

Case 5 (one of the vehicle tests described in Section 4.2): For this test case, the data from a frontal oblique offset test of a compact car (Test v10133, NHTSA 2017b) were utilized. In the test, a moving barrier was driven into the front‑left side of the vehicle at approx. 90 km/h. The THOR ATD was positioned in the driver's seat. The impact induced the occupant's head motion in the global reference frame.

10.3.2 Test cases – instrumentation

In all five test cases, the head was instrumented with three linear accelerometers (ACC) (Endevco, Meggitt Sensing Systems, CA, USA) and three angular rate sensors (ARS) (DTS ARS PRO, Diversified Technical Systems, Seal Beach, CA, USA). The sensor data were recorded at the sampling rate of 20 kHz. The local coordinate system of the head was defined as outlined in the SAE J211 document (Society of Automotive Engineers (SAE) 1995).

10.3.3 Baseline trajectory

This section describes the steps that were performed to obtain baseline responses (i.e., reference trajectories) for the ATD head in the five analyzed test cases. All five responses were computed in the same manner. For clarity, the procedure of determining the reference trajectory for the head was outlined in this section and examples are given using kinematics data from Test S0442 (Case 2) only.

Accelerometer and angular rate sensor time-histories recorded during the test were first filtered with a 4th-order Butterworth low pass Channel Frequency Class (CFC) 180 and CFC 60 filters,

respectively (Figure 105 and Figure 106). The data between -50ms to 250ms, where t=0 indicated the start of the test, were then assumed to be noiseless.
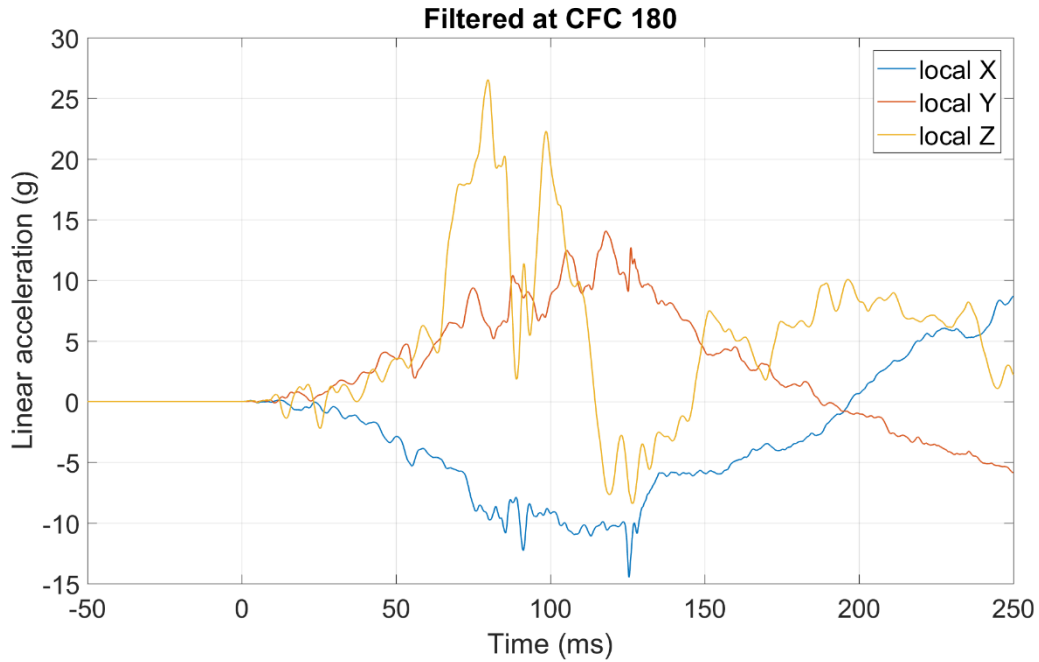
Figure 105. Noiseless acceleration signal obtained through filtering the test data.
.
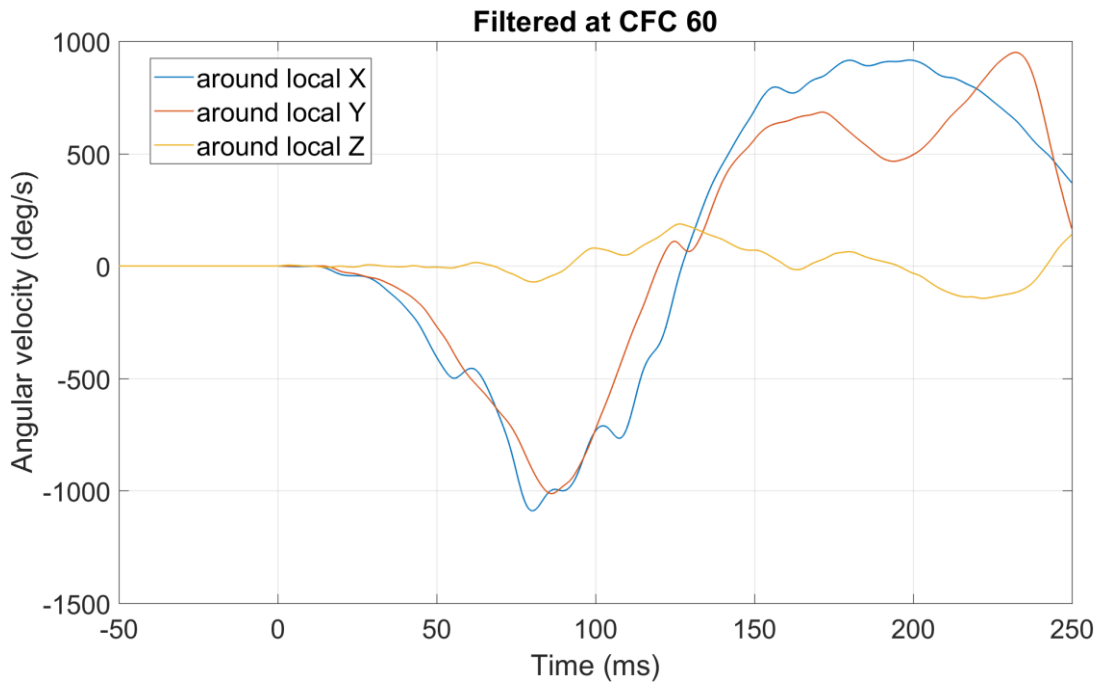
Figure 106. Noiseless angular rate signal obtained through filtering the test data.

In a real test, some noise level is expected to occur. To take that into consideration and to maintain the frequency content of the noise for the sensors used, the ACC/ARS corresponding pre-

trigger data (from -50ms to -10ms) were added copied multiple times along the noiseless signal (Figure 107 and Figure 108). This procedure was performed individually for each of the three linear accelerometers and three angular rate sensors to account for the between-sensor variability.
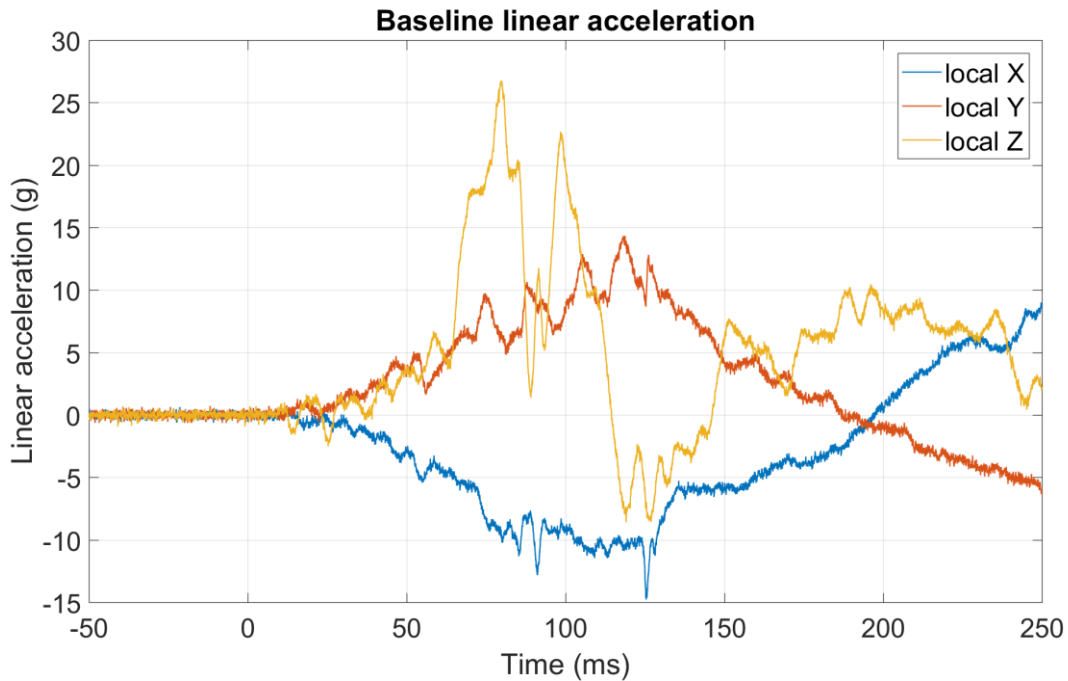
Figure 107. Acceleration signal trace with injected noise.
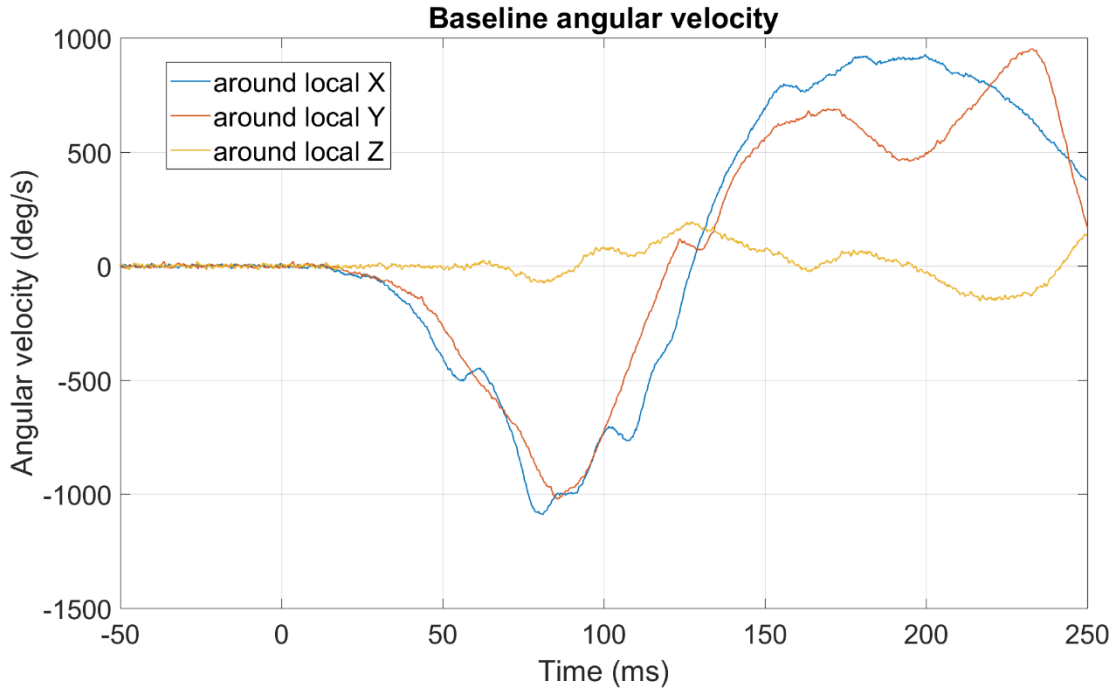
Figure 108. Angular rate signal traces with injected noise.

125

Next, the "noise-injected" data were used to calculate the 3D trajectory of the body as outlined in Section 1.2.3. The 3D response of the head in Test S0442 (Case 2) obtained with this method (Figure 109) was then treated as the baseline response for further error effects modeling analysis.
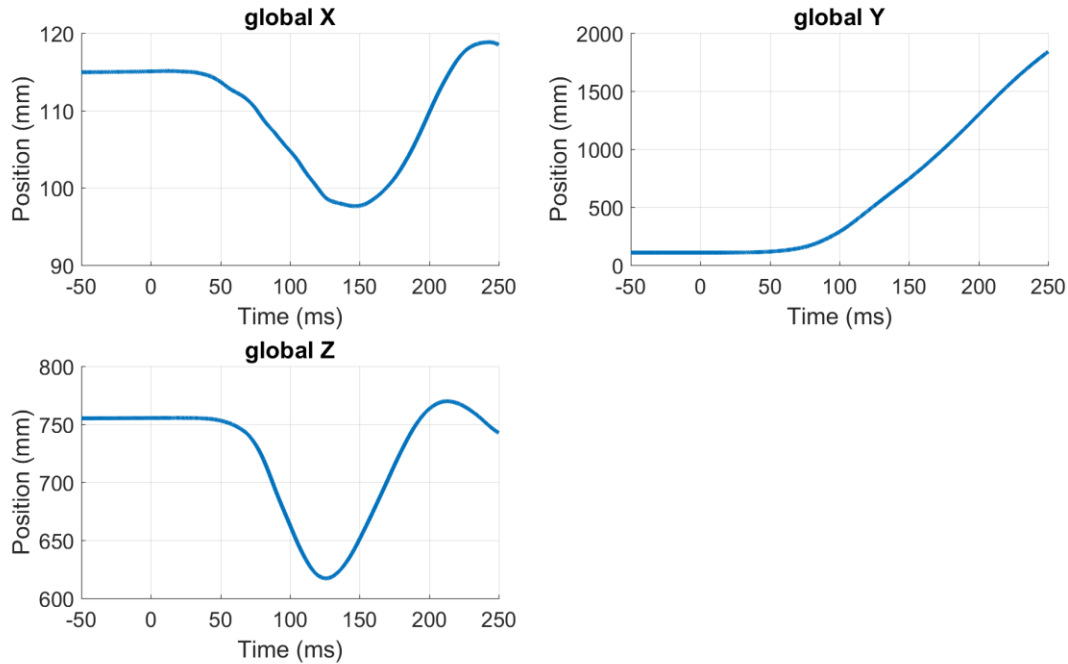
Figure 109. Baseline 3D trajectories used for further error effects analysis.

In the process of calculating the baseline response, it was also assumed that:

- the sensing axes of the three linear accelerometers as well as the angular rate sensors were perfectly aligned with the axes of the body local coordinate system;
- the center of gravity (CG) of an accelerometer seismic mass was at an offset from the origin of the head local coordinate frame only in the direction in which the sensor measured acceleration, i.e. the accelerometer position vector ρ had a non-zero component in the direction of accelerometer measurement.

10.3.4 List of errors (variables) used in the analysis

Based on the errors from Table 13 the following 11 error groups and 39 independent variables were identified and used in the following error effects analysis (Table 18).

Table 18. Independent variables used in the analysis.

Error type	Error group	Sensor type	Component	Variable #
Seismic mass CG position (in local body frame)	**1**	Accelerometer X	X	1
			Y	2

			Z	3
			X	4
		Accelerometer Y	Y	5
			Z	6
			X	7
		Accelerometer Z	Y	8
			Z	9
Head initial orientation (in global reference frame)	**2**	Not applicable	Yaw	10
			Pitch	11
			Roll	12
Head CG initial position (in global reference frame)	**3**	Not applicable	X	13
			Y	14
			Z	15
Sensitivity error	**4**	Accelerometer	X	16
			Y	17
			Z	18
	5	Angular Rate Sensor	X	19
			Y	20
			Z	21
Noise Level	**6**	Accelerometer	X	22
			Y	23
			Z	24
	7	Angular Rate Sensor	X	25
			Y	26
			Z	27

Debias error	**8**	Accelerometer	X	28
			Y	29
			Z	30
	9	Angular Rate Sensor	X	31
			Y	32
			Z	33
Angle misalignment	**10**	Accelerometer	X	34
			Y	35
			Z	36
	11	Angular Rate Sensor	X	37
			Y	38
			Z	39

10.3.5 Error metrics

Throughout the analysis the following metric was used to evaluate the deviation of the head's calculated trajectory from the baseline response:

$$Res_{err} = \sqrt{\frac{\sum_{i=1}^{N}\left[(x_{baseline,i}-x_{error,i})^2+(y_{baseline,i}-y_{error,i})^2+(z_{baseline,i}-z_{error,i})^2\right]}{N}} \qquad (10.8)$$

where N – number of data (time) points, $x_{baseline,i}$, $y_{baseline,i}$, $z_{baseline,i}$ – X, Y, Z components of the baseline trajectory at the data point i, $x_{error,i}$, $y_{error,i}$, $z_{error,i}$ – X, Y, Z components of the calculated trajectory (based on the data with introduced errors).

The maximum absolute difference (*diff_max*) between the calculated and reference trajectories was computed for all independent variables from Table 18. In the results section for the *Univariable analysis*, the maximum value of *Res_err* and *diff_max* (called *mRes_err* and *mdiff_max*, respectively) within the same error group was found. For the five linear regression models presented in the *Multivariable analysis* the coefficient of determination, R^2, was computed and presented.

10.3.6 Univariable analysis – methods

To assess the effect of the individual variables (Table 18) on the calculated 3D trajectory one error at a time was introduced into the analysis. To cover a bigger response space, for every investigated variable fifteen values were equally spaced in-between the error lower and upper bounds, with the bounds included. In cases where the middle value was zero (all except the

ACC/ARS sensor angle misalignment and the noise level) the "zero" condition was assumed to represent the baseline response, and thus it was not re-calculated again.

In total, 2,760 simulations were run (552 per test case). During the runs, the time history of body motion was calculated and, next, its deviation from the baseline response (in the form of Res_{err} and $diff_{max}$) was recorded. After 552 runs were completed for a test case, using all variables within the same error group (as defined in Table 18) $mRes_{err}$ and $mdiff_{max}$ were found for each group separately. When all 2,760 simulations were finished, the lower and upper bounds for $mRes_{err}$ and $mdiff_{max}$, for the same error group (second column in Table 18) but across the five test cases, were determined. Based on the descending order of the upper bounds for both used error metrics two lists were created and reported.

Remark: To update the orientation of the tracked body (its rotation matrix $\boldsymbol{R}$), head's local angular velocity and the method described by Huculak and Lankarani 2013 were utilized (see Chapter 8 for more detail about the method used).

10.3.7 Multivariable analysis – methods

As the first step, for all five test cases, Latin Hypercube Sampling (LHS; cf. McKay et al. 1979, cf. Eglajs et al. 1977, cf. Iman et al. 1981) was performed to create 10,000 combinations of the independent variables from Table 18. To design the experiment, MATLAB (MathWorks, Natick, MA, USA) function *lhsdesign* with the "correlation" option was selected. The function allowed for generation of near-random evenly sampled variable values from a multidimensional distribution (2D example shown in Figure 110).
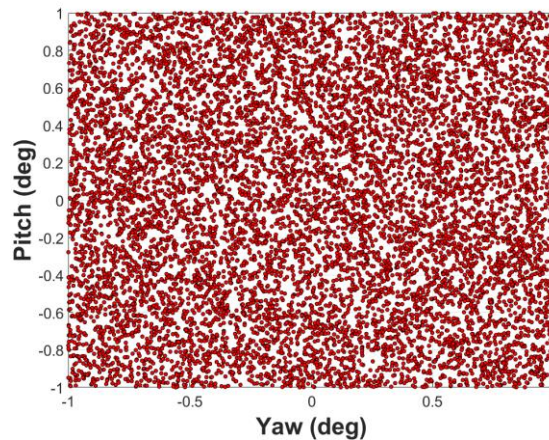
Figure 110. Variable values in Yaw-Pitch space obtained using Latin Hypercube Sampling.

In total, 50,000 simulations were carried out with all variables from Table 18 introduced at the same time. After the simulations were completed, Res_{err} was calculated for all 50,000 runs. Next, using the Res_{err} metric as the response variable and guided by Section 10.2 and the results from the *Univariable analysis*, an initial linear regression model (the same for all five tests) was built. The model (see APPENDIX O) was defined with the use of all variables within the following three error groups: ACC debias error, ARS debias error, and initial orientation error. Next, a stepwise regression algorithm (through MATLAB's *stepwiselm* function) was utilized to finalize the regression model separately for each of the five test cases. Even though the initial model was based

only on three error classes, the stepwise algorithm was given a pool of other error types (and the variables within them) to add terms from. Those additional error groups were: ACC sensitivity error, ARS sensitivity error, and noise level in the ACC signal. To add or remove a term (predictor) to/from the model, the *Akaike information criterion* (AIC) (commonly used for model evaluation and selection, Gagné et al. 2002, Hoeting et al. 2006, Lee et al. 2009, Kamel et al 2015, Mangan et al. 2017) was used (Akaike 1974). To minimize predictor bias and multicollinearity, all variables utilized as possible predictors were scaled to be within <-1, 1> range and centered at zero.

After the linear regression models were finalized, the model terms were divided into four categories:

- main effects: when a term contained a single predictor to the power of 1, e.g. c_{ars_y};
- higher order terms (H.O.T.): when a term contained a single predictor, but that predictor was to the power of 2 or higher, e.g. $c_{ars\_y}^3$;
- main interactions: when two or more predictors (to the power of 1) were multiplied by each other, e.g., $c_{ars\_x} * c_{ars\_z} * yaw_{err} * pitch_{err}$;
- interactions with H.O.T.: when a term contained multiple predictors, and one of the predictors was a H.O.T., e.g., $c_{ars\_y}^2 * yaw_{err} * pitch_{err}$.

Every term had a coefficient (estimate) associated with that term (see APPENDIX O). Those coefficients were utilized to sort the model terms in a descending order. Next, the main interaction with the highest absolute value of the estimated coefficient was identified. That value was then scaled to be one, and all other coefficients (their absolute values) were scaled accordingly. That procedure was carried out for the five test cases. After it was completed, all the model terms from the considered tests were gathered together, and the occurrence of these terms within that set was counted. If the term appeared in at least three tests and its scaled estimated coefficient was higher or equal to 0.05, the term was included in the following step of the analysis.

At this stage, all identified terms were axis dependent and thus specific to a loading condition. To remove the axis dependency and to generalize the results from the multivariable analysis, the terms were sorted again into main effects, main interaction, etc., keeping the division between the sensor groups when needed (see Table 19 for details).

Table 19. Generalization of axis specific terms. i, j, k = X, Y, Z.

Axis specific term (example)	Generalized term
c_{acc_i}	ACC debias error
c_{ars_i}	ARS debias error
$c_{acc\_i}^2$ or $c_{acc\_i}^3$	ACC debias error^2 or ACC debias error^3
$c_{acc\_i}^2$ or $c_{acc\_i}^3$	ARS debias error^2 or ARS debias error^3
$(c_{acc\_i} * c_{acc\_j})$ or $(c_{acc\_i} * c_{acc\_j} * c_{acc\_k})$	Multiplication of ACC debias errors
$(c_{ars\_i} * c_{ars\_j})$ or $(c_{ars\_i} * c_{ars\_j} * c_{ars\_k})$	Multiplication of ARS debias errors
$(yaw_{err} * pitch_{err})$ or $(pitch_{err} * roll_{err})$ or $(yaw_{err} * roll_{err})$ or $(yaw_{err} * pitch_{err} * roll_{err})$	Multiplication of errors in initial Euler Angles

Remark: To update the orientation of the tracked body (its rotation matrix $\boldsymbol{R}$), head's local angular velocity and the method described by Huculak and Lankarani 2013 were utilized.

10.3.8 Results

In this subsection, the results from the error effects investigations are presented: first, based on the *Univariable*, and next, based on the *Multivariable* analyses (Section 10.3.8.1 and Section 10.3.8.2, respectively).

10.3.8.1 Univariable analysis

When the upper bounds for *mRes_err* and *mdiff_max* were used across different error groups from Table 18, the resulting error hierarchies (Table 20 and Table 21 for *mRes_err* and *mdiff_max*, respectively) were well correlated. The only difference between the tables was the order of the last two rows, with *ARS angle misalignment* being above *Head CG initial position in IRF* according to *mRes_err*, and *Head CG initial position in IRF* being above *ARS angle misalignment* according to *mdiff_max*. It needs to be pointed out here that *mRes_err* and *mdiff_max*, in all five test cases and in all eleven error groups, were found when one of the two bounding values (for the error in question; as defined in Table 13) was used in the analysis, i.e., the following two lists were built based on the trajectory calculation process in which the maximum error value (worst case scenario) was utilized.

Table 20. Errors based on the upper bound of $mRes_{err}$ from the five test cases.

#	Error group	Range for $mRes_{err}$ (mm)		
		Lower bound (LB)	Upper bound (UB)	
			Value	% of UB
1.	ACC debias	356.84	394.62	100
2.	ARS debias	90.38	146.48	37.12
3.	ACC sensitivity	23.72	34.89	8.84
4.	Initial orientation in IRF	9.32	21.89	5.55
5.	ACC noise level	3.10	14.63	3.71
6.	ARS sensitivity	2.94	6.84	1.73
7.	ACC seismic mass CG position in BF	1.81	3.92	0.99
8.	ARS noise level	0.10	1.73	0.44
9.	ACC angle misalignment	0.78	1.14	0.29
10.	ARS angle misalignment	0.044	0.113	0.03
11.	Head CG initial position in IRF	2.022E-13	7.467E-13	1.9E-13

Table 21. Errors based on the upper bound of mdiff_max from the five test cases.

#	Error group	Range for *mdiff_max* (mm)		
		Lower bound (LB)	Upper bound (UB)	
			Value	% of UB
1.	ACC debias	711.88	882.21	100
2.	ARS debias	212.02	339.49	38.48
3.	ACC sensitivity	52.50	76.39	8.66
4.	Initial orientation in IRF	27.35	50.37	5.71
5.	ACC noise level	5.81	29.65	3.36

6.	ARS sensitivity	6.40	16.14	1.83
7.	ACC seismic mass CG position in BF	4.19	7.48	0.85
8.	ARS noise level	0.25	3.99	0.45
9.	ACC angle misalignment	1.72	2.52	0.29
10.	Head CG initial position in IRF	2.50	2.50	0.28
11.	ARS angle misalignment	0.10	0.24	0.03

The group with the highest $mRes_{err}$ and $mdiff_{max}$ (upper bound of 394.62 mm and 882.21, respectively) was the debias error for a linear accelerometer. It was followed by the error in the debias offset for an angular rate sensor. The sensitivity error in ACC (the third on both lists) had a greater effect on the calculated trajectory than the sensitivity error in ARS data (sixth). Within the first six error groups, only one class (*Initial orientation in IRF*; fourth on the lists; $mRes_{err}$ UB of 21.89 mm; $mdiff_{max}$ UB of 50.37 mm) was related to the accuracy of a geometric measurement, not to the accuracy of a sensor reading. The second highest "geometric" error (seventh on both lists) was *ACC seismic mass CG position in BF* with $mRes_{err}$ up to 3.92 mm and $mdiff_{max}$ up to 7.48 mm. Two misalignment errors as well as the error in the initial position of the tracked body had a negligible effect on the calculated trajectory ($mRes_{err}$ and $mdiff_{max}$ below 2.6 mm for the three error groups).

Remark: Errors based on $mRes_{err}$ and $mdiff_{max}$ in each of the five analyzed test cases can be found in APPENDIX P.

10.3.8.2 Multivariable analysis

In the analyzed test cases, the Res_{err} metric was calculated using results from analyses in which all 39 variables from Table 18 were used. Res_{err} was then modeled with regression curves that were built based on eleven of these variables only (see APPENDIX O). Even though, a limited number of the error descriptors was used, Res_{err} was approximated well in the five tests, with the coefficients of determination R^2 for the final regression models varying from 0.65 in Test S0442 to 0.7 in Test v10133 (Table 22).

Table 22. Coefficient of determination for the final regression models in the five test cases.

Case #	R^2
1	0.69
2	0.65
3	0.69
4	0.68
5	0.70

Based on the regression analysis performed in this study, six main interactions between errors, two higher order terms (H.O.T.), and three types of interactions involving H.O.T. were identified (Table 23). It is worth pointing out here that all terms from Table 23 were different configurations

of the same three errors: ACC debias, ARS debias, and the error in the initial Euler angles (i.e. the error in initial orientation of the ATD head).

Table 23. Higher order terms and error interactions identified based on the five test cases.

Higher Order Terms (H.O.T.)	Interactions with H.O.T.	Main interactions
ACC debias^2	ACC debias^2 * Multiplication of errors in initial Euler Angles	ACC debias * ARS debias
ARS debias^2	ARS debias^2 * Multiplication of errors in initial Euler Angles	Multiplication of ACC debias errors
	ARS debias^3 * Multiplication of errors in initial Euler Angles	Multiplication of errors in initial Euler Angles
		ACC debias * Multiplication of errors in initial Euler Angles
		ARS debias * Multiplication of errors in initial Euler Angles
		Multiplication of ARS debias errors * Multiplication of errors in initial Euler Angles

10.3.9 Conclusions

The aim of this study was: a) to evaluate, through numerical investigation, the effect of data signal errors (e.g. noise level) or test procedure inaccuracies (e.g. discrepancy between measured and true initial orientation of a body) on 3D component trajectories calculated for an ATD head in a crash-like scenario, and b) to identify the main interactions between the investigated error types.

The following can be concluded from the results of the study:

10.3.9.1 Debias error

- The debias error (either in acceleration or angular rate sensor data) had the greatest effect on the calculated 3D trajectories of the tracked body (Table 20 and Table 21).
- The error in acceleration caused a bigger discrepancy between the baseline and the calculated trajectories than the debias offset in the angular velocity data.
- Even though the debias error influences calculated trajectories substantially, it can be addressed with proper debiasing techniques. Instead of using "one point" debiasing, the entire available pre-trigger data (for the senor in question) should be utilized to estimate the debias offset for that sensor.

10.3.9.2 Sensitivity error in acceleration

- The sensitivity error in ACC had a greater effect on the calculated trajectory than the sensitivity error in ARS data.
- The error in the accelerometer sensitivity can influence the calculated 3D trajectory in a substantial way. In the investigated test scenarios, when the ACC sensitivity was modified by 4%, the absolute position peak error reached (in one of the cases) approximately 75 mm (1/10 of the peak difference, seen cross the five investigated cases, for the ACC debias error and 1/4 of the difference seen for the ARS debias error; Table 21).

- It is worth mentioning here that the ACC sensitivity error can occur with correct sensitivity value put into the data acquisition system, but with incorrect excitation voltage the sensor is run at. The sensitivity for the same accelerometer calibrated at 5V and at 10V can differ up to several percent.
- The error in sensitivity can be addressed by calibrating sensors frequently and by using the calibration voltage as the sensor excitation voltage during testing.

10.3.9.3 Initial orientation error

- A relatively small inaccuracy in measured initial orientation may have a substantial effect on the predicted 3D response. In one of the investigated test cases, the discrepancy of 1 degree between the baseline and "with error" initial Yaw angle caused a difference between the reference and the calculated trajectories of approx. 50 mm (Table 21) in the X direction.
- The error in initial Yaw angle (from the case mentioned above) influenced, through the rotation matrix, the definition of the global inertial frame used in the trajectory calculation process. That inertial frame was rotated by 1 degree (around Z) relative to the coordinate system used for the baseline response (Figure 111). On the test, the highest magnitude of motion was observed in the Y direction. As Figure 111 shows, the higher the magnitude of Y motion, the higher the error in X direction.
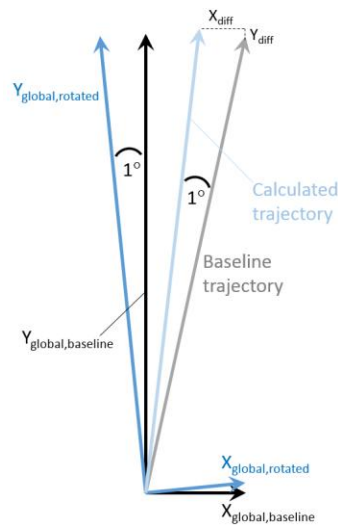
Figure 111. Coordinate systems for the baseline and the calculated trajectories. Z axes for both systems were perfectly aligned.

10.3.9.4 Smallest errors

- Within the error bounds from Table 13, the two misalignment errors (for ACC and ARS) as well as the error in the initial position of the tracked body had a negligible effect on the calculated 3D global trajectory of the ATD head ($mRes_{err}$ and $mdiff_{max}$ both below 2.6 mm for the three error groups; Table 20 and Table 21).

10.3.9.5 Main interactions

- Six main interactions between the errors used in the study were identified (Table 23).
- All six interactions were different configurations of the same three errors: ACC debias, ARS debias, and the error in the initial orientation.

11.INVESTIGATION OF THE EFFECT OF REDUNDANT SENSORS ON THE MAGNITUDE OF THE ERROR IN THE CALCULATED TRAJECTORY

Body motion in a three dimensional (3D) space can be described with the use of kinematics data from three linear accelerometers and three angular rate sensors rigidly attached to that body. As it was shown in Chapter 10, though, a sensor reading can have an error and that error can affect the obtained trajectory substantially. In addition, when one of the seniors fails during a test (for example, due to a broken connector), the kinematics data recorded are incomplete and cannot be used anymore to obtain the 3D position of the tracked body.

The goal of this task was to investigate if by introducing redundant sensors to the stock "3 ACC + 3 ARS" package, an inaccurate ("inconsistent") sensor can be identified or if a broken sensor can be accounted for in the trajectory calculation. In other words, the goal was to find an analytical relationship that relates a reading (measured quantity) from one of the sensors to readings from the other (including redundant) sensors. By doing so, it is expected for the error in the calculated trajectory to be minimized.

The chapter is organized as follows. The next section describes the analytical process utilized to determine a mathematical relationship between two vectors, where the magnitude and direction of one of the vectors, and the three components of the other vector are known. The following sections show how that relationship can be applied to account for a faulty angular rate sensor, first, and then a linear accelerometer. In the fourth section, the analytical relationship is evaluated using data from a computer simulation of a simple rigid body system. Concluding remarks are provided in the *Conclusions* section.

11.1 Analytical relationships between two vectors in a 3D space

Let's define two vectors, V and P in a 3D space, with angle θ being the angle between those two vectors (Figure 112).
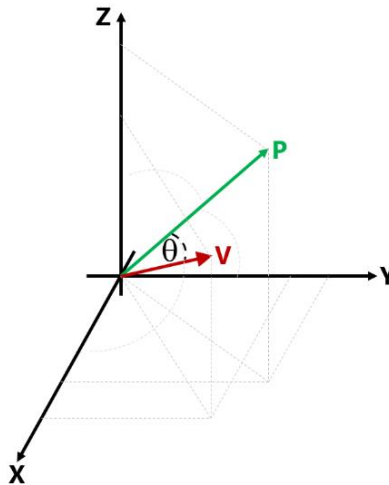
Figure 112. Two vectors, V and P, in a 3D space.

Assuming that vector P represents a portion of vector V, the cosine of the angle θ can be found from Eq. 11.1:

$$\cos\theta = \frac{\|P\|}{\|V\|} \tag{11.1}$$

where $\|P\|$ and $\|V\|$ are the magnitudes (lengths) of P and V, respectively.

The cosine of the angle between two vectors in a 3D space can also be found from the geometric definition of a dot product of those two vectors (Eq. 11.2):

$$V \cdot P = \|V\|\|P\|\cos\theta \Rightarrow \cos\theta = \frac{V \cdot P}{\|V\|\|P\|} \tag{11.2}$$

Now, let's assume that the following from Figure 113 is known:

- the magnitude $\|P\|$ of vector P,
- three angles, α, β, γ, defining the direction of vector P relative to the axes of the known coordinate system,
- three components of vector $V = (V_x, V_y, V_z)$.
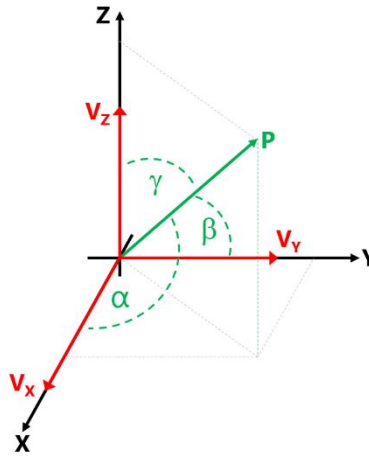
Figure 113. Known quantities needed in the analysis.

The magnitude (length) of vector V can be found from its three known components (Eq. 11.3):

$$\|V\| = \sqrt{V_x^2 + V_y^2 + V_z^2} \tag{11.3}$$

By substituting Eq. 11.3 into Eq. 11.1, the cosine of the angle θ can be defined as Eq. 11.4:

$$\cos\theta = \frac{\|P\|}{\sqrt{V_x^2 + V_y^2 + V_z^2}} \tag{11.4}$$

By knowing α, β, and γ, the three components of vector P (its projections on the X, Y, Z axes) can be determined (Eq. 11.5):

$$P = (P_x, P_y, P_z) = (\|P\|\cos\alpha, \|P\|\cos\beta, \|P\|\cos\gamma) \tag{11.5}$$

From the algebraic definition of the dot product of vectors V and P it can be found that (Eq. 11.6):

$$V \cdot P = V_x P_x + V_y P_y + V_z P_z = V_x\|P\|\cos\alpha + V_y\|P\|\cos\beta + V_z\|P\|\cos\gamma \tag{11.6}$$

By substituting Eq. 11.3, Eq. 11.5 and Eq. 11.6 into Eq. 11.2, the cosine of the angle θ can also be defined as Eq. 11.7:

$$\cos\theta = \frac{\boldsymbol{V}\cdot\boldsymbol{P}}{\|\boldsymbol{V}\|\|\boldsymbol{P}\|} = \frac{V_x\|\boldsymbol{P}\|\cos\alpha+V_y\|\boldsymbol{P}\|\cos\beta+V_z\|\boldsymbol{P}\|\cos\gamma}{\|\boldsymbol{P}\|\sqrt{V_x^2+V_y^2+V_z^2}} = \frac{V_x\cos\alpha+V_y\cos\beta+V_z\cos\gamma}{\sqrt{V_x^2+V_y^2+V_z^2}} \tag{11.7}$$

Then, by equating Eq. 11.4 with Eq. 11.7, an analytical relationship between all seven known quantities from Figure 113 can be determined (Eq. 11.8):

$$\frac{\|\boldsymbol{P}\|}{\sqrt{V_x^2+V_y^2+V_z^2}} = \frac{V_x\cos\alpha+V_y\cos\beta+V_z\cos\gamma}{\sqrt{V_x^2+V_y^2+V_z^2}} \Rightarrow \|\boldsymbol{P}\| = V_x\cos\alpha + V_y\cos\beta + V_z\cos\gamma \tag{11.8}$$

Eq. 11.8 relates the components of vector $\boldsymbol{V}$ to the magnitude of vector $\boldsymbol{P}$.

11.2 Redundant angular rate sensor

In most cases, a regular sensor package utilized to obtain body 3D kinematics contains three angular rate sensors (ARS). The three ARS have their sensing axes mutually orthogonal and they are usually aligned with the axes of the body local coordinate system. Unfortunately, if one of the ARS readings has an error, the obtained body kinematics based on that data are inaccurate. To correct for that "bad" ("inconsistent") sensor, more than three ARS are required.

It can be shown that by adding redundant angular rate sensors – at a fixed and known locations – to the "3 ARS" sensor package the sensor with the error in its signal can be identified and the reading can be corrected.

Let's define vector $\boldsymbol{\omega} = (\omega_x, \omega_y, \omega_z)$ that describes the angular velocity of a rigid body. ω_x, ω_y, and ω_z are the local coordinate system components of the $\boldsymbol{\omega}$ vector. The three components are equivalent to the V_x, V_y, and V_z components from Eq. 11.8. The orientation of the sensing axis of the added (fourth) angular rate sensor ω_p, relative to the three local coordinate axes, is known and defined by three angles: α, β, γ (Figure 113). If, at the same time, the angular velocity ω_p (recorded by the fourth ARS) corresponds to the $\|\boldsymbol{P}\|$ term in Eq. 11.8, the mathematical relationship between the redundant ARS and the three angular rate sensors aligned with the axes of the body local coordinate frame can be defined as:

$$\omega_p = \omega_x\cos\alpha + \omega_y\cos\beta + \omega_z\cos\gamma \tag{11.9}$$

And thus:

$$\omega_x = \frac{\omega_p-\omega_y\cos\beta-\omega_z\cos\gamma}{\cos\alpha} \tag{11.10a}$$

$$\omega_y = \frac{\omega_p-\omega_x\cos\alpha-\omega_z\cos\gamma}{\cos\beta} \tag{11.10b}$$

$$\omega_z = \frac{\omega_p-\omega_x\cos\alpha-\omega_y\cos\beta}{\cos\gamma} \tag{11.10c}$$

Using Eq. 11.9 and Eq. 11.10 any of the four ARS can be predicted based on the other three. These equations can be directly applied in a situation when one ARS fails during the test. The missing reading can be then found from the other three readings, assuming that these three measurements do not contain errors. It is needed to be mentioned here that for the method to work

all four ARS need to be perfectly aligned and angles α, β, γ be different than multiplications of ±90°.

One redundant ARS is also enough to asses if the recorded kinematics data are consistent, i.e., the predictions from Eq. 11.9 and Eq. 11.10 match the sensor measurements obtained during the test. If the predictions do not follow the measurements, it means that at least one of the four sensor readings contains an error. If only four ARS are utilized, through Eq. 11.9 and Eq. 11.10 it is not possible to identify which of the ARS is erroneous, as Eq. 11.9 and Eq. 11.10 are affected by the same error. To pinpoint the faulty sensor (assuming only one is "inconsistent"), a fifth ARS is needed in the senor package. With five ARS present, the following methodology can be applied to identify the erroneous reading:

Step 1: Pick an ARS for which the consistency check will be performed,

Step 2: Express the four remaining ARS readings in the function of three out of these four ARS measurements,

Step 3: For the four ARS (from Step 2), compute the error between the measurements obtained during the test and their predictions as calculated in Step 2,

Step 4: Compute the cumulative error for the four ARS from Step 3,

Step 5: Repeat Step 1 to Step 4 for the other four angular rate sensors,

Step 6: The sensor from Step 1 for which the cumulative error is the smallest, is the faulty sensor and its measurement should be replaced by the sensor prediction.

It is worth pointing out here, that if the sensing axes of both added ARS are aligned (i.e., both ARS are at the same angle), the two redundant sensors should give the same reading. In that case, when Eq. 11.9 and one of the added ARS match, but the second added sensor does not, it means that that second sensor is affected by an error. When Eq. 11.9 does not match with any of the two redundant sensors, but the two added sensor measurements follow each other, it implies that at least one of the X, Y, or Z ARS is "inconsistent". It can be shown, though, that with both redundant ARS at the same angle, Step 2 from the methodology described above does not have a unique solution (APPENDIX Q). For Step 2 to have a solution, the sensing axes of both added ARS cannot be aligned.

11.3 Redundant linear accelerometer

Similarly, based on Eq. 11.8 and by adding redundant linear accelerometers (ACC) to the sensor package, an inaccurate ACC can be identified and replaced by a "consistent" reading. To compare body's acceleration, though, the sensor readings need to be transformed to the same point first. To transform acceleration from a linear accelerometer to a different point (in this study, to the origin of the sensor block's local coordinate system) the following is needed:

- distance of the center of gravity (CG) for an accelerometer's seismic mass relative to the origin of the local frame of the sensor block, and
- angular velocity in the plane the sensing axis of the redundant ACC is normal to.

It is assumed that angular velocity $\boldsymbol{\omega} = (\omega_x, \omega_y, \omega_z)$ around the three axis of the local coordinate system was measured and it is known. Then, the transformation of the acceleration

readings for the three ACC perfectly aligned with the axes of the body local frame to the origin of the local coordinate system takes a form of Eq. 11.11:

$$a_{x,O} = a_x + \rho_{Ox} * \left(\omega_y^2 + \omega_z^2\right) \tag{11.11a}$$

$$a_{y,O} = a_y + \rho_{Oy} * \left(\omega_x^2 + \omega_z^2\right) \tag{11.11b}$$

$$a_{z,O} = a_z + \rho_{Oz} * \left(\omega_x^2 + \omega_y^2\right) \tag{11.11c}$$

where a_i – sensor reading for i^{th} accelerometer, $a_{i,O}$ – sensor reading for i^{th} accelerometer transformed to the origin of the local coordinate frame, ρ_{Oi} – distance between the ith accelerometer seismic mass and the origin of the body local frame, ω_i – body local angular rates; i = X, Y, Z.

To transform acceleration from the redundant accelerometer a_p to the origin of the sensor block coordinate system, the angular velocity $\omega_\perp$ needs to be found. $\omega_\perp$ describes angular rate around an axis in the plane the sensing axis of a_p is normal to (Figure 114).
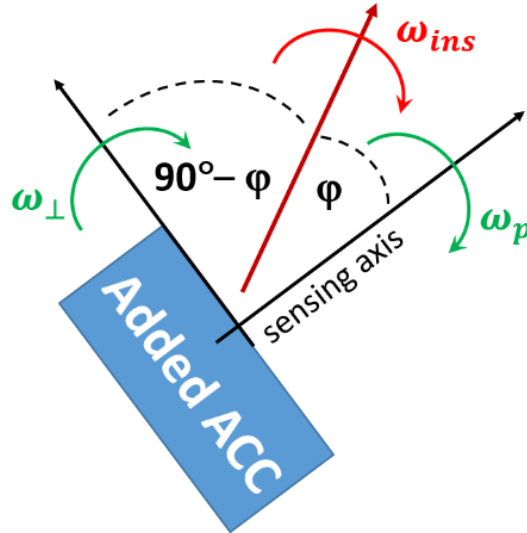
Figure 114. Schematic drawing depicting axes of rotations for the analyzed body and redundant accelerometer attached to that body. All three axis shown are always in the same plane.

To find $\omega_\perp$, first, the angular velocity ω_p around the sensing axis of a_p is determined using Eq. 11.9, three components of the local angular velocity $\boldsymbol{\omega}$ and known angles: α, β, γ (Figure 113) that define the orientation of a_p in the 3D space. Next, body angular velocity ω_{ins} around the instantaneous axis of rotation is found from Eq. 11.12:

$$\omega_{ins} = \sqrt{\omega_x^2 + \omega_y^2 + \omega_z^2} \tag{11.12}$$

When both, ω_p and ω_{res} are known the angle φ (Figure 114) between the body instantaneous axis of rotation and the a_p sensing axis can be determined (Eq. 11.13):

$$\cos \varphi = \frac{\omega_p}{\omega_{ins}} = \frac{\omega_p}{\sqrt{\omega_x^2 + \omega_y^2 + \omega_z^2}} \Rightarrow \varphi = \cos^{-1}\left(\frac{\omega_p}{\sqrt{\omega_x^2 + \omega_y^2 + \omega_z^2}}\right) \tag{11.13}$$

Finally, using Eq. 11.13, trigonometric relationships and simple algebraic manipulations, $\omega_\perp$ can be identified as (Eq. 11.14):

$$\cos(90° - \varphi) = \frac{\omega_\perp}{\omega_{ins}} \Rightarrow \sin \varphi = \frac{\omega_\perp}{\sqrt{\omega_x^2 + \omega_y^2 + \omega_z^2}} \Rightarrow \omega_\perp = \sin \varphi \sqrt{\omega_x^2 + \omega_y^2 + \omega_z^2} \tag{11.14}$$

It is known that:

$$\sin(\cos^{-1} x) = \sqrt{1 - x^2} \tag{11.15}$$

By using relationship described by Eq. 11.15, Eq. 11.14 can be rewritten as:

$$\omega_\perp = \sqrt{1 - \frac{\omega_p^2}{\omega_x^2 + \omega_y^2 + \omega_z^2}} * \sqrt{\omega_x^2 + \omega_y^2 + \omega_z^2} = \sqrt{\frac{\omega_x^2 + \omega_y^2 + \omega_z^2 - \omega_p^2}{\omega_x^2 + \omega_y^2 + \omega_z^2}} * (\omega_x^2 + \omega_y^2 + \omega_z^2) \Rightarrow$$

$$\omega_\perp = \sqrt{\omega_x^2 + \omega_y^2 + \omega_z^2 - \omega_p^2} \tag{11.16}$$

Utilizing Eq. 11.16 and assuming that vector $\boldsymbol{\rho_p} = (\rho_{px}, \rho_{py}, \rho_{pz})$, describing the local position of the redundant ACC (its seismic mass CG), is known, the accelerometer reading of the added sensor can be transformed to the origin of the local coordinate system with the use of Eq. 11.17:

$$a_{p,O} = a_p + \|\boldsymbol{\rho_p}\| * \omega_\perp^2 = a_p + \sqrt{\rho_{px}^2 + \rho_{py}^2 + \rho_{pz}^2} * (\omega_x^2 + \omega_y^2 + \omega_z^2 - \omega_p^2) \tag{11.17}$$

where a_p – reading of the redundant accelerometer, $a_{p,O}$ – reading of the redundant accelerometer transformed to the origin of the body local frame, $\|\boldsymbol{\rho_p}\|$ – magnitude of the position vector for the added ACC, i.e. the distance between the seismic mass of the redundant ACC and the origin of the local coordinate system, ω_x, ω_y, and ω_z – local coordinate system components of the body angular velocity $\boldsymbol{\omega}$, $\rho_{px}, \rho_{py}, \rho_{pz}$ – local position components of the seismic mass CG of the redundant sensor.

Remark: $\omega_\perp$ is a projection of ω_{ins} on the plane the sensing axis of the accelerometer a_p is normal to. Using an arbitrary angle ϕ between 0° and 90°, $\omega_\perp$ could be split into two orthogonal components, $\omega_{\perp,1} = \omega_\perp \cos \phi$ and $\omega_{\perp,2} = \omega_\perp \sin \phi$, contained within that same plane. Then, using trigonometric identities, it can be shown that:

$$\omega_\perp^2 = \omega_\perp^2(\cos^2 \phi + \sin^2 \phi) = (\omega_\perp \cos \phi)^2 + (\omega_\perp \sin \phi)^2 = (\omega_{\perp,1}^2 + \omega_{\perp,2}^2) \tag{11.18}$$

When all four sensor readings are transformed to the same point, the analytical relationship between the reading from one of the sensors and the readings from the other three is described by Eq. 11.19:

$$a_{p,O} = a_{x,O} \cos \alpha + a_{y,O} \cos \beta + a_{z,O} \cos \gamma \tag{11.19}$$

Through the expanded form of Eq. 11.19, the four sensor readings can be related directly by:

$$a_p = \left[a_x + \rho_{Ox} * (\omega_y^2 + \omega_z^2)\right] \cos\alpha + \left[a_y + \rho_{Oy} * (\omega_x^2 + \omega_z^2)\right] \cos\beta + \left[a_z + \rho_{Oz} * (\omega_x^2 + \omega_y^2)\right] \cos\gamma - \left[\sqrt{\rho_{px}^2 + \rho_{py}^2 + \rho_{pz}^2} * \left(\omega_x^2 + \omega_y^2 + \omega_z^2 - (\omega_x \cos\alpha + \omega_y \cos\beta + \omega_z \cos\gamma)^2\right)\right]$$

(11.20)

$$a_x = \left(\left[a_p + \sqrt{\rho_{px}^2 + \rho_{py}^2 + \rho_{pz}^2} * \left(\omega_x^2 + \omega_y^2 + \omega_z^2 - (\omega_x \cos\alpha + \omega_y \cos\beta + \omega_z \cos\gamma)^2\right)\right] - \left[a_y + \rho_{Oy} * (\omega_x^2 + \omega_z^2)\right] \cos\beta - \left[a_z + \rho_{Oz} * (\omega_x^2 + \omega_y^2)\right] \cos\gamma\right) / \cos\alpha - \rho_{Ox} * (\omega_y^2 + \omega_z^2)$$

(11.21)

$$a_y = \left(\left[a_p + \sqrt{\rho_{px}^2 + \rho_{py}^2 + \rho_{pz}^2} * \left(\omega_x^2 + \omega_y^2 + \omega_z^2 - (\omega_x \cos\alpha + \omega_y \cos\beta + \omega_z \cos\gamma)^2\right)\right] - \left[a_x + \rho_{Ox} * (\omega_y^2 + \omega_z^2)\right] \cos\alpha - \left[a_z + \rho_{Oz} * (\omega_x^2 + \omega_y^2)\right] \cos\gamma\right) / \cos\beta - \rho_{Oy} * (\omega_x^2 + \omega_z^2)$$

(11.22)

$$a_z = \left(\left[a_p + \sqrt{\rho_{px}^2 + \rho_{py}^2 + \rho_{pz}^2} * \left(\omega_x^2 + \omega_y^2 + \omega_z^2 - (\omega_x \cos\alpha + \omega_y \cos\beta + \omega_z \cos\gamma)^2\right)\right] - \left[a_x + \rho_{Ox} * (\omega_y^2 + \omega_z^2)\right] \cos\alpha - \left[a_y + \rho_{Oy} * (\omega_x^2 + \omega_z^2)\right] \cos\beta\right) / \cos\gamma - \rho_{Oz} * (\omega_x^2 + \omega_y^2)$$

(11.23)

Using Eq. 11.20 to Eq. 11.23 any of the four ACC can be predicted based on the other three. These equations can be directly applied in a situation when one ACC fails during the test. The missing reading can be then found from the other three readings, assuming that these three measurements do not contain errors. It is needed to be mentioned here, that for the method to work all four ACC need to be perfectly aligned, local angular rate measured, known and without errors, and angles α, β, γ to be different than multiplications of ±90°.

One redundant ACC is also enough to asses if the recorded kinematics data are consistent, i.e., the predictions from Eq. 11.20 and Eq. 11.23 match the sensor measurements obtained during the test. If the predictions do not follow the measurements, it means that at least one of the four ACC readings contains an error. If only four ACC are utilized, through Eq. 11.20 and Eq. 11.23 it is not possible to identify which of the ACC is erroneous, as Eq. 11.20 and Eq. 11.23 are affected by the same error. To pinpoint the faulty sensor (assuming only one is "inconsistent"), a fifth ACC and the consistency check analysis (as described in Section 11.2) are needed. Similarly to ARS, to have enough new information for the ACC consistency check, the sensing axis of the fifth linear accelerometer should be at a different angle than the axis for the already added (4th) ACC.

Remark: Eq. 11.20 to Eq. 11.23 assume that the angular velocity ω_p is not measured directly by an angular rate sensor. If that measurement is available, Eq. 11.20 to Eq. 11.23 can be simplified:

$$a_p = \left[a_x + \rho_{Ox} * (\omega_y^2 + \omega_z^2)\right] \cos\alpha + \left[a_y + \rho_{Oy} * (\omega_x^2 + \omega_z^2)\right] \cos\beta + \left[a_z + \rho_{Oz} * (\omega_x^2 + \omega_y^2)\right] \cos\gamma - \left[\sqrt{\rho_{px}^2 + \rho_{py}^2 + \rho_{pz}^2} * (\omega_x^2 + \omega_y^2 + \omega_z^2 - \omega_p^2)\right]$$

(11.24)

$$a_x = \left(\left[a_p + \sqrt{\rho_{px}^2 + \rho_{py}^2 + \rho_{pz}^2} * \left(\omega_x^2 + \omega_y^2 + \omega_z^2 - \omega_p^2\right)\right] - \left[a_y + \rho_{Oy} * \left(\omega_x^2 + \omega_z^2\right)\right]\cos\beta - \left[a_z + \rho_{Oz} * \left(\omega_x^2 + \omega_y^2\right)\right]\cos\gamma\right)/\cos\alpha - \rho_{Ox} * \left(\omega_y^2 + \omega_z^2\right)$$

$$(11.25)$$

$$a_y = \left(\left[a_p + \sqrt{\rho_{px}^2 + \rho_{py}^2 + \rho_{pz}^2} * \left(\omega_x^2 + \omega_y^2 + \omega_z^2 - \omega_p^2\right)\right] - \left[a_x + \rho_{Ox} * \left(\omega_y^2 + \omega_z^2\right)\right]\cos\alpha - \left[a_z + \rho_{Oz} * \left(\omega_x^2 + \omega_y^2\right)\right]\cos\gamma\right)/\cos\beta - \rho_{Oy} * \left(\omega_x^2 + \omega_z^2\right)$$

$$(11.26)$$

$$a_z = \left(\left[a_p + \sqrt{\rho_{px}^2 + \rho_{py}^2 + \rho_{pz}^2} * \left(\omega_x^2 + \omega_y^2 + \omega_z^2 - \omega_p^2\right)\right] - \left[a_x + \rho_{Ox} * \left(\omega_y^2 + \omega_z^2\right)\right]\cos\alpha - \left[a_y + \rho_{Oy} * \left(\omega_x^2 + \omega_z^2\right)\right]\cos\beta\right)/\cos\gamma - \rho_{Oz} * \left(\omega_x^2 + \omega_y^2\right)$$

$$(11.27)$$

11.4 Verification of sensor measurement predictions based on a computer simulation

11.4.1 Methods

As the final step, sensor measurement prediction capabilities (as defined by Eq. 11.9, Eq. 11.10, and Eq. 11.20 to Eq. 11.23) were verified using kinematics data obtained from a multi-body model (Figure 115) simulated in a commercial Finite Element (FE) package (LS-Dyna 9.2.0, LSTC, Livermore, CA).
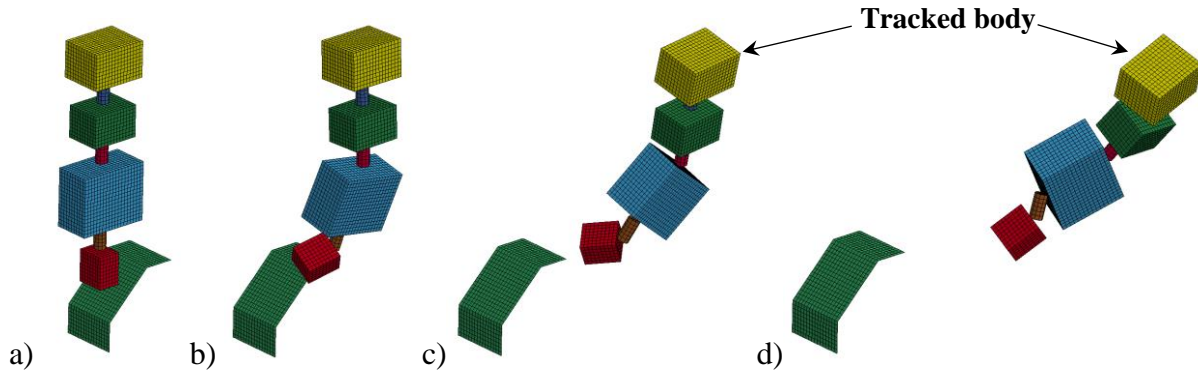
Figure 115. Multi-body model used in the analysis: a) front view, b) oblique view, c) model position later in the simulation.

The model consisted of rigid bodies connected with kinematic joints. It was given an initial velocity. The scenario was designed in a way that at some point during the simulation one of the bodies interacted with an undeformable barrier (rigidly fixed at 45° relative to the model travel direction). That contact disturbed the initial orientation of all connected bodies, causing relative translations and rotations of the parts (Figure 115c).

In the simulation, linear accelerations and angular velocities were measured in the local coordinate system of one of the articulated masses ("yellow" in Figure 115). Four different locations for numerical sensors were selected (Figure 116). Three ACC and three ARS were aligned with the axes of the body local coordinate system. One redundant ACC (a_p) and one redundant ARS (ω_p) were added at a distance from the origin of the local frame.
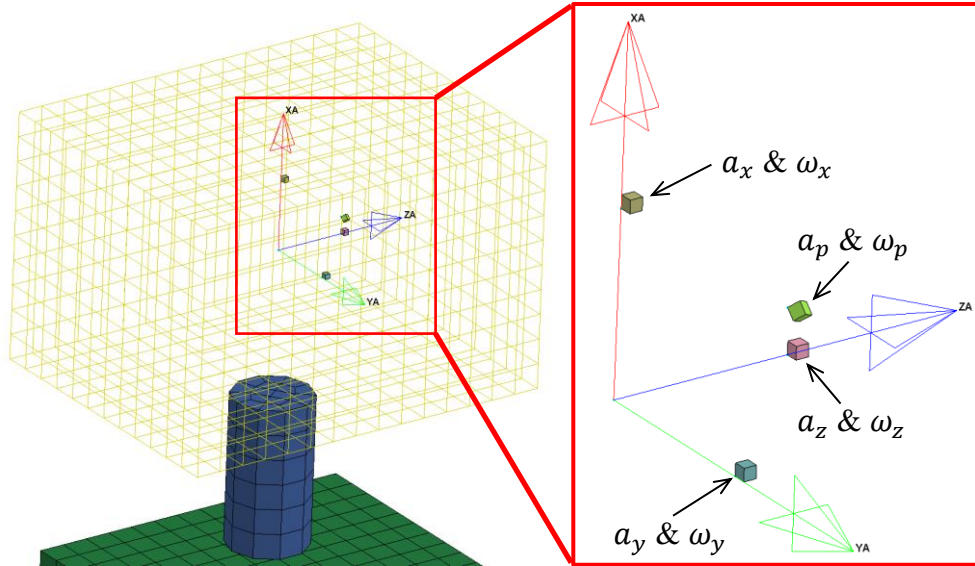
Figure 116. Sensor block configuration.

The coordinates of all of the numerical sensors, in the body-fixed local coordinate frame, were gathered in Table 24.

Table 24. Coordinates of the numerical sensors in local body frame: i = O for the X, Y, Z sensors and i = p for the redundant sensors.

Sensor	ρ_{ix} (mm)	ρ_{iy} (mm)	ρ_{iz} (m)m
a_x & ω_x	70	0	0
a_y & ω_y	0	70	0
a_z & ω_z	0	0	70
a_p & ω_p	40.5	40.5	40.5

Sensing axes of the two redundant sensors were collinear. Their orientation relative to the axes of the local coordinate system was defined with the use of three known angles: α, β, γ. All three angles were 54.7° to ensure equal components of the redundant readings after projection to each of the three axes of the body coordinate frame (Figure 117).

$$\cos\beta = \frac{a}{a\sqrt{3}} = \frac{1}{\sqrt{3}} \Rightarrow$$

$$\beta = \cos^{-1}\left(\frac{1}{\sqrt{3}}\right) = 54.7°$$
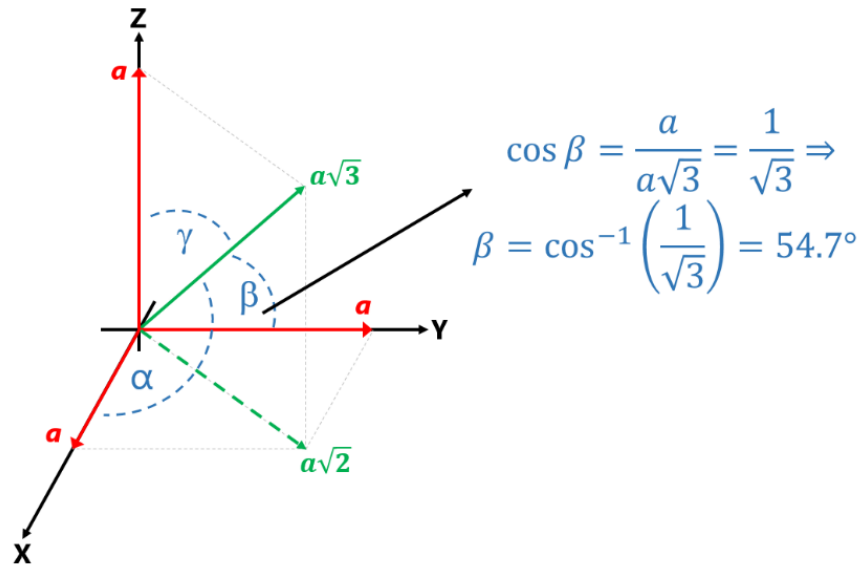
Figure 117. Orientation of the sensing axes of the redundant sensors.

The computer simulation was run up to 1 sec. The recorded kinematics data were utilized as an input to Eq. 11.9, Eq. 11.10, and Eqs. 11.20-11.23 to verify the consistency check methodology. It was done first for angular rate sensors, and next, using four linear accelerometers while assuming that only local X, Y, and Z angular rates were known. As a metric assessing the agreement between the FE sensor output and its prediction, the time history of an absolute difference between both was used.

11.4.2 Results

The results from both, the ARS analysis (Figure 118) and the ACC analysis (Figure 119) showed a good agreement between the predicted output and the output as calculated by the FE software. The entire time-history of the maximum absolute difference for all analyzed numerical sensors:

- for the ARS signals stayed below 0.35% of the maximum absolute value of recorded local body angular rate;
- for the ACC signals stayed below 0.2% of the maximum absolute value of recorded local acceleration.

The maximum absolute value (either for ARS or for ACC) was found based on the data from all four sensors of the same type.
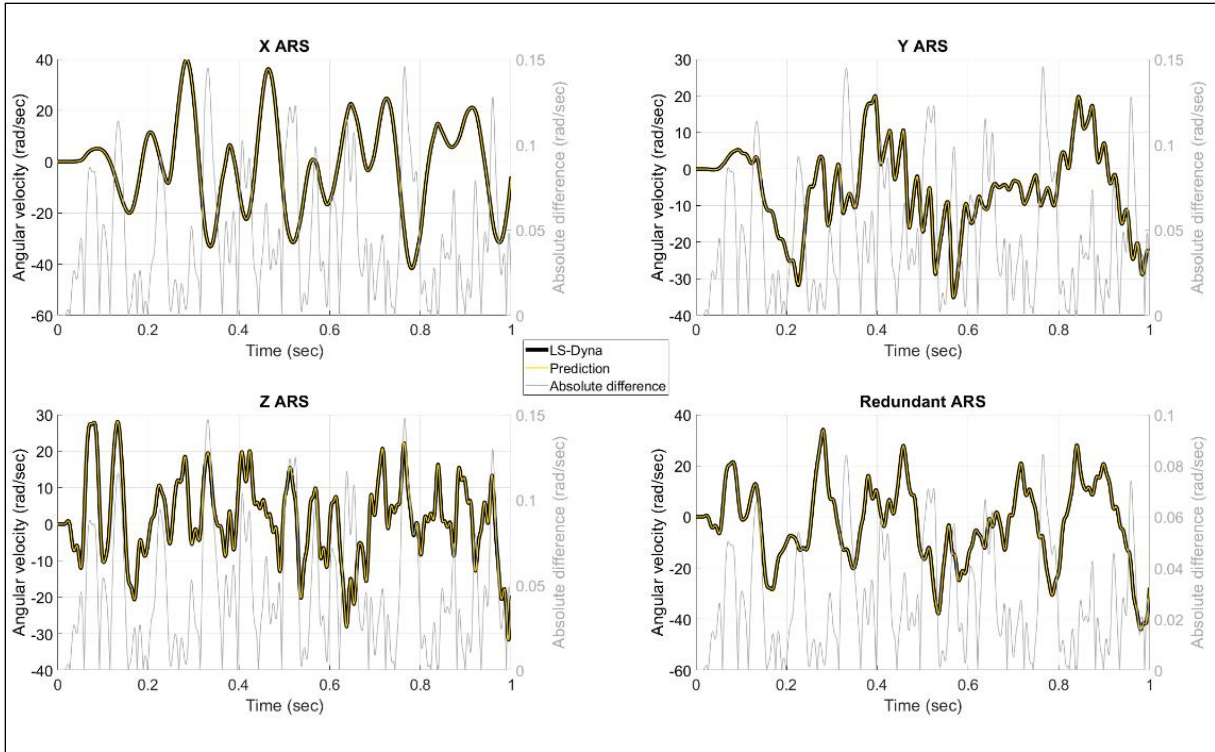
Figure 118. Recorded and predicted local angular velocity for the tracked body.
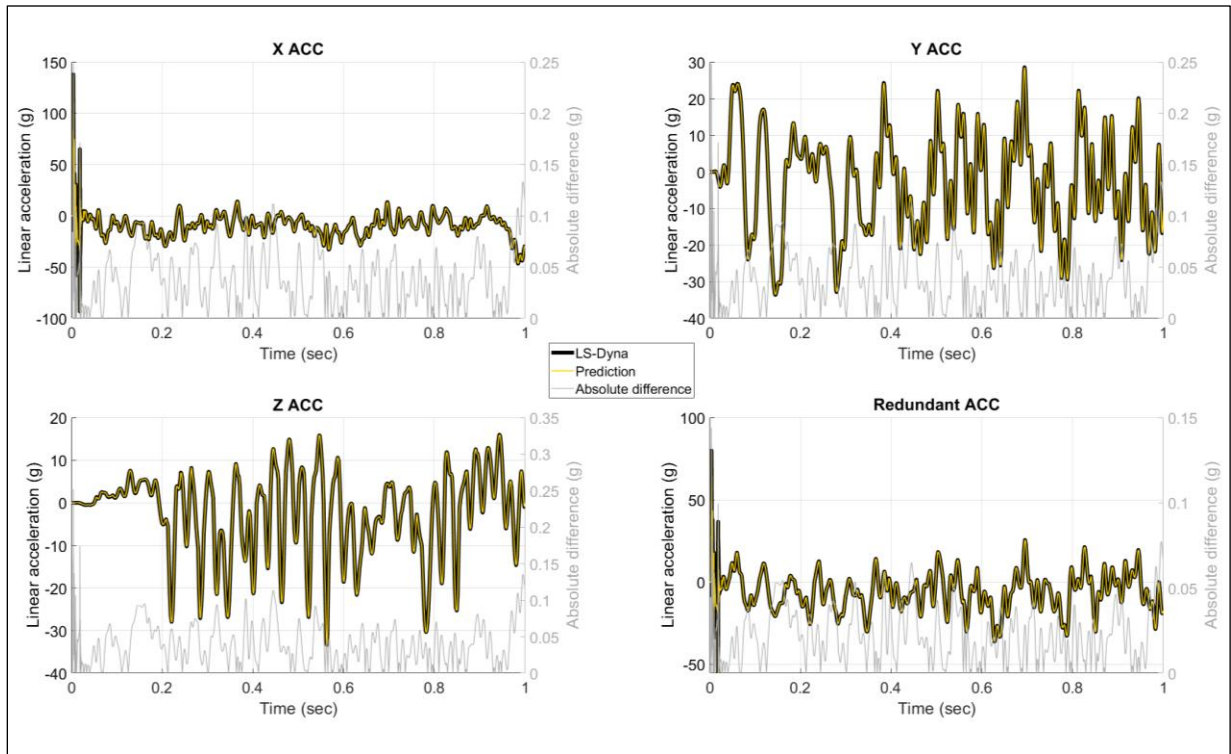
Figure 119. Recorded and predicted local linear acceleration for the tracked body.

145

11.5 Conclusions

In this section, a new method was proposed to account for a sensor that failed during a test or to identify an inaccurate ("inconsistent") sensor that was used to measure rigid body 3D kinematics.

To recover a measurement lost, for example, due to a broken connector or a cable, one added sensor (of the same type as the broken sensor) is needed. By adding two redundant angular rate sensors to a standard "3 ACC + 3 ARS" package, an ARS with errors in its signal can be identified. Similarly, by adding two redundant linear accelerometers, an accelerometer with a faulty response can be pinpointed.

The method is based on an analytical relationship that relates an output (measured quantity) from one of the sensors to the readings from the other sensors of the same type. That mathematical relationship was verified using data from a computer simulation of a simple rigid body system where both, the ARS and the ACC analyses showed a good agreement between the predicted sensor output (as calculated from Eq. 11.9 and 11.10 for ARS, and Eqs. 11.20 to 11.23 for ACC) and the output obtained directly from the FE software.

The presented method is a promising tool that can be utilized to minimize an error in measured body motion resulting from a faulty sensor. Further validation – using real test data – is required, though, to confirm the findings discussed in this study.

12.3D TRAJECTORY CALCULATION IN THOR TESTS UTILIZING THE SENSOR FUSION TECHNIQUE THROUGH THE KALMAN FILTER

The goal of this chapter was to analyze if by performing sensor fusion of two sets of linear accelerometers and angular rate sensors, the deviation between the computed and reference trajectories of the THOR ATD's head could be decreased.

The chapter is organized as follows. Section 12.1 introduces the reader to the concept of the Kalman filter and the senor fusion technique. The following sections describe the ATD instrumentation used in the analysis (Section 12.2), the mathematical equations employed in sensor fusion (Section 12.3), and the error metrics utilized through the study (Section 12.4). Next, the results from two test cases are presented in Section 12.5. Concluding remarks are provided in Section 12.6.

12.1 Introduction

A vehicle is traveling through a 3D space. That vehicle has two sensors attached to it: odometer and GPS. Both of the sensors can be used to determine the vehicle's position relative to the common reference frame. Both measurements give a slightly different response (i.e. position) and both have uncertainty (noise) associated with them. What can be done to discard that noise and obtain the true position of the vehicle? The simplest would be to take an average of the two signals. Due to different levels of uncertainty for different sensors, though, the approach might not always work for real-life problems. An alternative method that accounts for the measurement uncertainty is needed.

The Kalman filter (Kalman 1960) takes the information from both sensors and combines the measurements to find a better estimate $\bar{x}$ (Figure 120). The technique has been used widely in robotics, navigation, and gait studies in the position and orientation estimation (Freeston 2002, Bennett et al. 2013, Rebula et al. 2013, Ferrari et al. 2016, Santhanakrishnan et al. 2017, Zhang et al. 2018).
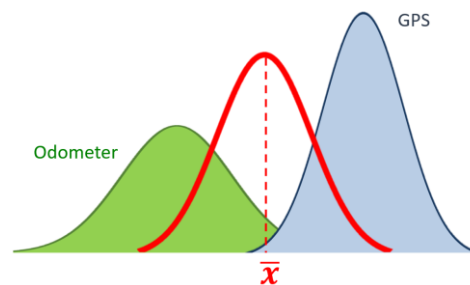
Figure 120. PDF of odometer (green) and GPS (blue) measurements combined to obtain a better estimate (red).

The Kalman filter is an iterative process that uses a set of equations and consecutive data inputs (with known initial variation) to estimate a measured variable (position/velocity/etc.), minimizing the variation in the combined probability density function (PDF) for that variable. The method involves two stages:

- Prediction, in which the measured variable is computed based on the best estimate from the previous step utilized as an input to the mathematical model of the investigated system. If the mathematical model is not available it can be replaced by an identity matrix (the current prediction is equal to the best estimate from the previous step);
- Measurement update, in which the variable from the current prediction step is updated with the data coming from an observation (sensor). In this step, sensor fusion can be performed. The fusion allows for data from more than one sensor to be used to update the prediction.

Sensor fusion combines the data from different sensors taking into account the variance associated with each measurement and finds the optimum averaging factor (so-called Kalman gain) for each consequent state. The Kalman gain assigns different weights to all sources of the input to minimize the influence of either inaccurate mathematical model (if used), or imprecise measurements. In other words, the Kalman filter calculates a weighted average of input signals with the signal weights assigned in a probabilistic way.

In the sled tests performed for this dissertation (with the Simplified Head or with the THOR Mod-kit ATD; APPENDIX A and APPENDIX D, respectively), different sensors were used to measure 3D kinematics of the same tracked object. These different measurements can be combined together with the use of the sensor fusion technique and then utilized in the trajectory calculation process to potentially decrease the high position error observed in the Simplified Head or THOR sled tests.

The goal of this study was to assess if by assuming an identity matrix for the prediction step and performing (in the measurement update step) the sensor fusion of two sets of linear accelerometers and angular rate sensors (with known measurement uncertainties), the deviation between the computed and reference trajectories of the ATD's head would be decreased in Test S0457 and Test S0458 (THOR ATD; no impact; treated here as exemplar cases; for more detail about the tests see Chapter 7).

12.2 Instrumentation

The head 6DOF kinematics were captured with two different types of linear accelerometers (ACC) and two types of angular rate sensors (ARS) (Table 25). The accelerometers were aligned in a way that both types shared the same measurement center. During the test, head's local acceleration and angular velocity were captured at 20 kHz.

Table 25. List of sensors used in both analyzed tests.

Location	Sensor type	Sensor model	Quantity
ATD's head	Linear accelerometer	Endevco 7264C	3
		Endevco 7290E	3
	Angular rate sensor	DTA ARS PRO with bandwidth up to 300 Hz	3
		DTA ARS PRO with bandwidth up to 2000 Hz	3

12.3 Sensor fusion

In this subsection, the sensor fusion algorithm (Section 12.3.1), and the method of obtaining the sensor measurement variance matrix needed for that algorithm (Section 12.3.2), were described.

Prior to the sensor fusion step, head's local linear acceleration was filtered with CFC 1000 and local angular rate with CFC 60.

The kinematics data obtained with the sensor fusion technique were utilized to compute 3D component trajectories of the head as described in Section 1.2.3. To update the orientation of the tracked body (its rotation matrix R), the head's local angular velocity and the method described by Rudd et al. 2006 were used.

12.3.1 Algorithm

The general form of the algorithm utilized to combine kinematics data from two sensors of the same type is given in Eqs. 12.1-12.4:

$$z_k = C_k x_k + q_k \tag{12.1}$$

$$K_k = \widehat{P}_k C_k^T \left(C_k \widehat{P}_k C_k^T + Q_k \right)^{-1} \tag{12.2}$$

$$\overline{x}_k = \widehat{x}_k + K_k (z_k - C_k \widehat{x}_k) \tag{12.3}$$

$$\overline{P}_k = (I - K_k C_k) \widehat{P}_k (I - K_k C_k)^{-1} + K_k Q_k K_k^{-1} \tag{12.4}$$

where x_k – state vector describing the analyzed system (here: 3 x 1 matrix containing components of either ACC or ARS), z_k – observation (here: 6 x 1 matrix containing the data from two sensors of the same type at time k), C_k – state transition matrix transforming the state vector x_k to the measurement domain (here: $C = \begin{bmatrix} I \\ I \end{bmatrix}$, where I – 3 x 3 identity matrix), q_k – Gaussian measurement noise ($\sim N(0, Q_k)$), Q_k – measurement covariance matrix (here: 6 x 6 matrix containing sensor uncertainties along the diagonal terms and zeros for $Q_k(i,j)$ when i $\neq$ j), K_k – Kalman gain (3 x 6 matrix containing weights associated with sensor observations), $\widehat{P}_k$ – a priori state covariance (covariance prior to the measurement update step), $\overline{P}_k$ – a posteriori state covariance (covariance after the measurement update), $\widehat{x}_k$ – a priori state vector (prior to the measurement update step), $\overline{x}_k$ – a posteriori state estimate (ACC or ARS after the sensor fusion).

12.3.2 Measurement variance matrix

Sensor uncertainties u utilized to build the initial measurement covariance matrix Q were obtained by using the combined uncertainty formula (Eq. 12.5):

$$u^2_{sen\_j,comb} = u^2_{calib\_sheet\_based} + u^2_{noise\_based} \tag{12.5}$$

where $u_{sen\_j,comb}$ – combined uncertainty for a sensor j, $u_{calib\_sheet\_based}$ – measurement uncertainty as obtained based on a sensor calibration sheet and measurements from a standardized calibration check test (see APPENDIX R), u_{noise_based} – standard deviation for the sensor signal (noise) before time t = 0.

After determining $u_{sen\_j,comb}$ for all six sensors of the same type, the matrix $\boldsymbol{Q}$ was defined as:

$$\boldsymbol{Q} = \begin{bmatrix} u^2_{sen\_1,comb} & 0 & 0 & & & \\ 0 & u^2_{sen\_2,comb} & 0 & & \boldsymbol{0} & \\ 0 & 0 & u^2_{sen\_3,comb} & & & \\ & & & u^2_{sen\_4,comb} & 0 & 0 \\ & \boldsymbol{0} & & 0 & u^2_{sen\_5,comb} & 0 \\ & & & 0 & 0 & u^2_{sen\_6,comb} \end{bmatrix} \quad (12.6)$$

12.4 Error metrics

Throughout the analysis, the following metric was used to evaluate the accuracy of the head's calculated trajectory:

$$Res_{err} = \sqrt{\frac{\sum_{i=1}^{N}\left[(x_{OSS,i}-x_{calc,i})^2+(y_{OSS,i}-y_{calc,i})^2+(z_{OSS,i}-z_{calc,i})^2\right]}{N}} \quad (12.7)$$

where N – number of data (time) points, $x_{OSS,i}$, $y_{OSS,i}$, $z_{OSS,i}$ – X, Y, Z components of the reference trajectory (from VICON OSS) at the data point i, $x_{calc,i}$, $y_{calc,i}$, $z_{calc,i}$ – X, Y, Z components of the calculated trajectory (based on sensor data).

In addition to Res_{err}, the maximum absolute difference $diff_{max}$ between the calculated and reference trajectories was computed and reported for the three trajectory components.

12.5 Results

After the kinematics data from the sensor fusion were utilized to calculate 3D component trajectories of the ATD's head, the error in the tracked object position was in-between the "best" and "worst" responses produced (with no application of the Kalman filter) by the four sensor packages used on the THOR sled runs (Table 26). In Test S0457 as well as in Test S0458, the Res_{err} metric was higher by 36.4% and 23.7%, respectively, relative to the "Endevco 7264C – DTS ARS PRO 2000Hz" sensor combination, a sensor package that gave the smallest Res_{err} in both tests.

Table 26. Res_{err} in both analyzed tests for kinematics data obtained: from sensor combination that gave the smallest Res_{err} (from the four combinations possible; Kalman filter not used), from sensor combination that gave the highest Res_{err} (from the four combinations possible; Kalman filter not used), after sensor fusion.

Sensor combination	Test S0457		Test S0458	
	Res_{err} (mm)	% increase in Res_{err} w.r.t best case	Res_{err} (mm)	% increase in Res_{err} w.r.t best case
END7264C-DTS2000Hz (best case)	42.91	0	58.54	0
END7290E-DTS300Hz (worst case)	78.45	82.8	86.57	47.9
Sensor fusion for ACC & ARS	58.51	36.4	72.43	23.7

The *diff$_{max}$* metric indicated a substantial increase in the position error for head's X and Y trajectory components, calculated using the sensor fused kinematics data, when compared to the results from the "Endevco 7264C – DTS ARS PRO 2000Hz" case (Table 27). When the Kalman filter was utilized, *diff$_{max}$* for the Z component was lower in Test S0457 and in Test S0458, by 5.9 mm and 1.86 mm respectively, when the trajectory from "Endevco 7264C – DTS ARS PRO 2000Hz" was used as a reference.

Table 27. diff$_{max}$ in both analyzed tests for kinematics data obtained: from sensor combination that gave the smallest Res$_{err}$ (from the four combinations possible; Kalman filter not used), after sensor fusion.

Test #	END7264C-DTS2000Hz (best case)			Sensor fusion for ACC & ARS		
	X (mm)	Y (mm)	Z (mm)	X (mm)	Y (mm)	Z (mm)
S0457	88.7	13.46	38.14	127.11	32.05	32.24
S0458	122.45	7.36	46.33	155.84	33.53	44.47

12.6 Conclusions

In summary, no improvements in the accuracy of the trajectory calculation algorithm were achieved by employing the sensor fusion technique in the two discussed tests. Because the Kalman filter computes a weighted average of the input signals, it is believed that due to the overall high position error seen across different sensor packages in most of the tests performed within this dissertation, the utilization of the sensor fusion technique in those tests also would not bring the trajectory error down. A different method of improving the accuracy of IMU-based position predictions is needed.

13.3D TRAJECTORY CALCULATION IN THOR TESTS UTILIZING THE KNOWLEDGE GAINED FROM THE ERROR EFFECTS ANALYSIS

The goal of this chapter was to analyze if by performing an optimization on either initial orientation or debias values for local acceleration and angular rate data, the deviation between the computed and reference trajectories of the THOR ATD's head could be decreased.

The chapter is organized as follows. Section 13.3.1 gives an overview of the stated problem. The following sections describe the ATD kinematics data used in the analysis (Section 13.3.2), and the optimization process itself, including the definition of objective function and optimization variables utilized in the analysis (Section 13.3.3). Next, the error metrics employed through the study are discussed (Section 13.3.4). The results from the analysis are presented in Section 13.3.5. Concluding remarks are provided in Section 13.3.6.

13.1 Introduction

As it was shown in the *Error effects analysis* (Chapter 10), the error in debias values for linear accelerometers and angular rate sensors, the error in accelerometer sensitivity, as well as the error in the initial orientation of an object can substantially affect the trajectory of the tracked body when its position is computed from the data obtained with locally-mounted inertial sensors.

The debias value depends on: a) the amount of pre-trigger data (before time t = 0) utilized to compute the offset for a sensor signal, and b) the noise level in that signal. The error in the initial orientation of the tracked body (i.e., its rotation matrix R at time t = 0) is related to the accuracy of the measurement method and/or equipment utilized to determine R at t = 0. The error in sensor sensitivity can be amplified by a continuous usage of a sensor that is not calibrated frequently or by running that sensor at a different excitation voltage that the sensor was calibrated at. All of these errors and many more could potentially be responsible for the high discrepancy between the head's computed and reference (VICON) trajectories observed in the THOR tests.

It is believed that because the sensors used in this dissertation were calibrated prior to testing and run at their calibration voltage during testing the error in the sensitivity for linear accelerometers (ACC) and angular rate sensors (ARS) utilized on the sled runs had a negligible effect on the computed head's trajectory. It is hypothesized that the other three error types discussed (ARS and ACC debias as well as the uncertainty in the initial orientation) were the main contributors to the high position error observed in the THOR sled tests. To verify that hypothesis and to minimize the effect of the debias (for both, ACC and ARS) and initial orientation errors, i.e. to improve the accuracy of the trajectory calculation algorithm, an optimization was performed on the data from Test S0455 and Tests S0457 to S0461, with the signal offset values and/or the initial Euler angles treated as optimization variables.

13.2 ATD head kinematics data

In all seven THOR tests, the ATD head local kinematics were captured by three linear accelerometers (Endevco 7264C, Meggitt Sensing Systems, CA, USA) and three angular rate sensors (DTS ARS PRO with bandwidth up to 2000 Hz, Diversified Technical Systems, Seal Beach, CA, USA) sampled at 20 kHz. On the test, in addition to the six sensors, an optical system

(VICON MX, VICON, Los Angeles, CA) was utilized to measure the head's position in the reference (global) coordinate frame. The results from the VICON system (treated in the analysis as the reference) were recorded at 1 kHz.

Before the sensor data were utilized to compute 3D component trajectories of the ATD head (as described in Section 1.2.3), linear acceleration was filtered with CFC 1000 and the local angular rate was filtered to CFC 60. To update the orientation of the tracked body (its rotation matrix R), the head's local angular velocity and the method described by Rudd et al. 2006 were used.

13.3 Description of the optimization process

In the optimization process, the trajectory for the measurement center (Figure 2) for the three Endevco 7264C accelerometers, mounted at the origin of the head local coordinate system, was calculated. Next, Res_{err} (Eq. 12.7) between the computed and the reference (VICON) trajectories was found. The objective of the optimization was to identify:

- a set of three head's initial Euler angles (Case 1),
- a set of three ACC debias values (Case 2),
- a set of three ARS debias values (Case 3),
- a set consisting of three ACC debias values and three head's initial Euler angles (Case 4),

that minimizes that Res_{err}. The MATLAB's gradient-based *fmincon Interior Point* solver (cf. Byrd et al. 2000, cf. Waltz et al. 2006) was used as the optimization algorithm. Varied parameters were: ACC and ARS debias (in X, Y, and Z directions for both types of sensors), as well as initial yaw, initial pitch and initial roll angles (used to build the head's rotation matrix R_{ini} according to the 3-2-1 convention as shown in Wu et al. 2009). The starting values for the sensor debias errors (used in the optimization process) were set to zero. The starting points for the angles were determined from the pre-trigger VICON data for the head, separately in each of the seven investigated THOR tests. The debias values were allowed to vary within ±2 g for ACC and within ±25 deg/sec for the ARS data. The initial Euler angles could vary within ±3 degrees from their starting points. To identify the global minimum, i.e. to minimize the possibility of finding a local minimum of the objective function $min(Res_{err})$, the MATLAB's *GlobalSearch algorithm* (cf. Ugray et al. 2007) was utilized.

13.4 Error metrics

Throughout the analysis the Res_{err} metric (Eq. 12.7) was used to evaluate the accuracy of the head's calculated trajectory. In addition to Res_{err}, the maximum absolute difference $diff_{max}$ between the calculated and reference trajectories was computed and reported for the three trajectory components.

13.5 Results

In this subsection, first, the effect of optimization of initial orientation (i.e. initial Euler angles of the ATD's head) on the error in IMU-based position estimations is discussed (Section 13.5.1). Next, the results from optimization of debias values for linear acceleration (Section 13.5.2) or body's local angular rate (Section 13.5.3) are described. In the final part (Section 13.5.4), the consequences of optimization (at the same time) of both, initial orientation and debias values for body's local linear acceleration are presented.

13.5.1 Optimization of initial orientation (Case 1)

Due to the optimization performed on the three initial Euler angles, Res_{err} was decreased in all seven investigated THOR tests (Table 28). In five tests (S0455 to S0459, and in Test S0462), the Res_{err} after the optimization was below 9.5 mm. In the other two tests, the resulting Res_{err} was above 17.5 mm (Test S0462) or above 23.8 mm (Test S0460). The decrease in the Res_{err} metric was associated with a relatively small change between the starting and the optimized Euler angles. The highest change across the three angles (2.86 deg for yaw) was observed in Test S0458, the smallest (0.07 deg for pitch) in Test S0460.

Table 28. Res_{err} before and after optimization and absolute difference in initial Euler angles due to optimization.

Test #	Res_{err} (mm)			Difference in initial Euler angles due to optimization		
	Before optimization	After optimization	% difference*	Yaw (deg)	Pitch (deg)	Roll (deg)
S0455	19.82	9.41	52.5	0.28	0.89	0.12
S0457	42.91	7.36	82.8	2	0.86	0.18
S0458	58.54	7.67	86.9	2.86	0.89	0.27
S0459	29.53	2.99	89.9	1.34	0.61	0.68
S0460	36.09	23.81	34.0	1.34	0.07	0.34
S0461	29.84	2.65	91.1	1.46	0.13	0.33
S0462	35.69	17.64	50.6	1.53	1.36	2.13

$$* \%diff = 100 - \frac{100 * value\_after\_optimization}{value\_before\_optimization}$$

Due to optimization, the $diff_{max}$ metric decreased for the X and Z trajectory components (with the exception of the Z component in Test S0460) in all seven analyzed test (Table 29). The error in the Y component decreased only in two tests (Test S0461 and Test S0462). In the other five tests, the error in Y increased by 4.6% in Test S0460 to 91.7% in Test S0458.

After the minimum of the objective function $min(Res_{err})$ was found:

- $diff_{max}$ for X was less than 11 mm in Test S0462 and below 7 mm in the remaining six THOR tests,
- $diff_{max}$ for Y varied between 5.4 mm (Test S0461) to 47.51 mm (Test S0460),
- $diff_{max}$ for Z stayed below 12 mm in Test S0460 and below 3.3 mm in the other THOR tests.

Table 29. $diff_{max}$ metric before and after optimization.

Test #	Before optimization			After optimization			% difference*		
	X (mm)	Y (mm)	Z (mm)	X (mm)	Y (mm)	Z (mm)	X	Y	Z
S0455	16.70	17.96	42.33	6.80	22.41	3.27	59.3	-24.7	92.3
S0457	88.7	13.46	38.14	4.15	17.99	2.34	95.3	-33.6	93.9
S0458	122.45	7.36	46.33	4.16	14.11	2.78	96.6	-91.7	94
S0459	48.76	6.21	38.38	4.05	7.39	1.22	91.7	-19	96.8
S0460	62.94	45.40	2.69	4.45	47.51	11.81	92.9	-4.6	-339.6
S0461	59.39	9.26	15.17	6.13	5.4	1.97	89.7	41.7	87
S0462	69.47	46.76	8.99	10.16	42.82	3.27	85.4	8.4	63.7

$$* \%diff = 100 - \frac{100 * value\_after\_optimization}{value\_before\_optimization}$$

13.5.2 Optimization of ACC debias (Case 2)

Due to the optimization performed on the three ACC debias values, Res_{err} was decreased – on average by 80% – in all seven investigated THOR tests (Table 30). In five tests (S0455 and in Test S0459 to Test S0462), the Res_{err} after the optimization was below 7 mm. In the other two tests, the resulting Res_{err} was 9.3 mm (Test S0457) or 10.71 mm (Test S0458). The decrease in the Res_{err} metric was associated with a relatively small change in the ACC debias values. The highest absolute change (0.163 g for ACC Y) was observed in Test S0458, the smallest (0.003 g for ACC Z) in Test S0462.

Table 30. Res_{err} before and after optimization and debias values due to optimization.

Test #	Res_{err} (mm)			Debias value		
	Before optimization	After optimization	% difference*	X (g)	Y (g)	Z (g)
S0455	19.82	3.93	80.2	-0.058	-0.011	-0.041
S0457	42.91	9.3	78.3	0.034	-0.124	-0.070
S0458	58.54	10.71	81.7	0.065	-0.163	-0.071
S0459	29.53	6.02	79.6	0.023	-0.083	-0.047
S0460	36.09	6.82	81.1	0.107	-0.055	-0.015
S0461	29.84	5.61	81.2	0.040	-0.086	0.025
S0462	35.69	5.63	84.2	0.022	0.122	-0.003

$$* \%diff = 100 - \frac{100 * value\_after\_optimization}{value\_before\_optimization}$$

Due to optimization, the $diff_{max}$ metric decreased for the three trajectory components in all seven analyzed test (Table 31). After the minimum of the objective function $min(Res_{err})$ was found:

- $diff_{max}$ for X varied between 4.02 mm (Test S0455) to above 20 mm (Test S0458),
- $diff_{max}$ for Y stayed below 8.4 mm in all seven tests,
- $diff_{max}$ for Z stayed below 9 mm in all seven THOR tests.

Table 31. $diff_{max}$ metric before and after optimization.

Test #	Before optimization			After optimization			% difference*		
	X (mm)	Y (mm)	Z (mm)	X (mm)	Y (mm)	Z (mm)	X	Y	Z
S0455	16.70	17.96	42.33	4.02	3.79	5.27	75.9	78.9	87.6
S0457	88.7	13.46	38.14	17.83	6.09	8.8	79.9	54.8	76.9
S0458	122.45	7.36	46.33	20.6	3.8	6.19	83.2	48.4	86.6
S0459	48.76	6.21	38.38	11.4	6.14	5.38	76.6	1.1	86.0
S0460	62.94	45.40	2.69	14.13	2.53	2.49	77.6	94.4	7.4
S0461	59.39	9.26	15.17	10.98	3.27	4.96	81.5	64.7	67.3
S0462	69.47	46.76	8.99	6.71	8.34	3.83	90.3	82.2	57.4

$$* \%diff = 100 - \frac{100 * value\_after\_optimization}{value\_before\_optimization}$$

13.5.3 Optimization of ARS debias (Case 3)

Due to the optimization performed on the three ARS debias values, Res_{err} was decreased in all seven investigated THOR tests (Table 32). In four tests (Test S0457 to Test S0459 and in Test S0461), the Res_{err} after the optimization was below 4.6 mm. In the other three tests, the resulting Res_{err} varied from 13.36 mm (Test S0455) to 20.88 mm (Test S0460). In multiple tests, the decrease in the Res_{err} metric was associated with a relatively large (absolute) change in the ARS

debias values (10 deg/sec or more), with the highest change of 24.99 deg/sec recorded in Test S0460.

Table 32. Res_{err} before and after optimization and debias values due to optimization.

Test #	Res_{err} (mm)			Debias value		
	Before optimization	**After optimization**	**% difference***	**X (deg/sec)**	**Y (deg/sec)**	**Z (deg/sec)**
S0455	19.82	13.36	32.6	-9.97	-8.66	-1.06
S0457	42.91	2.47	94.2	2.45	-5.69	11.08
S0458	58.54	4.03	93.1	5.22	-4.63	15.72
S0459	29.53	4.56	84.6	1.31	-5.92	7.51
S0460	36.09	20.88	42.1	24.99	10.61	9.48
S0461	29.84	2.45	91.8	-3.02	-0.10	8.65
S0462	35.69	18.9	47	24.96	13.21	-7.28

$$* \%diff = 100 - \frac{100 * value\_after\_optimization}{value\_before\_optimization}$$

Due to optimization, the *diff$_{max}$* metric decreased for the three trajectory components (except for the Y trajectory component in Test S0455 and the Z component in Test S0460 and Test S0462) in all seven analyzed test (Table 33). After the minimum of the objective function $min(Res_{err})$ was found:

- *diff$_{max}$* for X varied between 3.86 mm (Test S0457) to above 11 mm (Test S0462),
- *diff$_{max}$* for Y varied between 4.08 mm (Test S0457) to almost 40 mm (Test S0462),
- *diff$_{max}$* for Z varied between 1.44 mm (Test S0461) to 16.88 mm (Test S0462).

Table 33. diff$_{max}$ metric before and after optimization.

Test #	**Before optimization**			**After optimization**			**% difference***		
	X (mm)	**Y (mm)**	**Z (mm)**	**X (mm)**	**Y (mm)**	**Z (mm)**	**X**	**Y**	**Z**
S0455	16.70	17.96	42.33	10.35	25.9	15.13	38.0	-44.2	64.3
S0457	88.7	13.46	38.14	3.86	4.08	1.82	95.6	69.7	95.2
S0458	122.45	7.36	46.33	4.66	6.85	8.31	96.2	6.9	82.1
S0459	48.76	6.21	38.38	8.86	6.1	6.12	81.8	1.8	84.1
S0460	62.94	45.40	2.69	8.92	35.9	14.74	85.8	20.9	-448.0
S0461	59.39	9.26	15.17	4.49	4.88	1.44	92.4	47.3	90.5
S0462	69.47	46.76	8.99	11.47	39.42	16.88	83.5	15.7	-87.8

$$* \%diff = 100 - \frac{100 * value\_after\_optimization}{value\_before\_optimization}$$

13.5.4 Optimization of ACC debias and initial Euler angles (Case 4)

Guided by the results from Cases 1 to 3 (magnitude of Res_{err} after optimization and the relative change in the optimization parameters due to minimization of the objective function $min(Res_{err})$), it was decided that the combination of three ACC debias values and three initial Euler angles would be used as the optimization variables with the goal of fitting the head's trajectory calculated based on inertial measurements, as close as possible to the trajectory from the optical based system. It was believed that by using that combination of parameters the resulting relative change in the optimization variables would stay within physically possible bounds for the ACC debias errors and the initial orientation measurement inaccuracies.

Due to the optimization performed simultaneously on the three ACC debias values and the three initial Euler angles, Res_{err} was decreased – on average by 90% – in the seven investigated THOR tests (Table 34). In all tests other than Test S0462, the Res_{err} after the optimization was below 2.8 mm. In Test S0462, the resulting Res_{err} was 4.15 mm.

Table 34. Res_{err} before and after optimization.

Test #	Res_{err} (mm)		
	Before optimization	**After optimization**	**% difference***
S0455	19.82	2.77	86.0
S0457	42.91	2.21	94.8
S0458	58.54	2.44	95.8
S0459	29.53	1.80	93.9
S0460	36.09	2.71	92.5
S0461	29.84	2.54	91.5
S0462	35.69	4.15	88.4

$$* \%diff = 100 - \frac{100 * value\_after\_optimization}{value\_before\_optimization}$$

The decrease in the Res_{err} metric was again associated with a relatively small change in both, the ACC debias values and the initial Euler angles (Table 35). The highest absolute change for the offset in the acceleration signal (0.081 g for ACC Y) was observed in Test S0462, the smallest (0.001 g for ACC Z) in Test S0459. The highest change across the three initial angles (3.01 deg for yaw) was observed in Test S0458 (same test as in Case 1 but slightly larger value of the angle change), the smallest (0.07 deg for pitch) in Test S0460 (same test as in Case 1 and the same value of the angle change).

Table 35. ACC debias values and absolute difference in initial Euler angles due to optimization.

Test #	Debias value			Difference in initial Euler angles due to optimization		
	X (g)	**Y (g)**	**Z (g)**	**Yaw (deg)**	**Pitch (deg)**	**Roll (deg)**
S0455	-0.04	-0.02	-0.011	0.38	0.3	0.48
S0457	0.02	0.032	-0.004	2.39	1.02	0.1
S0458	0.023	0.019	-0.005	3.01	0.97	0.27
S0459	-0.004	0.033	0.001	1.8	0.55	1.11
S0460	0.07	0.057	0.005	1.71	0.11	0.51
S0461	0.007	-0.017	0.002	1.2	0.07	0.73
S0462	0.035	0.081	-0.004	0.66	0.7	1.29

Due to optimization, the *diff$_{max}$* metric decreased for the three trajectory components in all seven analyzed test (Table 36). After the minimum of the objective function $min(Res_{err})$ was found:

- *diff$_{max}$* for X varied between 2.69 mm (Test S0455) to 5.98 (Test S0461),
- *diff$_{max}$* for Y varied between 1.81 mm (Test S0459) to 7.63 (Test S0462),
- *diff$_{max}$* for Z varied between 1.35 mm (Test S0459) to 4.28 mm (Test S0458).

Table 36. diff$_{max}$ metric before and after optimization.

Test #	Before optimization			After optimization			% difference*		
	X (mm)	Y (mm)	Z (mm)	X (mm)	Y (mm)	Z (mm)	X	Y	Z
S0455	16.70	17.96	42.33	2.69	4.42	1.69	83.9	75.4	96.0
S0457	88.7	13.46	38.14	2.87	4.88	1.82	96.8	63.7	95.2
S0458	122.45	7.36	46.33	4	2.02	4.28	96.7	72.6	90.8
S0459	48.76	6.21	38.38	4.15	1.81	1.35	91.5	70.9	96.5
S0460	62.94	45.40	2.69	3.72	4.62	2.65	94.1	89.8	1.5
S0461	59.39	9.26	15.17	5.98	4.69	1.37	89.9	49.4	91.0
S0462	69.47	46.76	8.99	3.66	7.63	1.44	94.7	83.7	84.0

$$* \%diff = 100 - \frac{100 * value\_after\_optimization}{value\_before\_optimization}$$

13.6 Conclusions

In summary, when optimization of initial test and sensor parameters was performed using the kinematics data from the THOR sled runs, a substantial decrease in the head's position error was achieved in the discussed ATD tests. From the four investigated sets of optimization parameters (Cases 1 to 4), the combination of three ACC debias values and three initial orientation angles (Case 4) produced 3D component trajectories most closely matching the reference VICON data across the seven sled runs. Due to the optimization performed in Case 4, Res_{err} in all tests other than Test S0462, was below 2.8 mm. In Test S0462, the resulting Res_{err} was 4.15 mm. *diff$_{max}$* in Case 4 varied from 1.81 mm (the Y trajectory component in Test S0459) to 7.63 mm (Y component in Test S0462). In addition, the "Case 4" optimization generated a relatively small (and within physically possible bounds) change in the ACC debias offsets as well as the initial Euler angles relative to their starting (before optimization) values (Table 35).

14.3D TRAJECTORY CALCULATION IN THOR TESTS UTILIZING KNOWN POSITION INFORMATION FROM DATA POINTS AT A CONSTANT TIME INTERVAL

14.1 Introduction

This chapter investigated another approach (different from the one presented in Chapter 13) of improving the accuracy of trajectory prediction computed from inertial measurements. The goal of this study was to asses if by introducing known position information (obtained, e.g., from video tracking or a motion capture system) recorded at a much lower sampling rate than the sensor data, the position error in Test S0462 (treated here as an exemplar case study) would be decreased.

The chapter is organized as follows. Section 14.2 describes the ATD kinematics data used in the analysis. Section 14.3 presents a mathematical method that can be utilized to introduce known position information into the 3D calculation algorithm. Section 14.4 presents an overview of the test cases analyzed in the study. Section 14.5 discusses the error metrics employed through the analysis. The results are presented in Section 14.6. A short discussion about using known body orientation as part of position correction process is presented in Section 14.7. Concluding remarks are provided in Section 14.8.

14.2 ATD head kinematics data

In Test S0462, the ATD head local kinematics were captured by three linear accelerometers (Endevco 7264C, Meggitt Sensing Systems, CA, USA) and three angular rate sensors (DTS ARS PRO with bandwidth up to 2000 Hz, Diversified Technical Systems, Seal Beach, CA, USA) sampled at 20 kHz. On the test, in addition to the six sensors, an optical system (VICON MX, VICON, Los Angeles, CA) was utilized to measure the head's position in the reference (global) coordinate frame. The results from the VICON system (treated in the analysis as the reference) were recorded at 1 kHz. No occlusion of the head occurred during the test, making the VICON data a complete set that was used in the direct comparison with the trajectory obtained based on the locally-mounted inertial sensors.

Before the sensor data were utilized to compute 3D component trajectories of the ATD head (as described in Section 1.2.3), linear acceleration was filtered with CFC 1000 and the local angular rate was filtered to CFC 60. To update the orientation of the tracked body (its rotation matrix R), the head's local angular velocity and the method described by Rudd et al. 2006 were used.

14.3 Interpolation algorithm

It is known from the previous chapters that when the trajectory of the THOR's head (in Test S0462) was computed using inertial measurements and no optimization was run to account for the sensor and initial orientation errors, the maximum absolute deviation between the calculated and the reference trajectories was approx. 70 mm in the X direction, approx. 47 mm in Y, and approx. 9 mm in Z (Table 36). To decrease the error in the calculated response, information with known 3D position of the ATD's head (obtained from the motion capture system) was introduced into the

trajectory calculation algorithm at a constant time interval *Δ*. The correction (called from now on *X*) created a discontinuity in the response obtained from the sensors (Figure 121).
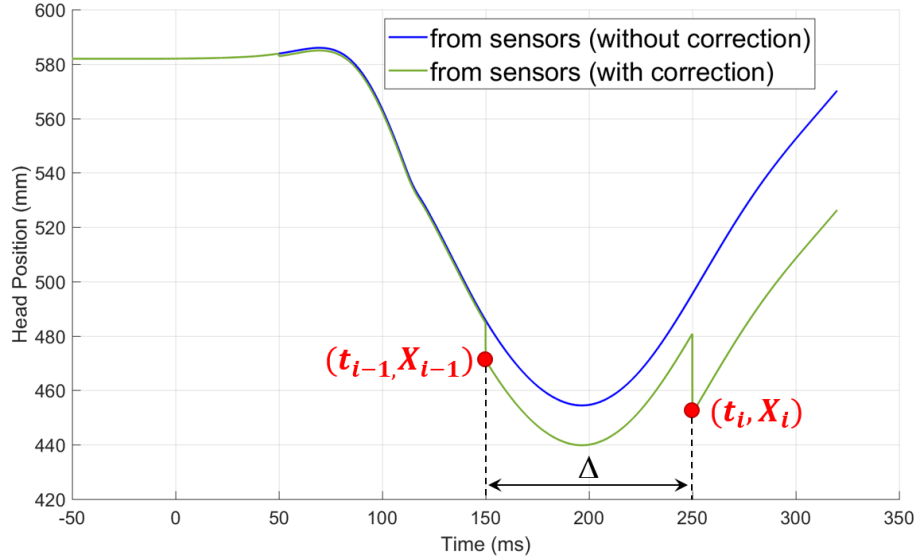
Figure 121. Head trajectory calculated using inertial sensor with (green) and without (blue) introduction of known position information X (red points).

To account for the discontinuity, an interpolation algorithm was employed for the trajectory between two consecutive corrections, X_{i-1} and X_i. The algorithm was adapted after Shaw et al. 2009 and it was as follows (Eq. 14.1):

$$f_{interp}(t) = f(t) - \frac{t - t_{i-1}}{\Delta} * (f(t_i) - X_i) \tag{14.1}$$

where t – time, t_{i-1} – time when X_{i-1} correction was introduced, t_i – time when X_i correction was introduced, $f_{interp}(t)$ – interpolated time-history of the position of the tracked body, $f(t)$ – trajectory at time t as calculated from inertial measurements after corrections were introduced (green line in Figure 121), $f(t_i)$ – trajectory as calculated based on the inertial measurement at time when the X_i correction was introduced, Δ – the time interval between two consecutive corrections.

For the cases when Δ was bigger than the time interval between the last introduced correction and the last available sensor data point, i.e., when X_{i-1} was known but X_i was not, Eq. 14.1 was modified to use the difference between the calculated and reference trajectories from the beginning of the interpolated time period:

$$f_{interp}(t) = f(t) - \frac{t - t_{i-1}}{\Delta} * \left(f(t_{i-1}) - X(t_{i-1}) \right) \tag{14.2}$$

14.4 Time intervals used

Nine different cases (nine values of *Δ*) where investigated in the study (Table 37).

Table 37. Nine cases investigated in the study.

Case #	Time interval Δ between consecutive corrections (sec)	Sampling rate of correction X (Hz)	# of sensor data points between corrections X	# of introduced corrections X
1	0.001	1000	20	370
2	0.002	500	40	185
3	0.004	250	80	92
4	0.008	125	160	46
5	0.01665	60	333	22
6	0.03325	30	665	11
7	0.0666	15	1332	5
8	0.1	10	2000	3
9	0.2	5	4000	1

14.5 Error metrics

In the Results section, Res_{err} (Eq. 12.7) of 35.69 mm, calculated for the trajectory of the THOR's head when no optimization was run to account for the sensor and initial orientation uncertainties, was treated as the reference error value. In all nine cases from Table 37, Res_{err} was recalculated and its percentage decrease (relative to Res_{err} of 35.69 mm) was reported. In addition to Res_{err}, the maximum absolute difference $diff_{max}$ between the computed and reference trajectories was found and presented for the three trajectory components. Finally, the time history of the absolute difference (error) between the computed and reference (from VICON) trajectories was presented for Case 8.

14.6 Results

In all cases other than Case 9, due to the introduction of position corrections X, Res_{err} from the "not corrected" test was decreased by more than 93% (Table 38). In the first five cases, where more than 20 corrections were used, the decrease in Res_{err} was above 99%. The smallest improvement in the computed trajectory was observed for Case 9. Even though only one point with known head position was utilized in that case, the resulting error in the calculated position was still reduced substantially, by approx. 45%.

Table 38. Res_{err} decrease in the nine investigated cases.

Case #	# of introduced corrections X	% decrease in error*
1	370	99.26
2	185	99.24
3	92	99.23
4	46	99.21
5	22	99.1
6	11	98.9
7	5	96.8
8	3	93.5
9	1	45.1

$$* \%diff = 100 - \frac{100 * Res_{err} \text{ of corrected trajecotry}}{Res_{err} \text{ of non-corrected trajecotry}}$$

In the "not corrected" test, the maximum absolute deviation between the calculated and the reference trajectories was approx. 70 mm in the X direction, approx. 47 mm in Y, and approx. 9 mm in Z (Table 36). Due to the introduction of known position points, the absolute error in the trajectory components was decreased in all nine cases (Table 39). In the cases where more than 10 corrections were utilized, $diff_{max}$ was less than 1.2 mm across all three trajectory components. In Cases 7 and 8 (respectively, 5 and 3 corrections introduced), the $diff_{max}$ metric was approx. 5 mm or less. The only case were the deviation between the computed and "from VICON" trajectories was still at a high level was Case 9 (one correction used), with the error in X up to 42 mm, error in Y up to 30 mm, and error in Z up to 3.8 mm (last row in Table 39).

Table 39. diff$_{max}$ in the nine investigated cases.

Case #	# of introduced corrections X	X (mm)	Y (mm)	Z (mm)
1	370	0.1	0.64	0.29
2	185	0.1	0.66	0.31
3	92	0.23	0.67	0.3
4	46	0.37	0.67	0.59
5	22	0.35	1.16	0.49
6	11	0.59	1.13	0.43
7	5	2.82	2.11	1.42
8	3	5.11	3.97	2.32
9	1	42.34	30.33	3.85

When only three known position points (Case 8) were introduced into the trajectory calculation algorithm, the interpolated response matched the reference response closely (Figure 122). As it was expected, between two consequent corrections X, the absolute error in the interpolated trajectory, first, grew for the first half of the time interval $\varDelta$, reached its maximum, and then decreased as it was approaching the time point at which the next correction was utilized. Due to $\varDelta$ being bigger than the time interval between the third X and the last available point in the sensor data, Eq. 14.2 was utilized to interpolate the last part of the trajectory. The use of the difference between the calculated and reference trajectories from the beginning of the interpolated time period led to the highest position error observed throughout the entire analysis recorded at the end of the test.
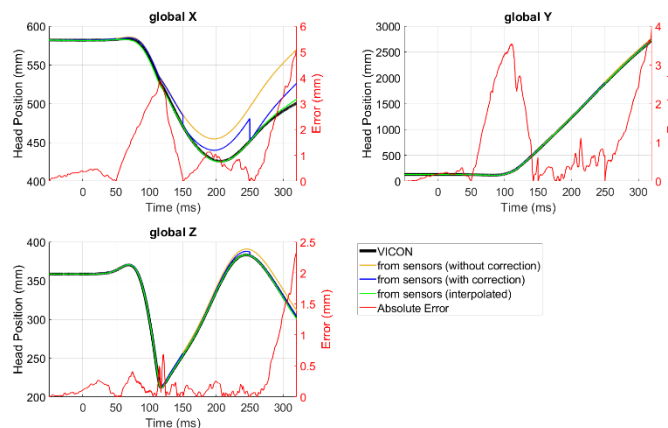
Figure 122. Head global trajectories for Case 8 (Sampling rate of correction: 10 Hz; three corrections introduced). Absolute error (in red) calculated between VICON and the interpolated response.

14.7 Known orientation – discussion

In Test S0462, multiple targets were attached to the ATD's head and tracked throughout the event. Based on those targets the whole time history of the head was obtained. When that complete orientation time history was utilized in the trajectory calculation algorithm, a decrease in the head's position error, when compared to the "not corrected" test, was observed (Figure 123). It is needed to mention here that interpolation was not employed in this analysis.
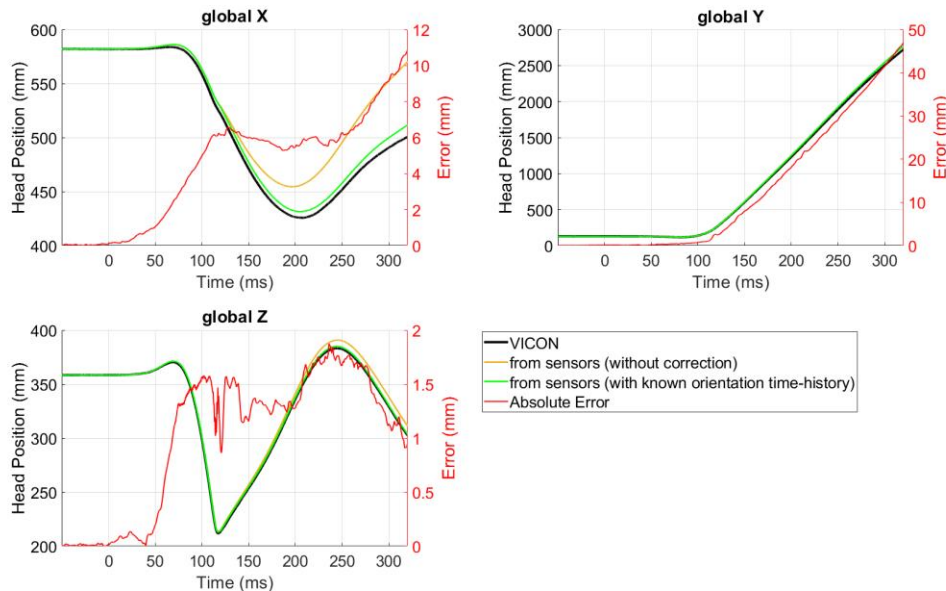
Figure 123. Head global trajectories assuming that the entire time-history of the body's orientation is known. Absolute error (in red) calculated between VICON and the response obtained using known time-history of the head's orientation.

The maximum absolute value of the difference between the computed and reference trajectories was approx. 11 mm in the X direction, above 45 mm in Y, and approx. 2 mm in Z. Even though the entire known orientation time history was utilized in this analysis, the resulting position error was still higher (for all three trajectory components) than in Case 8, when only three data points from VICON were used.

14.8 Conclusions

In summary, in Test S0462, when known information about 3D position of the tracked body was introduced into the trajectory calculation algorithm, a substantial improvement in the accuracy of the computed position was achieved in eight out of nine investigated test cases. In these eight cases, three or more corrections were utilized. Even when only three corrections X were used (Case 8), Res_{err} (when compared to a test without these three points) decreased by more than 93% and the maximum absolute difference for all three trajectory components stayed below 5.5 mm. When the entire known orientation time history was utilized in the analysis (no interpolation used), the absolute difference between the computed and reference trajectories was still higher (for all three trajectory components) than in Case 8.

15.INTERPOLATION OF MISSING OPTICAL DATA BASED ON INERTIAL MEASUREMENTS

The goal of this chapter was to evaluate two different techniques of providing kinematics data over a missing part of optical data caused by intermittent object obscuration.

The chapter is organized as follows. Section 15.1 gives an overview of the stated problem. The following sections describe the kinematics and optical data used in the analysis (Section 15.2), and all investigated test cases (Section 15.3). In Section 15.4, the error metrics employed through the study are discussed. The results from the analysis are presented in Section 15.5. Concluding remarks are provided in Section 15.6.

15.1 Introduction

Optical based systems are an accurate method of capturing motion of a body traveling through a 3D space (Lessley et al. 2011, Toczyski et al. 2015). The biggest disadvantage of these systems, though, is the requirement of a constant line of sight between the cameras and the tracked object throughout the event. When the object obscuration occurs, i.e., when the targets or predefined patterns on the tracked body are not detected by the cameras anymore, neither video tracking nor optical systems can provide accurate information about the body's orientation and position during the time when the body is not visible in the cameras' field of view. Often, however, information about the position of that body is available pre and/or post the obscuration phase (Figure 124).
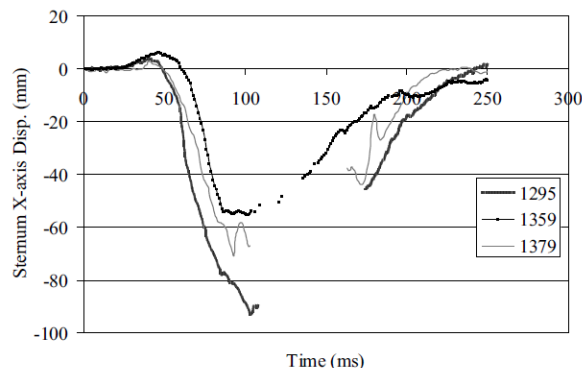
Figure 124. Example of trajectories with missing optical data (copied from Shaw et al. 2009; page 33, Figure D1).

The time intervals during which the optical data is missing will be referred to as "gaps" from here on.

Several researchers have investigated different methods of providing displacement data for gaps in 3D trajectory traces. Shaw et al. 2009 proposed an interpolation scheme that determines kinematic data over a gap using displacement information from tests of the same type as the one in which the gap occurred. Schoenebeck et al. 2009 utilized a method that uses inertial measurements recorded along with the optical data, to interpolate the missing part of the trajectory. Schoenebeck's method was based on optimization of initial conditions (position, velocity, and orientation) of the tracked body. In the technique, two trajectories (one with a gap and one

calculated with the use of inertial sensors) were tied together during the phases when the position data from video capture was available for the tracked ATD's head. Sinz et al. 2015 used similar approach as Schoenebeck but added sensor specific parameters (ACC/ARS debias values, and ACC/ARS sensitivity errors) as optimization variables with the goal of fitting the trajectory calculated based on inertial measurements, as close as possible to the trajectory from an optical based system. Klein et al. 2016 expanded on Sinz's research by investigating different optimization algorithms.

The goal of this study was to evaluate two techniques of interpolating an optical data gap using kinematics data from Test S0461 (treated here as an exemplar case study). The two techniques were:

- employment of inertial measurements in conjunction with optimization performed on initial orientation of the tracked body, varying amount of "visible" data used to tie partial VICON trajectories with the trajectories obtained from the sensors attached to the ATD's head,
- interpolation scheme from Eq. 14.1 utilizing the beginning and the end point of the gap.

15.2 Sensor and optical data

Sensor and optical data recorded during Test S0461 (THOR ATD sled test, with head-to-structure impact simulated) were used in the analysis. For the purpose of the study, it was assumed that the motion of the head was obscured through part of the test (Figure 125). The motion capture system was able to record the head's position between time t = -50 msec and t = 75 msec (where time t = 0 indicated the start of the sled motion) and then after t = 250 msec till the end of the test (t_{end} = 323 msec).
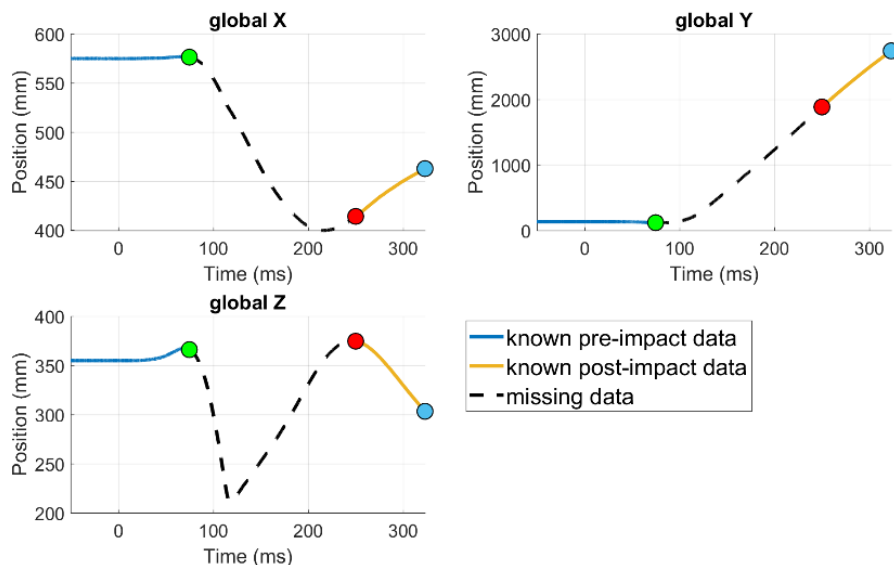
Figure 125. Test S0461 – Head global trajectory used in the analysis.

The ATD's head was instrumented with a 6DOF sensor package containing three linear accelerometers (Endevco 7264C, Meggitt Sensing Systems, CA, USA) and three angular rate

165

sensors (DTS ARS PRO with bandwidth up to 2000 Hz, Diversified Technical Systems, Seal Beach, CA, USA). On the test, the kinematics data were captured at 20 kHz.

Before the sensor data were utilized to compute 3D component trajectories of the ATD head (as described in Section 1.2.3), linear acceleration was filtered with CFC 1000 and the local angular rate was filtered to CFC 60. To update the orientation of the tracked body (its rotation matrix $\boldsymbol{R}$), the head's local angular velocity and the method described by Rudd et al. 2006 were used.

15.3 Considered cases

Seven cases were investigated in this study (Table 40). In six of the cases optimization of the head's initial Euler angles was performed varying the amount of partial information available from the optical system. The optimization technique used was the same as the approach described in Chapter 13, with the exception of different number of data points used to minimize the objective function. In the seventh case, the missing part of the trajectory was found using the senor data recorded on the test, two points from the motion capture system (green and red in Figure 125), and the interpolation method described in Chapter 14.

Table 40. Seven cases in which different amount of data from Figure 125 was used in the optimization process.

#	Case
1	Optimization based on blue point only
2	Optimization based on red point only
3	Optimization based on red + green points
4	Optimization based on pre-impact data
5	Optimization based on post-impact data
6	Optimization based on pre- and post-impact data
7	Interpolation based on red + green points

15.4 Error metrics

Throughout the analysis the Res_{err} metric (Eq. 12.7) between the computed response and the reference position time history from the VICON system (complete, without the gap), was used to evaluate the accuracy of the head's calculated trajectory. In addition, the maximum absolute difference $diff_{max}$ between the computed and reference trajectories was found and reported for the three trajectory components. Finally, in selected cases, the time history of the absolute difference (error) between the calculated and reference (VICON) trajectories was determined and presented.

15.5 Results

From the seven cases run within this study, in six of them Res_{err} was below 5 mm and the maximum deviation from the reference VICON data ($diff_{max}$ for all three trajectory components) was less than 12.1 mm (Table 41). In one case (Case 4, when only the pre-impact data, marked in blue in Figure 125, were utilized) the calculated trajectory deviated from optical data substantially, with Res_{err} reaching approx. 44 mm and $diff_{max}$ varying between 5.47 mm in Y to almost 97 mm in Z. Res_{err} in Case 4 was higher by approx. 91% than in Case 5 (only post-impact data used), approx. 90% higher relative to Case 1 (position from the blue point, i.e. the last available data

point, utilized; Figure 125), and approx. 89% higher than in Case 2 (end point of the gap, i.e., red point in Figure 125, used).

Table 41. Res$_{err}$ and diff$_{max}$ for the seven investigated cases.

#	Case	Res$_{err}$ (mm)	diff$_{max}$ (mm)		
			X	Y	Z
1	Optimization based on blue point only	4.45	5.96	3.85	4.21
2	Optimization based on red point only	4.92	12.04	7.26	9.95
3	Optimization based on red + green points	4.3	11.36	6.81	8.38
4	Optimization based on pre-impact data	44.11	26.75	5.47	96.89
5	Optimization based on post-impact data	3.86	5.15	3.79	4.1
6	Optimization based on pre- and post-impact data	3.76	4.25	5.35	5.39
7	Interpolation based on red + green points	3.71	8.62	2.89	2.83

Within the six cases, in which the optimization was performed, the smallest Res_{err} (of 3.76 mm) was recorded in Case 6 where both, known pre and post-impact data were utilized. Slightly higher Res_{err} (3.86 mm) was found for Case 5 in which only the post-impact data were used. In both scenarios in which optimization was based on one post-impact point (Case 1 and Case 2), Res_{err} stayed below 5 mm. The smallest Res_{err} (of 3.71 mm) as well as the smallest $diff_{max}$ for the Y and Z trajectory components (2.89 mm and 2.83 mm, respectively) were recorded in Case 7, the only case in which the interpolation algorithm from Chapter 14 was utilized instead of the optimization scheme.

15.5.1 Global position plots

In this section, the time histories of the calculated global position for the ATD head (and thus the missing gap in the optical data from Figure 125) were compared to the complete reference VICON data. For clarity only four cases were presented: Case 1 (Optimization based on blue point only), Case 4 (Optimization based on pre-impact data), Case 6 (Optimization based on pre- and post-impact data), and Case 7 (Interpolation based on red + green points from Figure 125). In the figures, the absolute error between the reference and calculated trajectories was indicated with a red line.

In Case 1 (Figure 126), Case 6 (Figure 128), and Case 7 (Figure 129), the computed trajectory matched the reference VICON response closely throughout the entire event. It is worth pointing out here that no substantial difference in the position error magnitude between Case 1 (the last available data point utilized in the optimization process) and Case 6 (both, pre- and post-impact VICON data used) was observed. In Case 4 (Figure 127), where only the pre-impact data were used in the initial orientation optimization, the trajectory determined from inertial measurements followed the VICON trajectory well till the impact between the head and the steel barrier occurred (at approx. t = 116 msec). After the impact, the head's calculated trajectory deviated substantially from the optical data in the X and Z direction, with the error in the Y component staying below 6 mm throughout the test (Figure 127).
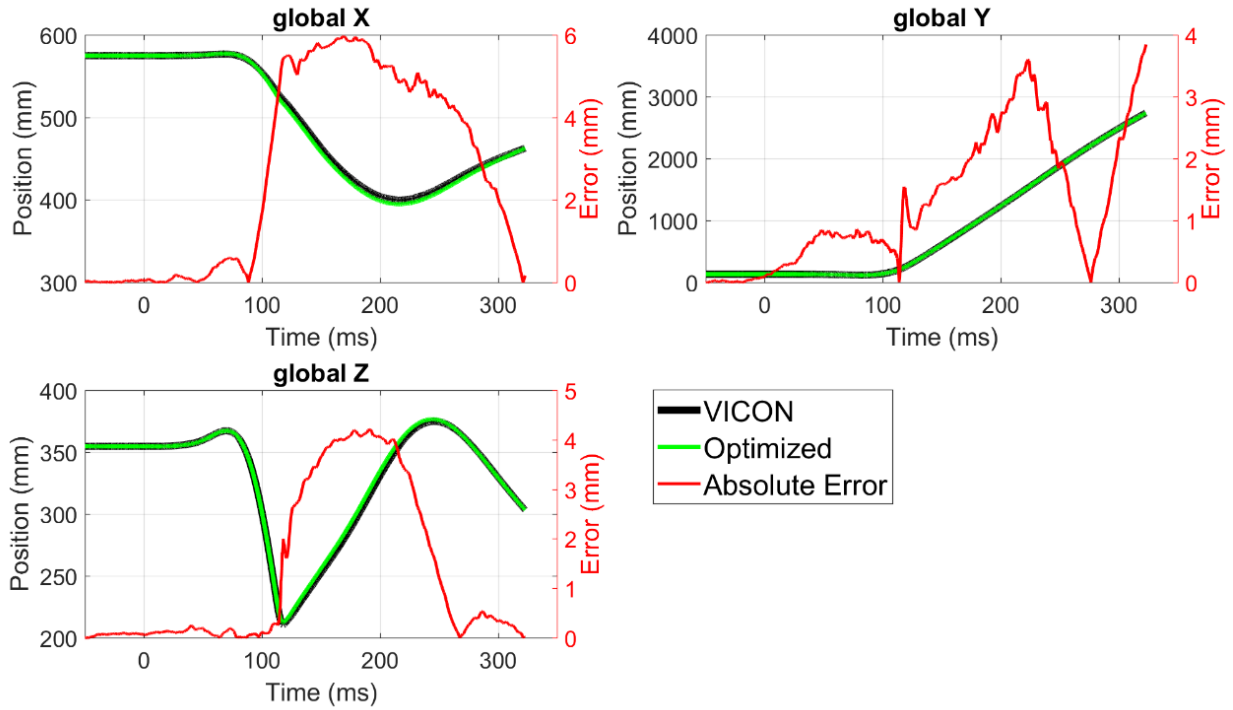
Figure 126. Case 1: Head global trajectories comparison: VICON (black) and response optimized based on the blue point only (green).
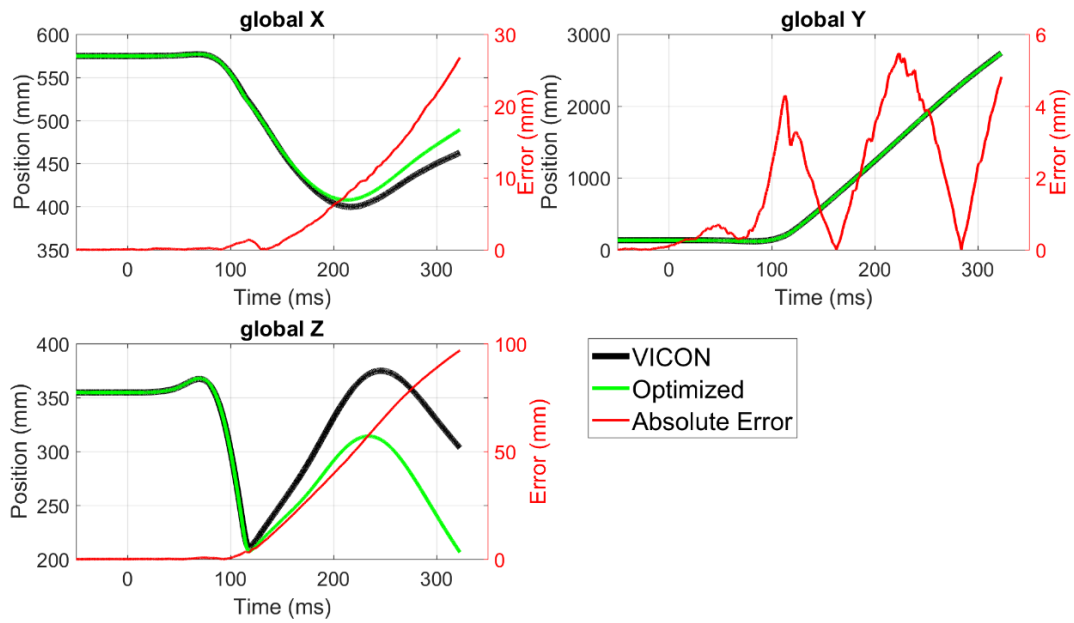
Figure 127. Case 4: Head global trajectories comparison: VICON (black) and response optimized based on pre-impact data only (green).

168
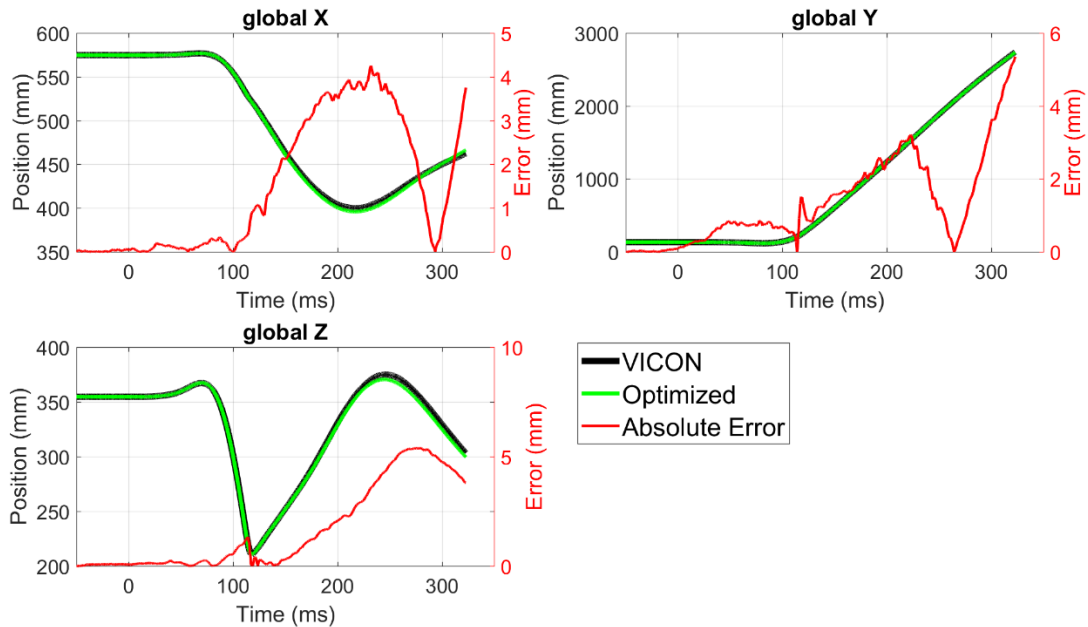
Figure 128. Case 6: Head global trajectories comparison: VICON (black) and response optimized based on pre- and post-impact data (green).
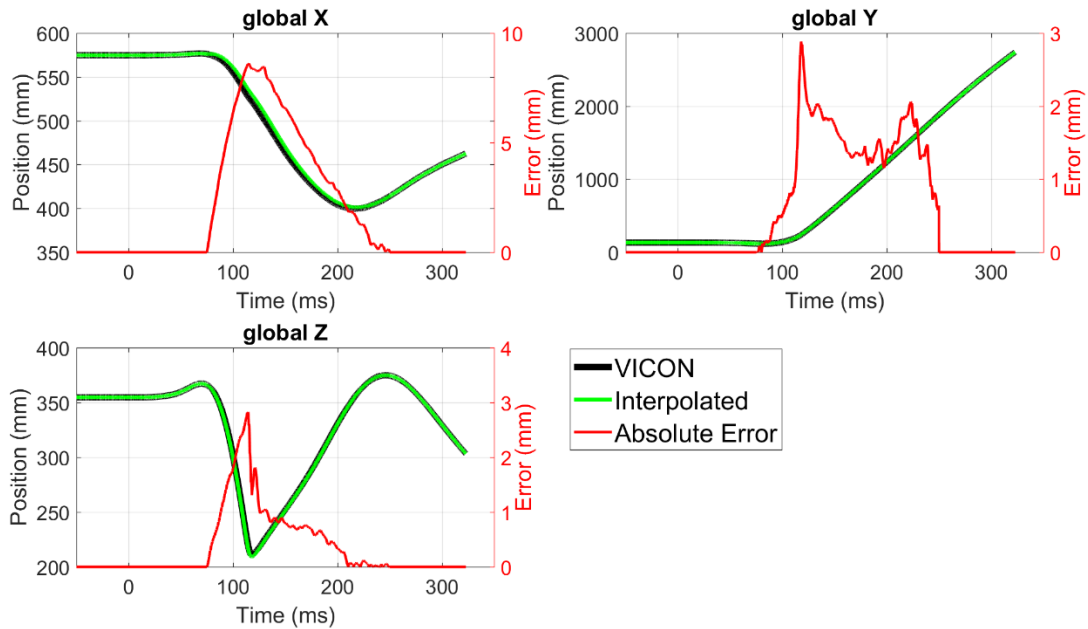
Figure 129. Case 7: Head global trajectories comparison: VICON (black) and response interpolated using the green and red points (green).

15.6 Conclusions

In summary, in Test S0461, both techniques utilized to provide the kinematics data over an optical data gap gave satisfactory results, with exception of the case where only pre-impact data were used in the analysis. Within the six cases, in which the optimization of the head's initial orientation was performed, the smallest position error (as defined by Res_{err}) was recorded when

both, known pre and post-impact data were utilized in the trajectory calculation algorithm (Case 6). It is worth pointing out, though, that there was no big difference in the position error magnitude between Case 1 and Case 2 (one post-impact point used during optimization) when compared to Case 6.

In this study, the smallest Res_{err} as well as the smallest $diff_{max}$ for the Y and Z trajectory components were found in Case 7, the only case in which the interpolation algorithm from Chapter 11 was utilized instead of the optimization scheme. Additionally, the wall clock time needed to perform the "Case 7" analysis was noticeably shorter (< 0.1 sec) than the wall clock time in the six optimization cases (> 5 min).

16. ATD HEAD MOTION RELATIVE TO THE VEHICLE: THE EFFECT OF VEHICLE INERTIAL SENSOR MOUNTING LOCATION

This chapter was published as a short communication in the proceedings of the IRCOBI 2018 conference. The conference took place in September 2018, in Athens, Greece. The authors were: Jacek Toczyski (main), Bronisław Gepner, and Jason R. Kerrigan. The full publication (modified by adding one more reference) can be found below.

16.1 Introduction

In vehicle crash testing, tracking occupant body segments kinematics is critical to the assessment of restraint functionality and injury risk. The occupant motion inside a vehicle has been investigated widely using either video tracking or 3D optical motion capture systems such as Vicon (Vicon MX, Vicon, Los Angeles, CA, USA) (Ólafsdóttir et al. 2013, van Rooij et al. 2013, Lessley et al. 2014, Zhang et al. 2014). Both of these methods, though, can be costly, time-consuming, and they require constant line of sight between the cameras and tracked markers throughout the whole event. In tests where motion of the occupant is obscured by the vehicle's interior components or safety systems, e.g., deployed airbags, neither video tracking nor optical systems can provide accurate information about the body segments orientation and position.

Anthropomorphic Test Devices (ATDs) used in crash testing nowadays are instrumented with sensor packages consisting of linear accelerometers and angular rate sensors. These sensor packages are usually mounted in several different body regions, including the head or the spine. Using the data from the sensors, time histories of 3D kinematics of each instrumented body part can be reconstructed. The same type of sensor package can be installed inside a vehicle to capture its motion (Wu et al. 2009). The data from the two sets of sensors permit description of the body segments motion relative to the vehicle. However, if, during the impact, the vehicle structure deforms at the sensor mounting location, this local deformation will affect the calculated orientation and position of the car, and, subsequently, the occupant's relative trajectory (Aparicio et al. 2009).

The goal of this study was to examine how vehicle deformations at sensor mounting locations affect predicted head (treated here as an exemplar body region being tracked) relative to vehicle kinematics in a full-scale oblique offset frontal crash test.

16.2 Methods

Occupant head motion relative to vehicle was calculated based on the data from a frontal oblique offset test of a pickup truck (NHTSA 2017a). In the test, a moving barrier was driven into the front-left side of the vehicle at approx. 90 km/h. The THOR ATD was positioned in the driver's seat, and its head was instrumented with the stock sensor package of three linear accelerometers and three angular rate sensors. Four identical 6 degree-of-freedom (DOF) sensor packages were mounted inside the truck to obtain the head motion relative to each of the four vehicle reference points. The mounting sites included the vehicle's center of gravity (CG), the bottom of the left and right B-pillars, and the truck bed. Prior to testing, the initial orientation of the THOR's head and

the mounting plates for the vehicle sensor cubes – in the global frame – were determined with a Coordinate Measuring Machine (CMM). During the test, the sensor data were recorded at 10 kHz.

Upon testing, a numerical algorithm with an input in the form of filtered local linear accelerations and angular rates was utilized to obtain the global acceleration vectors for the head and the four vehicle points. Next, the global acceleration vectors were double integrated to determine the position time-history of the head CG and the vehicle reference locations. Finally, using the vehicle reference frame (VRF) defined according to the SAE J211 document, the excursion of the ATD's head relative to each of the four truck points was obtained.

16.3 Findings

All four calculated head trajectories followed a similar *loop-like* pattern. After the impact, THOR's head moved forward (in positive X), outward (in negative Y) and downward (in positive Z) towards the driver's side A-pillar (Figure 130). After the contact with the frontal airbag, the head reached its maximum excursion and then rebounded. In the vehicle's XY plane, the four responses varied slightly in terms of the overall curve shape, with the *Veh CG* (red curve) having the smallest, and the *Left B-pillar* (blue) biggest *loop*. In the XZ plane, all four curves were close to each other until the peak Z value, with the *Left B-pillar* trajectory deviating noticeably from the other three after reaching the peak.
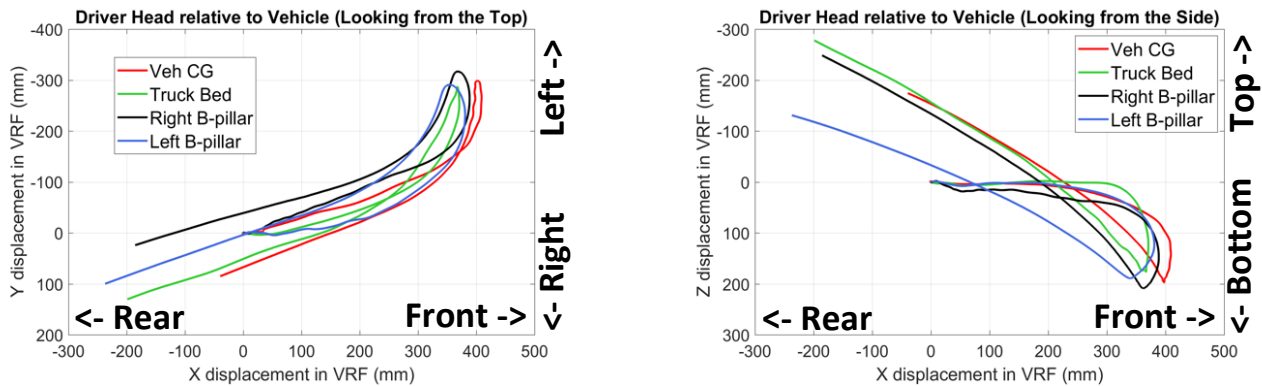
Figure 130. THOR's head excursion in vehicle's XY plane (left) and XZ plane (right) relative to four different locations inside the car.

The highest absolute value of the maximum excursion was 409 mm in X-axis (Veh CG), 317 mm in Y-axis (Right B-Pillar), and 209 mm in Z-axis (Right B-pillar) (Table 42). The average values of the maximum excursion were (value/standard deviation): 387 mm/±16.1 mm (X), -299 mm/±13 mm (Y), and 193 mm/±13.6 mm (Z). The largest maximum relative difference between the components of the four different trajectories was found to be 38 mm in the X-axis, while the lowest was 29 mm in the Y-axis.

Table 42. Maximum excursion of THOR's head relative to the four vehicle locations.

	Veh CG	Truck Bed	Right B-pillar	Left B-pillar	Max relative difference
X (mm)	409	371	388	381	38
Y (mm)	-299	-288	-317	-291	29
Z (mm)	198	177	209	189	32

16.4 Discussion

Assuming that a vehicle is a rigid body connecting the instrumented car sites, one would expect that the 3D trajectories calculated for the occupant would be the same independently from the vehicle location used as the reference. However, all four head's trajectories calculated in this study differed slightly from each other. One of the contributing factors is the local deformation, both dynamic and permanent, of the area around the sensor mounting plate's attachment points. The sensor package at the vehicle's CG was installed on top of the vehicle's centerline tunnel, a region composed of relatively thin sheet metal (high local deformation possible). On the other hand, the sensors at the bottom of the B-pillars were attached to a stiff, multilayer structure of hot stamped metal sections (smaller deformation expected). The trajectory calculation process also might have been influenced by the sensors characteristics, e.g., noise-to-signal ratio, or test measurement inaccuracies, e.g., the initial orientation error resulting from the accuracy of the CMM measurement. Overall, though, the maximum relative difference between the four trajectories was 39 mm, which is in the order of magnitude of permanent local deformation seen for the A-pillar and rocker panel in post-frontal-oblique-crash vehicles (Saunders et al. 2013).

The presented method is a promising alternative to optical capture systems for calculating vehicle and body segments position and orientation but further validation – using optical 3D motion tracking – is required to determine how these sensor predictions vary from actual trajectories.

16.5 Division of work between authors

Toczyski designed the study under the supervision of Kerrigan. Collection and processing of head and vehicle kinematics were performed by Toczyski. Gepner and Kerrigan provided scientific guidance. The short communication was written by Toczyski and edited by Gepner and Kerrigan.

17. CLOSING REMARKS

17.1 Conclusions

The main goal of this dissertation was to develop an algorithm that could be used to compute 3D component trajectories of a rigid body based on locally-mounted inertial sensors. The knowledge gained from different tasks was used to identify a method for computing 3D component trajectories that minimizes the error in the sensor-based position estimation.

The goal was accomplished through:

- identification of a method of updating body orientation based on body's angular rate, a method that minimizes the error in the calculated trajectory (Chapter 8),
- identification of a method of obtaining body's local angular acceleration that minimizes the error in the calculated trajectory (Chapter 9),
- analytical and numerical evaluation of the effect of sensor characteristics (e.g. noise level), sensor errors (e.g. error in sensitivity), test measurement inaccuracies (e.g. error in the measurement of initial orientation), and error interactions on trajectories computed with the use of data from IMUs (Chapter 10),
- investigation of the effect of redundant sensors added to a stock "3 ACC + 3 ARS" sensor package on the resulting position error (Chapter 11),
- investigation of different correction techniques that could be used to minimize the error in the calculated trajectory (Chapter 12 to Chapter 15).

The following conclusions were separated into groups based on the order of the chapters in the PhD dissertation.

17.1.1 Algorithm verification through computer simulations (Chapter 5)

The goal of Chapter 5 was to verify if the algorithm described in Section 1.2.3, i.e. the algorithm used throughout this dissertation to compute trajectories from inertial measurements, was coded correctly. The verification was performed using kinematics data obtained from a simple computer model (Figure 4).

The main conclusion of this study is as follows:

- There was a substantial difference in error calculations between kinematics data captured at 10 kHz (Simulation 1) vs. data captured at 100 kHz (Simulation 2). In fact, by increasing the sampling rate by a factor of 10, a 10 fold reduction in error was realized. This is because much of the error was related to an integration error, which could have a real effect on actual sensor data.

17.1.2 Simplified Head testing (Chapter 6)

The goal of Chapter 6 was to evaluate the ability of the algorithm described in Section 1.2.3 to calculate accurate trajectories in sled testing where a simplified structure representing an ATD's head-to-neck assembly was utilized. Forty sled tests were run for the purpose of the study.

The main conclusions of this study are as follows:

- This study found that variation in the ARS had a relatively small effect on the calculated orientation, except when the local angular rate exceeded the full range of a sensor (for example, IES sensor in Figure 32).
- In the Simplified head tests, the position errors calculated with the standard method (the one coded in the software described in APPENDIX S) varied between 2.9 mm (Endevco 7264C – DTS ARS PRO 2000Hz in Test S0450) to 123.2 mm (DTS6DX PRO ACC-DTS ARS PRO 300Hz; Test S0426) (APPENDIX C).

17.1.3 THOR Mod-kit testing (Chapter 7)

The aim of Chapter 7 was to evaluate the ability of the algorithm described in Section 1.2.3 to calculate accurate trajectories in a complex scenario where a crash test dummy was utilized. The following can be concluded from the results of the study:

- In THOR tests, in which the head-to-structure impact was simulated, the proposed algorithm of updating the head's orientation (based on the data from the angular rate sensors used on the tests), was able to capture the abrupt change in the head's rotational movement caused by the impact (e.g. Figure 62, Figure 63, and Figure 64).
- After excluding three cases with faulty sensor data from the analysis of the THOR tests, the highest position error (Res_{err} of 86.57 mm) was recorded in Test S0458 for the Endevco 7290E – DTS ARS Pro 300Hz sensor package. The lowest Res_{err} (of approx. 29.5 mm) was identified for Endevco 7264C – DTS ARS PRO 2000Hz in Test S0459 (see APPENDIX G).
- Across the THOR ATD tests, on average the deviation between the head's calculated and reference trajectories was noticeably higher than for the tracked body in the Simplified Head test series (APPENDIX G and APPENDIX C, respectively).

17.1.4 Update of body orientation (Chapter 8)

Chapter 8 investigated the use of seven previously published algorithms of updating the local-to-global rotation matrix R in crash-like scenarios to identify which one of those methods was most applicable for test conditions like these. Additionally, an analytical analysis focusing on the effect of the data sampling step Δt and the characteristics of the measured angular velocity signal (its magnitude and frequency) was performed.

The main conclusions of this study are as follows:

- For the analyzed test cases the most accurate methods of updating the rotation matrix R were two algorithms based on the Euler parameters derived from the angular velocity vector $\boldsymbol{\omega(t)}$. In addition, both methods appeared to be noticeably less susceptible (than the other discussed algorithms) to changes in error resulting from the increase in the sampling step Δt.
- The accuracy of the method used to update R depends strongly on the accuracy of the numerical integration scheme utilized to obtain finite rotations from $\boldsymbol{\omega(t)}$ or on the accuracy of the numerical method used to solve ordinary differential equations, if that step is required in the algorithm.

- Characteristics of the angular velocity signal (its magnitude, period, etc.) affect the magnitude of the error in the calculated rotation matrix $\boldsymbol{R}$. It was shown that for the same value of the time step Δt, the error in $\boldsymbol{R}$ is greater for greater magnitude or higher frequency of the input ARS data.
- In both, the analytical error analysis and when experimental data were used, the increase in the time step Δt of the ARS data (used as the input), caused an increase in the difference between the calculated and reference rotation matrix. Similarly, the error in the angle of rotation θ_{INS} increased with higher values of Δt.

17.1.5 Angular acceleration analysis (Chapter 9)

Chapter 9 investigated the use of different methods of obtaining angular acceleration utilized in the process of 3D trajectory calculation. Five different techniques were analyzed. In addition, the sensitivity of the calculated trajectory to the change in the filter class used on the AAC input data (either acceleration or angular rate) was evaluated.

The main conclusions of this study are as follows:
- In the four Simplified Head tests, after optimization of the initial orientation of the tracked body, the smallest deviation from the reference data was observed in cases where the $3a\omega$ method (method based on differentiation of local angular velocity) was utilized to compute body's local angular acceleration (Table 7 and Table 8).
- The trajectories computed with the $3a\omega$ configuration matched the mocap reference data well in shape and in magnitude in all five considered test cases. The highest absolute difference between the reference and calculated trajectories (across the five tests) was 10.11 mm (less than half of an inch; Table 11 and Figure 92).
- Relatively small values of standard deviation seen across the five methods of obtaining local angular acceleration (Table 9 and Table 10) suggest that, in the analyzed test configurations, the computed trajectories (within the same method of determining AAC) were not highly sensitive to the change in filtering of the AAC method input.
- While the $3a\omega$ method generated trajectories most closely matching the reference data, those trajectories were also characterized with the highest relative variability (coefficient of variation up to approx. 40%) among the five methods of obtaining AAC,
- The variation in the calculated trajectory was higher due to the choice in the method used to obtain AAC than due to the filter class used on the input data to that method.

17.1.6 Error effects analysis (Chapter 10)

The aim of Chapter 10 was to evaluate the effect of sensor characteristics (e.g. noise level), sensor errors (e.g. error in sensitivity), test measurement inaccuracies (e.g. error in the measurement of initial orientation), and error interactions on trajectories computed with the use of data from IMUs. First, different error types and bounds for these errors were identified (Section 10.1). Next, a simplified analytical analysis was performed to better understand the propagation of the errors in time (Section 10.2). In Section 10.3, guided by the analytical investigation, experimental analyses were carried out a) to quantify the effect of individual errors on the IMU-based trajectory estimation, and b) to identify main interaction between these errors.

The following can be concluded from the results of the analytical study:

- When it was assumed that the local acceleration vector of the tracked body was the same as the global acceleration vector:
    - When the additive term c (debias error) was introduced into the reading of one of the linear accelerometers, that error affected only one of the global position components of the tracked body (the one along the same direction as the acceleration with the error).
    - When only the debias error (additive term c) in one of the angular rate sensors was introduced into the analysis, it affected all three of the calculated position components.
    - When two ARS debias errors were included into the angular velocity signals, in one of the global position components the term $\left(c_{ars\_x}^2 + c_{arc\_z}^2\right)\frac{t^2}{2}$ (where t – time) was introduced.
    - When only the debias error in one of the angular acceleration components was introduced, it affected two position components along the two axes orthogonal to the axis around which the angular acceleration with the error was defined.
    - The error in the ACC sensitivity (scaling term b_{acc}) affected one position component, in the same direction as the measured acceleration with the error.
- When the global acceleration of the tracked body was assumed to be the product of body's local acceleration vector and rotation matrix that was constant in time:
    - When the additive term c (debias) was introduced into the reading of one of the linear accelerometers, that error affected all three calculated global position components.
    - All three position components were affected also when the debias error was introduced in one of the angular rate sensors or in one of the angular accelerometers.
- In both, the simplified case and the case where the rotation matrix was assumed to be constant:
    - The resulting error in position due to the debias error c_{acc} in a linear acceleration component grows in time and that effect can be described by the term $c_{acc}\frac{t^2}{2}$.
    - The resulting error in position due to the debias error in an angular velocity component grows in time as described by the term $c_{ars}^2\frac{t^2}{2}$.
    - When two ARS debias errors were introduced into the data, part of their effect was multiplicative, i.e., when, e.g., c_{ars_x} and c_{ars_z} were non-zero, the error term $c_{ars\_x}c_{ars\_z}\frac{t^2}{2}$ appeared in at least two of the calculated position components.
    - The error in one ARS sensitivity affected all three position components.
    - When two ARS sensitivity errors were introduced into the analysis, part of their effect was also multiplicative, i.e., when, e.g., b_{ars_x} and b_{ars_z} were different than

1, some of the terms in the global position components were scaled by the product of $b_{ars\_x}b_{ars\_z}$.

- o When an ARS sensitivity error and an ARS debias error were introduced into the analysis together, part of their effect was multiplicative as well, i.e., when, e.g., c_{ars_x} was non-zero and b_{ars_z} was different than 1, some of the terms in the three global position components were scaled by the product of $b_{ars\_z}c_{ars\_x}$.
- In the general case, i.e., when body rotates and translates at the same time, due to the nonlinear nature of R, the double integration of the body's global acceleration (determined from the multiplication of R and the body's local acceleration vector a) is non-trivial or impossible to accomplish analytically.
  - o The effect of sensor-related errors (that are present either in the measured angular rate $\omega(t)$ or the linear acceleration vector $a_o(t)$) on the calculated global position of the tracked body is convoluted and cannot be easily predicted analytically.

The following can be concluded from the results of the experimental study:

- This study showed that the debias error (either in acceleration or angular rate sensor data) had a substantial effect on the calculated 3D trajectories of the tracked body (Table 20 and Table 21).
- The error in acceleration debias caused a bigger discrepancy between the baseline and the calculated trajectories than the debias offset in the angular velocity data.
- The sensitivity error in ACC had a greater effect on the calculated trajectory than the sensitivity error in ARS data.
- The error in the accelerometer sensitivity can influence the calculated 3D trajectory in a substantial way. In the investigated test scenarios, when the ACC sensitivity was modified by 4%, the absolute position peak error reached (in one of the investigated cases) approximately 75 mm (1/10 of the peak difference, seen cross the five investigated cases, for the ACC debias error and 1/4 of the difference seen for the ARS debias error; Table 21).
- This study showed that a relatively small inaccuracy in measured initial orientation could have a substantial effect on the predicted 3D response, for example, in one of the investigated test cases, the error of 1 degree in initial Yaw angle caused a difference between the reference and the calculated trajectories of approx. 50 mm (Table 21).
- Within the error bounds from Table 13, the two misalignment errors (for ACC and ARS) as well as the error in the initial position of the tracked body had a negligible effect on the calculated 3D global trajectory of the ATD head ($mRes_{err}$ and $mdiff_{max}$ both below 2.6 mm for the three error groups; Table 20 and Table 21).
- The six main interactions between the investigated errors identified in this study were different configurations of the same three error groups: ACC debias, ARS debias, and the error in the initial orientation (Table 23).

17.1.7 Investigation of the effect of redundant sensors on the magnitude of the error in the calculated trajectory (Chapter 11)

The goal of this task was to investigate if by introducing redundant sensors to the stock "3 ACC + 3 ARS" package, an inaccurate ("inconsistent") sensor can be identified or if a broken sensor can be accounted for in the trajectory calculation. The method was based on an analytical relationship that relates an output (measured quantity) from one of the sensors to the readings from the other sensors of the same type. The following can be concluded from the results of the study:

- This study showed that by adding two redundant angular rate sensors to a standard "3 ACC + 3 ARS" package, an angular rate sensor with errors in its signal can be identified (Eq. 11.9 and Eq. 11.10).
- Similarly, by adding two redundant linear accelerometers, an accelerometer with a faulty response can be pinpointed (Eq. 11.20 to Eq. 11.23).
- To recover a measurement lost, for example, due to a broken connector or a cable, one added sensor (of the same type as the broken sensor) is needed.
- The analytical relationship was verified using data from a computer simulation of a simple rigid body system where both, the ARS and the ACC analyses showed a good agreement between the predicted sensor output and the output obtained directly from the FE software (Figure 118 and Figure 119).

17.1.8 3D trajectory calculation in THOR tests utilizing the sensor fusion technique through the Kalman filter (Chapter 12)

The aim of Chapter 12 was to assess if by performing the sensor fusion of two sets of linear accelerometers and angular rate sensors, the deviation between the computed and reference trajectories of the ATD's head would be decreased in exemplar THOR tests. The following can be concluded from the results of the study:

- No improvements in the accuracy of the trajectory calculation algorithm were achieved by employing the sensor fusion technique.
  - When sensor fusion was utilized, in both analyzed test cases, the position error was higher by 36.4% and 23.7% (Table 26), respectively, relative to the "Endevco 7264C – DTS ARS PRO 2000Hz" sensor combination, a sensor package that gave the smallest position estimation error in both tests.

17.1.9 3D trajectory calculation in THOR tests utilizing the knowledge gained from the error effects analysis (Chapter 13)

The aim of Chapter 13 was to investigate if by optimization performed on the debias values (for both, ACC and ARS) and initial orientation angles of the tracked body, the accuracy of the trajectory calculation algorithm would be improved. The following can be concluded from the results of the study:

- Due to optimization performed on three ACC debias values and three initial orientation angles, the resulting error in IMU based position estimation in the THOR tests decreased by approximately 90% (Table 34). The absolute difference between the reference and calculated trajectories across the three position components varied from 1.81 mm to 7.63 mm (Table 36).

- Due to optimization, the highest resulting change for the debias values in the acceleration signal was 0.081 g and the highest resulting change across the three initial angles was 3.01 degrees (Table 35).
- The above further supports the conclusion from this study describing how critical accurate initial orientation and the debias values for the recorded data are in order to obtain accurate IMU-based position estimation

17.1.10 3D trajectory calculation in THOR tests utilizing known position information from data points at a constant time interval (Chapter 14)

The goal of Chapter 14 was to asses if by introducing known position information (obtained, e.g., from video tracking or a motion capture system) recorded at a much lower sampling rate than the sensor data, the error in position estimation would be decreased. In the study, one THOR test was used as an exemplar case.

The main conclusions are as follows:

- When known information about 3D position of the tracked body was introduced into the trajectory calculation algorithm, a substantial improvement in the accuracy of the computed position was achieved (Table 38).
  - Even when only three position corrections were used, the position error (when compared to a test without these three points) decreased by more than 93% and the maximum absolute difference for all three trajectory components stayed below 5.5 mm (Table 38 and Table 39).
- When the entire known orientation time history was utilized in the analysis (Figure 123), the resulting position error was still higher (for all three trajectory components) than for the case in which three known position corrections were used in the trajectory calculation process instead.

17.1.11 Interpolation of missing optical data based on inertial measurements (Chapter 15)

The goal of this chapter was to evaluate two different techniques of providing kinematics data over a missing part of optical data caused by intermittent object obscuration.

The main conclusions of this study are as follows:

- In test cases in which the optimization of the head's initial orientation was performed, the smallest position error was recorded when both, known pre and post-impact data (from Figure 125) were utilized in the trajectory calculation algorithm (Table 41).
- This study found that by using optimization and only one known positon point further in time, the error in computed trajectory could be decreased in a substantial way. The resulting error from that case was comparable to the error from the case in which the entire known pre and post-impact data (from Figure 125) were utilized (Table 41).
- The highest error in position was recorded in a test in which only the pre-trigger data was used in the optimization algorithm (Table 41 and Figure 127).
- The smallest error in position estimation was found when the interpolation algorithm from Chapter 14 was utilized instead of the optimization scheme (Table 41).

The goal of this study was to examine how vehicle deformations at sensor mounting locations affect predicted head (treated here as an exemplar body region being tracked) relative to vehicle kinematics in a full-scale oblique offset frontal crash test. The following can be concluded from the results of the study:

- Predicted head to vehicle kinematics in a full-scale vehicle crash test was sensitive to the location where the vehicle sensor package was mounted.
- Overall, though, the maximum relative difference, between the head trajectories obtained using data from sensors mounted at four vehicle locations, was 39 mm, which is in the order of magnitude of permanent local deformation seen for the A-pillar and rocker panel in post-frontal-oblique-crash vehicles (Saunders et al. 2013).

17.2 Methodological steps that minimize position error estimation – summary

This section summarizes general steps that should be followed to minimize the error in position estimation obtained through IMU tracking.

The dissertation identified multiple error types that could potentially affect position computed based on the data from inertial sensors attached to the analyzed body. Within these errors, four of them appeared to have a very pronounced effect on the accuracy of the trajectory calculation. Three out of the four errors were sensor related (the debias error in acceleration, the debias error in the angular rate data, and the error in sensor sensitivity). The fourth error type that had a substantial influence on the computed position was the error in the initial orientation of the tracked object.

To minimize the effect of the debias errors, it is advised to calculate the debias values – for all sensors utilized during testing – by averaging as much of the available pre-trigger (prior to the start of the test) data as possible. It is **not** recommended to use 1-point debiasing or no debiasing. Another method of bounding the debias values would be to use the optimization methodology described in Chapter 13, if position data from an alternative source (for example, from video tracking) are available along with the inertial measurements.

To minimize the error in the sensor sensitivity, sensors should be calibrated frequently and the ones that do not regulate their excitation voltage internally should be run at the same excitation voltage as the calibration voltage.

As it was shown multiple times throughout the dissertation (Chapter 9, 10 and 13), the IMU-based position estimation is highly sensitive to the error in the initial orientation. Even a relatively small inaccuracy in the initial orientation of a tracked body can cause a substantial error in the computed trajectory for that body. If a coordinate measurement machine (CMM) is used to obtain the initial position information, the number of times when the machine is moved and realigned back with the position data, should be as small as possible. If the needed sensor position information cannot be measured in one take, it is advised to utilize the following procedure to minimize the initial orientation error:

Step 1: prior to testing the sensor block (and the sensors mounted on it) should be measured in relation to 3 (or more) previously defined landmarks on the mounting plate/fixture,

Step 2: the measured senor mount should be attached to the tracked body,

Step 3: the landmarks from Step 1 should be re-measured, but this time in the global reference frame,

Step 4: initial orientation of the tracked body can now be determined utilizing, for example, the Least-Squares Pose Estimator approach (Cappozzo et al. 1997) in conjunction with the local (Step 1) and global (Step 3) position information for the predefined landmarks on the mounting plate.

The research effort presented in this dissertation identified the undamped Endevco 7264C accelerometers (with the full-scale range of 2000 g) along with the DTS ARS PRO angular rate sensors (with the full-scale range of 8000 deg/sec and bandwidth of 2000 Hz) as the sensor combination that produced the most accurate trajectories when compared to the reference position data recorded by a motion capture system. With the measurements sampled at 20 kHz, the resulting error in the trajectory estimation was – on average – at the level of 15 mm in the Simplified Head tests (Chapter 6) and at the level of 36 mm in the THOR tests (Chapter 7). It is believed that the error in the THOR tests was higher due to the increased complexity in obtaining the initial orientation of the ATD's head sensor block utilized in the position analysis.

To update the tracked body's orientation (the rotation matrix R from Eq. 1.1), either the *UQ* method (Rudd et al. 2006) or the *ER* method (Huculak and Lankarani 2013) should be utilized. Both update methods are based on the Euler parameters and both use a higher order integration scheme as a subroutine at some step in the attitude algorithm. In Chapter 8, it was shown that the accuracy of the integration rule is one of the driving factors in the overall accuracy of the technique used to update R.

When a researcher wants to utilize inertial measurements to track a point that is at a distance from the IMU or when the sensors used are not perfectly aligned within the sensor block (for example due to mounting inaccuracies), the body local angular acceleration (AAC) needs to be taken into account in the 3D trajectory calculation process regardless of the scenario being investigated. In Chapter 9, it was shown that if the initial orientation error is minimized *a priori* (for example, through optimization of the initial orientation of the analyzed body) the method of obtaining angular acceleration that minimized the error in position estimation was the *3aω* method. To obtain AAC, *3aω* differentiates the body's local angular rate. *3aω* gave the most accurate results in all five analyzed tests (four Simplified Head tests and one THOR test) for the two (Simplified Head) or one (THOR test) tracked point. It needs to be mentioned here that even though the *3aω* method produced the most accurate trajectories it was also the most sensitive to the filter class used on the angular velocity data prior to differentiation.

In crash testing, achieving the position error below 10 mm using only the locally-mounted sensors is possible (Figure 41) but challenging. To improve the trajectory estimation accuracy, IMU tracking should be utilized along with position information obtained from another source (for example, video tracking). Even if the tracked body position from the alternative source is known only at one point in time but that point was measured later in the test, using this extra information (for example, in the optimization process of the sensor debias values and/or the error in initial

orientation as described in Chapter 13 and Chapter 15) can decrease the error in position estimation substantially.

To further improve the accuracy of 3D position obtained through IMU tracking, when possible at least one redundant linear accelerometer and one redundant angular rate sensor should be added to the sensor package utilized to measure body's kinematics (as shown in Chapter 11). By having one additional sensor of each type, it is possible to recover a lost measurement if one of the sensors fails during the test (for example, due to a broken connector). One additional sensor of each type is also enough to check consistency of the recorded data. If the data is inconsistent, to pinpoint the faulty sensor, more than one redundant linear accelerometer and more than one redundant angular rate sensor is needed.

The algorithm presented in this dissertation can be also used to obtain relative motion between two tracked bodies. In Chapter 16, it was shown, though, that this relative motion might be affected by the local deformation at the IMU mounting location. The local deformation effect needs to be taken into consideration when, for example, one wants to track motion of a crash test dummy relative to a vehicle during a crash. To minimize the error in the computed trajectory for an ATD in a car crash, the location of the sensor block mounted inside the vehicle should be chosen based on the test conditions and away from the impact point.

Lastly, the results of this study showed that the error in 3D position estimation depends not only on the data sampling step Δt but also on the characteristics of the input signal (its magnitude and the frequency content) used in the analysis. That indicates that when choosing data sampling rate, one needs to take into account the type of the event being investigated. When the time step Δt is larger than the period of the input data (either, global acceleration from Eq. 1.1 or local angular velocity used to update the rotation matrix $\boldsymbol{R}$), substantial part of the information contained in the input signal, will be lost. On the other hand, high sampling frequency appropriate for a crash test (short event with rapid changes in the angular velocity) might not be necessary, e.g., for a gait analysis (much longer event with smaller magnitude of angular rate than seen in crash).

17.2.1 Beyond crash-like applications

This section presents how the findings from the dissertation could be extrapolated beyond crash testing and applied in other fields.

The error in the debias values in the data from inertial sensors will always have a negative effect on the computed trajectory, regardless of the scenario being investigated. In Chapter 10 it was shown that the error in position due to the debias error in linear acceleration (c_{acc}) grows in time and that effect can be estimated with the term $c_{acc}\frac{t^2}{2}$, where t – time. The deviation in position due to inaccuracies in measurement debias for the angular velocity data (c_{ars}) grows in time as described by the term $c_{ars}^2\frac{t^2}{2}$. From the former it can be seen that the magnitude of the position error coming from the error in data debias depends strongly on the investigated event's time scale. In other words, the deviation in the computed position caused by debias errors will be more prevalent in scenarios, where the time scale is relatively large (gait analysis, mobile robot motion,

etc.) comparing, e.g., to blast, where the considered time period is often less than a few milliseconds.

As it was shown in Figure 111, the resulting error in position due to inaccuracies in the measured initial orientation depends strongly on the magnitude of the analyzed motion. In all crash and crash-like tests discussed in this dissertation, the maximum distance traveled for the tracked object was less than 5 m. In fields other than crash testing (e.g., fields related to mobile robots or underwater autonomous vehicles), the body's traveled distance might be substantially larger than a few meters and thus, the IMU-based position error, due to the initial orientation error, might be noticeably higher in those cases than for crash.

To address the error types mentioned in the two previous paragraphs and to account for the error in sensor sensitivity the same techniques as presented in the first section of Chapter 17.2 should be utilized. In addition, the correction techniques described in Chapter 13 and 15 (optimization of sensor parameters and initial orientation) or the interpolation method presented in Chapter 14 can be used as alternative ways of improving the IMU tracking accuracy in any situation in which position information from an additional source (for example, from a motion capture system) is available along with inertial measurements.

In events different than crash it is still advised to use either the *UQ method* (Rudd et al. 2006) or the *ER method* (Huculak and Lankarani 2013) to update the orientation of the tracked body (i.e., its rotation matrix *R*). Both of the methods are based on the Euler parameters and both use higher order integration schemes as part of the orientation algorithm. The biggest advantage of the Euler parameters over the Euler angles (which are used, for example, in the *2-1-3 method* from Chapter 8) is that the Euler parameters avoid a phenomenon called gimbal lock, i.e., they do have a unique solution regardless of the rotation angle. In Chapter 8, it was also shown that the method utilized for integration affects the accuracy of the computed attitude in a substantial way (Figure 71). Taking into account a) that the computation cost associated with the orientation algorithms that use the higher order integration is relatively small (less than half of a second to process almost 16,000 data points), and b) that these integration methods are known to be more accurate than the first order approaches, it is strongly advised to use higher order integration in the update of the tracked body's orientation.

The other finding (a method) that can be extrapolated from this dissertation to different fields is the consistency check (*CC*) described in Chapter 11. *CC* can be used to assess recorded kinematics data regardless of the nature of the application being investigated. The consistency check itself is governed by the laws of physics and it is independent of the time scale or the magnitude/frequency of the signal utilized as the input to *CC*.

Most of the sensor data used in this dissertation was sampled at 20 kHz. This sampling rate, commonly used in crash testing, might not be necessary, e.g., for a gait study (much longer event with smaller magnitude of acceleration and angular rate than seen in crash). The dissertation showed how sampling rate, sensor data magnitude and frequency could affect prediction results. In Chapter 8, it was presented that when it comes to orientation update there is a normalizing factor that can be utilized to match error results between scenarios characterized by different frequency

content. Even though that normalizing factor was found for a simple 2D model, it is expected that a mathematical relationship like this exists also for complex 3D scenarios.

To summarize, the focus of this dissertation was put on crash testing. Nevertheless, the results from the study can be extrapolated to other applications. When the relationships for different parameters describing measured signals (either linear acceleration or angular rate) are similar between investigated cases, the position algorithm proposed in this document should yield similar error results in those cases, regardless of the difference in the time scale or input signal's magnitude/frequency.

17.3 Contributions

In summary, the contributions from this dissertation are:

- Development of a stand-alone software package allowing for computing 3D component trajectories (based on the data from locally mounted inertial sensors) of any rigid body in a car crash (see APPENDIX S),
- A method that results in a minimization of the error in the calculated trajectory by introduction of known data points from an optical system,
- A method for filling the gaps in the trajectory obtained from video tracking or OSS, based on the kinematics data from IMUs,
- A method for determining boundaries for sensor and measurement error values based on partial data obtained from different tracking source than IMUs,
- Identification of the minimum number of sensors required to account for an "inaccurate" sensor,
- A method that utilizes redundant sensors and allows for a sensor consistency check (for both, linear accelerometers and angular rate sensors),
- Identification of a robust method to update body's orientation based on body's local angular velocity,
- Identification of a robust method of obtaining angular acceleration when needed in 3D trajectory calculation,
- Identification of trajectory errors resulting from sensor and test measurement errors and a set of instructions to guide test engineers in accounting for those errors to obtain an accurate occupant's trajectory in a crash-like scenario,
- Identification – through analytical and computational analyses – of error effects and their interactions, and how these errors and their combinations propagate in time.

17.4 Impact

The algorithms developed over the course of this dissertation were implemented in a stand-alone software package (APPENDIX S). The final version of that software, now being shared with the automotive safety community, offers additional insight on the ATD response in a car crash.

Moreover, the National Highway Traffic Safety Administration (NHTSA) is promoting the software package as a research tool for all crash tests with the THOR ATD carried out by or for

NHTSA. The agency is also considering of potentially utilizing the package in regulated (New Car Assessment Program, NCAP, NHTSA 2015b) tests. Government adoption of the software will encourage vehicle original equipment manufacturers (OEMs), suppliers, and other testing groups to adopt the algorithm and start using the software in their own internal research.

It is believed that the proposed algorithm, treated as a reliable research tool, will ultimately help in implementation of more advanced safety systems to protect the human body during a crash.

17.5 Possible applications

17.5.1 Example application – head motion tracking in NHTSA frontal oblique offset crash test

In September 2009, the National Highway Traffic Safety Administration published a report investigating why occupant fatalities still occur in frontal crashes despite the presence of advanced safety systems (Bean et al. 2009). Soon after, and due to the conclusions of the publication, NHTSA started the Oblique Research Moving Deformable Barrier (RMDB) crash test program "(…) capable of replicating the injury potentials from real-world frontal offset oblique crashes" (Saunders et al. 2013). In 2015, the oblique RMDB test configuration was proposed in the update to the New Car Assessment Program (NHTSA 2015b).

In the test, a moving deformable barrier is driven into a stationary vehicle at a speed of 90 km/h, a 15-degree angle, and a 35 percent overlap. During the RMDB test, the head of an ATD seated on the impacted side tends to move towards the vehicle's A-pillar. With both the frontal and curtain airbags deployed (all new cars from the US fleet have curtain and frontal airbags), there is an increased chance of the head obscuration (Figure 131).

Test v08787

Figure 131. Video sequence (from left to right) showing head obscuration due to deployed airbags during frontal oblique crash test (images from NHTSA 2014).

When none of the targets on the dummy head are visible, the head motion cannot be tracked by either video tracking or 3D optical systems. That creates a challenge in studying the occupant kinematics in the frontal oblique crash.

All currently used ATDs are instrumented with 6DOF IMUs. The sensor packages are usually mounted in several different ATD body regions, including the head and spine. Using the data from the sensors, the 3D kinematics of each instrumented body part can be reconstructed by solving rigid body motion equations. The same type of sensor package can be installed inside a vehicle to

capture its motion. The data from the two sets of sensors permit the description of the relative motion between the car and the occupant. A better understanding of occupant motion relative to the vehicle in an oblique crash test will improve our knowledge of possible injury outcomes, which, ultimately, will then lead to the design and implementation of more advanced safety systems to protect the human body during a crash.

17.5.2 Other applications

It is worth pointing out here that the methods developed in this dissertation can be applied to tracking of **any** rigid body. That includes:

- Occupant motion in scenarios where there is no line of sight between the tracked objects and the cameras throughout the event (e.g. inside a vehicle in a rollover test, where there is no possibility to mount an on-board camera system),
- Human bony structure, surrounded by flesh and skin, to which there is no access or the access is very limited during testing (e.g. pelvis or lumbar spine when the occupant is positioned in a regular car seat),
- Vehicle structure parts which would allow for tracking of their relative motion during a crash,
- etc.

This dissertation focused on crash scenarios mainly, but:

- findings about the body's orientation update (Chapter 8),
- findings about local angular acceleration and its effect on the calculated trajectory (Chapter 9),
- gained knowledge about propagation in time of different error types (Section 10.2),
- gained knowledge about the effect of sensor-related errors and their interactions on the calculated trajectory (Section 10.3 and Section 10.4),
- the method of identifying and eliminating an inconsistent (with an error) sensor by using additional linear accelerometers and redundant angular rate sensors (Chapter 11),
- the methods of improving the accuracy of 3D component trajectories (Chapter 13 and Chapter 14), and
- the method allowing for filling of a gap in the optical data (Chapter 15)

can be extrapolated and applied in other fields, ranging from gait and sport studies, through clinical trials and animal motion analysis, to tracking underwater or underground autonomous vehicles. This dissertation showed how sampling rate, sensor data magnitude and frequency could affect prediction results. The theories and approaches presented in this document can be applied to these different fields, because they are only really "different" due to the sampling rates, sensor signal magnitude and its frequency.

18. REFERENCES

Akaike H., 1974, "A new look at the statistical model identification," IEEE Transactions on Automatic Control, 19 (6): 716–723, DOI:10.1109/TAC.1974.1100705.

Amarasinghe, R., Dao, D. V., Toriyama, T., and Sugiyama, S., 2005, "Design and fabrication of a miniaturized six-degree-of-freedom piezo-resistive accelerometer," 18th IEEE International Conference on Micro Electro Mechanical Systems, MEMS 2005, pp. 351-354, DOI: 10.1109/MEMSYS.2005.1453939.

Aparicio A., Barrios J. M., Palacios E., Dávila A., and López J., 2009, "Improvement of Dummy Positioning and Vehicle Parts During a Crash Through the Integration and Filtering of Inertial Sensors," Proceedings of 21st ESV Conference, Paper Number: 09-0372, Stuttgart, Germany.

Barshan B., and Durrant-Whyte H. F., 1995, "Inertial Navigation Systems for Mobile Robots," IEEE Transactions on Robotics and Automation, Vol. 11, No. 3.

Bean J. D., Kahane C. J., Mynatt M., Rudd R. W., Rush C. J., and Wiacek C., 2009, "Fatalities in Frontal Crashes Despite Seat Belts and Air Bags – Review of All CDS Cases – Model and Calendar Years 2000-2007 – 122 Fatalities," NHTSA Technical Report, Report No. DOT HS 811 202, September 2009.

Beard D. A., and Schlick T., 2003, "Unbiased Rotational Moves for Rigid-Body Dynamics," Biophysical Journal, 85(5), pp. 2973–2976.

Bennett T., Jafari R., and Gans N., 2013, "An Extended Kalman Filter to Estimate Human Gait Parameters and Walking Distance," In Proceedings of American Control Conference, pp. 752–757. DOI:10.1109/ACC.2013.6579926.

Benser E. T., 2015, "Trends in Inertial Sensors and Applications," Proceedings of 2015 IEEE International Symposium on Inertial Sensors and Systems (ISISS), pp. 1–4, 23–26 March 2015. DOI: 10.1109/ISISS.2015.7102358.

Bortz J. E., 1971, "A new mathematical formulation for strapdown inertial navigation," IEEE Transactions on Aerospace and Electronic Systems. Vol. AES-7, No. 1. January 1971.

Bussone W. R., Bove R. T., Thomas R., Richards D., and Prange M. T., 2010, "Six-Degree-of-Freedom Accelerations: Linear Arrays Compared with Angular Rate Sensors," SAE Technical Papers; No. 2010-01-1017.

Byrd R. H., Gilbert J. C., and Nocedal J., 2000, "A Trust Region Method Based on Interior Point Techniques for Nonlinear Programming," Mathematical Programming, Vol 89, No. 1, pp. 149–185.

Cappozzo, A., Cappello, A., Della Croce, U., and Pensalf, F., 1997, "Surface-Marker Cluster Design Criteria for 3-D Bone Movement Reconstruction," IEEE Transactions on Biomedical Engineering, Vol. 44, No. 12, December 1997.

Carvalho, M. M., Cazo, R. M., Almeida, V. R., and Barbosa, C. L., 2013, "Fiber Bragg grating based angular accelerometer: A first approach," Proceedings of the Fifth European Workshop on Optical Fiber Sensors, Vol. 8794, DOI:10.1117/12.2026038.

Chen Ch., Chai W., Nasir A. K., and Roth H., 2012, "Low Cost IMU Based Indoor Mobile Robot Navigation with the Assist of Odometry and Wi-Fi Using Dynamic Constraints," Proceedings of the 2012

IEEE/ION Position, Location and Navigation Symposium, Myrtle Beach, SC, USA, DOI: 10.1109/PLANS.2012.6236984.

Cho B-S., Moon W-S., Seo WJ., and Baek K-R, 2011, "A dead reckoning localization system for mobile robots using inertial sensors and wheel revolution encoding," Journal of Mechanical Science and Technology, 25(11), pp. 2907-2917, DOI 10.1007/s12206-011-0805-1.

Demoz G. E., 2004, "Design of Multi-Sensor Attitude Determination Systems," IEEE Transactions on Aerospace and Electronic Systems, 40(2), pp. 627-649.

DiMasi F., 1995, "Transformation of nine-accelerometer-package (NAP) data for replicating headpart kinematics and dynamic loading," U.S. Department of Transportation, National Highway Traffic Safety Administration, DOT HS 808 282, DOT-VNTSC-NHTSA-94-5. Final Report, August 1995.

Eglajs V., Audze P., 1977, "New approach to the design of multifactor experiments," Problems of Dynamics and Strengths, 35 (in Russian), Riga: Zinatne Publishing House: 104–107.

Favre J., Aissaoui R., Jolles B. M., deGuise J. A., and Aminian K., 2009, "Functional calibration procedure for 3D knee joint angle description using inertial sensors," Journal of Biomechanics 42, pp. 2330–2335, DOI:10.1016/j.jbiomech.2009.06.025.

Ferrari A., Ginis P., Hardegger M., and Casamassima F., 2016, "A Mobile Kalman-Filter Based Solution for the Real-Time Estimation of Spatio-Temporal Gait Parameters," IEEE Transactions on Neural Systems and Rehabilitation Engineering, Vol. 24, No. 7, July 2016.

Filippeschi A., Schmitz N., Miezal M., Bleser G., Ruffaldi E., and Stricker D., 2017, "Survey of Motion Tracking Methods Based on Inertial Sensors: A Focus on Upper Limb Human Motion," Sensors 2017, 17, 1257, DOI: 10.3390/s17061257.

Forman J. L., Joodaki H., Forghani A., Riley P., Bollapragada V., Lessley D., Overby B., Heltzel S., and Crandall J., 2015, "Biofidelity Corridors for Whole-Body Pedestrian Impact with a Generic Buck," Proceedings of IRCOBI 2015 conference, IRC-15-49, pp. 356-372, Lyon, France.

Freeston L., 2002, "Applications of the Kalman Filter Algorithm to Robot Localisation and World Modelling," Electrical Engineering Final Year Project 2002, University of Newcastle, NSW, Australia, Available at: http://www8.cs.umu.se/research/ifor/dl/LOCALIZATION-NAVIGATION/Applications%20of%20the%20Kalman%20Filter%20slgorithm%20to%20robot%20localization%20and.pdf, Accessed March 26, 2018.

Gabler L. F., Crandall J. R., and Panzer M. B., 2016, "Assessment of Kinematic Brain Injury Metrics for Predicting Strain Responses in Diverse Automotive Impact Conditions", Annals of Biomedical Engineering, Vol. 44, No. 12, pp. 3705–3718, DOI: 10.1007/s10439-016-1697-0.

Gabler L. F., Crandall J. R., and Panzer M. B., 2018, "Development of a Metric for Predicting Brain Strain Responses Using Head Kinematics", Annals of Biomedical Engineering, Vol. 46, No. 7, pp. 972–985, DOI: 10.1007/s10439-018-2015-9.

Gagné Phill, and Dayton C. M., 2002, "Best Regression Model Using Information Criteria," Journal of Modern Applied Statistical Methods, 1(2), Article 57, DOI: 10.22237/jmasm/1036110180.

Hamano F., 2013, "Derivative of rotation matrix – direct matrix derivation of well-known formula," Proceedings of Green Energy and Systems Conference 2013. Available at: https://arxiv.org/ftp/arxiv/papers/1311/1311.6010.pdf. Accessed January 7, 2019.

Hardy W. N., Foster C., Mason M., Yang K., King A., and Tashman S., 2001, "Investigation of Head Injury Mechanism Using Neutral Density Technology and High-Speed Biplanar X-ray," Stapp Car Crash Journal, Vol. 45, pp. 337–368.

Hoeting J. A., Davis R. A., Merton A. A., and Thomspon S. E., 2002, "Model Selection for Geostatistical Models," Ecological Applications, 16(1), pp. 87–98.

Huculak R. D., 2011, "Evaluating Spatial Orientation and Position of an ATD Head Using Accelerometers and Angular Rate Sensors in Dynamic Impact Testing," Master's Thesis, Wichita State University, Wichita, KS.

Huculak R. D., and Lankarani H. M., 2013, "Use of Euler parameters for the evaluation of ATD head trajectory from angular rate sensor and accelerometer data in aircraft seat certification testing," International Journal of Crashworthiness. Vol. 18(2), pp. 174-182.

Iman R. L., Helton J. C., and Campbell J. E., 1981, "An approach to sensitivity analysis of computer models, Part 1. Introduction, input variable selection and preliminary variable assessment," Journal of Quality Technology, 13 (3): 174–183.

Jordan J. W., 1969, "An Accurate Strapdown Direction Cosine Algorithm," NASA Technical Note TN D-5384.

Kalman R. E., 1960, "A new approach to linear filtering and prediction problems," Journal of Basic Engineering, Vol. 82 (1): 35–45, DOI:10.1115/1.3662552.

Kamel A. H., Shaqlaih A. S., and Ibrahim E.A., 2015, "Model inference using the Akaike information criterion for turbulent flow of non-Newtonian crude oils in pipelines," Petroleum Science, 12:492, DOI: 10.1007/s12182-015-0032-y.

Kang Y-S., Moorhouse K., and Bolte J. H., 2011, "Measurement of Six Degrees of Freedom Head Kinematics in Impact Conditions Employing Six Accelerometers and Three Angular Rate Sensors (6aω Configuration)," Journal of Biomechanical Engineering. Vol. 133(11):111007, DOI: 10.1115/1.4005427.

Kang Y-S., Moorhouse K., and Bolte J. H., 2015, "Instrumentation Technique for Measuring Six Degrees of Freedom Head Kinematics in Impact Conditions using Six-Accelerometers and Three-Angular Rate Sensors (6aω Configuration) on a Lightweight Tetrahedron Fixture," Proceedings of 24th ESV Conference, Paper Number: 15-0288, Gothenburg, Sweden.

Kang Y-S., Goldman S., Moorhouse K., and Bolte J., 2017, "Evaluation of a coplanar 6a3ω configuration in the Hybrid III 50th percentile male head," Traffic Injury Prevention, 18:sup1, S129-S135, DOI: 10.1080/15389588.2017.1318210.

Kerrigan J. R., Dennis N. J., Parent D. P., Purtsezov S., Ash J. H., Crandall J. R., and Stein D., 2011, "Test system, vehicle and occupant response repeatability evaluation in rollover crash tests: the deceleration rollover sled test," International Journal of Crashworthiness, 16(6), pp. 583-605, DOI: 10.1080/13588265.2011.606996.

Kerrigan J. R., Seppi J., Lockerby J., Foltz P., Overby B., Bolton J., Kim T., Dennis N. J., and Crandall J., 2013, "Test Methodology and Initial Results from a Dynamic Rollover Test System," SAE Technical Paper: 2013-01-0468, DOI:10.4271/2013-01-0468.

Khoder W., Fassinut-Mombot B., and Benjelloun M., 2008, "Inertial Navigation Attitude Velocity and Position Algorithms using Quaternion Scaled Unscented Kalman Filtering," Proceedings of 34th Annual Conference of IEEE Industrial Electronics, Orlando, FL, November 10-13, 2008, pp. 1754-1759, DOI: 10.1109/IECON.2008.4758219.

Kitagawa N., and Ogihara, N., 2016, "Estimation of foot trajectory during human walking by a wearable inertial measurement unit mounted to the foot," Gait & Posture, Vol. 45, pp. 110–114.

Klein E. Ch., Sinz W., Moser J., and Greimel R., 2016, "Comparison of optimisation strategies for the determination of precise dummy head trajectories based on the fusion of electrical and optical measured data in frontal crash scenarios," International Journal of Vehicle Systems Modelling and Testing, 11(1), pp. 23-46.

Laird Wheaton GM, 2013, "GM Introduces Industry's First Front Center Air Bag - Safety at Laird Wheaton GM," YouTube, Published on October 18, 2013, https://www.youtube.com/watch?v=D-OKpFyTtvg, Accessed March 16, 2019.

Lee H., and Ghosh S. K., 2009, "Performance of Information Criteria for Spatial Models," Journal of Statistical Computation and Simulation, 79(1), pp. 93–106, DOI: 10.1080/00949650701611143.

Lessley D., Shaw G., Forman J., and Crandall J., 2011, "Assessment and Validation of a Methodology for Measuring Anatomical Kinematics of Restrained Occupants During Motor Vehicle Collisions," Journal of Biosensors and Bioelectronics, S1:002, DOI: 10.4172/2155-6210.S1-002.

Lessley D., Riley P., Zhang Q., Foltz P., Overby B., Heltzel S., Sochor M., Crandall J., and Kerrigan J. R., 2014, "Occupant Kinematics in Laboratory Rollover Tests: PMHS Response," Stapp Car Crash Journal, Vol. 58, pp. 251-316.

Li, J. L., Fang, J. C., Du, M., and Dong, H. F., 2013, "Analysis and fabrication of a novel MEMS pendulum angular accelerometer with electrostatic actuator feedback," Microsystem Technologies, 19:9, DOI: 10.1007/s00542-012-1630-x.

Liu Y. K., 1976, Discussion of "Measurement of angular acceleration of a rigid body using linear accelerometers", Journal of Applied Mechanics, Vol. 43(2), pp. 377–378.

Litmanovich Y. A., Lesyuchevsky V. M., and Gusinsky V. Z., 2000, "Two New Classes of Strapdown Navigation Algorithms," Journal of Guidance, Control, and Dynamics, 23(1), pp. 34-44.

Ma D-M., Shiau J-K., Chiang Wang I., and Lin Y-H., 2012, "Attitude Determination Using a MEMS-Based Flight Information Measurement Unit," Sensors, 12, pp. 1-23, DOI:10.3390/s120100001.

Mangan N. M., Kutz J. N., Brunton S. L., Proctor J. L., 2017, "Model selection for dynamical systems via sparse regression and information criteria," Proceedings. Mathematical, physical, and engineering sciences, A 473: 20170009, DOI: 10.1098/rspa.2017.0009.

Mannini A., and Sabatini A. M., 2014, "Walking speed estimation using foot-mounted inertial sensors: Comparing machine learning and strap-down integration methods," Medical Engineering & Physics 36, pp. 1312–1321, DOI: http://dx.doi.org/10.1016/j.medengphy.2014.07.022.

Mariani B., Hoskovec H., Rochat S., Bula Ch., Penders J., and Aminian K., 2010, "3D gait assessment in young and elderly subjects using foot-worn inertial sensors," Journal of Biomechanics 43, pp. 2999–3006, DOI: 10.1016/j.jbiomech.2010.07.003.

Martin P. G., Hall G. W., Crandall J. R., and Pilkey W. D., 1998, "Measuring the acceleration of a rigid body," Shock and Vibration, Vol. 5, pp. 211–224.

MEGGITT Endevco®, 2017, Piezoresistive accelerometer, Datasheet Model 7302BM5, Available at: https://buy.endevco.com/amfile/file/download/file_id/2628/product_id/2594/, Accessed January 18, 2019.

McKay M. D., Beckman R. J., and Conover W. J., 1979, "A Comparison of Three Methods for Selecting Values of Input Variables in the Analysis of Output from a Computer Code," Technometrics (JSTOR Abstract), American Statistical Association, 21 (2): 239–245, ISSN 0040-1706, JSTOR 1268522, OSTI 5236110, DOI: 10.2307/1268522.

Miller P. A., Farrell J. A., Zhao Y., Djapic V., 2010, "Autonomous Underwater Vehicle Navigation," IEEE Journal of Oceanic Engineering, 35(3), pp. 663-678.

Montesinos-Acosta S., Ash J. H., Lessley D. J., Shaw C. G., Heltzel S. B., and Crandall J. R., 2016, "Comparison of Whole Body Response in Oblique and Full Frontal Sled Tests," Proceedings of IRCOBI 2016 conference, IRC-16-94, pp. 740-752, Malaga, Spain.

National Highway Safety Administration, 2013, NHTSA Vehicle Database, Available at: https://www-nrd.nhtsa.dot.gov/database/VSR/veh/TestSeries.aspx?level=4&test=9120, Accessed February 5, 2018.

National Highway Safety Administration, 2014, NHTSA Vehicle Database, Available at: https://www-nrd.nhtsa.dot.gov/database/VSR/veh/TestSeries.aspx?level=4&test=8780, Accessed March 18, 2019.

National Highway Traffic Safety Administration, 2015a, "Laboratory Test Procedure for Oblique Offset Moving Deformable Barrier Impact Test," Draft from July 22, 2015, Available at: https://www.nhtsa.gov/sites/nhtsa.dot.gov/files/documents/15072220obliquetestproceduredraft_pdf.pdf, Accessed December 18, 2018.

National Highway Safety Administration, 2015b, "Update to New Car Assessment Program," Federal Register, Vol. 80, No. 241, Docket No. NHTSA–2015–0119.

National Highway Traffic Safety Administration, 2016, "3D Parametric Model, August 2016 Draft (Generic STEP)," Available at: https://www.nhtsa.gov/document/thor-50m-august-2016-stp-fileszip, Accessed December 6, 2018.

National Highway Safety Administration, 2017a, NHTSA Vehicle Database, Available at: https://www-nrd.nhtsa.dot.gov/database/VSR/veh/TestSeries.aspx?level=4&test=10110, Accessed February 5, 2018.

National Highway Safety Administration, 2017b, NHTSA Vehicle Database, Available at: https://www-nrd.nhtsa.dot.gov/database/VSR/veh/TestSeries.aspx?level=4&test=10130, Accessed February 5, 2018.

National Highway Safety Administration, 2018, THOR – Test Device for Human Occupant Restraint, Available at: https://www.nhtsa.gov/biomechanics-trauma/thor, Accessed August 15, 2018.

Nevins D., Petersen P., and Smith L., 2018, "Evaluation of a Differentiation Scheme for Estimating Angular Acceleration from Angular Velocity," Proceedings 2018, 2, 271, DOI:10.3390/proceedings2060271.

Nusbaum U., Klein I., and Rusnak I., 2018, "Angular Acceleration Sensors for Inertial Navigation," Proceedings of the 58th Israel Annual Conference on Aerospace Sciences, Tel-Aviv & Haifa, Israel, March 14-15, 2018.

Ólafsdóttir J., Östh J., Davidsson J., and Brolin K., 2013, "Passenger Kinematics and Muscle Responses in Autonomous Braking Events with Standard and Reversible Pre-tensioned Restraints," Proceedings of IRCOBI 2013 conference, IRC-13-70, pp. 602-617, Gothenburg, Sweden.

Padgaonkar A. J., Krieger K. W., and King A. I., 1975, "Measurement of Angular Acceleration of a Rigid Body Using Linear Accelerometers," Journal of Applied Mechanics, 42(3), 552-556. DOI:10.1115/1.3423640.

Qazizadaa M. E., and Pivarčiováa E., 2016, "Mobile robot controlling possibilities of inertial navigation system," Procedia Engineering 149, pp. 404 – 413.

Rebula J. R., Ojeda L. V., Adamczyk P. G., and Kuo A. D., 2013, "Measurement of foot placement and its variability with inertial sensors," Gait & Posture 38, pp. 974–980, DOI: http://dx.doi.org/10.1016/j.gaitpost.2013.05.012.

Rudd R., Kerrigan J. R., Crandall J. R., and Arregui C., 2006, "Kinematic Analysis of Head/Neck Motion in Pedestrian-Vehicle Collisions Using 6-Degree-of-Freedom Instrumentation Cubes," SAE Technical Paper: 2006-01-0681, DOI:10.4271/2006-01-0681.

Sanchez E. J., 2017, "Evaluation of the Efficacy of Head and Brain Injury Risk Functions," Master's Thesis, University of Virginia, Charlottesville, VA, USA.

Santhanakrishnan M. N., Balaguru Rayappan J. B., Kannan R., 2017, "Implementation of extended Kalman filter-based simultaneous localization and mapping: a point feature approach," Sadhana, Vol. 42, No. 9, September 2017, pp. 1495–1504, DOI: 10.1007/s12046-017-0692-y.

Saunders J., and Parent D., 2013, "Assessment of an Oblique Moving Deformable Barrier Test Procedure," Proceedings of 23rd ESV Conference, Paper Number: 13-0402, Seoul, South Korea.

Savage P. G., 1998, "Strapdown Inertial Navigation Integration Algorithm Design Part 1: Attitude Algorithms," Journal of Guidance, Control, and Dynamics, Vol. 21, No. 1, pp. 19-28. DOI: 10.2514/2.4228.

Savage P. G., 2002, "Analytical Modeling of Sensor Quantization in Strapdown Inertial Navigation Error Equations," Journal of Guidance, Control, and Dynamics, Vol. 25, No. 5, pp. 833-842. DOI: 10.2514/2.4963.

Savage P. G., 2010, "Coning Algorithm Design by Explicit Frequency Shaping," Journal of Guidance, Control, And Dynamics, 33(4), DOI: 10.2514/1.47337.

Schoenebeck K., Melbert J., and Weiser F., 2009, "Motion Tracking in Crash Test Applications with Inertial Measurement Units," SAE Technical Paper: 2009-01-0056, DOI: 10.4271/2009-01-0056.

Shabana A. A., 2010, Dynamics of Multibody Systems. 3rd Edition, Cambridge University Press, Cambridge, England, ISBN-13: 978-0521154222.

Shaw G., Parent D., Purtsezov S., Lessley D., Crandall J., Kent R., Guillemot H., Ridella S. A., Takhounts E., and Martin P., 2009, "Impact Response of Restrained PMHS in Frontal Sled Tests: Skeletal Deformation Patterns Under Seat Belt Loading," Stapp Car Crash Journal, Vol. 53, pp. 1-48.

Shaw G., Lessley D., Ash J., and Crandall J., 2014, "Development of an Alternative Frontal Impact Condition to Assess Thoracic Response Using the THOR Mod Kit Dummy," International Journal of Automotive Engineering, Vol. 5, Issue 1, pp. 39-46, DOI: https://doi.org/10.20485/jsaeijae.5.1_39.

Sinz W., Moser J., Klein C., Greimel R. et al., 2015, "Precise Dummy Head Trajectories in Crash Tests based on Fusion of Optical and Electrical Data: Influence of Sensor Errors and Initial Values," SAE Technical Paper: 2015-01-1442, DOI:10.4271/2015-01-1442.

Society of Automotive Engineers, 1995, "SAE J211: Instrumentation for Impact Test," SAE International, Warrendale, PA, USA.

Takhounts E. G., Hasija V., and Eppinger R. H., 2009, "Analysis of 3D Rigid Body Motion Using the Nine Accelerometer Array and the Randomly Distributed In-Plane Accelerometer Systems," Proceedings of the 21st (ESV) International Technical Conference on the Enhanced Safety of Vehicles, Paper Number: 09-0402, Stuttgart, Germany.

Toczyski J., Lessley D., Zhang Q., and Kerrigan J., 2015, "Occupant Motion Tracking in Rollover using 3D Optical Systems," Proceedings of IRCOBI 2015 conference, IRC-15-56, pp. 452-453, Lyon, France.

Trojaniello D., Ravaschio A., Hausdorff J. M., and Cereatti A., 2015, "Comparative assessment of different methods for the estimation of gait temporal parameters using a single inertial sensor: application to elderly, post-stroke, Parkinson's disease and Huntington's disease subjects," Gait & Posture 42, pp. 310–316, DOI: http://dx.doi.org/10.1016/j.gaitpost.2015.06.008.

Ugray Z., Lasdon L., Plummer J. C., Glover F., Kelly J., and Martí R., 2007, "Scatter Search and Local NLP Solvers: A Multistart Framework for Global Optimization," INFORMS Journal on Computing, Vol. 19, No. 3, pp. 328–340.

van Rooij L., Elrofai H., Philippens M. M. G. M., and Daanen H. A. M., 2013, "Volunteer Kinematics and Reaction in Lateral Emergency Maneuver Tests," Stapp Car Crash Journal, Vol. 57, pp. 313-342.

Vepa R., and Zhahir A., 2011, "High-Precision Kinematic Satellite and Doppler Aided Inertial Navigation System," The Journal of Navigation, Vol. 64, pp. 91–108, DOI: 10.1017/S0373463310000329.

Viano D. C., Melvin J. W., McCleary J. D., Madeira R. G., Shee T. R., and Horsch J. D., 1986, "Measurement of head dynamics and facial contact forces in the Hybrid III dummy," SAE Technical Paper: 861891.

Voo L., Merkle A., Chang S.-S., and Kleinberger M., 2003, "Comparison of Three Rotation Measurement Techniques in Rear Impact Application," SAE Technical Paper: 2003-01-0174.

Waltz R. A., Morales J. L., Nocedal J., and Orban D., "An interior algorithm for nonlinear optimization that combines line search and trust region steps," Mathematical Programming, Vol 107, No. 3, pp. 391–408.

Wang L-d., Jin W-r., Zhan X-q., and Zhang Y-h, 2011, "Performance improvement and study of the space-oriented strapdown inertial navigation system," Measurement Science and Technology, 22, DOI: 10.1088/0957-0233/22/11/115201.

Winter D. A., 2004, "Biomechanics and motor control of human movement," Third Edition, John Wiley & Sons, Inc.

Wolfaardt, H.J., and Heyns, P.S., 2008, "Dynamic modeling of a novel micro-fluidic channel angular accelerometer," Journal of Vibration and Control, Vol. 14, pp. 451–467.

Wu J., Shi Y., Kang J., and Nusholtz G. S., 2009, "Using Triaxial Angular Rate Sensor and Accelerometer to Determine Spatial Orientation and Position in Impact Tests," SAE Technical Paper: 2009-01-0055, DOI: 10.4271/2009-01-0055.

Yang S., Zhang J., Novak A. C., Brouwer B., and Li Q, 2012, "Estimation of spatio-temporal parameters for post-stroke hemiparetic gait using inertial sensors," Gait & Posture 37, pp. 354–358, DOI: http://dx.doi.org/10.1016/j.gaitpost.2012.07.032.

Yoganandan N., Zhang J., Pintar F. A., and Liu Y. K., 2006, "Lightweight low-profile nine accelerometer package to obtain head angular accelerations in short duration impacts," Journal of Biomechanics, Vol. 39, pp. 1347–1354.

Zhao, H., and Feng H., 2015, "A Novel Permanent Magnetic Angular Acceleration Sensor," Sensors 2015, Vol. 15, pp. 16136-16152; DOI:10.3390/s150716136.

Zhang Q., Lessley D., Riley P., Toczyski J., Lockerby J., Foltz P., Overby B., Seppi J., Crandall J. R., and Kerrigan J. R., 2014, "Occupant kinematics in laboratory rollover tests: ATD response and biofidelity," Stapp Car Crash Journal, Vol. 58, pp. 317-360.

Zhang Y., Yu F., Gao W., and Wang Y., 2018, "An Improved Strapdown Inertial Navigation System Initial Alignment Algorithm for Unmanned Vehicles," Sensors 2018, 18, 3297, DOI: 10.3390/s18103297.

Zhenhuan W., Xijun Ch., and Qingshuang Z., 2013, "Comparison of strapdown inertial navigation algorithm based on rotation vector and dual quaternion," Chinese Journal of Aeronautics, 26(2), pp. 442–448, DOI: 10.1016/j.cja.2013.02.022.

Zhuang Y., Gong J., Kerrigan D. C., Bennett B. C., Lach J., and Russell S., 2016, "Gait tracker shoe for accurate step-by-step determination of gait parameters," Proceedings of 2016 IEEE 13th International Conference on Wearable and Implantable Body Sensor Networks (BSN), San Francisco, CA, USA, DOI: 10.1109/BSN.2016.7516225.

APPENDIX A – SIMPLIFIED HEAD TESTS – TEST MATRIX

Table A1. Simplified Head Test Matrix.

Test ID	Orientation w.r.t. sled travel direction	Flat / wedge	Pulse (indicated by the peak value; Figure 21)	Minimum / 12.7mm offset	Top / bottom
S0415	45°	flat	4.9g	UVa 4acc block: minimum THOR's NAP block: n/a	UVa 4acc block: top THOR's NAP block: bottom
S0416	45°	flat	9.8g	UVa 4acc block: minimum THOR's NAP block: n/a	UVa 4acc block: top THOR's NAP block: bottom
S0417	45°	flat	14.7g	UVa 4acc block: minimum THOR's NAP block: n/a	UVa 4acc block: top THOR's NAP block: bottom
S0418	45°	flat	19.5g	UVa 4acc block: minimum THOR's NAP block: n/a	UVa 4acc block: top THOR's NAP block: bottom
S0419	45°	flat	29.3g	UVa 4acc block: minimum THOR's NAP block: n/a	UVa 4acc block: top THOR's NAP block: bottom
S0420	45°	flat	27g	UVa 4acc block: minimum THOR's NAP block: n/a	UVa 4acc block: top THOR's NAP block: bottom
S0421	0°	flat	27g	UVa 4acc block: minimum THOR's NAP block: n/a	UVa 4acc block: top THOR's NAP block: bottom
S0422	0°	flat	27g	UVa 4acc block: minimum THOR's NAP block: n/a	UVa 4acc block: top THOR's NAP block: bottom
S0423	0°	flat	27g	UVa 4acc block: 12.7mm THOR's NAP block: n/a	UVa 4acc block: top THOR's NAP block: bottom

S0424	45°	flat	27g	UVa 4acc block: 12.7mm THOR's NAP block: n/a	UVa 4acc block: top THOR's NAP block: bottom
S0425	45°	flat	27g	UVa 4acc block: 12.7mm THOR's NAP block: n/a	UVa 4acc block: bottom THOR's NAP block: top
S0426	0°	flat	27g	UVa 4acc block: 12.7mm THOR's NAP block: n/a	UVa 4acc block: bottom THOR's NAP block: top
S0427	0°	flat	27g	UVa 4acc block: 12.7mm THOR's NAP block: n/a	UVa 4acc block: bottom THOR's NAP block: top
S0428	0°	wedge	27g	UVa 4acc block: 12.7mm THOR's NAP block: n/a	UVa 4acc block: bottom THOR's NAP block: top
S0429	45°	wedge	27g	UVa 4acc block: 12.7mm THOR's NAP block: n/a	UVa 4acc block: bottom THOR's NAP block: top
S0430	45°	wedge	27g	UVa 4acc block: minimum THOR's NAP block: n/a	UVa 4acc block: bottom THOR's NAP block: top
S0431	45°	wedge	27g	UVa 4acc block: minimum THOR's NAP block: n/a	UVa 4acc block: bottom THOR's NAP block: top
S0432	0°	wedge	27g	UVa 4acc block: minimum THOR's NAP block: n/a	UVa 4acc block: bottom THOR's NAP block: top
S0433	0°	flat	27g	UVa 4acc block: minimum THOR's NAP block: n/a	UVa 4acc block: bottom THOR's NAP block: top
S0434	45°	flat	27g	UVa 4acc block: minimum THOR's NAP block: n/a	UVa 4acc block: bottom THOR's NAP block: top

S0435	0°	wedge	27g	UVa 4acc block: minimum THOR's NAP block: n/a	UVa 4acc block: top THOR's NAP block: bottom
S0436	45°	wedge	27g	UVa 4acc block: minimum THOR's NAP block: n/a	UVa 4acc block: top THOR's NAP block: bottom
S0437	45°	wedge	27g	UVa 4acc block: 12.7mm THOR's NAP block: n/a	UVa 4acc block: top THOR's NAP block: bottom
S0438	0°	wedge	27g	UVa 4acc block: 12.7mm THOR's NAP block: n/a	UVa 4acc block: top THOR's NAP block: bottom
S0439	45°	flat	27g	UVa 4acc block: minimum UVa NAP block: 12.7mm	UVa 4acc block: top UVa NAP block: bottom
S0440	45°	wedge	27g	UVa 4acc block: minimum UVa NAP block: 12.7mm	UVa 4acc block: top UVa NAP block: bottom
S0441	45°	wedge	27g	UVa 4acc block: minimum UVa NAP block: minimum	UVa 4acc block: top UVa NAP block: bottom
S0442	45°	flat	27g	UVa 4acc block: minimum UVa NAP block: minimum	UVa 4acc block: top UVa NAP block: bottom
S0443	45°	flat	27g	UVa 4acc block: minimum UVa NAP block: minimum	UVa 4acc block: top UVa NAP block: bottom
S0444	45°	flat	27g	UVa 4acc block: minimum	UVa 4acc block: top UVa NAP block: bottom

				UVa NAP block: minimum	
S0445	45°	flat	27g	UVa 4acc block: minimum UVa NAP block: minimum	UVa 4acc block: top UVa NAP block: bottom
S0446	45°	flat	27g	UVa 4acc block: minimum UVa NAP block: minimum	UVa 4acc block: top UVa NAP block: bottom
S0447	45°	flat	27g	UVa 4acc block: minimum UVa NAP block: minimum	UVa 4acc block: top UVa NAP block: bottom
S0448	45°	flat	27g	UVa 4acc block: minimum UVa NAP block: minimum	UVa 4acc block: top UVa NAP block: bottom
S0449	45°	flat	27g	UVa 4acc block: minimum UVa NAP block: minimum	UVa 4acc block: top UVa NAP block: bottom
S0450	45°	flat	27g	UVa 4acc block: minimum UVa NAP block: minimum	UVa 4acc block: top UVa NAP block: bottom
S0451	45°	flat	27g	UVa 4acc block: minimum UVa NAP block: minimum	UVa 4acc block: top UVa NAP block: bottom
S0452	45°	flat	27g	UVa 4acc block: minimum	UVa 4acc block: top UVa NAP block: bottom

				UVa NAP block: minimum	
S0453	45°	flat	27g	UVa 4acc block: minimum UVa NAP block: minimum	UVa 4acc block: top UVa NAP block: bottom
S0454	45°	flat	27g	UVa 4acc block: minimum UVa NAP block: minimum	UVa 4acc block: top UVa NAP block: bottom
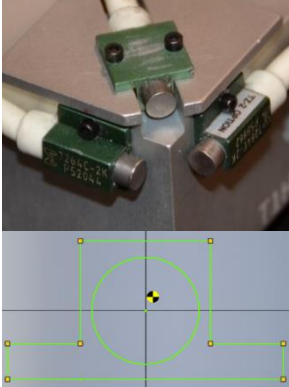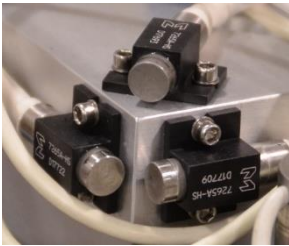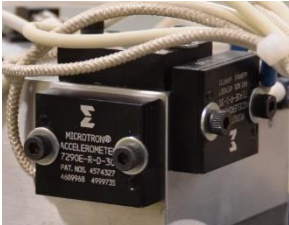
Additional remarks:

- Due to the hardware incompatibility, the signal recorded for Endevco 7290Es in Tests S0415÷ S0425 was not valid for the trajectory calculation (non-physical cut off at approx. 10g in one of the directions).
- Tests S0442 to S0449 (except for S0448) were run in the same configuration, one after another, and can be treated as repeated tests.
- In Test S0448, a sensor cable was tangled behind one of the VICON markers. During the test, the cable restrained the head changing its kinematics.
- In the last five tests (S0450 to S0454) a change in data acquisition system (DAS) and/or sensor parameters was made:
  - S0450: Where possible full scale range for accelerometers (ACC) was set to ±64g (25% higher than the maximum absolute value seen among the repeated tests);
  - S0451: Where possible full scale range for angular rate sensors (ARS) was set to ±1410 deg/s (25% higher than the maximum absolute value seen among the repeated tests);
  - S0452: Where possible full scale ranges for ACC and ARS were set to ±64g and ±1410 deg/s, respectively;
  - S0453: Excitation voltage for all piezoresistive accelerometers, attached to the simplified head, running previously at 10V, was changed to 2V;
  - S0454: All ARS and DTS 6DX PRO sensors were moved from DTS TDAS G5 to DTS TDAS PRO. DTS 6DX PRO ACC were excited at 2V. All other sensors connected to TDAS PRO were excited at 10V.

APPENDIX B – SIMPLIFIED HEAD TESTS – INSTRUMENTATION AND DATA ACQUISITION SYSTEMS

Six different linear accelerometer types (Table B1), four different angular rate sensor types (Table B2), one type of a piezoresistive angular accelerometer (Table B3) and three different DAS types (Table B4) were used during testing. The sensors were calibrated prior to the tests. In all forty sled tests the data were recorded at 20 kHz.

Table B1. Linear accelerometer summary

Manufacturer	Model	Quantity	Photo	General parameters
Endevco Meggitt Sensing Systems	7264C	9		• Piezoresistive • Full range: 2000g • Sensitivity: ~0.2 mV/g • Frequency response: from 0 up to 5000Hz • Damping ratio: 0.005 • Calibrated at 10V excitation • Run at 10V excitation (except for Test S0453, where run at 2V) • Seismic mass CG (marked in the picture on the left with a photo target) not on the main axis of the sensor
	7265A-HS	3		• Piezoresistive • Full range: 20g • Sensitivity: ~25 mV/g • Frequency response: from 0 up to 500Hz • Damping ratio: 0.707 • Calibrated at 10V excitation • Run at 10V excitation (except for Test S0453, where run at 2V)
	7290E	3		• Variable capacitance • Full range: 30g • Sensitivity: ~66 mV/g • Frequency response: from 0 up to 1000Hz • Damping ratio: 0.7 • Calibrated at 11V excitation • Not proportional to excitation
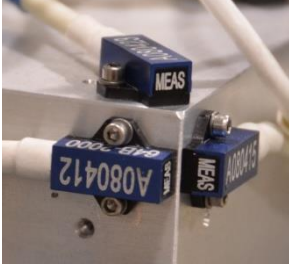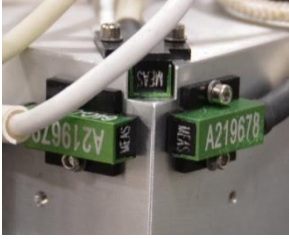
Measurement Specialties (MSI)	64B	3		• Piezoresistive • Full range: 2000g • Sensitivity: ~0.15 mV/g • Frequency response: from 0 up to 3000Hz • Damping ratio: 0.05 • Calibrated at 10V excitation • Run at 10V excitation (except for Test S0453, where run at 2V)
	64C	3		• Piezoresistive • Full range: 100g • Sensitivity: ~0.9 mV/g • Frequency response: from 0 up to 500Hz • Damping ratio: 0.5 • Calibrated at 10V excitation • Run at 10V excitation (except for Test S0453, where run at 2V)
Diversified Technical Systems (DTS)	6DX PRO	1 cube (3 accelerometers inside)		• Piezoresistive • Full range: 2000g • Sensitivity: ~0.2 mV/g • Frequency response: from 0 up to 10000Hz • Damping ratio: n/a • Calibrated at 5V excitation • Run at 5V excitation (except for Test S0454, where run at 2V)

Table B2. Angular rate sensors summary

Manufacturer	Model	Quantity	Photo	General parameters
Diversified Technical Systems (DTS)	ARS PRO-8K 300Hz	3		• Full range: 8000 deg/s • Not proportional to excitation • Frequency response: from 0 up to 300Hz • Internally regulated excitation
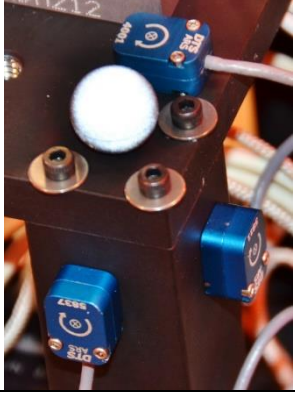
	ARS PRO-8K 2000Hz	3		• Full range: 8000 deg/s • Not proportional to excitation • Frequency response: from 0 up to 2000Hz • Internally regulated excitation
	6DX PRO	1 cube (3 angular rate sensors inside)		• Full range: 18000 deg/s • Not proportional to excitation • Frequency response: from 0 up to 2000Hz • Internally regulated excitation • Tri-axial
IES	3103-600	1		• Full range: 600 deg/s • Not proportional to excitation • Frequency response: from 0 up to 100Hz • Internally regulated excitation • Tri-axial

Table B3. Angular acceleration sensors summary
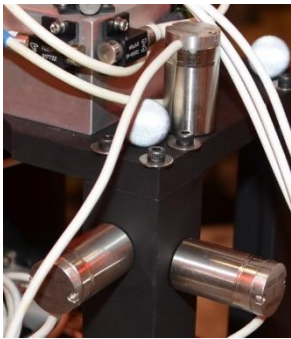
Manufacturer	Model	Quantity	Photo	General parameters
Endevco Meggitt Sensing Systems	7302BM5	3		• Piezoresistive • Full range: 50000 rad/s2 • Sensitivity: ~2.5 mV/Krad/s2 (5V excitation) or 5 mV/Krad/s2 (10V excitation) • Frequency response: from 3 up to 1000Hz • Frequency content of the signal discussed in APPENDIX H

Table B4. DAS summary

Manufacturer	Model	Quantity	Photo	General parameters
Diversified Technical Systems (DTS)	TDAS PRO	2		• Voltage Insertion Type: 16-bit DAC • Resolution: 16-bit • Max sampling rate: 304k samples/sec/module • Excitation voltage levels: 2 & 10V • # of channels: 30 • Anti-alias filter: low pass, 8-pole Butterworth, 2.9 kHz • Overhead room added to the sensor full scale range: 20%
	TDAS G5	1		• Voltage Insertion Type: 16-bit DAC • Resolution: 16-bit • Max sampling rate: 100k samples/sec/module • Excitation voltage levels: 5V • # of channels: 32 • Anti-alias filter: low pass, 4-pole Butterworth, 2.9 kHz • Overhead room added to the sensor full scale range: 20%
	SLICE Micro	1		• Resolution: 16-bit • Excitation voltage level: 5V • Bandwidth: DC to 40 kHz • # of channels: 15 • Anti-alias filter: low pass, 4-pole Butterworth, 40 kHz • Overhead room added to the sensor full scale range: 20% • Used since Test S0426 and only for Endevco 7290Es

APPENDIX C – SIMPLIFIED HEAD TESTING – *RES*_{ERR} (IN MILLIMITERS) FOR ALL SENSOR COMBINATIONS

Table C1. Res_{err} (in millimeters) for all sensor combinations for Tests S0415 to S0434.

Sensor combination	S0415	S0416	S0417	S0418	S0419	S0420	S0421	S0422	S0423	S0424	S0425	S0426	S0427	S0428	S0429	S0430	S0431	S0432	S0433	S0434
DTS6DX_Acc-DTS6DX_Ars	202.65	616.91	269.84	108.47	55.63	75.54	60.68	92.19	89.63	72.08	92.72	103.64	81.50	84.06	78.38	65.97	88.25	105.49	62.58	58.88
DTS6DX_Acc-DTS300Hz	203.00	635.78	276.93	113.79	55.04	79.67	67.99	101.39	101.50	65.76	94.65	123.24	106.94	112.53	74.86	69.94	84.33	113.14	75.51	65.10
DTS6DX_Acc-DTS2000Hz	213.19	625.07	271.26	109.35	52.19	75.73	64.05	94.14	96.00	67.95	86.23	106.73	82.27	89.94	81.92	61.13	85.96	106.60	60.11	57.76
DTS6DX_Acc-IES	207.44	627.40	273.76	111.28	109.92	103.03	128.32	247.82	201.81	120.82	164.84	271.40	275.09	153.86	93.63	75.40	98.80	151.15	239.40	115.96
END7264C-DTS6DX_Ars	128.00	120.64	27.09	39.24	24.01	9.25	15.12	25.23	19.92	26.56	15.16	16.30	9.03	21.32	7.27	25.01	17.96	27.59	15.00	14.19
END7264C-DTS300Hz	123.11	86.29	35.35	29.50	19.18	23.00	19.95	25.18	14.19	30.75	14.85	28.22	39.84	21.09	21.08	17.85	25.49	13.43	17.60	18.74
END7264C-DTS2000Hz	114.72	103.40	22.61	37.51	22.99	10.70	15.03	21.62	12.86	25.80	18.72	12.55	9.47	13.42	3.35	27.52	20.47	22.12	14.50	19.69
END7264C-IES	118.58	103.54	21.95	34.94	56.93	32.57	68.53	170.36	127.12	44.24	102.40	203.66	234.50	79.75	12.55	26.07	7.83	55.15	194.94	61.51
END7265A-DTS6DX_Ars	29.88	54.52	60.77	49.65	57.50	32.36	15.10	27.06	24.81	51.46	44.23	29.46	31.27	36.02	37.00	34.52	37.98	36.67	25.47	30.51
END7265A-DTS300Hz	17.40	43.65	61.55	52.01	73.91	48.62	19.88	38.50	25.18	62.91	51.05	36.19	39.98	34.30	39.48	40.05	40.26	37.06	29.14	34.22
END7265A-DTS2000Hz	18.68	45.50	56.96	49.46	64.08	35.15	13.79	26.05	17.61	53.37	44.56	28.54	29.72	33.76	34.13	37.21	37.95	36.26	26.54	28.77
END7265A-IES	14.16	41.48	53.26	46.99	47.81	46.35	116.82	271.91	200.80	72.11	66.73	145.22	168.15	68.46	36.07	33.95	35.36	54.06	138.02	46.71
END7290E-DTS6DX_Ars	n/a	n/a	n/a	n/a	n/a	n/a	n/a	n/a	n/a	n/a	n/a	16.53	17.80	19.37	7.94	8.95	8.76	13.34	15.39	8.96
END7290E-DTS300Hz	n/a	n/a	n/a	n/a	n/a	n/a	n/a	n/a	n/a	n/a	n/a	29.77	33.81	24.44	15.32	18.58	16.95	17.68	24.98	21.14
END7290E-DTS2000Hz	n/a	n/a	n/a	n/a	n/a	n/a	n/a	n/a	n/a	n/a	n/a	16.01	18.21	15.81	11.29	8.60	8.78	10.78	16.52	8.73
END7290E-IES	n/a	n/a	n/a	n/a	n/a	n/a	n/a	n/a	n/a	n/a	n/a	139.17	161.29	56.03	14.71	12.13	9.56	39.07	131.51	45.47
MSI64B-DTS6DX_Ars	99.47	240.70	218.22	63.86	30.26	29.13	13.87	20.91	13.51	38.20	107.78	12.18	24.44	20.31	13.18	31.33	16.71	39.71	28.80	29.41
MSI64B-DTS300Hz	116.45	230.40	243.98	77.82	32.72	54.42	13.90	28.57	28.36	29.49	120.19	20.82	17.77	16.95	15.90	45.95	24.50	26.80	30.88	31.03
MSI64B-DTS2000Hz	100.08	235.47	234.96	66.36	31.42	34.54	8.72	15.19	6.87	34.06	110.64	10.93	22.77	13.74	11.98	32.29	17.20	35.54	26.25	29.17
MSI64B-IES	108.16	231.54	222.78	59.35	82.97	33.39	117.61	288.41	196.63	89.42	51.23	154.52	160.56	62.87	19.07	27.34	10.53	71.35	158.35	35.48
MSI64C-DTS6DX_Ars	26.12	41.26	39.56	31.14	25.14	26.17	21.65	43.98	37.63	40.03	27.69	25.91	26.33	35.69	20.41	15.86	20.27	33.25	25.82	18.88
MSI64C-DTS300Hz	10.18	29.71	34.26	30.09	29.11	30.17	9.84	25.17	18.94	38.79	32.87	9.93	11.68	23.47	18.85	18.07	19.85	17.44	15.71	20.28
MSI64C-DTS2000Hz	18.51	29.44	32.60	29.65	26.33	23.84	14.64	36.75	34.17	37.62	28.52	22.53	25.53	28.72	19.47	18.35	20.21	28.52	24.23	19.82
MSI64C-IES	9.98	26.18	29.58	27.28	92.78	61.13	129.85	296.07	223.93	91.96	63.76	161.24	185.03	83.41	23.88	19.76	22.01	64.12	150.03	45.14

Table C2. Res_err (in millimeters) for all sensor combinations for Tests S0435 to S0454.

Sensor combination	S0435	S0436	S0437	S0438	S0439	S0440	S0441	S0442	S0443	S0444	S0445	S0446	S0447	S0448	S0449	S0450	S0451	S0452	S0453	S0454
DTS6DX_Acc-DTS6DX_Ars	72.99	60.05	62.73	69.37	39.84	82.56	85.95	61.21	55.23	71.01	44.75	54.46	69.78	38.80	58.91	35.48	44.53	30.63	40.12	44.38
DTS6DX_Acc-DTS300Hz	76.92	64.41	69.18	79.54	30.24	75.73	93.55	61.27	66.01	66.55	48.91	51.94	68.85	33.96	52.95	34.72	43.98	30.87	35.15	55.09
DTS6DX_Acc-DTS2000Hz	72.01	57.93	64.43	73.45	34.08	77.16	86.83	56.32	55.38	77.63	42.62	52.59	67.32	36.30	54.39	34.13	42.75	29.47	34.46	44.83
DTS6DX_Acc-IES	106.06	63.46	71.22	117.23	74.32	86.42	101.04	94.58	91.61	123.60	79.82	82.63	109.56	62.40	94.33	67.59	74.08	55.88	66.28	72.33
END7264C-DTS6DX_Ars	24.90	10.93	14.69	22.89	16.02	6.35	18.93	11.69	17.10	13.19	7.07	14.66	16.55	5.52	16.07	4.60	9.80	5.11	42.59	18.37
END7264C-DTS300Hz	14.11	15.79	11.68	7.92	12.39	6.38	11.09	7.54	14.19	6.82	5.13	13.58	4.92	12.36	14.38	14.26	13.01	10.00	48.70	7.91
END7264C-DTS2000Hz	20.27	9.38	13.11	17.47	16.40	7.34	18.12	10.17	14.02	18.27	4.87	16.68	10.93	3.48	16.35	2.86	10.28	4.51	45.04	17.47
END7264C-IES	56.08	15.76	8.51	54.68	47.13	13.22	14.59	43.16	60.18	70.29	45.54	27.94	63.42	32.60	48.68	41.55	40.71	35.09	39.90	47.02
END7265A-DTS6DX_Ars	27.18	26.54	32.03	31.72	23.99	28.77	39.87	25.74	28.44	43.58	27.01	22.58	39.16	20.10	25.70	27.74	27.67	22.95	21.83	28.48
END7265A-DTS300Hz	23.02	36.62	34.31	27.13	40.34	38.37	41.77	35.63	45.75	58.14	31.09	26.61	50.51	32.04	40.07	35.67	37.38	29.01	34.91	32.37
END7265A-DTS2000Hz	27.45	33.75	33.66	26.09	30.13	33.01	39.01	32.32	34.50	36.41	30.97	25.69	41.80	23.77	30.37	28.16	30.24	25.14	30.96	28.22
END7265A-IES	58.91	27.77	27.18	75.52	55.45	27.36	31.58	54.60	67.55	72.49	51.34	36.32	67.10	33.50	59.15	51.10	44.20	41.23	29.30	53.57
END7290E-DTS6DX_Ars	19.84	15.89	14.87	24.10	16.89	13.66	16.39	15.54	15.36	14.62	10.41	8.67	16.59	9.19	15.86	10.28	7.16	6.99	12.54	11.08
END7290E-DTS300Hz	18.68	19.90	19.73	22.67	27.31	18.52	23.46	20.74	24.91	34.69	17.28	14.83	28.36	17.08	25.18	20.17	16.26	12.26	16.74	20.82
END7290E-DTS2000Hz	17.85	11.87	13.59	20.69	15.84	11.67	16.00	12.56	10.07	17.01	9.65	10.16	14.13	8.97	12.20	12.96	7.76	5.43	8.86	11.97
END7290E-IES	64.23	16.16	18.94	83.89	69.06	19.48	22.73	70.24	86.00	93.36	67.68	51.64	84.53	47.73	75.45	62.69	62.49	51.38	54.06	62.59
MSI64B-DTS6DX_Ars	19.89	29.99	14.41	26.62	18.73	26.34	48.84	18.72	36.57	37.40	12.36	10.01	20.22	21.69	12.37	11.74	9.62	12.46	13.76	16.42
MSI64B-DTS300Hz	16.30	48.03	15.47	40.33	37.61	41.04	54.00	34.71	45.96	52.53	23.34	9.49	36.25	36.12	32.59	15.42	15.80	8.56	10.47	32.61
MSI64B-DTS2000Hz	14.17	38.85	11.73	25.88	23.03	29.75	47.39	26.94	39.92	30.58	12.79	9.99	19.88	25.68	11.95	13.36	9.70	9.45	6.60	17.15
MSI64B-IES	77.53	28.71	21.98	61.17	54.30	16.56	25.56	46.92	52.39	63.77	74.17	55.16	93.36	22.93	70.16	69.24	63.52	57.39	58.69	49.48
MSI64C-DTS6DX_Ars	39.32	18.46	16.46	42.55	19.16	17.06	22.36	19.75	23.09	25.71	15.36	11.35	25.74	10.29	23.01	19.02	16.94	18.79	15.02	22.73
MSI64C-DTS300Hz	24.13	16.84	12.12	22.66	23.01	18.77	21.38	17.78	26.28	34.65	13.59	10.70	27.22	16.05	21.76	19.08	18.39	16.74	10.54	21.40
MSI64C-DTS2000Hz	32.40	17.58	15.18	38.40	19.70	17.75	21.92	18.94	21.73	22.60	16.10	12.77	24.56	11.38	21.33	20.69	17.26	17.90	12.52	21.37
MSI64C-IES	90.00	23.65	22.35	108.94	70.39	24.49	28.38	70.37	86.30	93.89	66.77	49.80	87.16	46.91	78.54	64.52	62.65	53.27	53.50	67.25

206

APPENDIX D – THOR MOD-KIT TESTS – TEST MATRIX

Table D1. THOR Test Matrix.

Test ID	Head type	Sensor Block	Head tether	Simulated impact	Seat belt force limit (FL)
S0455	Simplified	UVa	NOT used	NO	2 kN
S0456	Regular	UVa	NOT used	NO	4 kN
S0457	Regular	UVa	NOT used	NO	4 kN
S0458	Regular	UVa	USED: 1 layer of Gaffer's tape; short	NO	4 kN
S0459	Regular	UVa	USED: 4 layers of Gaffer's tape; long	NO	4 kN
S0460	Regular	UVa	NOT used	Yes	4 kN
S0461	Regular	UVa	NOT used	Yes	4 kN
S0462	Regular	THOR stock	NOT used	Yes	4 kN

Additional remarks:
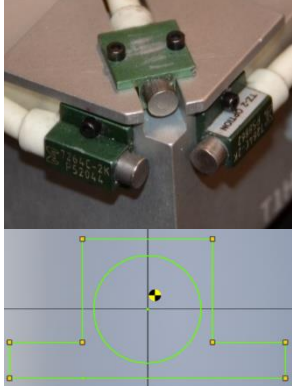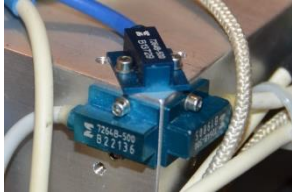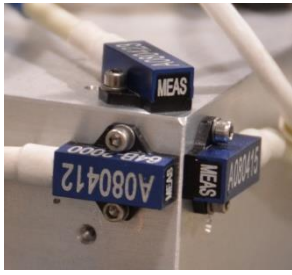
- Test S0456 – Head ACC X (Endevco 7264C) recorded only noise due to a broken connector.
- Tests S0460 and Test S0461 – ACC X and ACC Z (Endevco 7290E) exceeded their maximum full-scale range of 30g.

APPENDIX E – THOR MOD-KIT TESTS – INSTRUMENTATION AND DATA ACQUISITION SYSTEMS

Test S0455:

Five different linear accelerometer types (Table E1), two different angular rate sensor types (Table E2), and three different DAS types (Table E3) were used during the test. Data were recorded at 20 kHz.

Table E1. Linear accelerometer summary.

Manufacturer	Model	Quantity	Photo	General parameters
Endevco Meggitt Sensing Systems	7264C	9		• Piezoresistive • Full range: 2000g • Sensitivity: ~0.2 mV/g • Frequency response: from 0 up to 5000Hz • Damping ratio: 0.005 • Calibrated at 10V excitation • Run at 10V excitation • Seismic mass CG (marked in the picture on the left with a photo target) not on the main axis of the sensor
	7264B	3		• Piezoresistive • Full range: 500g • Sensitivity: ~0.8 mV/g • Frequency response: from 0 up to 3000Hz • Damping ratio: 0.005 • Calibrated at 10V excitation • Run at 10V excitation
	7290E	3		• Variable capacitance • Full range: 30g • Sensitivity: ~66 mV/g • Frequency response: from 0 up to 1000Hz • Damping ratio: 0.7 • Calibrated at 11V excitation • Not proportional to excitation
Measurement Specialties (MSI)	64B	3		• Piezoresistive • Full range: 2000g • Sensitivity: ~0.15 mV/g • Frequency response: from 0 up to 3000Hz • Damping ratio: 0.05 • Calibrated at 10V excitation • Run at 10V excitation
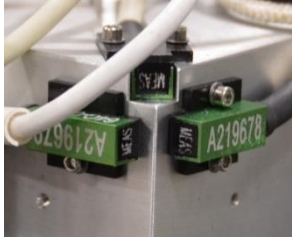
	64C	3		• Piezoresistive • Full range: 100g • Sensitivity: ~0.9 mV/g • Frequency response: from 0 up to 500Hz • Damping ratio: 0.5 • Calibrated at 10V excitation • Run at 10V excitation

Table E2. Angular rate sensors summary

Manufacturer	Model	Quantity	Photo	General parameters
Diversified Technical Systems (DTS)	ARS PRO-8K 300Hz	3		• Full range: 8000 deg/s • Not proportional to excitation • Frequency response: from 0 up to 300Hz • Internally regulated excitation
	ARS PRO-8K 2000Hz	3		• Full range: 8000 deg/s • Not proportional to excitation • Frequency response: from 0 up to 2000Hz • Internally regulated excitation

Table E3. DAS summary

Manufacturer	Model	Quantity	Photo	General parameters
Diversified Technical Systems (DTS)	TDAS PRO	1		• Voltage Insertion Type: 16-bit DAC • Resolution: 16-bit • Max sampling rate: 304k samples/sec/module • Excitation voltage levels: 2 & 10V • # of channels: 30 • Anti-alias filter: low pass, 8-pole Butterworth, 2.9 kHz • Overhead room added to the sensor full scale range: 20%
	TDAS G5	1		• Voltage Insertion Type: 16-bit DAC • Resolution: 16-bit • Max sampling rate: 100k samples/sec/module

| | | | | • Excitation voltage levels: 5V
• # of channels: 32
• Anti-alias filter: low pass, 4-pole Butterworth, 2.9 kHz
• Overhead room added to the sensor full scale range: 20% |
| SLICE Micro | 1 | | • Resolution: 16-bit
• Excitation voltage level: 5V
• Bandwidth: DC to 40 kHz
• # of channels: 15
• Anti-alias filter: low pass, 4-pole Butterworth, 40 kHz
• Overhead room added to the sensor full scale range: 20%
• Used only for Endevco 7290Es |

Tests S0456 – S0462:

Two different linear accelerometer types (Table E4), two different angular rate sensor types (Table E5), and three different DAS types (Table E6) were used during testing. Data were recorded at 20 kHz.

Table E4. Linear accelerometer summary
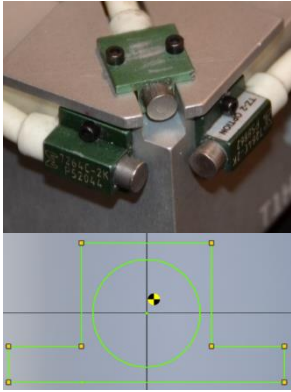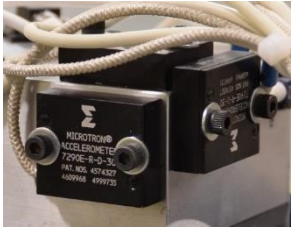
Manufacturer	Model	Quantity	Photo	General parameters
Endevco Meggitt Sensing Systems	7264C	3		• Piezoresistive • Full range: 2000g • Sensitivity: ~0.2 mV/g • Frequency response: from 0 up to 5000Hz • Damping ratio: 0.005 • Calibrated at 10V excitation • Run at 10V excitation • Seismic mass CG (marked in the picture on the left with a photo target) not on the main axis of the sensor
	7290E	3		• Variable capacitance • Full range: 30g • Sensitivity: ~66 mV/g • Frequency response: from 0 up to 1000Hz • Damping ratio: 0.7 • Calibrated at 11V excitation • Not proportional to excitation

Table E5. Angular rate sensors summary

Manufacturer	Model	Quantity	Photo	General parameters
Diversified Technical Systems (DTS)	ARS PRO-8K 300Hz	3		• Full range: 8000 deg/s • Not proportional to excitation • Frequency response: from 0 up to 300Hz • Internally regulated excitation
	ARS PRO-8K 2000Hz	3		• Full range: 8000 deg/s • Not proportional to excitation • Frequency response: from 0 up to 2000Hz • Internally regulated excitation

Table E6. DAS summary

Manufacturer	Model	Quantity	Photo	General parameters
Diversified Technical Systems (DTS)	TDAS PRO	1		• Voltage Insertion Type: 16-bit DAC • Resolution: 16-bit • Max sampling rate: 304k samples/sec/module • Excitation voltage levels: 2 & 10V • # of channels: 30 • Anti-alias filter: low pass, 8-pole Butterworth, 2.9 kHz • Overhead room added to the sensor full scale range: 20%
	TDAS G5	1		• Voltage Insertion Type: 16-bit DAC • Resolution: 16-bit • Max sampling rate: 100k samples/sec/module • Excitation voltage levels: 5V • # of channels: 32 • Anti-alias filter: low pass, 4-pole Butterworth, 2.9 kHz • Overhead room added to the sensor full scale range: 20%

| | SLICE Micro | 1 | | • Resolution: 16-bit
• Excitation voltage level: 5V
• Bandwidth: DC to 40 kHz
• # of channels: 15
• Anti-alias filter: low pass, 4-pole Butterworth, 40 kHz
• Overhead room added to the sensor full scale range: 20%
• Used only for Endevco 7290Es |

Test S0462:

One linear accelerometer type (Table E7), one angular rate sensor type (Table E8), and two different DAS types (Table E9) were used during the test. Data were recorded at 20 kHz.

Table E7. Linear accelerometer summary
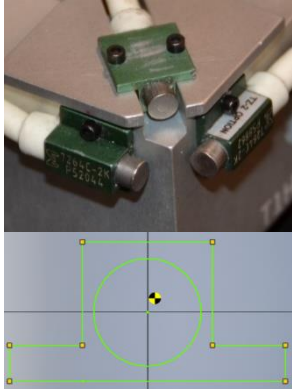
Manufacturer	Model	Quantity	Photo	General parameters
Endevco Meggitt Sensing Systems	7264C	3		• Piezoresistive • Full range: 2000g • Sensitivity: ~0.2 mV/g • Frequency response: from 0 up to 5000Hz • Damping ratio: 0.005 • Calibrated at 10V excitation • Run at 10V excitation (except for Test S0453, where run at 2V) • Seismic mass CG (marked in the picture on the left with a photo target) not on the main axis of the sensor

Table E8. Angular rate sensors summary

Manufacturer	Model	Quantity	Photo	General parameters
Diversified Technical Systems (DTS)	ARS PRO-18K 2000Hz	3		• Full range: 18000 deg/s • Not proportional to excitation • Frequency response: from 0 up to 2000Hz • Internally regulated excitation
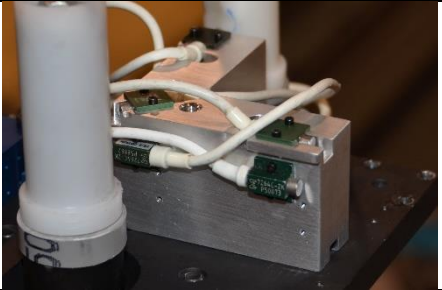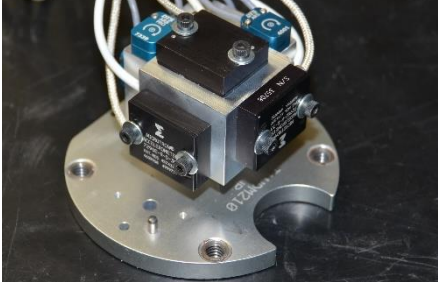
Table E9. DAS summary

Manufacturer	Model	Quantity	Photo	General parameters
Diversified Technical Systems (DTS)	TDAS PRO	1		• Voltage Insertion Type: 16-bit DAC • Resolution: 16-bit • Max sampling rate: 304k samples/sec/module • Excitation voltage levels: 2 & 10V • # of channels: 30 • Anti-alias filter: low pass, 8-pole Butterworth, 2.9 kHz • Overhead room added to the sensor full scale range: 20%
	TDAS G5	1		• Voltage Insertion Type: 16-bit DAC • Resolution: 16-bit • Max sampling rate: 100k samples/sec/module • Excitation voltage levels: 5V • # of channels: 32 • Anti-alias filter: low pass, 4-pole Butterworth, 2.9 kHz • Overhead room added to the sensor full scale range: 20%

APPENDIX F – THOR MOD-KIT TESTS – SENSOR BLOCKS USED DURING TESTING

Several different sensor blocks were used during testing. In Test S0461, THOR ATD stock head accelerometer block was investigated. Sensor blocks fabricated at UVa were used in the other seven tests (Table F1).

Table F1. Sensor blocks used during testing.

Sensor block	Sensor list	Figure
UVa NAP (used only in Test S0455)	9 Endevco 7264C	
UVa 4-ACC (used only in Test S0455)	3 x Endevco 7264B 3 x Endevco 7290E 3 x MSI 64B 3 x MSI 64C	
UVa THOR Head (used in Tests S0455-S0461)	3 x Endevco 7264C 3 x Endevco 7290E 3 x DTS ARS Pro 8k (bandwidth up to 300Hz) 3 x DTS ARS Pro 8k (bandwidth up to 2000Hz)	
NHTSA THOR Head (stock; used only in Test S0462)	3 x Endevco 7264C 3 x DTS ARS Pro 18k (bandwidth up to 2000Hz)	

APPENDIX G – THOR MOD-KIT TESTS – RES_{ERR} (IN MILLIMITERS) FOR ALL SENSOR COMBINATIONS

Table G1. Res$_{err}$ (in millimeters) for all sensor combinations for Test S0455.

Sensor combination	S0455
END7264B-DTS300Hz	50.6
END7264B-DTS2000Hz	24.14
END7264C-DTS300Hz	37.7
END7264C-DTS2000Hz	19.82
END7290E-DTS300Hz	50.04
END7290E-DTS2000Hz	33.76
MSI64B-DTS300Hz	46.83
MSI64B-DTS2000Hz	28.17
MSI64C-DTS300Hz	33.07
MSI64C-DTS2000Hz	51.33

Table G2. Res$_{err}$ (in millimeters) for all sensor combinations for Test S0456 to S0461.

Sensor combination	S0456	S0457	S0458	S0459	S0460	S0461
END7264C-DTS300Hz	n/a	55.19	66.05	62.07	37.56	44.93
END7264C-DTS2000Hz	n/a	42.91	58.54	29.53	36.09	29.84
END7290E-DTS300Hz	51.63	78.45	86.57	85.69	436.31*	460.04*
END7290E-DTS2000Hz	45.95	64.82	77.19	51.76	452.41*	473.45*

* full scale range of the sensor excided

Table G3. Res$_{err}$ (in millimeters) for all sensor combinations for Test S0462.

Sensor combination	S0462
END7264C-DTS2000Hz (full scale range: 18k deg/sec)	35.69

APPENDIX H – FREQUENCY CONTENT OF THE SIGNAL FROM ANGULAR ACCELEROMETERS

The raw unfiltered data from the Endevco 7302BM5 angular accelerometers recorded on the four Simplified Head tests discussed in Section 6 contained noise of noticeably high magnitude (Figure H1). If not filtered, that level of noise can make the analysis of the recorded angular acceleration problematic and the results difficult to interpret.
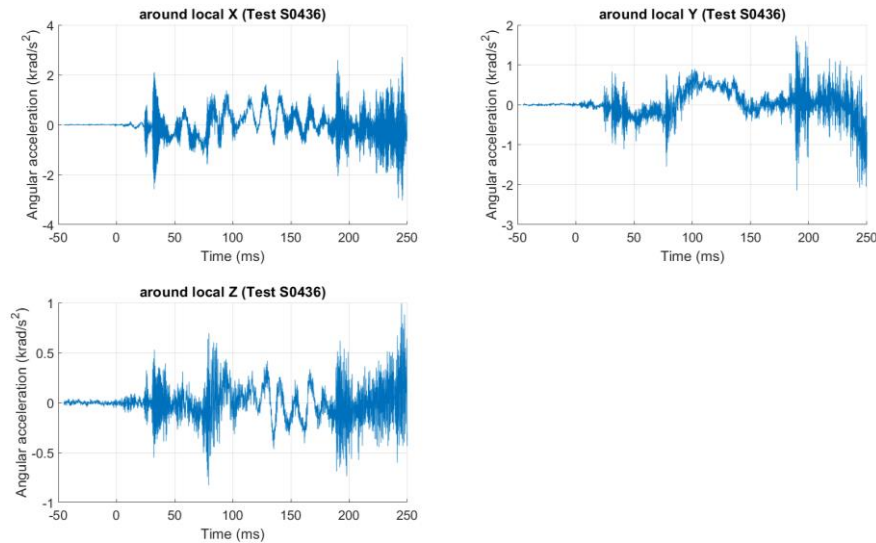
Figure H1. Exemplar raw (not filtered) AAC data recorded by the angular accelerometers.

When the Fast Fourier transform (FFT) was performed on the Endevco AAC data, it became clear that in all four analyzed Simplified Head tests the angular accelerometers exhibited high magnitude of the signal noise in the frequency range between 2000 Hz to 3500 Hz (Figure H2). That frequency range matched the mounted resonance frequency for the 7302BM5 sensors as given by the manufacturer (between 2500 Hz to 3500 Hz; MEGGITT Endevco® 2017).
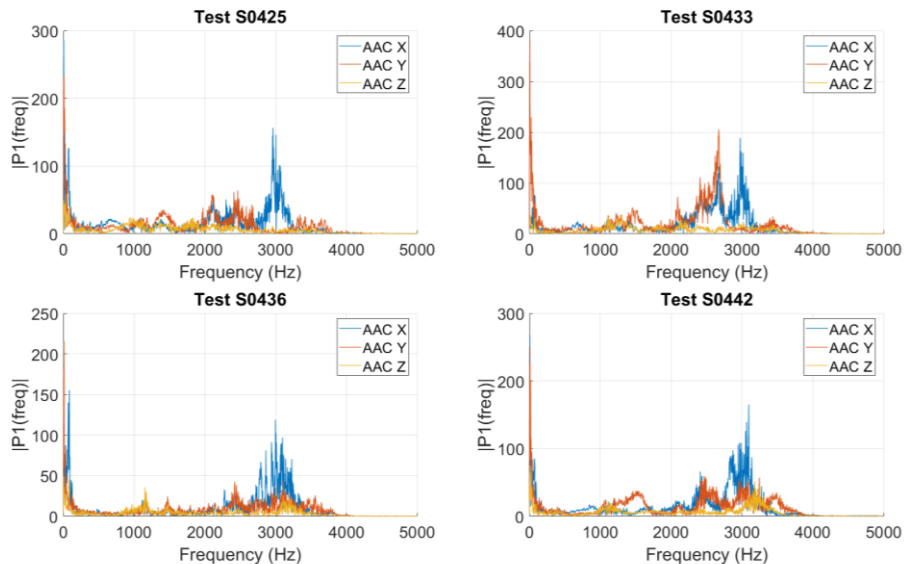
Figure H2. Frequency content of the signal recorded by the Endevco angular accelerometers in the four analyzed Simplified Head tests.

The frequency content of the sled input acceleration time-history (Figure 21) was within the DC response (0 Hz) to approximately 150 Hz. Due to the complexity of the Simplified-Head-to-sled system, interactions between different parts during the test, and due to the electrical and ambient noise always present in a laboratory environment, the entire analyzed structure was subjected to vibrations of a spectrum than was broader than the one bounded by the sled input. That introduced noise into the measured signal, including vibrations close or at the sensor natural frequency. With the data sampling rate set to 20 kHz, the Endevco sensors were able to capture the natural resonance of the mechanical structure of the accelerometers themselves, which then resulted in a high magnitude noise seen in the recorded angular acceleration data.

APPENDIX I – DATA UTILIZED TO FIND EQ. 8.18

As the first step, the error in the rotation matrix R was found in the function of the normalized frequency (Figure 76a) varying f (frequency of the angular velocity data from Eq. 8.12) and using the magnitude parameter A of 15. One of the curves from Figure 76a was then designated to be a reference response and the frequency associated with it was assumed to be f_{ref}. To match an error curve (for the investigated f) to the reference error curve (f_{ref} case) a scaling factor (SF) was applied to the normalized frequency ($\Delta t * f$). SF was found manually for different ratios of f/f_{ref} (Table I1).

Table I1. Data used to define Eq. 8.18.

f/f_{ref}	Scaling factor determined manually (SF)	SF computed based on Eq. 8.18 (power fit to SF determined manually)
0.25	1.9	1.87
0.5	1.4	1.38
1	1	1.03
2	0.75	0.76
4	0.55	0.57
8	0.44	0.42

Next, a power function was fitted to the SF data (second column of Table I1) to determine the mathematical relationship between the scaling factors determined manually and the f/f_{ref} ratio. The resulting power fit was then utilized as Eq. 8.18.
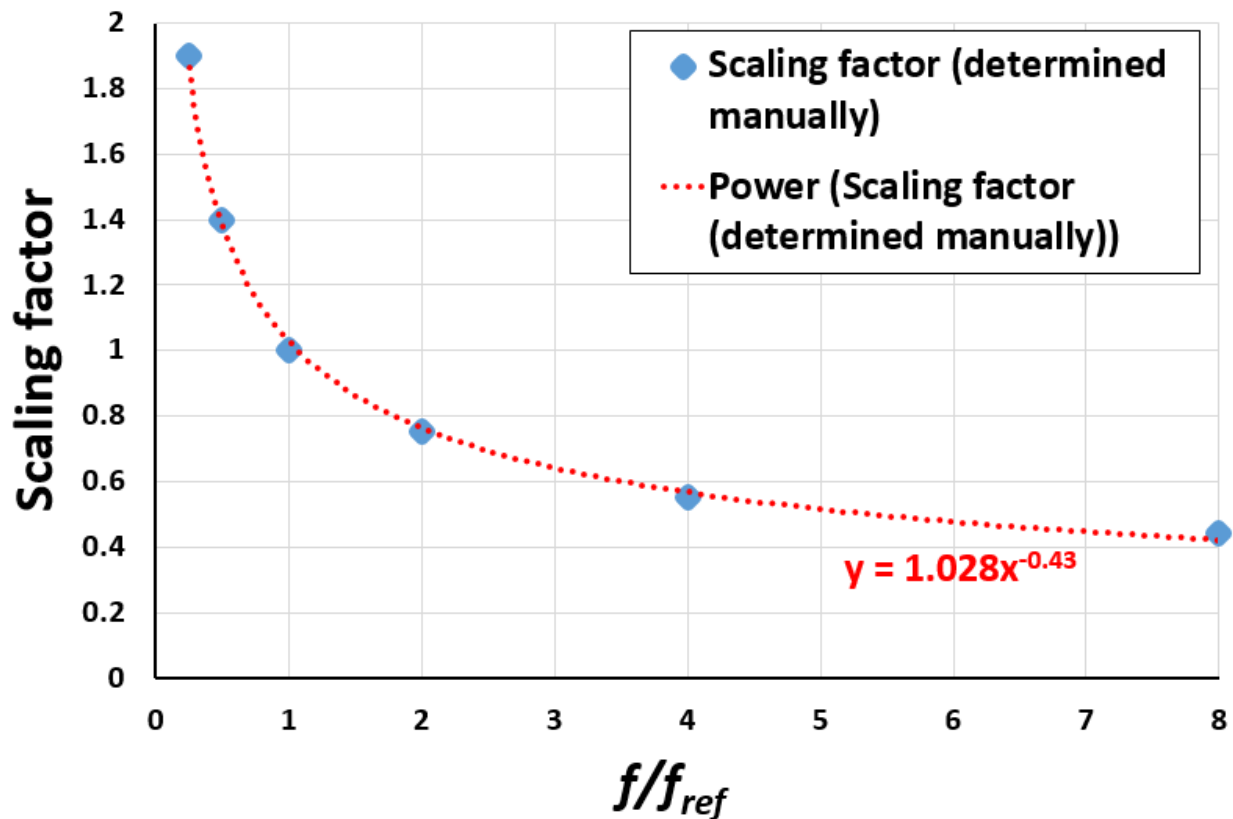
Figure I1. Power function fit (dotted in red) to the scaling factors determined manually (blue markers).

APPENDIX J – AAC ANALYSIS – LOCATIONS OF LINEAR ACCELEROMETER SEISMIC MASS CGS RELATIVE TO THE MARKER POSITIONS

Table J1. Test S0425: Linear accelerometer location relative to Marker 1. (0,0,0) is the marker center.

CG of:	Local coordinate frame (origin: center of VICON marker)		
	X coordinate (mm)	Y coordinate (mm)	Z coordinate (mm)
X Accelerometer	-22.8	-51.3	-19.2
Y Accelerometer	-31.4	-43.3	-19.2
Z Accelerometer	-31.0	-50.9	-25.3

Table J2. Test S0425: Linear accelerometer location relative to Marker 2. (0,0,0) is the marker center.

CG of:	Local coordinate frame (origin: center of VICON marker)		
	X coordinate (mm)	Y coordinate (mm)	Z coordinate (mm)
X Accelerometer	73.3	-52.8	-125.3
Y Accelerometer	64.6	-44.8	-125.3
Z Accelerometer	65.1	-52.5	-131.5

Table J3. Test S0433: Linear accelerometer location relative to Marker 1. (0,0,0) is the marker center.

CG of:	Local coordinate frame (origin: center of VICON marker)		
	X coordinate (mm)	Y coordinate (mm)	Z coordinate (mm)
X Accelerometer	-21.9	-51.1	-20.1
Y Accelerometer	-30.6	-43.1	-20.1
Z Accelerometer	-30.1	-50.8	-26.2

Table J4. Test S0433: Linear accelerometer location relative to Marker 2. (0,0,0) is the marker center.

CG of:	Local coordinate frame (origin: center of VICON marker)		
	X coordinate (mm)	Y coordinate (mm)	Z coordinate (mm)
X Accelerometer	74.7	-51.4	-125.4
Y Accelerometer	66.0	-43.4	-125.4
Z Accelerometer	66.5	-51.0	-131.6

Table J5. Test S0436: Linear accelerometer location relative to Marker 1. (0,0,0) is the marker center.

CG of:	Local coordinate frame (origin: center of VICON marker)		
	X coordinate (mm)	Y coordinate (mm)	Z coordinate (mm)
X Accelerometer	-22.3	-50.9	93.1
Y Accelerometer	-30.9	-42.9	93.1
Z Accelerometer	-30.4	-50.6	86.9

Table J6. Test S0436: Linear accelerometer location relative to Marker 2. (0,0,0) is the marker center.

CG of:	Local coordinate frame (origin: center of VICON marker)		
	X coordinate (mm)	Y coordinate (mm)	Z coordinate (mm)
X Accelerometer	73.3	-52.1	-12.7
Y Accelerometer	64.6	-44.0	-12.7
Z Accelerometer	65.1	-51.7	-18.8

Table J7. Test S0442: Linear accelerometer location relative to Marker 1. (0,0,0) is the marker center.

CG of:	Local coordinate frame (origin: center of VICON marker)		
	X coordinate (mm)	Y coordinate (mm)	Z coordinate (mm)
X Accelerometer	-23.0	-50.7	94.9
Y Accelerometer	-30.5	-43.0	94.9
Z Accelerometer	-30.4	-50.5	87.3

Table J8. Test S0442: Linear accelerometer location relative to Marker 2. (0,0,0) is the marker center.

CG of:	Local coordinate frame (origin: center of VICON marker)		
	X coordinate (mm)	Y coordinate (mm)	Z coordinate (mm)
X Accelerometer	73.4	-52.3	-10.8
Y Accelerometer	65.9	-44.6	-10.8
Z Accelerometer	66.0	-52.1	-18.4

Table J9. Test S0461: Linear accelerometer location relative to THOR marker. (0,0,0) is the marker center.

CG of:	Local coordinate frame (origin: center of VICON marker)		
	X coordinate (mm)	Y coordinate (mm)	Z coordinate (mm)
X Accelerometer	-51.9	64.1	-86.3
Y Accelerometer	-59.6	71.4	-86.3
Z Accelerometer	-59.4	64.4	-93.9

APPENDIX K – AAC ANALYSIS – OPTIMIZATION METHODS AND RESULTS

Methods:

As it was shown in *Error Effect Analysis* (Chapter 10) and *3D Trajectory Calculation in the THOR Tests Utilizing the Knowledge Gained from Error Effects Analysis* (Chapter 13), the error in the initial orientation ($\boldsymbol{R_{ini}}$) of a tracked body can substantially affect the calculated trajectory. To minimize that effect, an optimization of the initial Euler angles for both, the Simplified Head and the THOR ATD's head (in the five tests discussed in Chapter 9) was performed before the AAC analysis was carried out.

In the optimization process, the trajectory for the measurement center (Figure 2) for the three Endevco 7264C accelerometers, mounted at the origin of the local coordinate system, was calculated. Next, Res_{err} between the calculated and the reference (i.e. from VICON) trajectories was computed. The objective of the optimization was to identify a set of three initial Euler angles that minimizes that Res_{err}. The MATLAB's gradient-based *fmincon Interior Point* solver (cf. Byrd et al. 2000, cf. Waltz et al. 2006) was used as the optimization algorithm. Varied parameters were: initial yaw, initial pitch and initial roll angles (used to build the rotation matrix $\boldsymbol{R_{ini}}$ according to the 3-2-1 convention as shown in Wu et al. 2009). The starting points (angle values) for the optimization algorithm were determined from the pre-trigger VICON data for the head. Those three values were then allowed to vary within ±3 degrees from the starting point. To identify the global minimum, i.e. to minimize the possibility of finding a local minimum of the objective function $min(Res_{err})$, the MATLAB's *GlobalSearch algorithm* (cf. Ugray et al. 2007) was utilized.

Results:

By optimizing the three initial Euler angles, in all five test configurations the error Res_{err} in the measurement center's trajectory for the three linear accelerometers used in the analysis was decreased substantially: by 63.5% in Test S0442 to 93% in Test S0433 (Table K1). The highest absolute difference between the angles before and after optimization was: 2.84 degrees for yaw (Test S0425), 1.57 degrees for pitch (Test S0433), and 1.7 degrees for roll (Test S0425) (Table K1).

Table K1. Res$_{err}$ before and after optimization and absolute difference in initial Euler angles due to optimization.

Test #	Res_{err} (mm)			Difference in initial Euler angles due to optimization		
	Before optimization	**After optimization**	**% difference***	**Yaw (deg)**	**Pitch (deg)**	**Roll (deg)**
S0425	28.35	2.6	90.8	2.84	0.99	1.7
S0433	24.58	1.72	93	2.33	1.57	1.38
S0436	26.69	4.36	83.7	2.01	1.13	1.31
S0442	5.64	2.06	63.5	0.29	0.54	0.23
S0461	29.84	2.65	91.1	1.46	0.13	0.33

$$* \%diff = 100 - \frac{100 * value\_after\_optimization}{value\_before\_optimization}$$

Through minimization of Res_{err}, the maximum absolute difference, $diff_{max}$, for the three trajectory components decreased as well (Table K2), with the exception of the Y component in Test S0425 where $diff_{max}$ increased by approx. 50%: from 6.53 mm to 9.89 mm. On average, $diff_{max}$ decreased by approx. 90% in X, by approx. 27% in Y (after excluding Test S0425), and by approx. 90% in Z (Table K2).

Table K2. $diff_{max}$ metric before and after optimization.

Test #	Before optimization			After optimization			% difference*		
	X (mm)	Y (mm)	Z (mm)	X (mm)	Y (mm)	Z (mm)	X	Y	Z
S0425	88.91	6.53	64.6	4	9.89	1.23	95.5	-51.5	98.1
S0433	73.67	11.92	49.43	0.53	9.21	2.85	99.3	22.7	94.2
S0436	72.21	10.73	54.42	1.54	7.05	3.4	97.9	34.3	93.8
S0442	10.4	4.92	17.88	1.65	4.45	1.53	84.1	9.6	91.4
S0461	59.39	9.26	15.17	6.13	5.4	1.97	89.7	41.7	87.0

$$* \ \%diff = 100 - \frac{100 * value\_after\_optimization}{value\_before\_optimization}$$

APPENDIX L – AAC ANALYSIS – ANGULAR ACCELERATION PLOTS
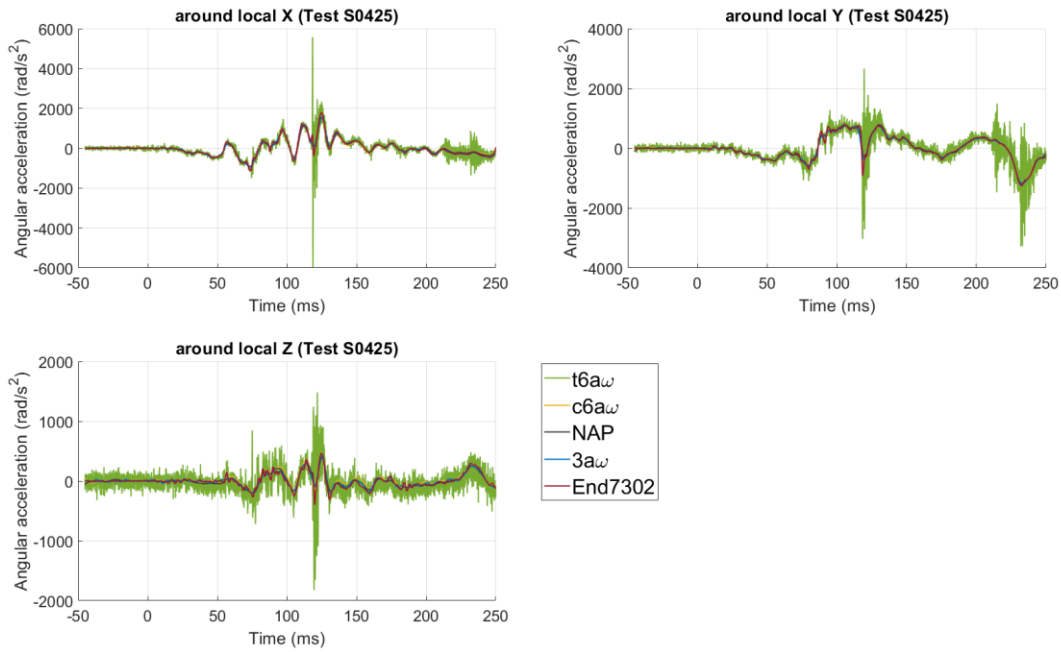
Figure L1. Test S0425 – Marker 1: Angular acceleration data from the five discussed methods of obtaining AAC for the filter combination that minimized Res_{err}***.***
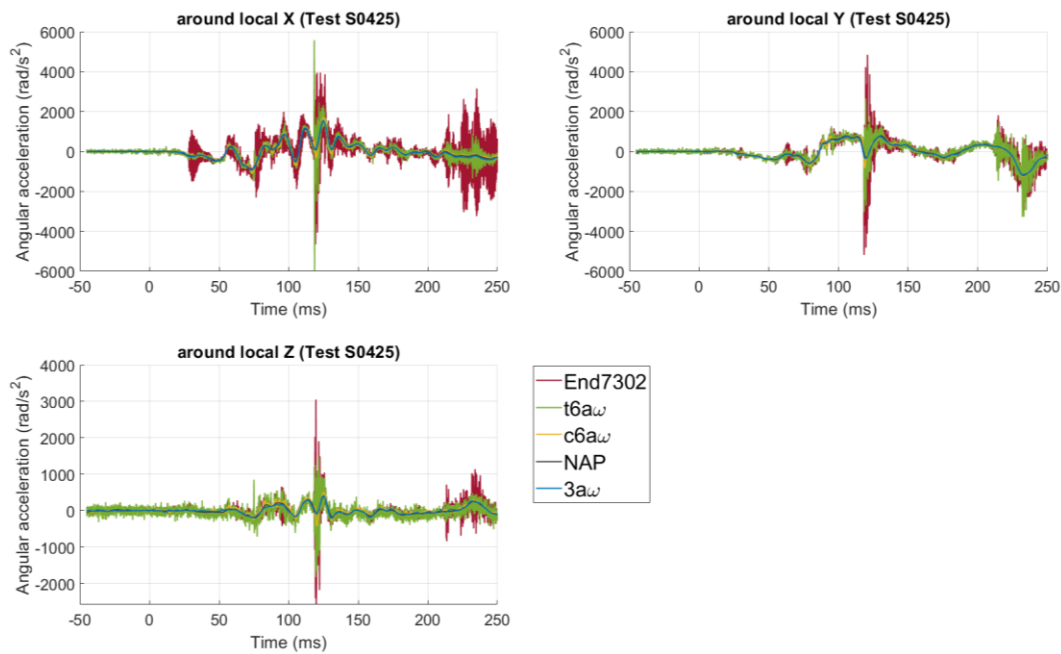
Figure L2. Test S0425 – Marker 2: Angular acceleration data from the five discussed methods of obtaining AAC for the filter combination that minimized Res_{err}***.***
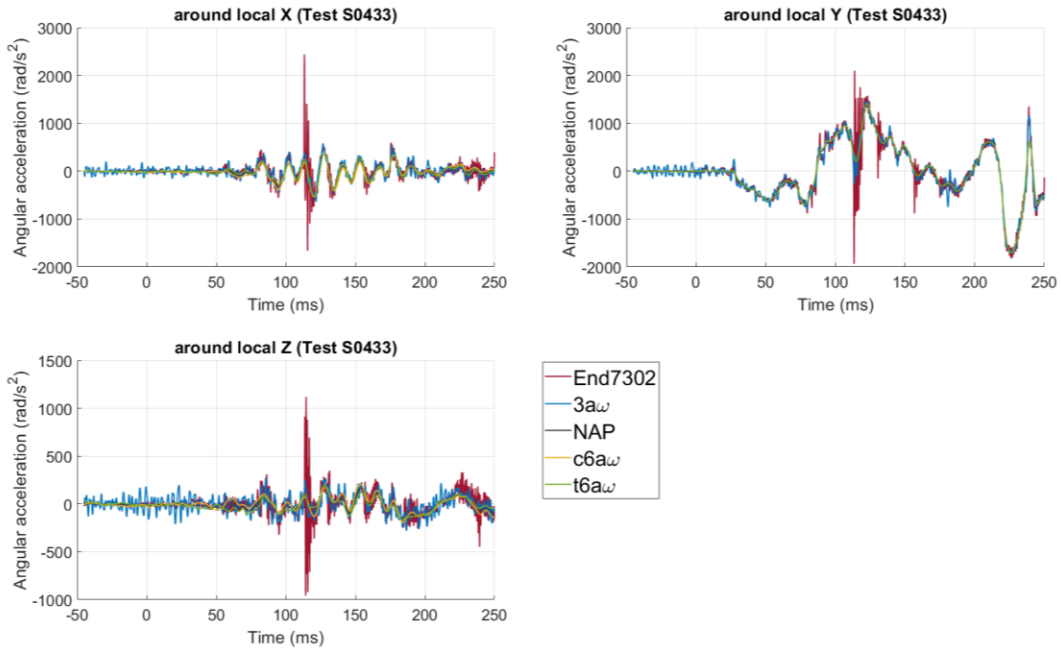
Figure L3. Test S0433 – Marker 1: Angular acceleration data from the five discussed methods of obtaining AAC for the filter combination that minimized Res_{err}.
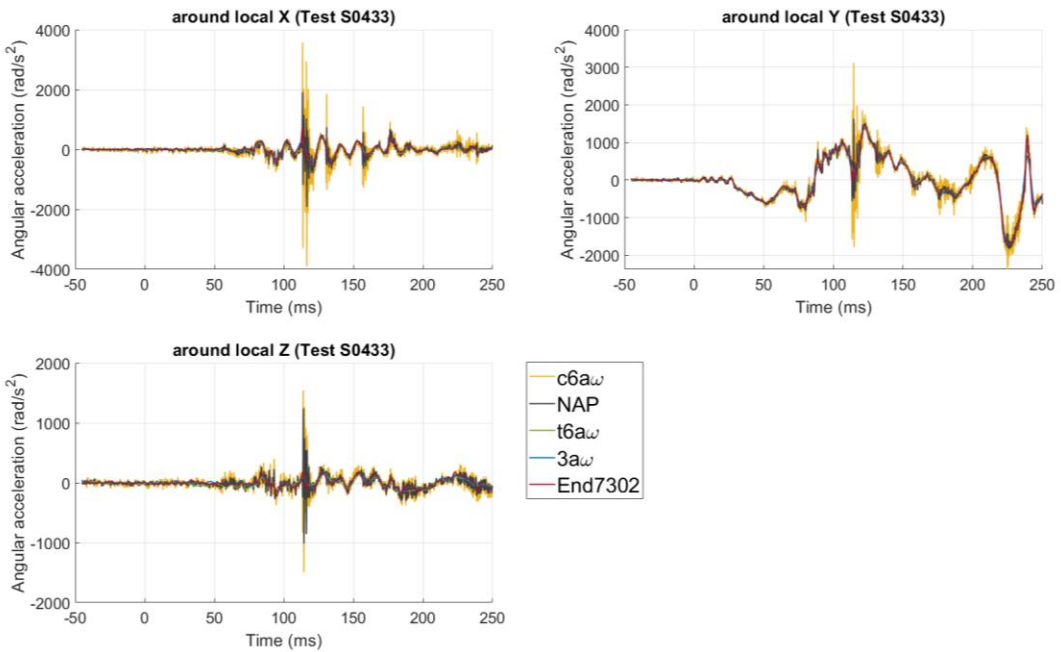
Figure L4. Test S0433 – Marker 2: Angular acceleration data from the five discussed methods of obtaining AAC for the filter combination that minimized Res_{err}.
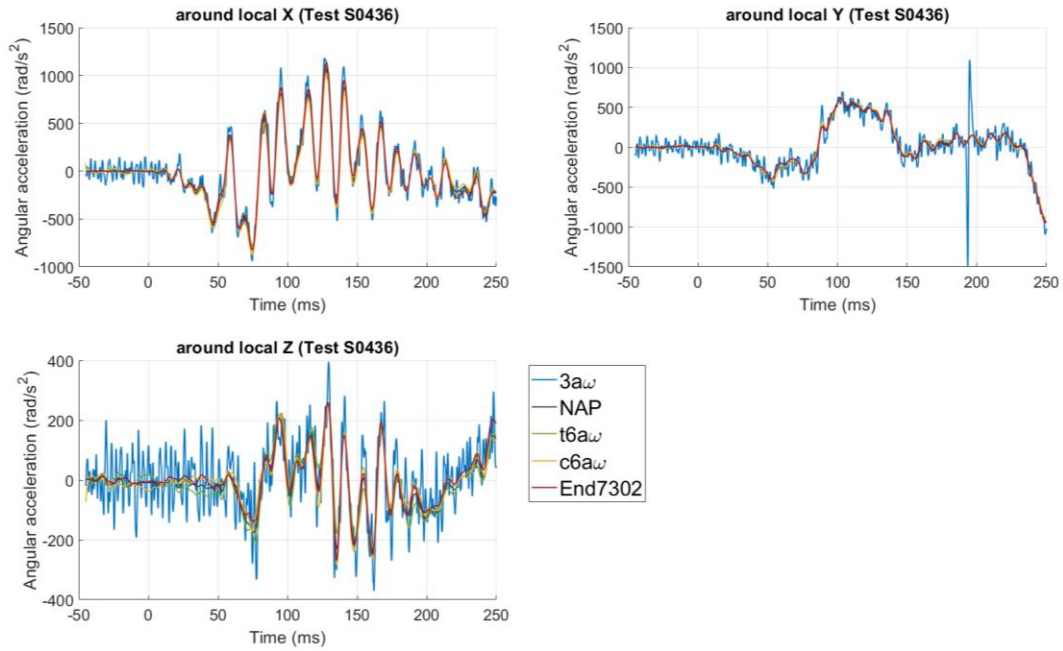
Figure L5. Test S0436 – Marker 1: Angular acceleration data from the five discussed methods of obtaining AAC for the filter combination that minimized Res_{err}.
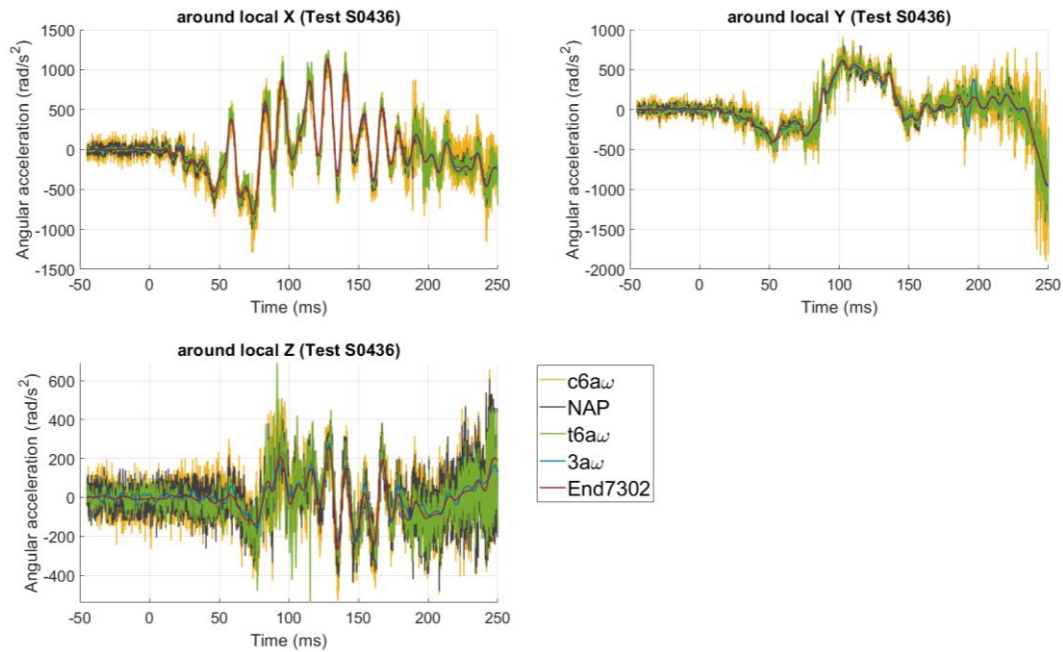
Figure L6. Test S0436 – Marker 2: Angular acceleration data from the five discussed methods of obtaining AAC for the filter combination that minimized Res_{err}.
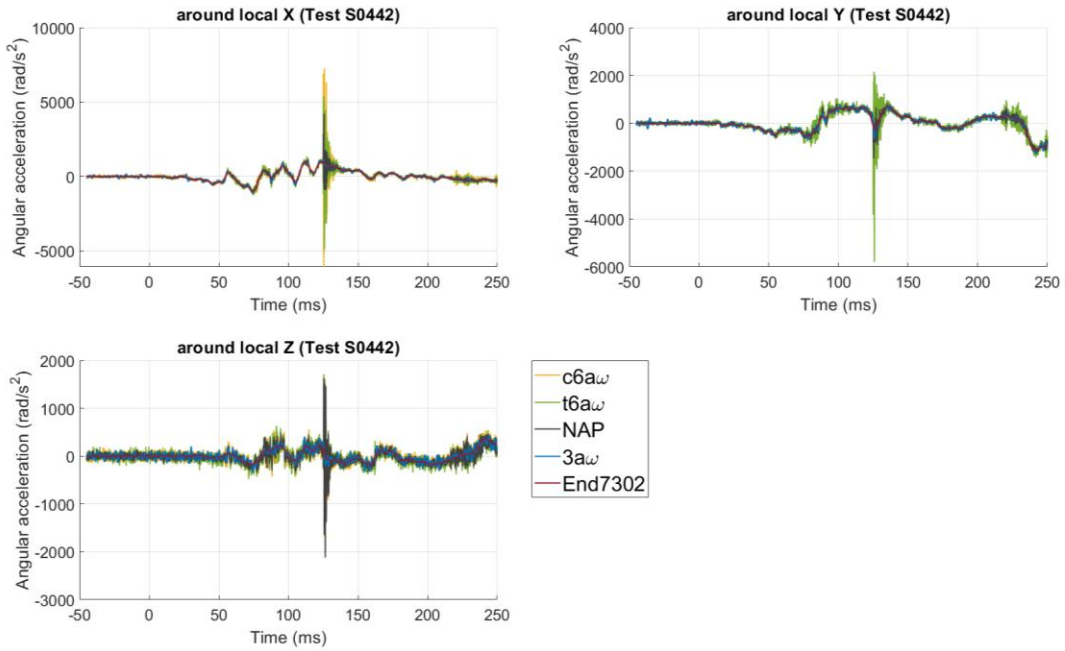
Figure L7. Test S0442 – Marker 1: Angular acceleration data from the five discussed methods of obtaining AAC for the filter combination that minimized Res_{err}.
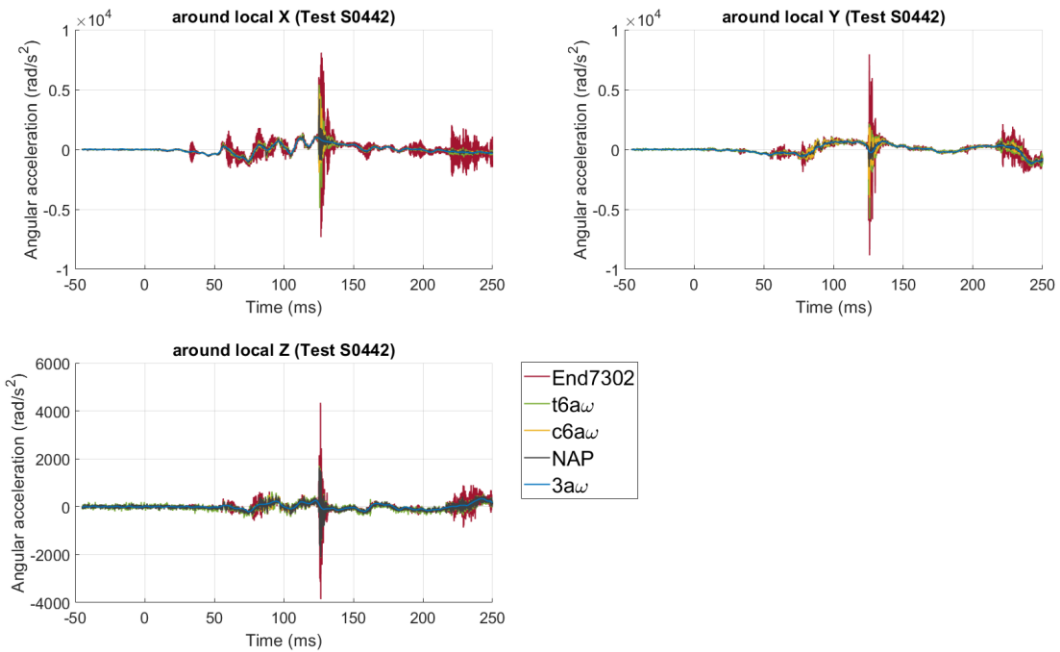
Figure L8. Test S0442 – Marker 2: Angular acceleration data from the five discussed methods of obtaining AAC for the filter combination that minimized Res_{err}.
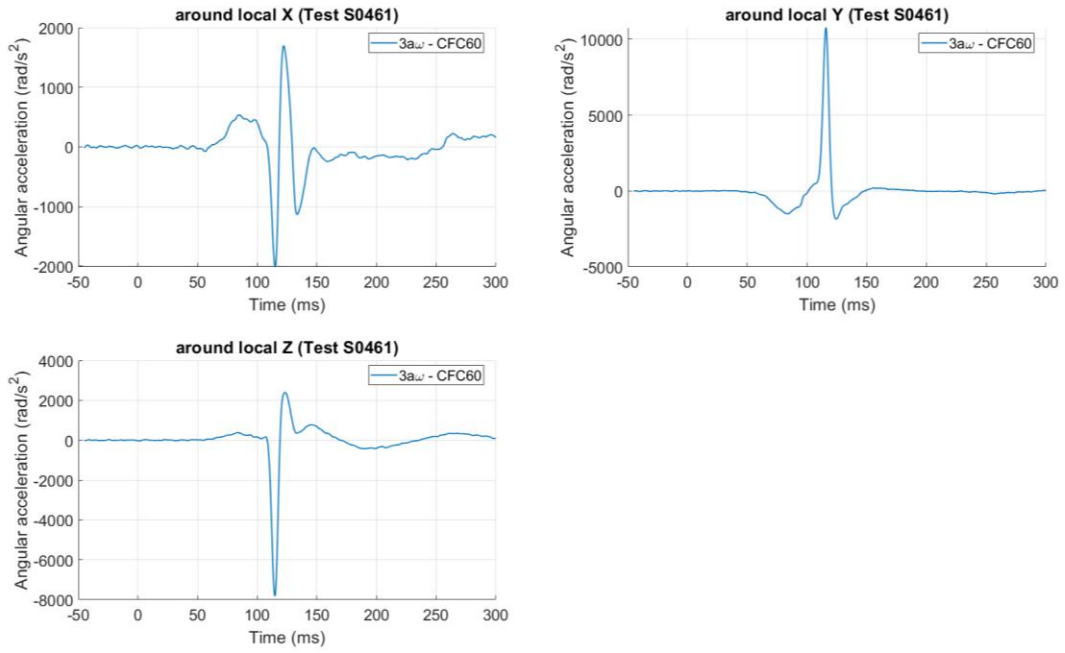
Figure L9. Test S0461: Angular acceleration after filtering ARS data to CFC 60.

APPENDIX M – AAC ANALYSIS – RES_{ERR} IN SIMPLFIED HEAD TESTS

Table M1. NAP method: Res_{err} for both tracked markers. Minimum value of the metric for each of the analyzed tests indicated in green. CFC filters utilized on the input ACC data.

Test #	Res_{err} (in millimeters)									
	Marker 1					Marker 2				
	CFC 60	CFC 180	CFC 600	CFC 1000	Raw	CFC 60	CFC 180	CFC 600	CFC 1000	Raw
S0425	**11.78**	11.81	11.85	11.85	11.84	**21.42**	21.77	21.98	21.99	21.99
S0433	**28.12**	28.14	28.15	28.14	28.15	71.20	71.11	**71.10**	71.11	71.16
S0436	**41.49**	41.71	41.82	41.84	41.84	23.68	23.39	23.31	23.30	**23.30**
S0442	16.44	16.09	15.98	15.98	**15.97**	17.55	17.12	16.99	16.98	**16.97**

Table M2. c6aω method: Res_{err} for both tracked markers. Minimum value of the metric for each of the analyzed tests indicated in green. CFC filters utilized on the input ARS and ACC data.

	Test S0425 – Res_{err} (in millimeters)									
	Marker 1					Marker 2				
ARS filter / ACC filter	CFC 60	CFC 180	CFC 600	CFC 1000	Raw	CFC 60	CFC 180	CFC 600	CFC 1000	Raw
CFC 60	17.52	17.52	17.52	17.51	**17.51**	18.01	18.01	18.00	18.00	18.00
CFC 180	17.61	17.61	17.61	17.61	17.61	17.99	17.98	**17.98**	17.98	17.98
CFC 600	17.65	17.65	17.65	17.65	17.65	18.04	18.03	18.03	18.03	18.03
CFC 1000	17.66	17.66	17.66	17.66	17.66	18.05	18.04	18.04	18.04	18.04
Raw	17.69	17.69	17.69	17.69	17.69	18.06	18.05	18.05	18.05	18.05
	Test S0433 – Res_{err} (in millimeters)									
	Marker 1					Marker 2				
ARS filter / ACC filter	CFC 60	CFC 180	CFC 600	CFC 1000	Raw	CFC 60	CFC 180	CFC 600	CFC 1000	Raw
CFC 60	**39.41**	39.41	39.41	39.41	39.41	89.83	89.82	89.82	89.82	89.82
CFC 180	39.45	39.45	39.45	39.45	39.45	89.62	89.62	89.61	89.61	89.61
CFC 600	39.44	39.44	39.44	39.44	39.44	89.49	89.49	89.48	89.48	89.48
CFC 1000	39.43	39.44	39.44	39.44	39.44	89.48	89.47	89.47	**89.47**	89.47
Raw	39.45	39.45	39.45	39.45	39.45	89.52	89.51	89.51	89.51	89.51
	Test S0436 – Res_{err} (in millimeters)									
	Marker 1					Marker 2				
ARS filter / ACC filter	CFC 60	CFC 180	CFC 600	CFC 1000	Raw	CFC 60	CFC 180	CFC 600	CFC 1000	Raw
CFC 60	**74.07**	74.08	74.08	74.08	74.08	27.94	27.93	27.93	27.93	27.93
CFC 180	74.88	74.89	74.89	74.89	74.89	27.86	27.85	27.85	27.85	27.85
CFC 600	75.21	75.22	75.22	75.22	75.22	27.82	27.81	27.81	27.81	27.81
CFC 1000	75.27	75.28	75.28	75.28	75.28	27.82	27.81	27.81	27.81	27.80
Raw	75.31	75.31	75.31	75.31	75.31	27.81	27.80	27.80	27.80	**27.79**
	Test S0442 – Res_{err} (in millimeters)									
	Marker 1					Marker 2				
ARS filter / ACC filter	CFC 60	CFC 180	CFC 600	CFC 1000	Raw	CFC 60	CFC 180	CFC 600	CFC 1000	Raw
CFC 60	19.31	19.31	19.31	19.31	19.32	12.93	12.93	12.93	12.93	12.93
CFC 180	19.03	19.04	19.04	19.04	19.04	12.42	12.42	12.42	12.42	12.42
CFC 600	18.95	18.96	18.96	18.96	18.96	12.22	12.23	12.22	12.22	12.22

CFC 1000	18.95	18.96	18.96	18.96	18.96	**12.21**	12.21	12.21	12.21	12.21
Raw	**18.94**	18.95	18.95	18.95	18.95	12.21	12.22	12.21	12.21	12.22

Table M3. t6aω method: Res$_{err}$ for both tracked markers. Minimum value of the metric for each of the analyzed tests indicated in green. CFC filters utilized on the input ARS and ACC data.

	Test S0425 – Res$_{err}$ (in millimeters)								
	Marker 1					**Marker 2**			
ARS filter / ACC filter	**CFC 60**	**CFC 180**	**CFC 600**	**CFC 1000**	**Raw**	**CFC 60**	**CFC 180**	**CFC 600**	**CFC 1000**	**Raw**
CFC 60	17.40	17.40	17.40	17.40	17.40	37.18	37.20	37.20	37.20	37.20
CFC 180	16.62	16.62	16.62	16.62	16.62	36.83	36.85	36.85	36.85	36.85
CFC 600	16.40	16.40	16.41	16.40	16.40	36.77	36.78	36.79	36.79	36.78
CFC 1000	16.39	16.39	16.39	16.39	16.39	36.74	36.76	36.76	36.76	36.76
Raw	**16.34**	16.34	16.35	16.35	16.35	**36.66**	36.68	36.68	36.68	36.68

	Test S0433 – Res$_{err}$ (in millimeters)									
	Marker 1					**Marker 2**				
ARS filter / ACC filter	**CFC 60**	**CFC 180**	**CFC 600**	**CFC 1000**	**Raw**	**CFC 60**	**CFC 180**	**CFC 600**	**CFC 1000**	**Raw**
CFC 60	**27.97**	27.97	27.97	27.97	27.97	**59.72**	59.73	59.73	59.73	59.73
CFC 180	28.34	28.34	28.34	28.34	28.34	60.30	60.31	60.31	60.31	60.31
CFC 600	28.52	28.53	28.53	28.53	28.53	60.61	60.62	60.62	60.62	60.62
CFC 1000	28.56	28.56	28.57	28.56	28.56	60.69	60.69	60.69	60.70	60.70
Raw	28.60	28.60	28.60	28.60	28.60	60.76	60.77	60.77	60.77	60.77

	Test S0436 – Res$_{err}$ (in millimeters)									
	Marker 1					**Marker 2**				
ARS filter / ACC filter	**CFC 60**	**CFC 180**	**CFC 600**	**CFC 1000**	**Raw**	**CFC 60**	**CFC 180**	**CFC 600**	**CFC 1000**	**Raw**
CFC 60	**17.32**	17.33	17.33	17.33	17.33	23.64	23.65	23.65	23.65	23.65
CFC 180	17.43	17.44	17.44	17.44	17.44	22.98	22.98	22.98	22.98	22.98
CFC 600	17.51	17.52	17.53	17.53	17.53	22.80	22.81	22.81	22.81	22.81
CFC 1000	17.51	17.53	17.53	17.53	17.53	**22.80**	22.81	22.81	22.81	22.81
Raw	17.52	17.53	17.53	17.53	17.53	22.81	22.82	22.81	22.81	22.81

	Test S0442 – Res$_{err}$ (in millimeters)									
	Marker 1					**Marker 2**				
ARS filter / ACC filter	**CFC 60**	**CFC 180**	**CFC 600**	**CFC 1000**	**Raw**	**CFC 60**	**CFC 180**	**CFC 600**	**CFC 1000**	**Raw**
CFC 60	19.63	19.63	19.63	19.63	19.63	24.09	24.09	24.09	24.09	24.09
CFC 180	19.39	19.39	19.39	19.39	19.39	23.76	23.76	23.76	23.76	23.76
CFC 600	19.32	19.32	19.32	19.32	19.32	23.70	23.71	23.71	23.71	23.71
CFC 1000	19.30	19.30	19.30	19.30	19.30	23.70	23.70	23.70	23.70	23.70
Raw	**19.26**	19.26	19.26	19.26	19.26	**23.66**	23.66	23.66	23.66	23.66

Table M4. 3aω method: Res$_{err}$ for both tracked markers. Minimum value of the metric for each of the analyzed tests indicated in green. CFC filters utilized on the input ARS data.

	Res$_{err}$ (in millimeters)									
Test #	**Marker 1**					**Marker 2**				
	CFC 60	**CFC 180**	**CFC 600**	**CFC 1000**	**Raw**	**CFC 60**	**CFC 180**	**CFC 600**	**CFC 1000**	**Raw**
S0425	**4.19**	4.95	4.99	5.24	5.89	**3.19**	3.56	4.61	4.91	6.13

Test #									
S0433	2.83	**2.73**	2.86	2.92	2.85	**2.60**	2.85	3.53	3.99	4.24
S0436	5.95	**5.94**	6.65	7.03	6.31	**5.41**	5.71	6.08	6.27	6.35
S0442	3.54	**3.42**	5.06	6.64	8.85	**3.12**	3.19	3.41	4.20	5.85

Table M5. Endevco 7302BM5: Res_{err} for both tracked markers. Minimum value of the metric for each of the analyzed tests indicated in green. CFC filters utilized on the input AAC data.

Test #	Res_{err} (in millimeters)									
	Marker 1					Marker 2				
	CFC 60	**CFC 180**	**CFC 600**	**CFC 1000**	**Raw**	**CFC 60**	**CFC 180**	**CFC 600**	**CFC 1000**	**Raw**
S0425	4.41	**4.39**	4.39	4.39	4.40	7.92	7.84	7.81	7.81	**7.81**
S0433	10.38	10.34	**10.32**	10.33	10.33	15.66	**15.61**	15.61	15.63	15.64
S0436	**16.98**	17.03	17.02	17.03	17.03	**10.80**	10.87	10.90	10.90	10.90
S0442	**5.16**	5.22	5.21	5.20	5.18	4.60	4.45	4.39	4.38	**4.38**

APPENDIX N – ERROR EFFECTS – ANALYTICAL ANALYSIS

$$\iint_0^t (b_{acc\_x}a_{px}(t) + c_{acc\_x})dtdt = b_{acc\_x}\iint_0^t a_{px}dtdt + c_{acc\_x}\iint_0^t dtdt$$

$$= b_{acc\_x}A_{px}(t) + c_{acc\_x}\frac{t^2}{2}$$

(N1)

$$\iint_0^t \rho_x\left(b_{ars\_y}\omega_y(t) + c_{ars\_y}\right)^2 dtdt$$

$$= \rho_x \iint_0^t \left(b_{ars\_y}^2\omega_y^2 + 2b_{ars\_y}c_{ars\_y}\omega_y + c_{ars\_y}^2\right)dtdt$$

$$= \rho_x\left(b_{ars\_y}^2\iint_0^t \omega_y^2 dtdt + 2b_{ars\_y}c_{ars\_y}\iint_0^t \omega_y dtdt + c_{ars\_y}^2\iint_0^t dtdt\right)$$

$$= \rho_x\left(b_{ars\_y}^2 W_{y^2}(t) + 2b_{ars\_y}c_{ars\_y}W_y(t) + c_{ars\_y}^2\frac{t^2}{2}\right)$$

(N2)

$$\iint_0^t \rho_y\left(b_{ars\_x}\omega_x(t) + c_{ars\_x}\right)\left(b_{ars\_y}\omega_y(t) + c_{ars\_y}\right)dtdt$$

$$= \rho_y \iint_0^t \left(b_{ars\_x}b_{ars\_y}\omega_x\omega_y + b_{ars\_x}c_{ars\_y}\omega_x + b_{ars\_y}c_{ars\_x}\omega_y\right.$$

$$\left. + c_{ars\_x}c_{ars\_y}\right)dtdt$$

$$= \rho_y\left(b_{ars\_x}b_{ars\_y}\iint_0^t \omega_x\omega_y dtdt + b_{ars\_x}c_{ars\_y}\iint_0^t \omega_x dtdt\right.$$

$$\left. + b_{ars\_y}c_{ars\_x}\iint_0^t \omega_y dtdt + c_{ars\_x}c_{ars\_y}\iint_0^t dtdt\right)$$

$$= \rho_y\left(b_{ars\_x}b_{ars\_y}W_{xy}(t) + b_{ars\_x}c_{ars\_y}W_x(t) + b_{ars\_y}c_{ars\_x}W_y(t)\right.$$

$$\left. + c_{ars\_x}c_{ars\_y}\frac{t^2}{2}\right)$$

(N3)

$$\iint_0^t \rho_z\left(b_{aac\_y}\alpha_y(t) + c_{aac\_y}\right)dtdt = \rho_z\left(b_{aac\_y}\iint_0^t \alpha_y dtdt + c_{aac\_y}\iint_0^t dtdt\right)$$

$$= \rho_z\left(b_{aac\_y}\Phi_y(t) + c_{aac\_y}\frac{t^2}{2}\right)$$

(N4)

APPENDIX O – ERROR EFFECTS – REGRESSION MODELS

Initial regression model:

$$Res_{err} = -1 + (yaw_{err} * pitch_{err} + yaw_{err} * roll_{err} + roll_{err} * pitch_{err}) * (c_{acc\_x} + c_{acc\_y} + c_{acc\_z} + c_{acc\_x}^2 + c_{acc\_y}^2 + c_{acc\_z}^2 + c_{ars\_x} * c_{ars\_y} + c_{ars\_x} * c_{ars\_z} + c_{ars\_y} * c_{ars\_z} + c_{ars\_x}^3 + c_{ars\_y}^3 + c_{ars\_z}^3)$$

where "-1" means "no intercept"

Table O1. Linear regression model for Case 1 and Case 2.

No.	Case 1 (Test S0433)		Case 2 (Test S0442)	
	Coefficient	Term	Coefficient	Term
1	0.0008	c_{acc_x}	-0.0028	b_{acc_z}
2	0.0012	c_{acc_y}	0.0030	b_{ars_x}
3	0.0029	c_{acc_z}	0.0013	c_{acc_x}
4	0.0021	c_{ars_x}	-0.0018	c_{acc_y}
5	0.0000	c_{ars_y}	0.0014	c_{acc_z}
6	0.0002	c_{ars_z}	0.0011	c_{ars_x}
7	-0.0022	$roll_{err}$	0.0001	c_{ars_y}
8	0.0054	$c_{acc\_x} * c_{acc\_y}$	-0.0010	c_{ars_z}
9	-0.0573	$c_{acc\_x} * c_{ars\_y}$	0.0034	$b_{acc\_z} * c_{acc\_x}$
10	0.0585	$c_{acc\_y} * c_{ars\_x}$	0.0043	$b_{acc\_z} * c_{acc\_z}$
11	-0.0032	$c_{acc\_z} * c_{ars\_y}$	0.0044	$b_{ars\_x} * c_{acc\_y}$
12	-0.0010	$c_{ars\_x} * c_{ars\_y}$	0.0035	$b_{ars\_x} * c_{acc\_z}$
13	0.0014	$c_{ars\_x} * c_{ars\_z}$	-0.0033	$c_{acc\_x} * c_{ars\_x}$
14	0.0019	$c_{ars\_y} * c_{ars\_z}$	-0.0380	$c_{acc\_x} * c_{ars\_y}$
15	-0.0039	$yaw_{err} * pitch_{err}$	-0.0037	$c_{acc\_x} * c_{ars\_z}$
16	-0.0058	$yaw_{err} * roll_{err}$	0.0335	$c_{acc\_y} * c_{acc\_z}$
17	0.0062	$pitch_{err} * roll_{err}$	0.0392	$c_{acc\_y} * c_{ars\_x}$
18	0.2303	$c_{acc\_x}^2$	0.0033	$c_{ars\_x} * c_{ars\_y}$
19	0.2178	$c_{acc\_y}^2$	0.0016	$c_{ars\_x} * c_{ars\_z}$
20	0.0768	$c_{acc\_z}^2$	0.0041	$c_{ars\_y} * c_{ars\_z}$
21	0.0816	$c_{ars\_x}^2$	-0.0066	$yaw_{err} * roll_{err}$
22	0.0849	$c_{ars\_y}^2$	-0.0002	$pitch_{err} * roll_{err}$
23	0.0800	$c_{ars\_z}^2$	0.2224	$c_{acc\_x}^2$
24	0.0011	$c_{acc\_x} * pitch_{err} * roll_{err}$	0.2146	$c_{acc\_y}^2$
25	0.0062	$c_{acc\_y} * yaw_{err} * pitch_{err}$	0.0818	$c_{acc\_z}^2$
26	0.0031	$c_{ars\_x} * yaw_{err} * pitch_{err}$	0.0824	$c_{ars\_x}^2$
27	0.0072	$c_{ars\_x} * yaw_{err} * roll_{err}$	0.0815	$c_{ars\_y}^2$
28	-0.0099	$c_{ars\_x} * pitch_{err} * roll_{err}$	0.0799	$c_{ars\_z}^2$
29	-0.0126	$c_{ars\_y} * yaw_{err} * pitch_{err}$	0.0022	$c_{acc\_y} * yaw_{err} * roll_{err}$
30	-0.0099	$c_{ars\_y} * yaw_{err} * roll_{err}$	-0.0024	$c_{acc\_z} * pitch_{err} * roll_{err}$
31	0.0229	$c_{ars\_y} * pitch_{err} * roll_{err}$	0.0026	$c_{ars\_x} * pitch_{err} * roll_{err}$
32	0.0032	$c_{ars\_z} * yaw_{err} * pitch_{err}$	-0.0083	$c_{ars\_z} * yaw_{err} * roll_{err}$
33	0.0037	$c_{ars\_z} * pitch_{err} * roll_{err}$	-0.0022	$c_{ars\_z} * pitch_{err} * roll_{err}$

No.	Coefficient	Term	Coefficient	Term
34	-0.0013	$c_{ars\_y}^3$	-0.0143	$c_{ars\_x} * c_{ars\_z} * pitch_{err} * roll_{err}$
35	-0.0098	$c_{ars\_x} * c_{ars\_y} * yaw_{err} * pitch_{err}$	0.0136	$c_{acc\_y}^2 * yaw_{err} * roll_{err}$
36	-0.0106	$c_{ars\_x} * c_{ars\_z} * yaw_{err} * pitch_{err}$	0.0140	$c_{acc\_z}^2 * pitch_{err} * roll_{err}$
37	-0.0105	$c_{ars\_x} * c_{ars\_z} * pitch_{err} * roll_{err}$	-0.0142	$c_{ars\_z}^2 * pitch_{err} * roll_{err}$
38	-0.0145	$c_{ars\_y} * c_{ars\_z} * yaw_{err} * pitch_{err}$		
39	-0.0121	$c_{acc\_x}^2 * pitch_{err} * roll_{err}$		
40	0.0120	$c_{ars\_x}^2 * yaw_{err} * roll_{err}$		
41	0.0091	$c_{ars\_y}^2 * yaw_{err} * pitch_{err}$		
42	-0.0018	$c_{ars\_y}^2 * pitch_{err} * roll_{err}$		
43	0.0282	$c_{ars\_y}^3 * yaw_{err} * pitch_{err}$		
44	-0.0355	$c_{ars\_y}^3 * pitch_{err} * roll_{err}$		

Table O2. Linear regression model for Case 3 and Case 4.

No.	Case 3 (Test S0457)		Case 4 (Test S0461)	
	Coefficient	Term	Coefficient	Term
1	0.0022	c_{acc_x}	0.0001	c_{acc_x}
2	-0.0014	c_{acc_y}	0.0006	c_{acc_y}
3	0.0019	c_{acc_z}	0.0017	c_{acc_z}
4	0.0020	c_{ars_x}	0.0016	c_{ars_x}
5	-0.0004	c_{ars_y}	0.0005	c_{ars_y}
6	0.0000	c_{ars_z}	0.0041	c_{ars_z}
7	-0.0029	$roll_{err}$	0.0040	$c_{acc\_x} * c_{ars\_x}$
8	-0.0046	$c_{acc\_x} * c_{acc\_y}$	-0.0493	$c_{acc\_x} * c_{ars\_y}$
9	-0.0135	$c_{acc\_x} * c_{acc\_z}$	-0.0204	$c_{acc\_y} * c_{acc\_z}$
10	-0.0484	$c_{acc\_x} * c_{ars\_y}$	0.0516	$c_{acc\_y} * c_{ars\_x}$
11	-0.0173	$c_{acc\_x} * roll_{err}$	-0.0043	$c_{acc\_z} * c_{ars\_x}$
12	-0.0142	$c_{acc\_y} * c_{acc\_z}$	-0.0033	$c_{acc\_z} * c_{ars\_y}$
13	0.0446	$c_{acc\_y} * c_{ars\_x}$	0.0014	$c_{ars\_x} * c_{ars\_z}$
14	0.0015	$c_{ars\_x} * c_{ars\_z}$	0.0023	$c_{ars\_y} * c_{ars\_z}$
15	0.0133	$c_{ars\_x} * roll_{err}$	-0.0037	$yaw_{err} * pitch_{err}$
16	0.0022	$c_{ars\_y} * c_{ars\_z}$	-0.0054	$yaw_{err} * roll_{err}$
17	0.0157	$c_{ars\_y} * roll_{err}$	0.0061	$pitch_{err} * roll_{err}$
18	-0.0036	$yaw_{err} * pitch_{err}$	0.2254	$c_{acc\_x}^2$
19	-0.0069	$yaw_{err} * roll_{err}$	0.2191	$c_{acc\_y}^2$
20	0.0061	$pitch_{err} * roll_{err}$	0.0783	$c_{acc\_z}^2$
21	0.2249	$c_{acc\_x}^2$	0.0807	$c_{ars\_x}^2$
22	0.2062	$c_{acc\_y}^2$	0.0850	$c_{ars\_y}^2$
23	0.0741	$c_{acc\_z}^2$	0.0809	$c_{ars\_z}^2$
24	0.0767	$c_{ars\_x}^2$	0.0008	$c_{acc\_x} * pitch_{err} * roll_{err}$
25	0.0809	$c_{ars\_y}^2$	0.0062	$c_{acc\_y} * yaw_{err} * pitch_{err}$
26	0.0767	$c_{ars\_z}^2$	0.0033	$c_{ars\_x} * yaw_{err} * pitch_{err}$
27	0.0012	$c_{acc\_x} * pitch_{err} * roll_{err}$	0.0080	$c_{ars\_x} * yaw_{err} * roll_{err}$
28	0.0056	$c_{acc\_y} * yaw_{err} * pitch_{err}$	-0.0095	$c_{ars\_x} * pitch_{err} * roll_{err}$

No.	Coefficient	Term	Coefficient	Term
29	0.0025	$c_{ars\_x} * yaw_{err} * pitch_{err}$	-0.0129	$c_{ars\_y} * yaw_{err} * pitch_{err}$
30	0.0069	$c_{ars\_x} * yaw_{err} * roll_{err}$	-0.0099	$c_{ars\_y} * yaw_{err} * roll_{err}$
31	-0.0089	$c_{ars\_x} * pitch_{err} * roll_{err}$	0.0224	$c_{ars\_y} * pitch_{err} * roll_{err}$
32	-0.0125	$c_{ars\_y} * yaw_{err} * pitch_{err}$	0.0039	$c_{ars\_z} * yaw_{err} * pitch_{err}$
33	-0.0097	$c_{ars\_y} * yaw_{err} * roll_{err}$	0.0178	$c_{ars\_z} * pitch_{err} * roll_{err}$
34	0.0223	$c_{ars\_y} * pitch_{err} * roll_{err}$	-0.0020	$c_{ars\_y}^3$
35	0.0035	$c_{ars\_z} * yaw_{err} * pitch_{err}$	-0.0066	$c_{ars\_z}^3$
36	0.0037	$c_{ars\_z} * pitch_{err} * roll_{err}$	-0.0101	$c_{ars\_x} * c_{ars\_z} * yaw_{err} * pitch_{err}$
37	-0.0016	$c_{ars\_y}^3$	-0.0106	$c_{ars\_x} * c_{ars\_z} * pitch_{err} * roll_{err}$
38	-0.0100	$c_{ars\_x} * c_{ars\_z} * yaw_{err} * pitch_{err}$	-0.0149	$c_{ars\_y} * c_{ars\_z} * yaw_{err} * pitch_{err}$
39	-0.0098	$c_{ars\_x} * c_{ars\_z} * pitch_{err} * roll_{err}$	-0.0120	$c_{acc\_x}^2 * pitch_{err} * roll_{err}$
40	-0.0145	$c_{ars\_y} * c_{ars\_z} * yaw_{err} * pitch_{err}$	0.0130	$c_{ars\_x}^2 * yaw_{err} * roll_{err}$
41	-0.0122	$c_{acc\_x}^2 * pitch_{err} * roll_{err}$	0.0105	$c_{ars\_y}^2 * yaw_{err} * pitch_{err}$
42	0.0111	$c_{ars\_x}^2 * yaw_{err} * roll_{err}$	-0.0034	$c_{ars\_y}^2 * pitch_{err} * roll_{err}$
43	0.0091	$c_{ars\_y}^2 * yaw_{err} * pitch_{err}$	-0.0003	$c_{ars\_z}^2 * pitch_{err} * roll_{err}$
44	-0.0026	$c_{ars\_y}^2 * pitch_{err} * roll_{err}$	0.0268	$c_{ars\_y}^3 * yaw_{err} * pitch_{err}$
45	0.0263	$c_{ars\_y}^3 * yaw_{err} * pitch_{err}$	-0.0347	$c_{ars\_y}^3 * pitch_{err} * roll_{err}$
46	-0.0353	$c_{ars\_y}^3 * pitch_{err} * roll_{err}$	-0.0239	$c_{ars\_z}^3 * pitch_{err} * roll_{err}$

Table O3. Linear regression model for Case 5.

No.	Case 5 (Test v10133)		No.	Case 5 (Test v10133)	
	Coefficient	Term		Coefficient	Term
1	-0.0024	b_{acc_z}	31	0.2064	$c_{acc\_x}^2$
2	0.0031	b_{ars_x}	32	0.2093	$c_{acc\_y}^2$
3	0.0029	c_{acc_x}	33	0.0797	$c_{acc\_z}^2$
4	0.0030	c_{acc_y}	34	0.0878	$c_{ars\_x}^2$
5	0.0014	c_{acc_z}	35	0.0892	$c_{ars\_y}^2$
6	0.0020	c_{ars_x}	36	0.0773	$c_{ars\_z}^2$
7	-0.0013	c_{ars_y}	37	0.0082	$c_{acc\_x} * yaw_{err} * roll_{err}$
8	-0.0005	c_{ars_z}	38	-0.0001	$c_{acc\_y} * yaw_{err} * roll_{err}$
9	-0.0028	$roll_{err}$	39	0.0008	$c_{acc\_y} * pitch_{err} * roll_{err}$
10	0.0034	$b_{acc\_z} * c_{acc\_x}$	40	-0.0037	$c_{acc\_z} * pitch_{err} * roll_{err}$
11	0.0046	$b_{acc\_z} * c_{acc\_z}$	41	0.0031	$c_{ars\_x} * pitch_{err} * roll_{err}$
12	0.0054	$b_{ars\_x} * c_{acc\_y}$	42	0.0139	$c_{ars\_y} * yaw_{err} * pitch_{err}$
13	-0.0217	$c_{acc\_x} * c_{acc\_y}$	43	0.0157	$c_{ars\_y} * pitch_{err} * roll_{err}$
14	-0.0196	$c_{acc\_x} * c_{acc\_z}$	44	0.0060	$c_{ars\_z} * yaw_{err} * pitch_{err}$
15	-0.0155	$c_{acc\_x} * c_{ars\_x}$	45	-0.0059	$c_{ars\_z} * yaw_{err} * roll_{err}$
16	-0.0731	$c_{acc\_x} * c_{ars\_y}$	46	-0.0039	$c_{ars\_z} * pitch_{err} * roll_{err}$
17	-0.0037	$c_{acc\_x} * c_{ars\_z}$	47	-0.0005	$c_{ars\_y}^3$
18	0.0192	$c_{acc\_x} * roll_{err}$	48	-0.0116	$c_{ars\_x} * c_{ars\_z} * pitch_{err} * roll_{err}$
19	0.0304	$c_{acc\_y} * c_{acc\_z}$	49	0.0105	$c_{acc\_y}^2 * yaw_{err} * roll_{err}$
20	0.0747	$c_{acc\_y} * c_{ars\_x}$	50	-0.0118	$c_{acc\_y}^2 * pitch_{err} * roll_{err}$
21	-0.0279	$c_{acc\_y} * roll_{err}$	51	0.0125	$c_{acc\_z}^2 * pitch_{err} * roll_{err}$

22	0.0086	$c_{acc\_z} * c_{ars\_x}$	**52**	0.0041	$c_{ars\_y}^2 * yaw_{err} * pitch_{err}$
23	-0.0067	$c_{acc\_z} * roll_{err}$	**53**	0.0061	$c_{ars\_y}^2 * pitch_{err} * roll_{err}$
24	0.0008	$c_{ars\_x} * c_{ars\_z}$	**54**	-0.0288	$c_{ars\_y}^3 * yaw_{err} * pitch_{err}$
25	0.0204	$c_{ars\_x} * roll_{err}$			
26	0.0037	$c_{ars\_y} * c_{ars\_z}$			
27	-0.0471	$c_{ars\_y} * roll_{err}$			
28	-0.0022	$yaw_{err} * pitch_{err}$			
29	-0.0015	$yaw_{err} * roll_{err}$			
30	-0.0031	$pitch_{err} * roll_{err}$			

APPENDIX P – ERROR EFFECTS – ERROR HIERARCHY BASED ON *mRES$_{ERR}$* AND *mDIFF$_{MAX}$*

Table P1. Error hierarchy based on mRes$_{err}$ for each of the five test cases.

#	Case 1	Case 2	Case 3	Case 4	Case 5
1	ACC debias	ACC debias	ACC debias	ACC debias	ACC debias
2	ARS debias	ARS debias	ARS debias	ARS debias	ARS debias
3	ACC sensitivity	ACC sensitivity	ACC sensitivity	ACC sensitivity	ACC sensitivity
4	Initial orientation in IRF	Initial orientation in IRF	ACC noise	Initial orientation in IRF	Initial orientation in IRF
5	ACC noise	ACC noise	Initial orientation in IRF	ARS sensitivity	ACC noise
6	ARS sensitivity	ARS sensitivity	ARS sensitivity	ACC seismic mass CG position in BF	ARS sensitivity
7	ACC seismic mass CG position in BF	ACC seismic mass CG position in BF	ACC seismic mass CG position in BF	ACC Noise	ACC seismic mass CG position in BF
8	ACC angle misalignment	ACC angle misalignment	ACC angle misalignment	ACC angle misalignment	ARS noise
9	ARS noise	ARS noise	ARS noise	ARS noise	ACC angle misalignment
10	ARS angle misalignment	ARS angle misalignment	ARS angle misalignment	ARS angle misalignment	ARS angle misalignment
11	Head CG initial position in IRF	Head CG initial position in IRF	Head CG initial position in IRF	Head CG initial position in IRF	Head CG initial position in IRF

Table P2. Error hierarchy based on mdiff$_{max}$ for each of the five test cases.

#	Case 1	Case 2	Case 3	Case 4	Case 5
1	ACC debias	ACC debias	ACC debias	ACC debias	ACC debias
2	ARS debias	ARS debias	ARS debias	ARS debias	ARS debias
3	ACC sensitivity	ACC sensitivity	ACC sensitivity	ACC sensitivity	ACC sensitivity
4	Initial orientation in IRF	Initial orientation in IRF	Initial orientation in IRF	Initial orientation in IRF	Initial orientation in IRF
5	ACC noise	ARS sensitivity	ACC noise	ARS sensitivity	ACC noise
6	ARS sensitivity	ACC Noise	ARS sensitivity	ACC noise	ARS sensitivity
7	ACC seismic mass CG position in BF	ACC seismic mass CG position in BF	ACC seismic mass CG position in BF	ACC seismic mass CG position in BF	ACC seismic mass CG position in BF
8	ACC Angle misalignment	Head CG initial position in IRF	Head CG initial position in IRF	Head CG initial position in IRF	ARS Noise
9	Head CG initial position in IRF	ACC Angle misalignment	ACC Angle misalignment	ACC Angle misalignment	Head CG initial position in IRF
10	ARS noise	ARS noise	ARS noise	ARS noise	ACC angle misalignment
11	ARS angle misalignment	ARS angle misalignment	ARS angle misalignment	ARS angle misalignment	ARS angle misalignment

APPENDIX Q – REDUNDANT SENSORS – CONSISTENCY CHECK – STEP 2 – NON-UNIQUE SOLUTION

Let us assume that two angular rate sensors, ω_{p1} and ω_{p2}, were added to a sensor block. The sensing axes of the two redundant ARS were aligned together and the angles defining their orientation (as defined in Figure 113) were known. Based on Eq. 11.9, the relationship between both redundant ARS and the three ARS measuring body's angular velocity around the axes of the body's local coordinate system can be then defined as:

$$\omega_{p1} = \omega_{p2} = \omega_x \cos\alpha + \omega_y \cos\beta + \omega_z \cos\gamma \tag{Q.1}$$

Utilizing the angular velocity measured by one of the added sensors, for example ω_{p2}, the time-history of angular rate around the local Y-axis (treated here as potentially affected by an error) can be predicted as:

$$\omega_y = \frac{\omega_{p2} - \omega_x \cos\alpha - \omega_z \cos\gamma}{\cos\beta} \tag{Q.2}$$

To eliminate the effect of a potentially faulty ω_y reading on the prediction, for example, of ω_x, Eq. Q.2 was substituted into Eq. Q.1. After simple algebraic manipulations, the reading for ω_x was expressed in the function of the two redundant ARS and ω_z:

$$\omega_x = \frac{\omega_{p1} - \left[\frac{\omega_{p2} - \omega_x \cos\alpha - \omega_z \cos\gamma}{\cos\beta}\right] \cos\beta - \omega_z \cos\gamma}{\cos\alpha} \tag{Q.3}$$

Using Eq. Q.3 it can be shown that when the sensing axes of the two redundant ARS are at the same angle, ω_x cannot be predicted, i.e., Eq. Q.3 does not have a unique solution:

$$\omega_x \cos\alpha = \omega_{p1} - \omega_{p2} + \omega_x \cos\alpha + \omega_z \cos\gamma - \omega_z \cos\gamma \tag{Q.4}$$

$$\omega_x \cos\alpha = \omega_x \cos\alpha \Rightarrow 1 = 1 \tag{Q.5}$$

APPENDIX R – SENSOR FUSION IN THOR TESTS – SENSOR UNCERTAINTIES BASED ON CALIBRATION SHEETS

STD – reference value (i.e., value sensor should measure)
UUT – unit under test (i.e., value as recorded by sensor)
FS – full scale range

Table R1. Measurement deviation for ARS X based on standardized calibration check test. As recorded on senor calibration sheet.

Angular rate sensor aligned with local X axis							
DTS ARS PRO 300 Hz				DTS ARS PRO 2000 Hz			
STD	UUT	Deviation of UUT from STD		STD	UUT	Deviation of UUT from STD	
deg/s	deg/s	% FS	deg/s	deg/s	deg/s	% FS	deg/s
-8399.4	-8397.9	0.01875	1.5	-8399.5	-8403.4	-0.04875	-3.9
-8009.4	-8009.2	0.0025	0.2	-8009.4	-8012.9	-0.04375	-3.5
-5999.6	-6004.1	-0.05625	-4.5	-5999.5	-6001.4	-0.02375	-1.9
-4499.6	-4505.2	-0.07	-5.6	-4499.6	-4500.3	-0.00875	-0.7
-2999.8	-3004.6	-0.06	-4.8	-2999.8	-2999.9	-0.00125	-0.1
-1499.8	-1503	-0.04	-3.2	-1499.9	-1499.8	0.00125	0.1
1500	1501.9	0.02375	1.9	1500	1499.6	-0.005	-0.4
2999.9	3002.9	0.0375	3	2999.9	2999	-0.01125	-0.9
4499.8	4503.1	0.04125	3.3	4499.8	4498.1	-0.02125	-1.7
5999.7	6001.3	0.02	1.6	5999.7	5997.3	-0.03	-2.4
8009.6	8003.9	-0.07125	-5.7	8009.5	8005.9	-0.045	-3.6
8399.5	8391.9	-0.095	-7.6	8399.6	8395.6	-0.05	-4
RMSE (treated as $u_{calib\_sheet\_based}$)			4.12	RMSE (treated as $u_{calib\_sheet\_based}$)			2.42

Table R2. Measurement deviation for ARS Y based on standardized calibration check test. As recorded on senor calibration sheet.

Angular rate sensor aligned with local Y axis							
DTS ARS PRO 300 Hz				DTS ARS PRO 2000 Hz			
STD	UUT	Deviation of UUT from STD		STD	UUT	Deviation of UUT from STD	
deg/s	deg/s	% FS	deg/s	deg/s	deg/s	% FS	deg/s
-8399.4	-8398.1	0.01625	1.3	-8399.4	-8404.1	-0.05875	-4.7
-8009.4	-8010.3	-0.01125	-0.9	-8009.4	-8013.7	-0.05375	-4.3
-5999.6	-6005.2	-0.07	-5.6	-5999.6	-6001.5	-0.02375	-1.9
-4499.6	-4505.5	-0.07375	-5.9	-4499.6	-4500.4	-0.01	-0.8
-2999.8	-3004.9	-0.06375	-5.1	-2999.8	-3000.2	-0.005	-0.4
-1499.8	-1503	-0.04	-3.2	-1499.8	-1499.8	0	0.0
1499.9	1502.5	0.0325	2.6	1500	1499.7	-0.00375	-0.3
2999.9	3004.3	0.055	4.4	2999.9	2999	-0.01125	-0.9
4499.7	4504.4	0.05875	4.7	4499.7	4498.2	-0.01875	-1.5
5999.7	6002.3	0.0325	2.6	5999.7	5997.2	-0.03125	-2.5
8009.6	8003.7	-0.07375	-5.9	8009.6	8005.4	-0.0525	-4.2

8399.5	8391.2	-0.10375	-8.3	8399.5	8395.2	-0.05375	-4.3
RMSE (treated as $u_{calib\_sheet\_based}$)			4.69	RMSE (treated as $u_{calib\_sheet\_based}$)			2.75

Table R3. Measurement deviation for ARS Z based on standardized calibration check test. As recorded on senor calibration sheet.

Angular rate sensor aligned with local Z axis							
DTS ARS PRO 300 Hz				DTS ARS PRO 2000 Hz			
STD	UUT	Deviation of UUT from STD		STD	UUT	Deviation of UUT from STD	
deg/s	deg/s	% FS	deg/s	deg/s	deg/s	% FS	deg/s
-8399.4	-8399.4	0	0	-8399.4	-8403	-0.045	-3.6
-8009.4	-8010	-0.0075	-0.6	-8009.4	-8012.7	-0.04125	-3.3
-5999.6	-6003.2	-0.045	-3.6	-5999.5	-6001	-0.01875	-1.5
-4499.6	-4503.9	-0.05375	-4.3	-4499.6	-4500.3	-0.00875	-0.7
-2999.8	-3003	-0.04	-3.2	-2999.8	-3000	-0.0025	-0.2
-1499.9	-1502.1	-0.0275	-2.2	-1499.8	-1499.7	0.00125	0.1
1499.9	1500.9	0.0125	1	1499.9	1499.5	-0.005	-0.4
2999.9	3002.5	0.0325	2.6	2999.9	2999.2	-0.00875	-0.7
4499.7	4502.2	0.03125	2.5	4499.7	4498.2	-0.01875	-1.5
5999.7	6000.4	0.00875	0.7	5999.7	5997.8	-0.02375	-1.9
8009.6	8005.3	-0.05375	-4.3	8009.5	8006.3	-0.04	-3.2
8399.6	8393.1	-0.08125	-6.5	8399.6	8396.2	-0.0425	-3.4
RMSE (treated as $u_{calib\_sheet\_based}$)			3.19	RMSE (treated as $u_{calib\_sheet\_based}$)			2.14

Table R4. Measurement deviation for ACC X based on standardized calibration check test. As recorded on senor calibration sheet.

Linear accelerometer aligned with local X axis			
Endevco 7264C		Endevco 7290E	
Frequency (Hz)	% deviation of UUT from STD at 30 g (g)	Frequency (Hz)	% deviation of UUT from STD at 30 g (g)
20	0.126844	10	-0.217566
22	0.126844	12.5	-0.223655
25	0.023379	16	-0.135610
27	0.023379	20	-0.108390
30	-0.054692	25	-0.093289
33	0.023379	31.5	-0.090271
36	0.023379	40	-0.090271
40	0.023379	50	-0.090271
44	0.023379	63	-0.093289
48	0.023379	80	-0.003000
54	0.023379	100	0.000000
59	0.023379	125	-0.042059

Frequency	% dev	Frequency	% dev
66	0.023379	160	-0.114435
72	0.023379	200	-0.015008
78	0.023379	250	-0.024019
87	0.023379	315	-0.015008
96	0.023379	400	-0.057109
104	0.023379	500	-0.030030
117	0.023379	630	-0.021015
129	0.023379	800	0.000000
142	0.023379	1000	-0.015008
155	0.023379		
172	0.023379	RMSE (treated as $u_{calib\_sheet\_base}$)	0.0951
189	0.023379		
209	0.023379		
229	0.023379		
254	0.023379		
279	0.023379		
309	0.023379		
339	-0.054692		
371	-0.054692		
413	-0.054692		
453	-0.054692		
500	-0.054692		
550	-0.054692		
613	-0.054692		
666	-0.028623		
733	-0.054692		
813	-0.054692		
890	-0.028623		
987	-0.028623		
RMSE (treated as $u_{calib\_sheet\_based}$)	0.0438		

Table R5. Measurement deviation for ACC Y based on standardized calibration check test. As recorded on senor calibration sheet.

Linear accelerometer aligned with local Y axis			
Endevco 7264C		Endevco 7290E	
Frequency (Hz)	% deviation of UUT from STD at 30 g (g)	Frequency (Hz)	% deviation of UUT from STD at 30 g (g)
20	0.074813	10	-0.232793
22	0.074813	12.5	-0.223655

25	0.000000	16	-0.153784
27	0.000000	20	-0.117458
30	0.000000	25	-0.099328
33	0.000000	31.5	-0.096308
36	0.024979	40	-0.099328
40	0.000000	50	-0.102348
44	0.000000	63	-0.108390
49	0.000000	80	0.008997
54	0.074813	100	0.000000
59	0.000000	125	-0.045068
66	0.000000	160	-0.114435
72	0.000000	200	-0.015008
79	0.000000	250	-0.015008
87	0.000000	315	-0.018011
96	0.000000	400	-0.036043
103	0.000000	500	0.000000
107	0.000000	630	0.038949
117	0.000000	800	0.101654
130	0.000000	1000	0.152224
142	0.000000		
155	0.000000	RMSE (treated as $u_{calib\_sheet\_base}$)	0.1081
172	0.000000		
189	0.000000		
210	0.000000		
230	0.000000		
254	0.000000		
279	0.000000		
309	0.000000		
339	-0.100334		
373	-0.075188		
412	-0.075188		
454	-0.075188		
501	-0.100334		
550	-0.075188		
612	-0.075188		
671	-0.100334		
735	-0.100334		
819	-0.075188		
887	-0.100334		
984	-0.075188		

RMSE (treated as $u_{calib\_sheet\_based}$)	0.0505

Table R6. Measurement deviation for ACC Z based on standardized calibration check test. As recorded on senor calibration sheet.

Linear accelerometer aligned with local Z axis			
Endevco 7264C		Endevco 7290E	
Frequency (Hz)	% deviation of UUT from STD at 30 g (g)	Frequency (Hz)	% deviation of UUT from STD at 30 g (g)
20	0.083275	10	-0.226700
22	0.084436	12.5	-0.208438
25	0.007716	16	-0.135610
27	0.008928	20	-0.108390
30	0.009960	25	-0.096308
33	0.011126	31.5	-0.087253
36	0.012158	40	-0.090271
40	0.013190	50	-0.093289
44	0.014356	63	-0.099328
48	0.015298	80	0.003000
54	0.016554	100	0.000000
59	0.017585	125	-0.045068
65	0.018751	160	-0.111412
72	0.019783	200	-0.015008
79	0.020814	250	-0.018011
87	0.021935	315	-0.012005
95	0.023011	400	-0.042059
105	0.024087	500	-0.006001
116	0.025252	630	0.020985
129	0.026417	800	0.071828
142	0.027448	1000	0.104634
155	0.002510		
172	0.003677	RMSE (treated as $u_{calib\_sheet\_base}$)	0.0981
188	0.004709		
209	0.031840		
229	0.032870		
254	0.008075		
278	0.009107		
307	0.010229		
338	-0.040738		
371	-0.039702		
411	-0.038532		

452	-0.037452
501	-0.010245
552	-0.035201
612	-0.034031
670	-0.032996
734	-0.031961
815	-0.030792
893	-0.029757
990	-0.028587
RMSE (treated as $u_{calib\_sheet\_based}$)	0.0298

APPENDIX S – SOFTWARE DEVELOPED TO COMPUTE 3D TRAJECTORIES OF A RIGID BODY

S.1. Description

The tracking software (called *DHT software* from here on) developed within this dissertation can be used to compute 3D component trajectories of a body from locally-mounted inertial sensors. These inertial sensors include linear accelerometers, angular rate sensors, and angular accelerometers.

Even though the software was developed mainly for use with the THOR ATD's head as Body 1 (default selection on Screen 1; Figure S1), the DHT package allows for an arbitrary rigid body to be defined as Body 1. As an option, the software enables calculation of 3D component trajectories of an arbitrary Body 2 (e.g. vehicle, ATD's pelvis, etc.) in the global (inertial) coordinate system. When Body 2 is selected, the software computes also the motion of Body 1 in the Body 2's local frame.
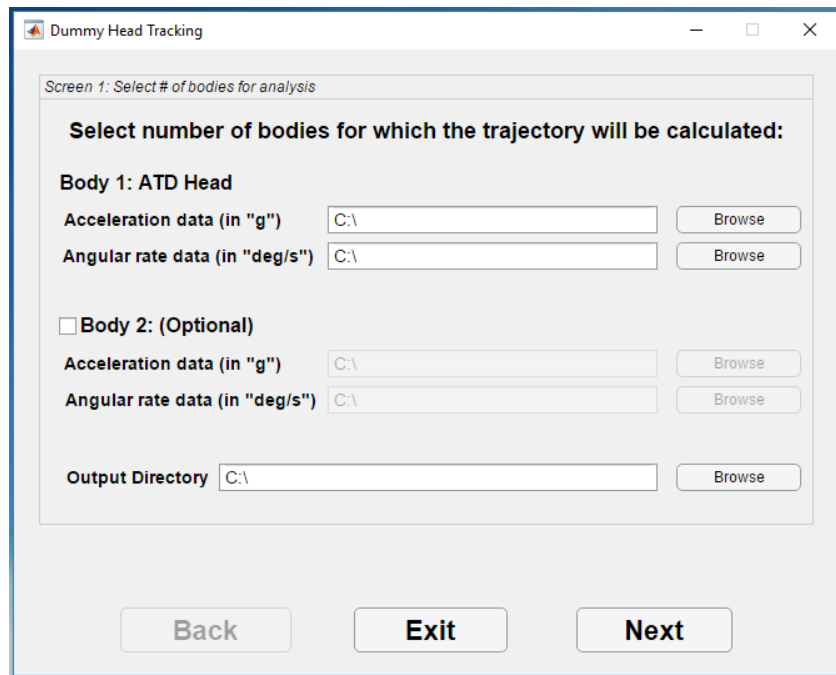
Figure S1. DHT software – Screen 1: Select # of bodies for analysis.

The graphical user interface (GUI) was developed in MATLAB 2017a (MathWorks, Natick, MA, USA).

S.2. Input data files

The *.xlsx or *.xls files with the input linear or angular accelerations as well as angular rates should be always formatted in the way depicted in Figure S2. The data should be given in the first sheet of the input file.

	A	B	C	D	
1	Time	ACC X	ACC Y	ACC Z	**Channel name**
2	s	g	g	g	**Channel units**
3	-0.05	-0.05	-0.05	-0.05	**Time at first data point**
4	0.0001	0.0001	0.0001	0.0001	**Time step**
5	s	s	s	s	**Time unit**
6	-0.05	0.139369	-0.38491	0.271667	
7	-0.0499	0.124029	-0.32698	0.225881	
8	-0.0498	0.108579	-0.27206	0.183897	
9	-0.0497	0.093977	-0.22203	0.146963	
10	-0.0496	0.080551	-0.17799	0.115847	
11	-0.0495	0.068014	-0.1405	0.09085	
12	-0.0494	0.05546	-0.10973	0.071843	
13	-0.0493	0.041699	-0.08539	0.058206	**Input Data**
14	-0.0492	0.026033	-0.06681	0.04887	
15	-0.0491	0.008937	-0.05305	0.042711	
16	-0.049	-0.00794	-0.04312	0.039104	
17	-0.0489	-0.02248	-0.03616	0.038127	
18	-0.0488	-0.03293	-0.03159	0.04017	
19	-0.0487	-0.03841	-0.02916	0.045372	
20	-0.0486	-0.03897	-0.02874	0.053345	

Figure S2. Input data format for accelerometers and angular rate sensors.

Depending on the software step (screen), the number of columns in the input file may vary. To fully capture the local acceleration of the origin of a rigid body one time column and three acceleration components are required (4 columns in total). If the user plans to use the Nine Accelerometer Package (NAP) approach to calculate the body's angular acceleration, data from nine accelerometers are needed. The acceleration input file for NAP will then have 10 columns (time + 9 acceleration traces). If the 6aω method is used, the acceleration input file will have 7 columns (time + 6 acceleration signals). Both, angular rate and angular acceleration input files need to have 4 columns. The number of rows is limited only by the computer memory.

The order of the data columns for different data input files is as follows:

- Linear Acceleration:

Time	X acceleration	Y acceleration	Z acceleration

  * Acceleration components are given in the body's local coordinate system.

- Angular Rate:

Time	X angular rate	Y angular rate	Z angular rate

  * Angular rate components are given in the body's local coordinate system.

- Angular acceleration:

Time	X acceleration	Y acceleration	Z acceleration

  * Acceleration components are given in the body's local coordinate system.

- Linear Acceleration for NAP:

Time	OX	OY	OZ	XY	XZ	YX	YZ	ZX	ZY

  * Acceleration components are given in the NAP's local coordinate system. The first letter defines the origin (O) or the arm direction. The second letter defines the direction in which the acceleration was measured.

- Linear Acceleration for 6aω:

Time	OX	OY	OZ	XY	XZ	YZ

  * Acceleration components are given in the 6aω fixture's local coordinate system. The first letter defines the origin (O) or the arm direction. The second letter defines the direction in which the acceleration was measured.

- Linear Acceleration for t6aω:

Time	OX	OY	OZ	XZ	YX	ZY

  * Acceleration components are given in the tetrahedron's local coordinate system. The first letter defines the origin (O) or the arm direction. The second letter defines the direction in which the acceleration was measured.

All input files (all data columns) for a single body should always have the same length. The length, time, and the time-step are determined based on the input linear acceleration file from Screen 1 for Body 1 and Body 2 separately. The data for Body 2 can have different length than for Body 1, but that length cannot be shorter than for Body 1. The time-step needs to be consistent between both analyzed bodies. All the input data, other than the file headers, need to be numeric and given in the units specified on the software screen.

The software does not apply any filter to the data. If filtering of the input data is required, it needs to be performed outside the DHT package.

S.3.   Sensor/landmark locations

On several DHT screens the user will be asked to provide point coordinates either to specify the location of linear accelerometers in the local coordinate system of the tracked body (Figure S3) or to establish body's initial position and orientation (Figure S4 and Figure S5).
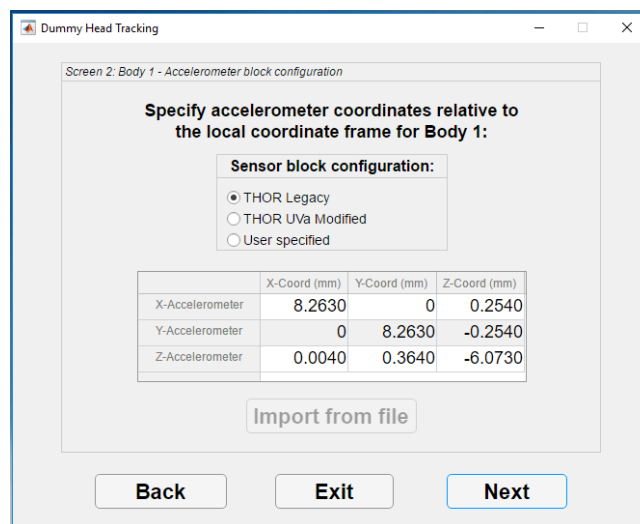

Figure S3. Screen 2 (Body 1) – Linear accelerometer coordinates in the local frame of Body 1. The user has three options to choose from: THOR Legacy (THOR stock sensor block with Endevco 7264Cs; as of August 2016), THOR UVa Modified (modification proposed by UVa), User specified (based on the input from the user).
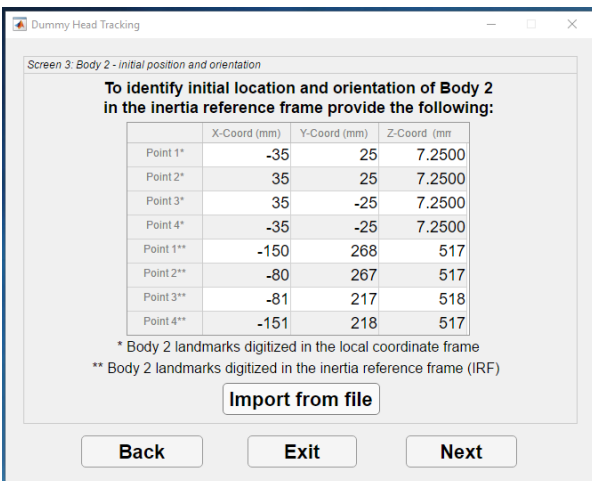
In most cases, the user can type the coordinates in manually or import them from an *.xlsx or *.xls file. The format of the *xls(x) file should be always consistent with the table on the DHT screen (examples shown in Figure S4 and Figure S5). All the input data, other than the file headers, need to be numeric and given in the units specified on the software screen. If "Import from file" is used, the data should be given in the first sheet of the input file.
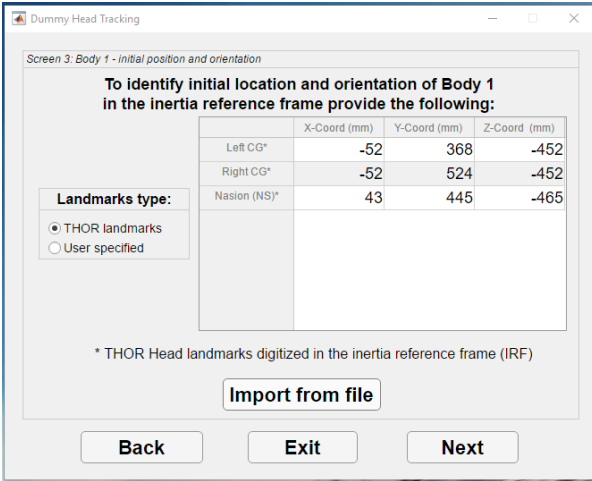
Figure S4. Screen 3 (Body 1) – exemplar input data (point coordinates) to establish the THOR's head initial position and orientation (left) and corresponding *.xls(x) file used with the "Import from file" button (right).

To identify the body initial orientation and position the user will be asked to provide point coordinates for four points on the body/fixture measured in the body/fixture local coordinate system (with the origin and local axes defined according to the following section: *Tracked Point*, see next page). Next, for the same four points, the user will be required to input the coordinates measured in the global (inertial) frame (example shown in Figure S5).

Figure S5. Screen 3 (Body 2) – exemplar input data (point coordinates) to establish Body 2's initial position and orientation (left) and corresponding *.xls(x) file used with the "Import from file" button (right).

247

S.4.   Tracked point

If *THOR landmarks* is selected for Body 1 (Screen 3; Figure S4), it is assumed that the midpoint between the Left and Right CG points is the point being tracked. For *User specified* and for Body 2, the DHT software tracks the origin of the body local coordinate system as determined based on the user input (point coordinates given on Screen 3). In all the cases mentioned above it is assumed that the origin of the body local coordinate system (LCS) is coincident with the accelerometer measurement center (Figure S6) and the LCS axes are aligned with the sensor sensing axes.
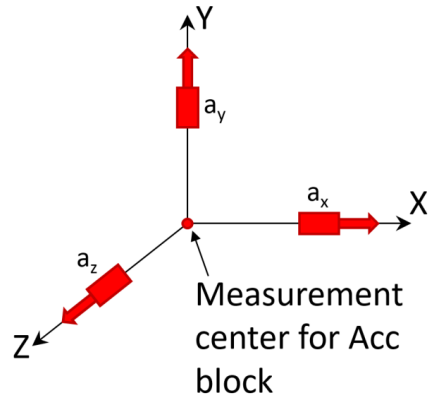
Figure S6. Schematic drawing showing the measurement center for three accelerometers mounted on the tracked body.

S.5.   Angular acceleration

DHT software allows for calculation of body's local angular acceleration (AAC). The user can select between four different methods of obtaining AAC (Figure S7). These methods are:
- Differentiation of the angular velocity vector (default option; the first order divided difference, based on the current and previous time step, is used here),
- Nine Accelerometer Package approach (NAP; Padgaonkar et al. 1975),
- 6aω (Kang et al. 2017) or its variation t6aω (Kang et al. 2015), and
- Angular acceleration can be read from an input file.

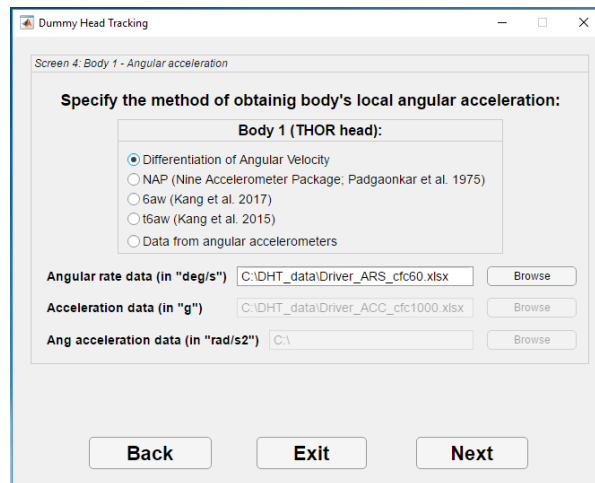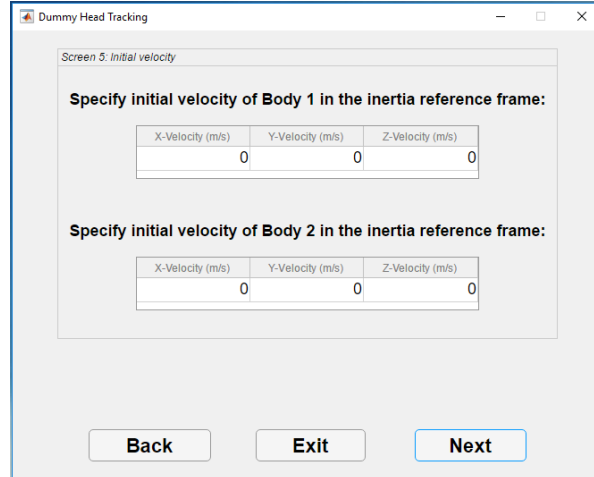***Figure S7. DHT software – Screen 4: Angular acceleration – method selection.***

248

S.6. Initial velocity

If required, the user can specify initial velocity components (in global frame) for Body 1 (always) and Body 2 (if selected). The default value for both bodies, for all three velocity components, is zero (Figure S8).
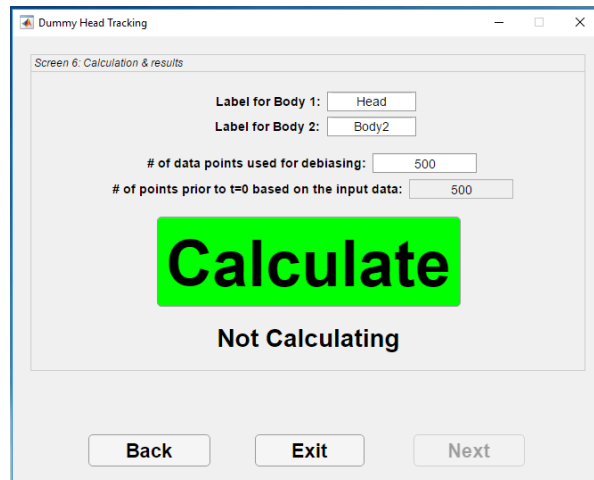

Figure S8. DHT software – Screen 5: Initial velocity.

S.7. Debias and labeling

On the last screen (Figure S9), number of points for data debiasing is specified. The value of "# of points prior to t=0" is determined based on the input linear acceleration file from Screen 1 for Body 1. The initial value of "# of data points used for debiasing" is populated from "# of points prior to t=0", but can be changed by the user, if required. No debiasing (value of "0") or one-pint debiasing (value of "1") are possible, but not recommended. The same number of data points will be used for debiasing of all data input files (for Body 1 and Body 2, if selected).

Screen 6 allows also to change the labels for Body 1 and Body 2. The labels are populated in the output files and output graphs. The labels cannot be longer that 13 characters.

Figure S9. Final DHT screen (Screen 6) with labeling and debias information.

249

S.8.   Output

The output files will be always written to "Output directory\DHT_Results\" folder. In "DHT_Results" the user will find the following:

- **Pos_of_CG.xlsx**:
  - calculated time histories of the position of the ATD head and Body 2 (if selected) in the global (inertial) coordinate system,
  - time-history of the position of the ATD head in Body 2's local coordinate system (if Body 2 selected),
- **MinMaxValues.xlsx**: min and max values and time of their occurrence for both analyzed bodies for acceleration (both, linear and angular), velocity, and position,
- **Additional/Aac_of_CG.xlsx**: calculated time histories of the local angular acceleration for the ATD head and Body 2 (if selected),
- **Additional/Acc_of_CG.xlsx**: calculated time histories of the local and global linear acceleration for the ATD head and Body 2 (if selected),
- **Additional/Body_label_Input_check.xlsx**: Input data gathered in one file, including debias information. A separate file is created for each of the two bodies (if Body 2 is selected),
- **Additional/Orientation.xlsx**: calculated time histories of the local-to-global transformation matrix for the ATD head and Body 2 (if selected),
- **Additional/Vel_of_CG.xlsx**: calculated time histories of the velocity of the ATD head and Body 2 (if selected) in the global (inertial) coordinate system.

In addition, up to three graphs will be created and saved in the folder. The graphs depict the time-history of the global trajectory components for Body 1 and Body 2, and Body 1 relative to Body 2, if Body 2 is selected on Screen 1.

S.9.   Good practices/tips
1. To minimize the error in sensor sensitivity, all not internally regulated sensors used during testing should be run at the same excitation voltage as they were run during sensor calibration.
2. If a coordinate measurement machine (CMM) is used to obtain the input position information, the number of times when the machine is moved and realigned back with the position data, should be as small as possible. Every leapfrogging step introduces an error into the position data, which can then lead to an error in the body initial orientation. Initial orientation error can have a substantial effect on the calculated trajectory.
3. If it is not possible to obtain all needed sensor position information in one take, first, measure the sensor block (and the sensors mounted on it) in relation to selected landmarks on the mounting plate/fixture, and then mount the plate/fixture on the body you want to track and measure the same landmarks again, but this time in the global reference frame.
4. It is not recommended to use 1-point data debiasing or no debiasing.
5. Be sure that the local coordinate system of your sensor block (as specified in the software) is aligned with the local coordinate system of the tracked body.

S.10. References

Local-to-global transformation: Rudd R., Kerrigan J. R., Crandall J. R., and Arregui C., 2006, "Kinematic Analysis of Head/Neck Motion in Pedestrian-Vehicle Collisions Using 6-Degree-of-Freedom Instrumentation Cubes," SAE Technical Paper: 2006-01-0681, DOI:10.4271/2006-01-0681.

NAP method: Padgaonkar A. J., Krieger K. W., and King A. I., 1975, "Measurement of Angular Acceleration of a Rigid Body Using Linear Accelerometers," Journal of Applied Mechanics, 42(3), 552-556, DOI:10.1115/1.3423640.

6aω method: Kang Y-S., Goldman S., Moorhouse K., and Bolte J., 2017, "Evaluation of a coplanar 6a3ω configuration in the Hybrid III 50th percentile male head," Traffic Injury Prevention, 18:sup1, S129-S135, DOI: 10.1080/15389588.2017.1318210.

t6aω method: Kang Y-S., Moorhouse K., and Bolte J., 2015, "Instrumentation Technique for Measuring Six Degrees of Freedom Head Kinematics in Impact Conditions using Six-Accelerometers and Three-Angular Rate Sensors (6aω Configuration) on a Lightweight Tetrahedron Fixture", In proceedings from the 24th International Technical Conference on the Enhanced Safety of Vehicles (ESV), Paper Number: 15-0288, Gothenburg, Sweden.

Method used to determine the initial orientation of Body 2 or the t6aω tetrahedron, based on 4 points in the local frame and the same 4 points taken in the global frame: Cappozzo A., Cappello A., Della Croce U., and Pensalf F., 1997, "Surface-Marker Cluster Design Criteria for 3-D Bone Movement Reconstruction," IEEE Transactions on Biomedical Engineering, Vol. 44, No. 12, December 1997.